



Cite this: *Chem. Soc. Rev.*, 2025, 54, 266

Metal complex-based TADF: design, characterization, and lighting devices

Afsaneh Farokhi,^{†a} Sophia Lipinski,^{†b} Luca M. Cavinato,^{†b} Hashem Shahroosvand,^{†b} Babak Pashaei,^{†c} Soheila Karimi,^a Sebastiano Bellani,^{de} Francesco Bonaccorso,^{de} and Rubén D. Costa^{†b}

The development of novel, efficient and cost-effective emitters for solid-state lighting devices (SSLDs) is ubiquitous to meet the increasingly demanding needs of advanced lighting technologies. In this context, the emergence of thermally activated delayed fluorescence (TADF) materials has stunned the photonics community. In particular, inorganic TADF material-based compounds can be *ad hoc* engineered by chemical modification of the coordinated ligands and the type of metal centre, allowing control of their ultimate photo-/electroluminescence properties, while providing a viable emitter platform for enhancing the efficiency of state-of-the-art organic light-emitting diodes (OLEDs) and light-emitting electrochemical cells (LECs). By presenting an overview of the state of the art of all metal complex-based TADF compounds, this review aims to provide a comprehensive, authoritative and critical reference for their design, characterization and device application, highlighting the advantages and drawbacks for the chemical, photonic and optoelectronic communities involved in this interdisciplinary research field.

Received 27th July 2024

DOI: 10.1039/d3cs01102j

rsc.li/chem-soc-rev

^a Group for Molecular Engineering of Advanced Functional Materials (GMA), Chemistry Department, University of Zanjan, Zanjan, Iran

^b Technical University of Munich, Campus Straubing for Biotechnology and Sustainability, Chair of Biogenic Functional Materials, Schulgasse 22, Straubing 94315, Germany. E-mail: ruben.costa@tum.de

^c Department of Inorganic Chemistry, Faculty of Chemistry, University of Mazandaran, Babolsar, Iran

^d Graphene Labs, Istituto Italiano di Tecnologia, 16163 Genova, Italy

^e BeDimensional Spa., 16163 Genova, Italy

[†] Equally contributed.

1. Introduction

Over the past decade, the global energy demand has been growing exponentially because of population growth and industrial development.¹ While the transition to renewable energy sources, such as wind, solar and nuclear energy,^{2,3} ubiquitous cornerstone for long-term sustainable socioeconomic,^{4,5} the introduction of efficient optoelectronics is necessary to reduce



Afsaneh Farokhi

Dr Afsaneh Farokhi completed both her BSc (2009) and MSc (2011) studies in Chemistry at the University of Zanjan (ZNU). She received her PhD degree in Inorganic Chemistry from the ZNU in 2017 to investigate the “synthesis, characterization and catalytic activity of asymmetric manganese porphyrin nanocatalysts”. From 2020 to now, Afsaneh have been a postdoctoral researcher under Prof. Hashem Shahroosvand at the

ZNU. Her current research interests are mainly focused on the design and synthesis of novel hole transport materials in perovskite solar cells (PSCs).



Sophia Lipinski

Sophia Lipinski received her bachelor's degree in chemistry from the Technical University of Munich (TUM) and her master's degree in chemistry from the University of Konstanz. Currently, she is a PhD student in Prof. Costa's group at the Chair of Biogenic Functional Materials at TUM. Her main research focuses on the synthesis and characterization of sustainable d¹⁰ transition metal complexes and their implementation in light-emitting electrochemical cells.



electric power consumption and heat dissipation towards mitigating the energy crisis. As example, Fig. 1a shows the widespread use of electricity at night, as mapped by the NASA Earth Observatory.⁶ In this context, SSLDs exhibiting 90% higher luminous efficacy (defined as the ratio of luminous flux to power) and 25 times longer lasting lighting performance in comparison with those of traditional incandescent bulbs and fluorescent compact lamps are playing a major role – Fig. 1b and c. SSL technologies can be classified into three categories: (i) inorganic light-emitting diodes (LEDs), (ii) organic light-emitting diodes (OLED), and (iii) light-emitting electrochemical cells (LECs).⁷ Their basic device structures are depicted in Fig. 2.

Briefly, SSLs are based on semiconducting materials as high-efficiency illumination sources through direct conversion of

electric energy into visible light, that is, the electroluminescence concept.^{30,31} Inorganic LEDs are based on direct band-gap inorganic semiconductors as the light-emitting materials,^{32–34} such as group III-nitrides^{35–38} and inorganic phosphors as color down-converting filters.^{39,40} The basic architecture is based on a three-layered structure of a p-type semiconductor, a n-type semiconductor, and a depletion layer,^{41–43} leading to a p–n junction diode structure.^{41–43} Once the LED is forward biased, the electrons at the conduction of band recombine with the holes at the valence band, releasing radiative energy. By doing so, inorganic LEDs can theoretically reach an internal quantum efficiency (IQE) of 100%. The optical emission wavelength can be adjusted by changing active material composition, which determines the optical and



Luca M. Cavinato

Luca Maria Cavinato got his BSc in Chemistry and Chemical Technologies and his MSc in Industrial Chemistry at the University of Turin followed by one year as Research Associate at IMDEA Materials Institute. Currently, he is a final year PhD Student at the Chair of Biogenic functional Materials at the Technical University of Munich under the supervision of Prof. Dr Costa. His research activity focuses on the study and development of innovative organic and organo-metallic materials for photovoltaic and lightning purposes.



Hashem Shahroosvand

Hashem Shahroosvand is a full professor in Inorganic Chemistry at University of Zanjan from 2009, as head of Group for Molecular Engineering of Advanced Functional Materials (GMA). Shahroos appeared in the list of 50 excellent scientists in IRAN by Iran Science Elites Federation from 2017 by now. His research encompasses molecularly engineered hole transport materials (HTMs) for perovskite solar cells (PSCs) and new emitters for light-emitting electrochemical cells (LEC) applications. New directions of cost effective optoelectronic devices based on carbon derivative electrodes are also in progress in his lab. Shahroos also extensively dealing with the philosophical objects in Chemistry.



Babak Pashaei

artificial photosynthesis, light-emitting electrochemical cells, dye-sensitized solar cells, and PSCs.

Babak Pashaei (BP) received his PhD in Inorganic Chemistry in 2019 from Zanjan University, Zanjan, Iran, under the guidance of Prof. Shahroosvand. He worked as a postdoctoral researcher in the same lab from 2019 to 2020, focusing on the synthesis of hole transporting materials for application in perovskite solar cells (PSCs). BP is currently Assistant Professor at Mazandaran University, Babolsar, Iran. His research focuses on



Rubén D. Costa

is Full Professor at the Technical University of Munich, heading the Chair of Biogenic Functional Materials. His research encompasses fluorescent protein engineering and protein-/d¹⁰-complex chemistry to advance sustainable concepts for lighting/PV technologies.

Rubén D. Costa received his BSc/ MSc (2006) and PhD (2010) in Chemistry from the U. Valencia. In 2011–2013, he was Humboldt Postdoc at the U. Erlangen-Nürnberg, working on nano-carbon-based PVs. In 2014, he became Liebig group leader focused on fluorescent proteins and d¹⁰-materials for lighting. In 2017, he moved to IMDEA Materials and was appointed as Associate Professor at the U. Waseda in 2018. Since 2020 he



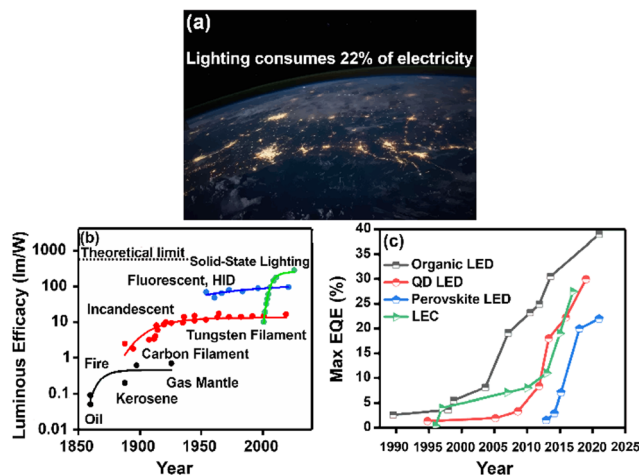


Fig. 1 (a) The image of Earth's city lights (credit: image courtesy NASA). (b) Historical evolution of light sources' performance as a function of time. (c) Comparison of EQE in display technologies based on organic LEDs, quantum dot LEDs, and perovskite LEDs. Data are taken from references as follows: OLEDs, ref. 8–15; QD LEDs, ref. 16–22; and PeLEDs, ref. 23–27, LEC, ref. 28,29.

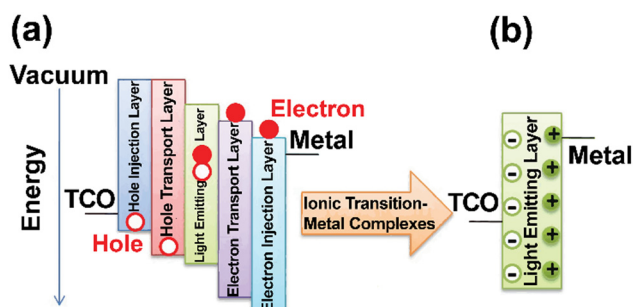


Fig. 2 SSLD structures along with the mechanisms. (a) OLED and (b) LEC. Reproduced from ref. 7. Copyright 2019, Royal Society of Chemistry.

electronic properties of the material itself.^{41,42} Typical examples of active regions are made of Ge,^{44,45} GaAs,^{46–48} group-III nitrides (*e.g.*, GaN, InGaN)^{36,49,50} and phosphides (*e.g.*, InP,⁵¹ GaAsP,⁵² and AlGaInP⁵³).

Even though inorganic LEDs could reach nearly 100% of IQE,⁵⁴ there are a few problems, such as low color-rendering index (CRI) for white light sources⁵⁵ and high cost of materials⁵⁶ and related processing,^{57,58} in particular over large-areas substrates.⁵⁹ Nevertheless, the inorganic LED market rules many application fields, such as medical,^{60–62} optical communication^{63,64} and display technologies.^{32,65} For the interested reader, there are several recent reviews about the limitations and challenges of inorganic LEDs.^{66,67} However, the TADF mechanism has not been applied to this technology and, in turn, it will not be further discussed in this review.

In parallel, the interest on organic molecular materials as emitters has significantly grown since Tang and Van Slyke revealed their electroluminescence behavior in a simple two-layer device based on 8-hydroxyquinoline aluminum (Alq₃) as

the light-emitting materials and an aromatic diamine as the hole transporting layer.⁶⁸ Afterwards, intensive research efforts on organic semiconductors led to the strong development of OLEDs – Fig. 2, which use organic molecules and/or compounds as the electroluminescent (EL) materials forming the so-called light-emitting layer (LEL),⁶⁹ but also for hole/electron injection layers (HIL and EIL), hole/electron transport layers (HTL and ETL) and LEL – Fig. 2a. Thus, their architecture is best described as multilayered active layer placed between a transparent anode, such as indium tin oxide (ITO), and an air-sensitive cathode, such as Ca or Mg.^{70,71} The charge injection/transporting layers transfer the carriers until they reach each other in the LEL and prevent the hole/electron diffusion toward the electrodes, leading to an efficient exciton confinement at the LEL. Given that exciton generation in fluorescent organic molecules under electrical bias yields 25% singlet excitons and 75% triplet excitons, a significant portion of the electrical energy, namely 75%, is dissipated as heat due to triplet exciton non-radiative deactivation. As a consequence, the theoretical maximum external quantum efficiency (EQE) can reach approximately 5%, considering a typical light out-coupling factor of around 20%.⁷²

Though OLEDs offer the possibility to fabricate lightweight, large-area, flexible and through low-cost solution-based manufacturing processes,^{73–76} *e.g.*, spin coating,^{77,78} casting,⁷⁹ and printing techniques.^{80,81} The manufacturing of commercially available OLEDs currently takes place through high-cost and time-consuming vacuum thermal evaporation,⁸² significantly increasing the final OLED cost. Moreover, the oxygen sensitivity of organic LELs, as well as the use of chemically reactive electrodes requires rigorous encapsulation. Despite these drawbacks, the performance of OLEDs in terms of stability and efficiency has rapidly increased, making them extremely attractive.^{73,83} Indeed, today's global market is predicted to rise over 13% during the forecast period 2020–2025, with applications in residential,^{84,85} commercial^{86,87} and industrial sectors.^{88,89} This has been strongly related to (i) the development of emitters going from fluorescent organic molecules/conjugated polymers, phosphorescent transition metal complexes, quantum dots, perovskites, and now TADF molecules, (ii) host:guest active layers,^{72,90–93} and (iii) device architectures, such as tandem and micro-OLEDs for advanced sensing systems and displays (*e.g.*, portability^{94,95} and wearability^{96,97}). In the context of the different emitter generations, the reader is invited to check the following reviews along with a short description in Section 2.⁹⁸ Herein, we will concentrate on metal complex-based TADF emitters applied to OLEDs, highlighting their photo-/electro-luminescence features with respect to the current challenges.

As a final SSL family, LECs shine as the simplest, cheapest, and moderate performing devices.^{99–102} They consist of a single ion-based LEL sandwiched by two air-stable electrodes – Fig. 2b. The application of electric bias causes a redistribution of ions at the electrode surface allowing carrier injection as well as the growth of the p- and n-doped regions close to each electrode. This generates the so-called p–i–n junction, in which



excitons are formed at the neutral (i) region flanked by the p-/n-doped regions, that is, the so-called p-i-n junction. A major advantage of LECs is their easy fabrication using spray coating^{103,104} on any arbitrary 3D-shape electrode with a good thickness tolerance¹⁰⁵ and encapsulation requirements.¹⁰⁶ Likewise OLEDs, the LEL of LECs consists of emitters, such as fluorescent organic molecules/conjugated polymers blended with ion polyelectrolytes, phosphorescent ionic transition metal complexes (iTMCs) with ionic liquids, quantum dots with ion polyelectrolytes, perovskites, and more recently neutral and ionic TADF emitters with electrolytes.^{107–112} Among them, iTMC-based LECs exhibit several advantages over polymeric-LECs,^{106,113} as they are easily dissolved in polar solvents, which can be consequently processed in form of dispersion/solution through printing methods avoiding phase separation. Indeed, Cu(I), Ru(II), Pt(III), Os(II) and Ir(III) iTMCs used in LECs are mostly ionic and they have achieved high stabilities (>5000 h) and EQEs >10% without using electrolytes.^{73,106,114–116} Afterwards, small organic molecules have been also revealed to be suitable LEL materials for LECs because of their high photoluminescence quantum yields (PLQYs), simple molecular modifications, and presence of TADF mechanism. Here, design rules for the device composition (emitter, electrolyte, host:guest type and composition, etc.) have led to good brightness levels (2000 cd m⁻²) at high EQE (up to 27.5%) as achieved by researchers at Umeå and Linköping universities.²⁹ Based on these advances, medical, signing and human services are realistic niches for LECs.¹¹⁷ Excellent reviews about each type of emitters, electrolytes, unconventional architectures, and device *modus operandi* are provided for the interested reader.^{112,118} Likewise the OLEDs, this review will also concentrate on the design and implementation metal complex-based TADF emitters in the LECs field.

Finally, it is important to stress that organic TADF field has been widely advanced in the last decades. In this context, the interest on metal complex-based TADF is two-fold. On one hand, the presence of a metal ion core can lead to short excited state lifetimes due to the high spin-orbit coupling (SOC) reducing the probability of parasite non-radiative decay pathways, such as exciton-polaron quenching and chemical degradation. On the other hand, purely organic TADF emitters require complex multi-step synthesis that are in antithesis with sustainability requirements.^{119,120} It is still poorly understood why the device performance are not comparable (OLEDs and LECs) between both families of TADF emitters. Thus, a comprehensive overview is necessary to foster new advances in the near future of metal complex-based TADF emitters.

In view of all of the aforementioned, the scope of this review is a comprehensive overview of the progress of metal complex-based TADF as potential emitters for SSLs. Other reviews have been focused on describing photo-/electro-luminescent behavior of either TADF organic molecules^{120,121} or all-inorganic TADF emitters,¹¹⁹ while much less attention has been placed on TMCs with a few reviews focused on either device performance or photophysical behavior of particular families.^{90,122} Herein, we wish to provide to the reader a comprehensive

overview, including design rules of metal complex-based TADF emitters and how to characterize them in Section 2 as well as the lessons learnt from their device performance in OLEDs and LECs in Section 3. This is finalized with a conclusion and outlook, highlighting the limitations/challenges in this ever-growing field.

2. TADF emitters

2.1. Physics and designs

Although TADF materials were discovered in the 1960s,^{91–93} their use in optoelectronics was first proposed by Adachi and co-workers in 2009,¹²³ paving the way toward a new generation of highly efficient OLEDs^{14,124–128} and LECs.¹²⁹ Fig. 3 shows the number of TADF material-related publications per year from 2011, reflecting how TADF materials influenced both the photonic and optics research communities during the last years.

Thanks to their photophysical properties, TADF materials provide several advantages in SSLs. This is best reflected in the OLED evolution – Fig. 4. In the 1st generation OLEDs (until the 90s), green and red fluorescent materials have been used, with a low theoretical IQE of 25% and a short operational lifespan.¹³⁰ The issues were partially solved with the 2nd generation of OLEDs (up to 00 s), based on phosphorescent Pt(II) and Ir(III) organometallic complexes – Fig. 4. The theoretical IQE improved up to 100% thanks to the high SOC of such materials, and the operational lifespan reached incredibly high values (>50 000 h). However, some challenges remained unsolved (lack of stable blue emitters), and new ones rose (dependence on rare and expensive elements). Especially the former is particularly relevant because it hinders the development of white OLEDs (WOLEDs) with a high color rendering index (CRI).¹³⁰ TADF materials constitute the so-called 3rd-generation OLEDs.¹³¹ They can upconvert triplet states (T₁) into singlet states (S₁) through reversible intersystem crossing

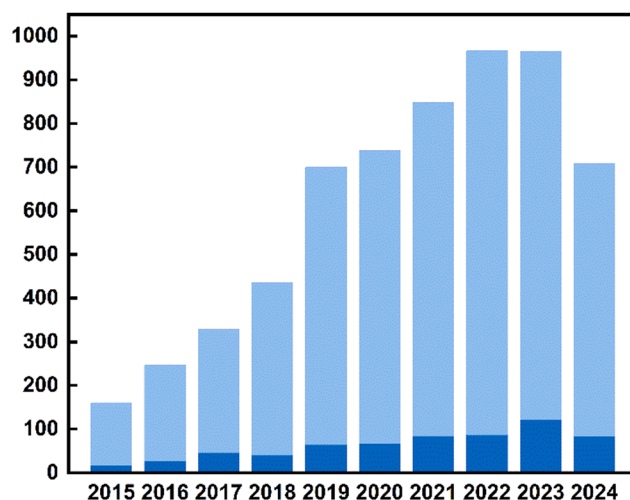


Fig. 3 The number of publications related to TADF emitters (light blue) highlighting the metal complex-based TADF emitters (deep blue).



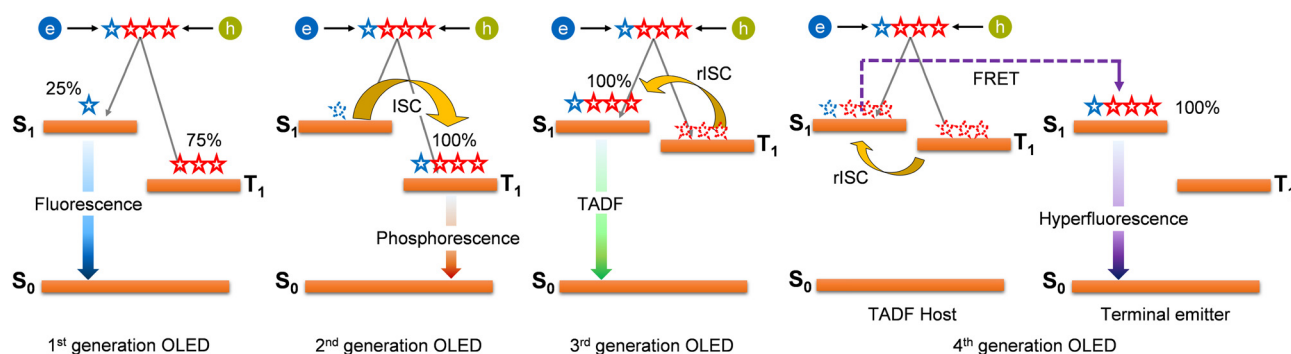


Fig. 4 Sketch of the working principles of 1st, 2nd, 3rd, and 4th generation OLEDs. The transition processes of photogenerated excitons for fluorescence, phosphorescence, TADF, and hyperfluorescence are highlighted.

(rISC) mechanism – Fig. 4, unlocking their theoretical IQE beyond 25% and up to 100% through the (delayed) fluorescence given by the radiative decay of their excited singlet states (*i.e.*, $S_1 \rightarrow S_0$).^{7,14} Notably, the electroluminescence mechanism leading to theoretical IQE up to 100% is substantial different from those of phosphorescent emitters belonging to the 2nd-generation OLEDs, whose luminescence results from the T_1 decay toward S_0 (*i.e.*, $T_1 \rightarrow S_0$).⁹ The theoretical 100% IQE of TADF material-based OLEDs^{14,132,133} relies on the reduced energy difference between the lowest singlet (*i.e.*, S_1) and triplet (*i.e.*, T_1) excited states (ΔE_{ST} , also referred to singlet-triplet energy splitting) in TADF materials compared to fluorescent molecules. Such optical characteristic promotes the rISC ($T_1 \rightarrow S_1$) effects,¹³⁴ thus the TADF mechanism. Though TADF is not typically encountered in fluorescent emitters, since their large ΔE_{ST} prohibits efficient rISC,^{135,136} the design of TADF organic emitters has been successful (*e.g.*, Tetrakis-*N*-carbazoyl-isophthalonitrile).^{137,138} Here, the energetic features of TADF materials partially resembles the one of phosphorescent emitters,¹³⁹ in which small ΔE_{ST} (but higher compared to TADF materials), the presence of heavy transition metals (such as Ir in Ir(ppy)₃, ppy is 2-phenylpyridine) and the involvement of singlet and triplet states belonging to different electronic configurations promote the intersystem crossing (ISC), in accordance with El-Sayed rules^{136,140,141} The ISC is the isoenergetic radiationless process, involving a transition between the two electronic states with different states spin multiplicity. In phosphorescent emitters, it enables the filling of excited T_1 states that provide phosphorescence, acting as light-emitting sources.¹⁴²

Clearly, the rational design of materials with proper ΔE_{ST} (typically $< 1613 \text{ cm}^{-1}$) enables the competition between phosphorescence and TADF processes to be controlled *via* ISC and rISC, determining the final nature (TADF or phosphorescence) of the emitters in OLEDs. All TADF molecules contain donor and acceptor moieties, which have electron-rich functional units with deep highest occupied molecular orbital (HOMO) and electron-deficient functional units with a deep lowest unoccupied molecular orbital (LUMO),^{143,144} respectively. As a result, the donor and acceptor moieties participate in the hole transport and electron transport, respectively.

Based on this rationale, numerous families of small organic molecules have been recently produced and investigated containing spiro derivatives,¹⁴⁵ triazines,¹⁴⁶ spiro-acridines,¹⁴⁷ phenazines and carbazoyl dicyanobenzene (CDCB).^{14,148} Likewise, d^x-TMCs, such as (i) d⁶ Ir(III), (ii) d⁸ Pd(0), Pd(II), Pt(II), and Au(III), and (iii) d¹⁰ Cu(I), Ag(I), Au(I), and Zn(II), have also shown a similar charge transfer (CT) character that allows measuring TADF emitters.

However, TADF materials development is still relatively new (< 25 years; Fig. 3), with stability and color purity needing of further optimization. Moreover, the synthesis of advanced organic materials became more intricate and complex, dramatically influencing cost and scalability. Finally, achieving high-power TADF-based devices remains challenging due to their high degradation rate at high applied current densities.

To overcome these limitations, hyperfluorescence and hyperphosphorescence systems are currently being developed, constituting the 4th generation OLEDs – Fig. 4.^{149–152} The primary exciton formation is confined to the terminal fluorescence/phosphorescence emitter by controlling the doping concentration ratio of the TADF assist dopant. Thus, the triplet excitons are first upconverted into the S_1 state *via* rISC in the TADF material. Then, they are transferred by Förster resonance energy transfer (FRET) to the final emitter molecule. The idea is based on two key points: (i) fluorescent emitters' high stability and narrow emission spectra, which lead to high color purity, and (ii) TADF molecules' effective rISC process. Nevertheless, this is in its early stage, facing material design and a limited understanding of the hyperfluorescence mechanism. Demonstrators and performance optimization are yet to be realized. Long-term stability and commercial viability are unknown.^{153,154}

2.2. How to characterize metal complex-based TADF emitters? Models, characterization methods, and assumptions

In general, efficient TADF emitters must meet two key criteria simultaneously: (i) maintaining a small energy gap between the singlet and triplet excited states (ΔE_{ST}) and (ii) minimizing non-radiative decay. This ensures that the triplet excited state features a prolonged existence, maximizing the opportunity for triplet harvesting through the thermally activated rISC



and, consequently, enhancing the emission yield. The critical factor in maximizing the rISC rate constant is achieving a small ΔE_{ST} , as defined by eqn (1), so understanding how to minimize it in molecular structures becomes crucial.

$$k_{rISC} = k_{ISC} \times e^{\left(-\frac{\Delta E_{ST}}{k_B T}\right)} \quad (1)$$

Calculating the energy of the lowest singlet (E_{S_1}) and triplet (E_{T_1}) excited states involves considering three aspects: (i) the orbital energy (E_{orb}), (ii) the electron repulsion energy (K), and (iii) the exchange energy (J). These factors affect the HOMO and LUMO energies and topological distribution.¹⁵⁵ Thus, they are equally relevant on the singlet and triplet excited states that featured identical electronic configurations. Indeed, the exchange term increases the singlet energy and decreases the triplet energy by an equal amount, as per eqn (2) and (3).¹²⁴ Consequently, the singlet–triplet energy gap ΔE_{ST} is determined by eqn (4), and it is evident that minimizing this gap requires reducing the exchange energy J , calculated using eqn (5).

$$E_{S_1} = E_{orb} + K + J \quad (2)$$

$$E_{T_1} = E_{orb} + K - J \quad (3)$$

$$\Delta E_{ST} = E_{S_1} - E_{T_1} = 2J \quad (4)$$

$$J = \iint \Phi(r_1)\psi(r_2) \left(\frac{e^2}{r_1 - r_2}\right) \Phi(r_2)\psi(r_1) dr_1 dr_2 \quad (5)$$

Here, Φ and ψ represent the HOMO and LUMO wavefunctions, respectively, and e is the electron charge. In the context of HOMO–LUMO transitions, the Φ and ψ parameters are replaced with the many-body electronic wavefunction for the singlet and triplet states. This shows that minimizing J reduces the HOMO and LUMO overlapping, which can be achieved initially by spatially separating these frontier orbitals.¹⁵⁶

Organic molecules exhibiting TADF typically contain electron acceptor (A) and donor (D) moieties that promote D–A charge transfer (CT) characteristics in the excited state. These molecules are usually composed of D and A units connected *via* an aromatic bridge, resulting in excited states with strong CT characteristics. The energy difference between the singlet and triplet excited states can be further minimized by twisting the D and A units around the D–A axis, creating near-orthogonal D–A relative orientations, or by increasing the D–A distance through the use of a longer bridge – Section 2.3.¹⁵⁷ Similarly, for TMCs, this is related to the occurrence of metal-to-ligand charge-transfer (MLCT) (and ligand-to-ligand charge-transfer (LLCT)) states having frontier orbitals, which are spatially largely separated – Section 2.3. Finally, on the context of solid-state light-emitting devices, in which TADF materials are employed, their properties are intricately tied to the permissibility of the $S_1 \rightarrow S_0$ transition. This is because: (i) the radiative rate $k_r(S_1 \rightarrow S_0)$ should be maximized for high PLQYs and (ii) short decay times play a crucial role in minimizing roll-off effects and enhancing stability.^{158,159} In the last decades, numerous researchers have endeavored to comprehend the photophysics of TADF materials

by employing a conventional rate equation approach to curve-fit time-resolved photoluminescence decays, wherein each decay process is considered. While this strategy is easy to apply, prior analyses often relied on several *a priori* assumptions, resulting in significant deviations from experimental observations or, at times, erroneous conclusions. Based on excellent works from several groups (Penfold, Thompson, Adachi, Monkman, Yersin, Tsuchiya, Zysman-Colman, Samuel, *etc.*),^{155,160–164} we will consider three cases: (i) $k_{ISC} \gg k_r(S_1 \rightarrow S_0)$, (ii) $k_{ISC} \ll k_r(S_1 \rightarrow S_0)$, and (iii) general case with $k_{ISC} \cong k_r(S_1 \rightarrow S_0)$. Thus, TADF molecules can be categorized into three main groups based on their photophysical features of coordination complexes.

2.2.1. $k_{ISC} \gg k_r(S_1 \rightarrow S_0)$. In 1983, McMillin and colleagues¹⁶⁵ elucidated the TADF behavior of a tetrahedral Cu(I) complex for the first time using a Boltzmann statistical analysis of the population equilibrium of excitons in the S_1 and T_1 states, incorporating various assumptions: (i) nearly unity ISC efficiency (Φ_{ISC}) and (ii) rate constants of non-radiative decay from S_1 (non-radiative rate constant $k_{nr}(S_1 \rightarrow S_0)$) and T_1 ($k_{nr}(T_1 \rightarrow S_0)$) of 0. This specific approach can be extended generally to d¹⁰ TMCs (Cu(I), Ag(I), and Au(I)) since these boundary conditions are often true due to fast ISC rates ($k_{ISC} = 10^{10}$ – 10^{11} s^{−1}) compared to $k_r(S_1 \rightarrow S_0)$ due to high SOC imparted by the central metal ion and nearly unity quantum yields.^{166–169}

In this situation, the decay time $\tau(T)$ of the luminescent molecule is described by eqn (6):

$$\tau(T) = \frac{3 + e^{\left(-\frac{\Delta E_{ST}}{k_B T}\right)}}{3k(T_1) + k(S_1)e^{\left(-\frac{\Delta E_{ST}}{k_B T}\right)}} \quad (6)$$

$k(T_1)$ and $k(S_1)$ stand for $k_r(T_1 \rightarrow S_0)$ and $k_r(S_1 \rightarrow S_0)$, respectively. Within the assumption of PLQY ≈ 1 , they are equal to $1/\tau(T_1 \text{ or } S_1)$. In particular, $\tau(T)$ is the experimentally accessible emission decay time at a given temperature and at very low (often < 77 K) temperature, it is assumed $\tau(T) \approx \tau_{ph}$. *Vice versa*, above room temperature $\tau(T)$ is similar to the lifetime of the delayed fluorescence process (τ_{DF}) – Fig. 5. In addition, those systems often lack a “prompt” process due to rapid equilibration between the S_1 and T_1 states, resulting in a single exponential signal on the μ s–ms scale.

In such systems, the rate constants are easily accessible through the system of eqn (7):¹⁷⁰

$$\begin{cases} \frac{k_{rISC}}{k_{ISC}} = \frac{\tau_{PF}}{\tau_{DF}} \\ \frac{k_{rISC}}{k_{ISC}} = \frac{1}{3} e^{\left(-\frac{\Delta E_{ST}}{k_B T}\right)} \\ \ln(k_{DF}) = \ln\left[\frac{k_{ISC}}{3} \times \left(1 - \frac{k_{ISC}}{k_{PF} + k_{ISC}}\right)\right] - \frac{\Delta E_{ST}}{k_B T} \end{cases} \quad (7)$$

In this context, assuming that k_{ISC} is temperature-independent, it is possible to obtain directly the k_{rISC} and k_{DF} from the corresponding Arrhenius plots. However, this set of



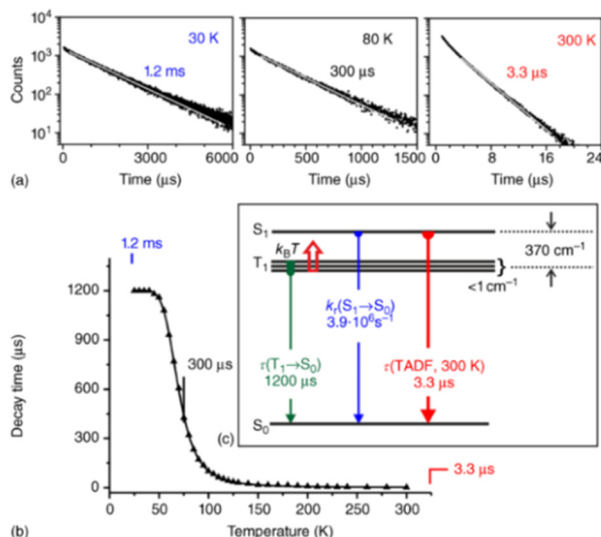


Fig. 5 (a) Emission decay profiles of Cu(dppb)(pz₂Bph₂) (**Cu10**) (powder) at 30, 80, and 300 K recorded after pulsed excitation at $\lambda_{\text{exc}} = 378$ nm and detected at $\lambda_{\text{det}} = 540$ nm. (b) Emission decay time τ versus temperature. The solid line represents a fit of eqn (6) to the experimental $\tau(T)$ values fixing $\tau(T_1) = 1.2$ ms as measured at $T = 30$ K. The fit parameters are $\tau(S_1) = 180$ ns and $\Delta E_{\text{ST}} = 370$ cm⁻¹, respectively. Reproduced with permission from ref. 128.

equations holds only within the assumption of unity PLQY, neglecting the non-radiative pathways and, often, they are applied outside their boundary conditions.^{169–172}

In low-emissive systems formally only the general equation can be applied in a wide range of temperature (*i.e.*, 77–300 K):¹⁷⁰

$$k_{\text{DF}} = \frac{k_{\text{PF}}\tau_{\text{PF}}^2}{(\phi_{\text{tot}} - k_{\text{PF}}\tau_{\text{PF}})} \frac{k_{\text{ISC}}^2}{3} e^{\left(-\frac{\Delta E_{\text{ST}}}{k_{\text{B}}T}\right)} \quad (8)$$

As discussed deeper in the next sections, the photophysical properties are connected to the molecular geometry. For instance, in a family of luminescent Cu(I) complexes, [Cu(DPEPhos)-(N^N)] [BF₄], (DPEPhos = bis[2 (diphenylphosphino)-phenyl]ether and N^N = sulfur-bridged dipyrilidyl ligands) the exploration of the influence of the bridging sulfur atom oxidation state, sulfide(II) or sulfone(VI), and also substituents in the 6,6'-sites of the pyridyl rings (R = H, Me, Ph) was carried out.¹⁷³ It was shown that through these structural modification, various complex geometries can be obtained so that the proton (Cu-DPS, Cu-DPSO₂) and phenyl (Cu-Ph-DPS, Cu-Ph-DPSO₂) substituted derivatives form monometallic complexes, whereas methyl-substituted derivatives (Cu-Me-DPS, Cu-Me-DPSO₂) have a “Goldilocks” degree of steric bulk, which results in bimetallic species. All complexes except Cu-Ph-DPS, were demonstrated to emit through a TADF mechanism, while the photoluminescence characteristics of Cu-Ph-DPS were found to be in line with triplet ligand-centered (³LC) emission. Moreover, the reduction in the long lifetime component on cooling for Cu-Ph-DPS – Fig. 6, indicates that this is not TADF

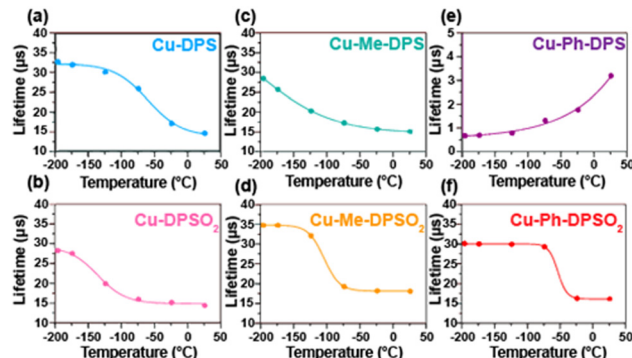


Fig. 6 Solid-state photoluminescence lifetimes of (a) Cu-DPS; (b) Cu-DPSO₂; (c) Cu-Me-DPS; (d) Cu-Me-DPSO₂; (e) Cu-Ph-DPS; and (f) Cu-Ph-DPSO₂ from –196 to 25 °C. Samples drop-cast as neat thin-films from MeOH on quartz slides ($\lambda_{\text{exc}} = 370$ nm). Reproduced from ref. 173. Copyright 2019, American Chemical Society.

emitter. In addition, in Cu-Me-DPS the relation $\tau(T) \approx \tau_{\text{ph}}$ is not reached at 77 K, but lower temperatures are required.

2.2.2. $k_{\text{ISC}} \ll k_{\text{r}}(S_1 \rightarrow S_0)$. This scenario is the most straightforward to analyze. After absorption, the electron will not have the time to move to a triplet excited state before radiative or non-radiative decay occurs. In organic small molecules with slow ISC rates ($k_{\text{ISC}} = 10^5$ – 10^8 s⁻¹), attributed to weak SOC,¹⁷⁴ the emission will occur through fluorescence (with a lifetime denoted by τ_{S_1}) and the T₁ state will undergo non-radiative decay. The emitters employed in the 1st generation of OLEDs fall in this category, and they have been specifically designed to have slow ISC rates to reduce triplet-triplet annihilation.^{175–178} However, such molecular design is reviving again thanks to 4th generation OLEDs, in which a slow ISC rate of the terminal fluorescent emitter is required to reduce non-radiative pathways.¹⁵³

2.2.3. $k_{\text{ISC}} \cong k_{\text{r}}(S_1 \rightarrow S_0)$. When k_{ISC} and $k_{\text{r}}(S_1 \rightarrow S_0)$ are in the same order of magnitude and the non-radiative constants from S₁ and T₁ cannot be neglected, the situation is more complicated. This situation is typical for organic TADF emitters, in which there are no metal atoms to guarantee strong SOC, and for low-emissive TMCs. Taking into account all the process in a three-state system the combined decay rates from S₁ and T₁ can be written as:

$$\begin{cases} \frac{d[S_1]}{dt} = -(k_{\text{r}}(S_1 \rightarrow S_0) + k_{\text{nr}}(S_1 \rightarrow S_0) + k_{\text{ISC}})[S_1] + k_{\text{rISC}}[T_1] \\ \frac{d[T_1]}{dt} = -(k_{\text{r}}(T_1 \rightarrow S_0) + k_{\text{nr}}(T_1 \rightarrow S_0) + k_{\text{rISC}})[T_1] + k_{\text{ISC}}[S_1] \end{cases} \quad (9)$$

With [S₁] and [T₁] being the population of the respective excited states. The solution of this system of differential equations provided two different eigenvalues:¹⁷⁴

$$\lambda_{1,2} = -\frac{1}{2} \left(S + T \pm \sqrt{(S - T)^2 + 4k_{\text{ISC}}k_{\text{rISC}}} \right) \quad (10)$$

S and T are $S = k_{\text{r}}(S_1 \rightarrow S_0) + k_{\text{nr}}(S_1 \rightarrow S_0) + k_{\text{ISC}}$ and $T = k_{\text{r}}(T_1 \rightarrow S_0) + k_{\text{nr}}(T_1 \rightarrow S_0) + k_{\text{rISC}}$, respectively, which have been condensed for



the sake of clarity. In this context, it is possible to extract the relation:

$$S + T = k_{PF} + k_{DF} \quad (11)$$

k_{PF} and k_{DF} are the experimental rate obtained from the bi-exponential fitting of the excited state decay lifetime at room temperature. More in details, when taking into account all the possible processes, namely: the emission from S_1 upon direct photoexcitation and indirect population from T_1 , and direct phosphorescence from T_1 state it is possible to model exactly the emission decay as follow:¹⁷⁴

$$I(t) = \frac{[S_1]_{t=0}}{k_{PF} - k_{DF}} \left\{ \left[(S - k_{DF}) \frac{k_{r(S_1-S_0)}}{S} - k_{ISC} \frac{k_{r(T_1-S_0)}}{T} \right] e^{(-k_{PF}t)} + \left[(k_{PF} - S) \frac{k_{r(S_1-S_0)}}{S} + k_{ISC} \frac{k_{r(T_1-S_0)}}{T} \right] e^{(-k_{DF}t)} \right\} \quad (12)$$

However, despite being the most complete and accurate model equation obtained so far, it is difficult to use it as it is, without any assumptions. Likely, since the T_1 level is lower in energy than S_1 in conventional TADF emitters, it is possible to assume that $S \gg k_{ISC}$, which means that at least one of the three parameters ($k_{r(S_1-S_0)} + k_{nr(S_1-S_0)} + k_{ISC}$) is greater than k_{ISC} . Thus, we can simplify eqn (11):

$$I(t) = (A_{PF} + A_{DF})e^{(-k_{PF}t)} + A_d[-e^{(-k_{PF}t)} + e^{(-k_{DF}t)}] \quad (13)$$

APF and ADF are the pre-exponential factors of the biexponential curve.^{174,179} Eqn (13) is the one that must be used to fit experimental excited state decay profiles. From A_{PF} , A_{DF} , k_{PF} , k_{DF} , and the PLQY at room temperature (Φ_{tot}), it is possible to derive the specific quantum efficiency of the prompt fluorescence (Φ_{PF}) and delayed emission taking into account both delayed fluorescence and phosphorescence ($\Phi_{DF} + \Phi_{ph}$):

$$\begin{cases} \Phi_{PF} = \frac{(A_{PF} + A_{DF}) \times k_{DF}}{A_{PF}k_{DF} + A_{DF}k_{PF}} \Phi_{tot} \\ \Phi_{DF} + \Phi_{ph} = \frac{A_{DF}(k_{PF} - k_{DF})}{A_{PF}k_{DF} + A_{DF}k_{PF}} \Phi_{tot} \end{cases} \quad (14)$$

From this point on, it is possible to derive without any further assumptions the exact solutions from S_1 and T_1 decays:¹⁷⁴

$$\begin{cases} S = k_{PF} - k_{DF} \frac{\Phi_{DF} + \Phi_{ph}}{\Phi_{PF}} + k_{ISC} \frac{k_{r(S_1-S_0)}}{k_{r(T_1-S_0)}} \frac{S}{T} \\ \frac{k_{r(T_1-S_0)}}{T} = \frac{k_{PF}k_{DF}(\Phi_{DF} + \Phi_{ph}) \left(1 - \frac{\Phi_{DF}}{\Phi_{DF} + \Phi_{ph}} \right)}{(k_{PF} + k_{DF} - S)(k_{ISC} + k_{PF} - S)} \end{cases} \quad (15)$$

However, due to the presence of terms S and k_{ISC} in the equations as both independent and dependent variables, precise rates determination requires a numerical analysis. Nevertheless, in most TADF organic molecules the phosphorescence efficiency is close to zero ($\Phi_{ph} \cong 0$), thus, the system of equations simplifies to eqn (16)–(20), which are the most

commonly used:¹⁷⁴

$$S = k_{PF} - k_{DF} \frac{\Phi_{DF}}{\Phi_{PF}} \quad (16)$$

$$k_{r(S_1-S_0)} = k_{PF}\Phi_{PF} \quad (17)$$

$$k_{nr(S_1-S_0)} = k_{PF} \frac{\Phi_{PF}}{\Phi_{tot}} (1 - \Phi_{tot}) \quad (18)$$

$$k_{ISC} = k_{PF} \frac{\Phi_{DF}}{\Phi_{tot}} - k_{DF} \frac{\Phi_{DF}}{\Phi_{PF}} \quad (19)$$

$$k_{rISC} = k_{DF} \frac{\Phi_{tot}}{\Phi_{PF}} \quad (20)$$

In summary, an exact solution of the kinetics in TADF materials is possible only numerically from steady-state and transient emission spectroscopy experimental data.

Within this case are lying also the metal complex-based TADF emitters with light atoms, such as Al, as demonstrated by the work of Sasabe – see next section.¹⁸⁰ In such complexes a prompt fluorescent component is present – Fig. 7.

2.3. Which design rules must be followed for metal complex-based TADF emitters?

In general, metal complex-based TADF emitters are anticipated to possess several distinctive attributes: (i) heightened thermal stability and molecular rigidity through complexation and rigidification, (ii) enhanced PLQY *via* reinforcing acceptor aptitude and structural rigidity, (iii) anticipated reduction ΔE_{ST} by altering the acceptor moiety of conjugated ligands, and (iv) shorten of excited state decay lifetime due to the heavy atom

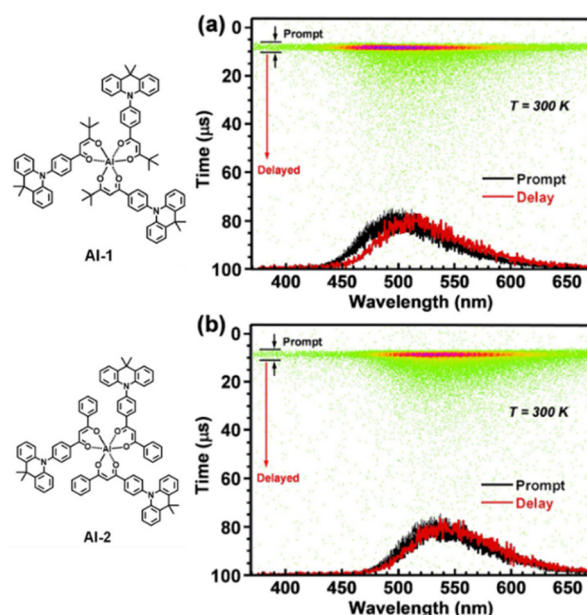


Fig. 7 Streak images and prompt and delayed PL spectra at 300 K; green dots represent PL photon counts for (a) 30 wt% Al1- and (b) Al2-doped 4,4'-bis(*n*-carbazolyl)-1,1'-biphenyl (CBP) film. Reproduced with permission ref. 180.



effect (higher SOC). Similar to organic molecules, the golden design rule to follow is the spatial separation of the HOMO and LUMO. However, the d^x -metal complexes design is complex due to the energy proximity of various transitions (*i.e.*, MLCT, LLCT, *etc.*).

In addition, it is important to consider that some families of complexes are prone to geometrical changes upon excitation (*e.g.* flattening distortion, change of coordination geometry/sphere). This results in new non-radiative deactivation pathways. This is reflected in high non-radiative rates and small PLQYs in low-energy emitting metal complexes, hampering their TADF study – Section 2.2.¹²⁸ Rational design strategies to minimize or even circumvent these undesired geometrical changes will be, therefore, discussed below. Finally, the energy splitting between the singlet and triplet excited states, ΔE_{ST} , must be $<1613\text{ cm}^{-1}/0.2\text{ eV}$ to ensure efficient rISC at room temperature.¹⁸¹ This is mainly achieved by a small spatial overlap of the HOMO and LUMO orbitals and other orbitals involved in the lowest excited state transitions. These requirements are best fulfilled when the lowest excited states are of CT character (*e.g.*, MLCT or LLCT). However, the reduction of ΔE_{ST} values below $200\text{--}300\text{ cm}^{-1}$ is not beneficial anymore; instead, such small ΔE_{ST} values lead to significantly decreased radiative rates, $k_r(S_1 \rightarrow S_0)$ representing the third parameter. To obtain highly efficient TADF emitters, the allowedness of the $S_1 \rightarrow S_0$ transition should be as high as possible.

This allows the achievement of short TADF decay times that are highly desired for device applications to avoid any adverse impact on their performances, *e.g.* roll-off effects, and stability problems – Section 3.¹²⁸ However, quantum mechanical calculations reveal a close relation between $k_r(S_1 \rightarrow S_0)$ and ΔE_{ST} . In detail, a small overlap of the HOMO and the LUMO benefits a small ΔE_{ST} , but results in a small oscillator strength of the $S_1 \rightarrow S_0$ transition and large τ_{TADF} – *vice versa*; Fig. 8.¹²⁸

Based on the above concepts and according to the population of the d-orbitals of the metallic core, several design rules have been identified. The following will summarize the molecular strategies to achieve TADF metal complexes up to date.

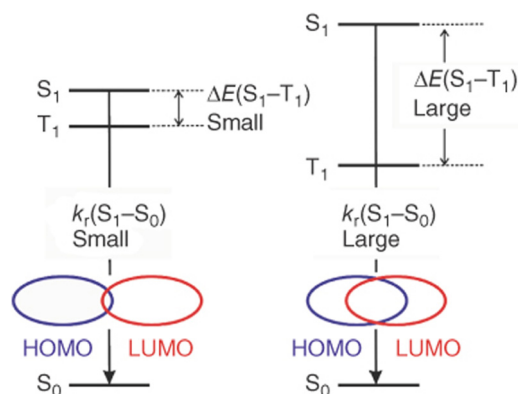
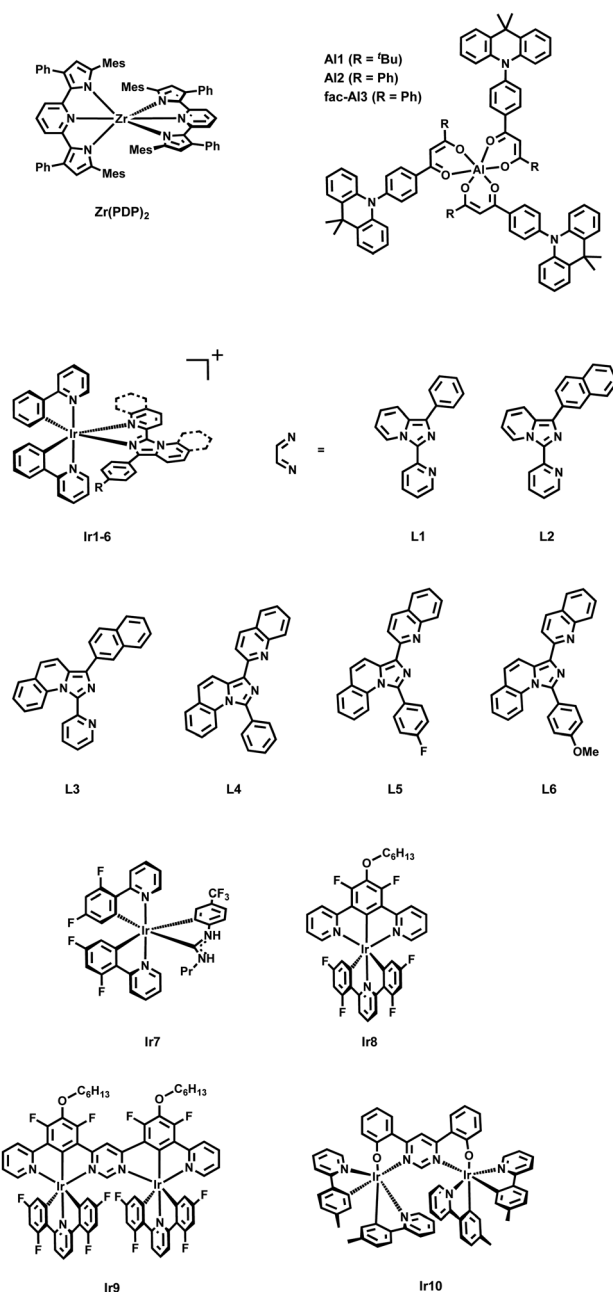


Fig. 8 Schematic representation of the relationship between ΔE_{ST} , $k_r(S_1 \rightarrow S_0)$, and the spatial overlap of the HOMO and LUMO – represented with permission ref. 181.

2.3.1. Zr- and Al-complexes. Recently, Milsman's group¹⁸² have demonstrated that Zr(IV) complexes incorporating electron-rich pyridinepyrrolide and pyridinedipyrrolide (PDP) ligands exhibit prolonged photoluminescence from excited states with ligand-to-metal CT characteristics. This distinction arises from its exceptionally long τ of $325\text{ }\mu\text{s}$ and its readily accessible reductive redox chemistry. Through temperature-dependent emission studies coupled with picosecond transient absorption (TA) spectroscopy, they conclusively establish that the emission of the novel Zr(PDP)₂ complexes (Scheme 1) predominantly originates from TADF. In detail, the data were effectively modeled using Boltzmann type model. The extracted



Scheme 1 Structural representations of Zr(PDP)₂, Al1–3 and Ir1–10.

time constants for the S_1 and T_1 states ($\tau_{S_1} = 35 \pm 4$ ns, $\tau_{T_1} = 1.04 \pm 0.05$ ms) closely align with those reported for TADF processes in photoluminescent Cu(I) complexes and purely organic emitters. The ΔE_{ST} was around 1652 ± 32 cm $^{-1}$ and concurs excellently with the value derived from the respective fluorescence and phosphorescence spectra measured in solution. Despite not being used for lighting applications, their success in photoredox chemistry highlights the relevance of this family that is expected to flourish.

By contrast with the seminal field of TADF Zr(IV)-based materials, recent advancements have led to the development of mononuclear Al(III) complexes, showing promising properties in lighting devices. In 2020, Kido and Sasabe¹⁸⁰ introduced a groundbreaking series of highly luminescent Al(III) complexes, incorporating phenylacridine-modified asymmetric acetylacetonate (acac)-type ligands (**Al1** and **Al2**, Scheme 1). These complexes exhibited PLQYs of up to 79% associated to TADF, outperforming conventional ligand components. Notably, the shorter τ_{DF} of the complexes compared to that of the ligand suggests an enhancement in luminescence efficiency upon coordination with Al(III). The discovery of mononuclear Al(III) complexes exhibiting TADF behavior opens up new avenues for the design and development of advanced optoelectronic materials. The exceptional PLQYs and efficient TADF properties of these complexes hold promise for their application in OLEDs (Section 3). Two years later, the same group achieved a TADF Al(III) complex with near-unity PLQY (**Al3**, Scheme 1).¹⁸³ They re-designed the chemical configuration of the β -diketone ligand by introducing an additional donor unit. The new complex emitted yellow light with a rapid radiative decay rate of 10^7 s $^{-1}$, a brief delay time below 2.0 μ s in solid form, and its OLEDs showed EQE surpassing 18%. So far, the design by Sasabe is the only one that has led to highly luminescent and TADF mononuclear complexes for OLED applications. In these examples, the TADF is metal-mediated as the spatial distribution of the ligands is locked so that LLCT and ILCT transitions become dominant and highly emissive. Thus, the D-A ligand design turns out to be a key aspect as in other metal complexes based on Pd(II) and Ag(I) – *vide infra*.

2.3.2. Ir-complexes. Homoleptic and heteroleptic Ir(III) complexes based on C N (e.g., 2-phenylpyridine) and diimine ancillary ligands have been widely utilized as phosphorescent emitters due to their versatile color range, spanning from red to green, and blue.^{184–186} However, achieving blue phosphorescent OLEDs typically involves incorporating electron-withdrawing substituents, such as fluorine, to lower the energy of the HOMO or, alternatively, the introduction of electron-rich heterocycles in place of the ppy moiety, such as imidazole ligands, to raise the LUMO energy. Both strategies lead to poor electrochemical stability and reduced operational lifetimes, since the excited metal-centered states become accessible.¹⁸⁷ However, electron-rich ligands, such as imidazo[1,5-*a*]pyridine have recently shown TADF. In short, Schlettwein's group reported for the first time this novel family in 2019 without indicating any TADF.¹⁸⁸ However, Göttlich's group systematically investigated the impact of the π -system size, substitution,

complexation position, and temperature on the luminescence characteristics of Ir(III) complexes based on imidazo[1,5-*a*]pyridine and quinoline derivatives (**Ir1–6**, Scheme 1).¹⁸⁹ Interestingly, all the complexes show two luminescent bands, the first one in the blue region decaying in around 4 ns (ligand centered fluorescent) and a second one in the green-yellow region decaying bi-exponentially. The latter has been attributed to TADF through time-dependent density-functional theory (TD-DFT) calculations, confirming the poor HOMO–LUMO overlap, reaching $\Delta E_{ST} < 807$ cm $^{-1}$ in all cases.

Despite the novel complexes have not been employed in lighting devices yet, their work is a milestone in the development of TADF Ir(III) complexes. To date, only other two families of mononuclear Ir(III) complexes have been proved to show TADF. First, a cyclometalated Ir(III) complex with two C N ligands (C N = 2-(2,4-difluorophenyl)pyridine, F₂ppy) and one acyclic diamino carbene (ADC) ancillary ligand (**Ir7**) reported in 2018 by Teets' group.¹⁹⁰ In this context, it is worth to mention also the theoretical work by Zhang's group that nicely deepens the discussion about the excited-state dynamic of **Ir7** (Scheme 1).¹⁹¹ Indeed, it is very interestingly not only because it is the first example of metal-mediated nucleophilic addition to a coordinated isocyanide followed by orthometalation of the formed ADC in mild conditions, but also due to its highly emissive nature (PLQY of 79% in PMMA) with relatively short lifetime (0.9 μ s). Again, it only exists a small overlap between HOMO and LUMO, which leads to small ΔE_{ST} . Combined with the proper strength of the SOC, the rate of rISC calculated from the triplet excited state to the singlet excited state is higher than the phosphorescence emission from the former to the ground state. This has been related to efficient TADF, reaching k_{rISC} of 1.86×10^9 s $^{-1}$ that is among the highest rate also compared with traditional organic molecules – Fig. 9. Lastly, Shafikov and Kozhevnikov's groups reported a non-stereogenic dinuclear complexes that show TADF in both, the monomeric and dimeric forms in 2021 (**Ir8–9**, Scheme 1).¹⁹² Importantly, utilizing symmetrical dianionic C N C ligands simplified the synthesis process, avoiding the formation of detrimental diastereomers. Moreover, this approach eliminated the need for monodentate ligands, such as chlorides, which may contribute to direct SOC in the T_1 state to ground state. In detail, they used 2,6-di(2,4-difluorophenyl)pyridine as C N C ligand and 4,6-difluoro-5-*n*-hexyloxy-1,3-di(pyridine-2-yl)benzene as N C C N for the mononuclear complex **Ir8** and its pyrimidine derivatives for the dinuclear complex **Ir9**. At room temperature, they show k_r of 1.50×10^5 s $^{-1}$ and 6.1×10^5 s $^{-1}$ for **Ir8** and **Ir9**, respectively. These values are remarkably high with respect to other red-emitting Ir(III) complexes. In addition, the unstructured shapes of their emission spectra and their significant overlap with the corresponding $S_0 \rightarrow S_1$ absorption bands indicate a charge-transfer character of the emitting state T_1 and its close energetic proximity to the excited singlet states. Gao and Cui's groups demonstrated through detailed theoretical work that the energy of the triplet excited state is only slightly lower than the one of singlet excited (only 2.2 kcal mol $^{-1}$).¹⁹³ The d_z orbital is mostly located on the central Ir atom and the phenyl group of



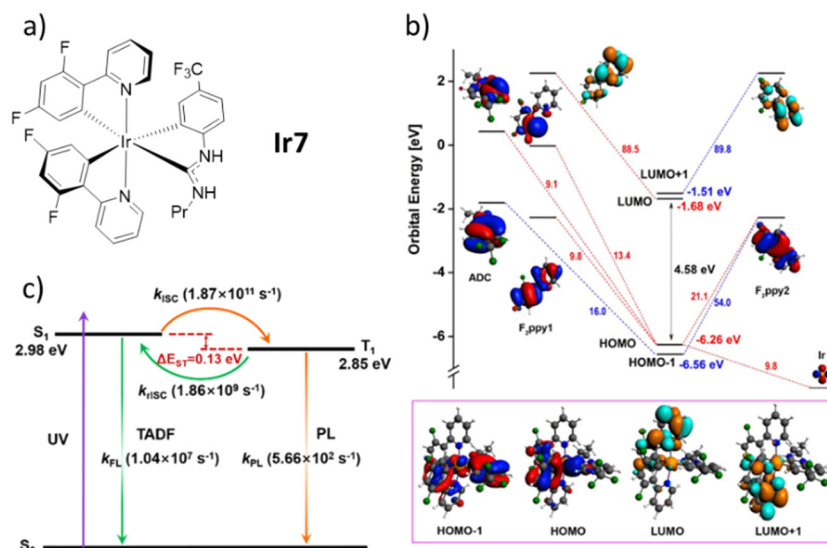


Fig. 9 (a) Structure of **Ir7**. (b) Fragment analysis of frontier molecular orbitals at the S_0 minima for compound **Ir7**. Also shown are the molecular orbital energies (in eV). (c) TADF working mechanism for the **Ir7**. Reproduced with permission from ref. 190 and 191.

the $N^{\wedge}C^{\wedge}N$ ligand, whereas the π_3^* orbital is spread across the entire length of the $N^{\wedge}C^{\wedge}N$ ligand. This leads to a poor HOMO–LUMO overlap. They also estimated the k_{ISC} of **Ir8** to be as high as $2.29 \times 10^9 \text{ s}^{-1}$, sufficiently high to guarantee an efficient TADF mechanism at room temperature.

Although the experimental insights for a TADF mechanism of **Ir9** were only limited, Kozhevnikov's group, in a recent follow-up paper, confirmed the behavior more in detail in a close-related dinuclear complex (**Ir10**, Scheme 1) using 4,6-bis(2-hydroxyphenyl)pyrimidine as bis- $N^{\wedge}O$ bridging coordinating ligand.¹⁹⁴ In this case, the short linker has been useful also to perform a diastereospecific reaction, leading to only the *rac*- $\Lambda\Lambda$ or *rac*- $\Delta\Delta$. The temperature-dependent steady-state spectra indicate the presence of two luminescent parts: a broad, featureless higher-energy part prevalent at elevated temperatures, and a lower-energy part with a noticeable vibronic shoulder at lower temperatures. Furthermore, the variation of the observed excited state lifetime with temperature follows a Boltzmann's distribution, confirming the fast equilibrium between the two states. Finally, OLEDs were fabricated (Section 3). These seminal works expand the comprehension of potential emissive routes in mononuclear and dinuclear Ir-complexes, moving beyond the model reliant on SOC. TADF emerges as a probable yet overlooked pathway in such complexes led by the poor HOMO–LUMO overlapping.

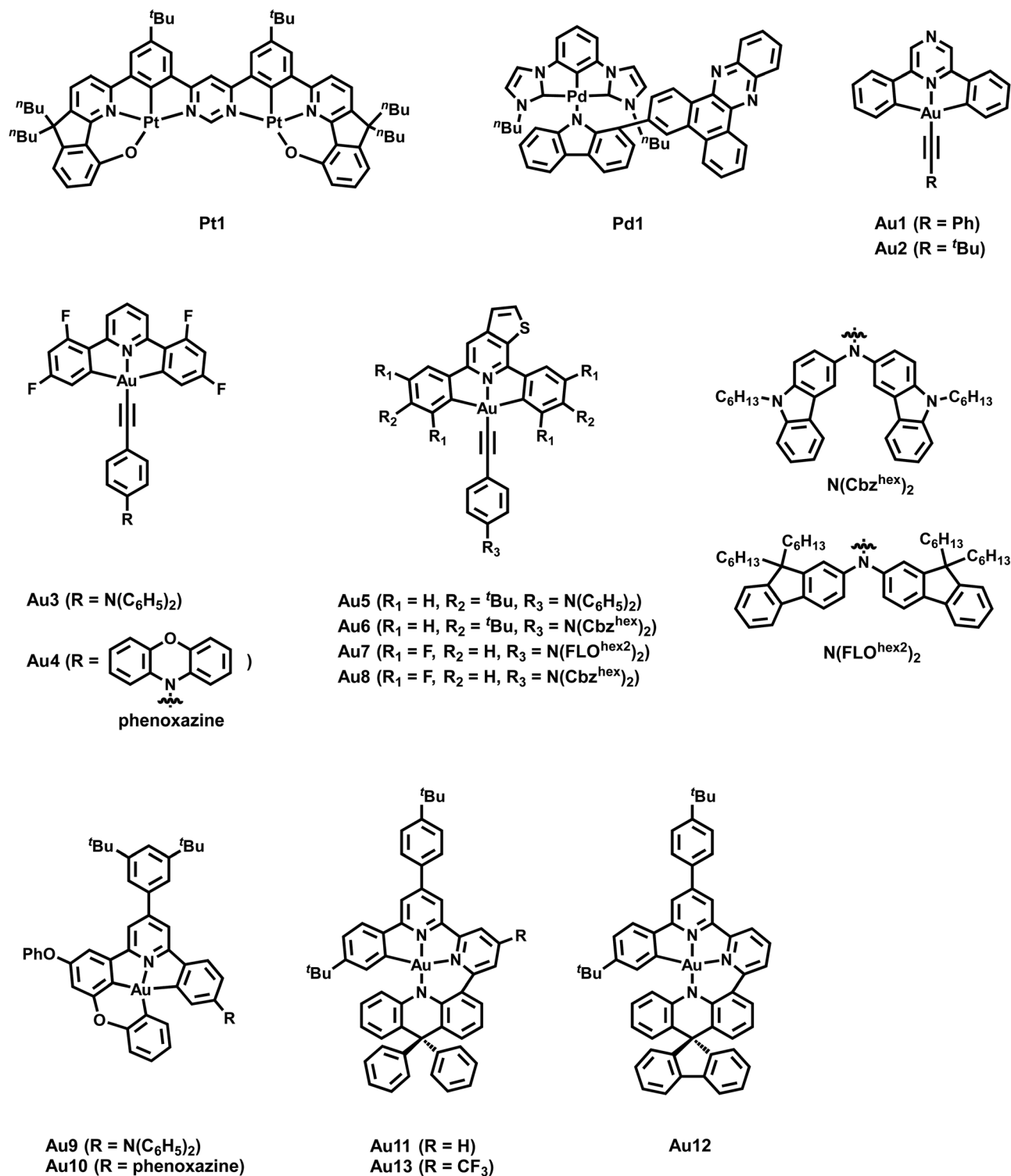
2.3.3. Pd-, Pt-, and Au-complexes. Changing the emission from phosphorescence to TADF in Pd(II) complexes has been recently attempted,^{195–199} but a clear design is still missing. In 2023, Li and coworkers reported the only Pd(II) complexes showing pure TADF (Scheme 2, Fig. 10 and Table 1).²⁰⁰ TADF was achieved through the coordination of a D–A type ligand based on a carbazole (Cz)-modified phenazine derivative. The concept of metal-perturbation distinctly affects the TADF as (i) the d-orbital contribution to the HOMO increases and thus, the

SOC effect is enhanced and (ii) the larger torsion angle between the D–A units caused by steric hindrance due to the metal ion coordination gives a smaller ΔE_{ST} . Finally, the red-emitting **Pd1** ($\lambda_{\text{em}} = 637 \text{ nm}$, Scheme 2) complex with high PLQY up to 89% in PMMA film and high radiative rates was proven as an efficient TADF emitter. Variable-temperature (VT) studies combined with Arrhenius and Boltzmann-type fittings gave energy splitting of 726 and 589 cm^{-1} , respectively.

Likewise, Pt(II) complexes are widely used to exploit their phosphorescent-dominated emissions, but only little is known about their TADF. As revealed by previous studies, the introduction of a second metal center was found to strongly increase the k_r constant and concomitantly reduce ΔE_{ST} .^{202,203} Dias and coworkers successfully applied this strategy, whilst obtaining a new dinuclear Pt(II) TADF complex, **Pt1** – Scheme 2, with remarkably small energy splitting of 556 cm^{-1} and short excited state lifetimes in the range of 1–2 μs – Table 1.²⁰¹ Both, the Pt(II) d-orbital admixtures in the ILCT character of the lowest-energy transition and the small HOMO–LUMO overlap strongly favor the TADF emission in the reported complex. In a subsequent study of the same group, a similar dinuclear Pt-complex was found to display a dual emission involving TADF from S_1 state and phosphorescence from the T_1 state.²⁰⁴

Finally, Au(III) exhibits low-lying d orbitals as further reflected in its relatively high reduction potential. Consequently, the lowest excited states are mostly LC with small metal contributions and thus, efficient phosphorescence displays the main emissive pathway further favored by its high SOC constant. The concomitant long triplet emission lifetimes limit their performance in OLEDs as roll-off effects are evident.^{205–212} In 2015, Bochmann and coworkers reported the first Au(III) complexes with TADF at room temperature.²¹³ Alkynyl Au(III) complexes containing pincer-like pyrazine moieties ($C^{\wedge}N^{\wedge}C$) for the first time, **Au1–2** – Scheme 2, showed a



Scheme 2 Molecular structures of **Pd1**, **Pt1** and **Au1–13**.

blue-shifted emission behavior upon a temperature increase from 77 to 298 K in the solid state. The transitions are characterized by metal-perturbed LLCT nature ($\pi(\text{C}\equiv\text{CPh}) \rightarrow \pi^*(\text{C}^{\wedge}\text{N}^{\text{Pz}}\text{C})$). Distinct modulations in solution *via* protonation or the addition of AgOTf or CuOTf lead to enhanced TADF

emission arising from the coexistence of high energy TADF and ^3IL ($\text{C}^{\wedge}\text{N}^{\text{Pz}}\text{C}/3\text{LLCT}$ ($\text{X} \rightarrow \text{C}^{\wedge}\text{N}^{\text{Pz}}\text{C}$) transitions.

In the following years, research started to focus on changing the nature of the lowest excited state of cyclometalated ($\text{C}^{\wedge}\text{N}^{\wedge}\text{C}/\text{C}^{\wedge}\text{C}^{\wedge}\text{N}$) Au(III) complexes to induce efficient TADF. In detail,



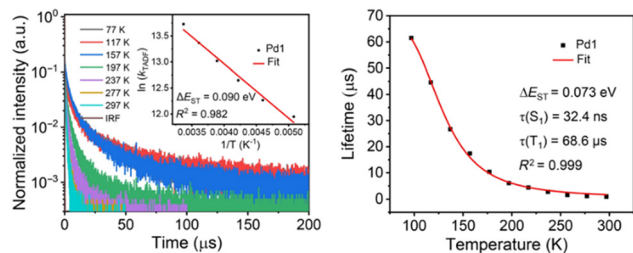


Fig. 10 Left: Temperature-dependent transient PL characteristics of **Pd1** in PMMA films. Inset: Arrhenius fit of the k_{DF} value vs. temperature. Right: Boltzmann-type fitting of the emission lifetimes of **Pd1** in PMMA film at various temperatures. Printed with permission from ref. 200.

emissions from ^3IL states with rather long-lived excited state lifetimes and small k_r rates mainly dominate the emission pathway of cyclometalated Au(III) complexes. To achieve CT nature of the lowest excited state, several strategies to increase (i) the energy of the ^3IL states, (ii) the energy difference between the ^3IL and $^3\text{LLCT}$ states and/or (iii) to lower the energy of the $^1/3\text{LLCT}$ states were assessed. In this context, Che *et al.* reported several cyclometalated Au(III) complexes with donor-substituted amino-alkyl auxiliary ligands.^{214,215} Due to their limited thermal stability, Che's group focused on alkynyl ligands owing to the stronger Au(III)–C_{sp}(acetylide) bond character, **Au3–4** (Scheme 2).²¹⁶ They hypothesized that the combination of 2,6-bis(2,4-difluorophenyl)pyridine or 2,6-bis(2,4-diterbutylphenyl)pyrazine accepting-pincer ligands (C^NC) with alkynyl ligands bearing strong donor groups, *e.g.* *p*-NPh₂, *m*-NPh₂, phenoxazine, provoke higher ^3IL states and larger energy separations between $^3\text{IL}/^3\text{LLCT}$ states that can facilitate TADF. The spatially well-separated donor (alkynyl) and acceptor (C^NC) units led to efficient TADF emitters, **Au3–4**, which was substantially supported by DFT/TD-DFT calculations. The latter also gives evidence for the high rotational flexibility of the auxiliary ligand, owing to the presence of the C≡C bond and thus, an increased distance between the two ligands. This results in decreased steric hindrances between the protons of the phenyl moiety (alkynyl ligand) and those of

phenyl rings of C^NC. In the case of **Au3**, the energy splitting $\Delta E(\text{S}_1\text{--T}_1)$ was found to strongly relate with the dihedral angle between the C^NC plane and the phenyl group connected to the C≡C bond, δ . For instance, ΔE_{ST} drastically decreases from 2660 cm^{−1} ($\delta = 5.4^\circ$) to 182 cm^{−1} for δ of 101°. In a subsequent work, Yam and coworkers presented several in-depth studies involving DFT/TD-DFT calculations and nanosecond TA measurements to rationalize the design of cyclometalated (C^NC/C^NC) Au(III) alkynyl/carbazolyl TADF emitters.^{217–219} Among other ligands systems, we exemplarily discuss how the nature of the excited states of three alkynyl Au(III) complexes, **Au5–8** (Scheme 2), were manipulated to enable TADF. As indicated by the vibronic-structured emission band of **Au5** and its relatively long excited state lifetime of 96.1 μs with a small k_r of $5.93 \times 10^3 \text{ s}^{-1}$, TD-DFT calculations further confirmed that the emission originates from ^3IL states [$\pi \rightarrow \pi^*(\text{C}^{\text{N}}\text{THPY}^{\text{C}})$]. Next, the donor strength of the alkynyl ligands was increased by replacing the triphenylamine unit with a Cz-triphenylamine moiety, **Au6–8**, to destabilize the HOMO energy. This finally results in achieving energetically lower lying $^1/3\text{LLCT}$ [$\pi(\text{fused heterocyclic alkynyl}) \rightarrow \pi^*(\text{C}^{\text{N}}\text{THPY}^{\text{C}})$] states and thus TADF is induced (Fig. 11) as indicated by short excited state lifetimes of 0.4–5.7 μs and high k_r up to $1.00 \times 10^6 \text{ s}^{-1}$. This was further corroborated by temperature-dependent studies of **Au6** and **Au7**, as the same structureless and broad emission band evolved at 77 K, but with a small shoulder around 525 nm that was assigned to ^3IL transitions.

The ΔE_{ST} was then estimated with an Arrhenius plot derived from a full kinetic scheme for two-level systems – Fig. 11, but only in the range from 200 to 360 K to reduce the contribution of the ^3IL excited state in this fitting procedure. The experimentally obtained ΔE_{ST} value of 250 cm^{−1} (**Au6**, Scheme 2) and 259 cm^{−1} (**Au7**, Scheme 2) is in agreement with the one obtained from TD-DFT ($\Delta E_{\text{ST,calc}} = 435 \text{ cm}^{-1}$ for **Au6**). A further increase of the energy splitting between ^3IL and $^1/3\text{LLCT}$ was achieved by replacing the *tert*-butyl-substituted cyclometalating ligand in **Au6** by the *fluor*-substituted one that gives **Au7** and **Au8** – Scheme 2, Fig. 11 and Table 2.

Table 1 Photophysical properties of Zr, Al, Ir, Pd, Pt-complexes showing TADF in the solid state

Complex	λ_{max} (298 K)/ λ_{max} (77 K) [nm]	PLQY [%]	τ_{DF} [μs]	ΔE_{ST} [cm ^{−1}]	$k_r \times 10^5$ [s ^{−1}]	$k_{\text{nr}} \times 10^5$ [s ^{−1}]	Ref.
Zr(PDP)2	595	45	350	1652	281	—	182
Al1	497	65	4.4	1694	—	—	180
Al2	534	79	3.9	645	—	—	180
Al3	554	92	<2	516	210	—	183
Ir1	465, 560	6	0.54	<800	—	—	189
Ir2	475, 560	2	0.30	<800	—	—	189
Ir3	470, 615	6	0.61	<800	—	—	189
Ir4	465, 575	12	0.68	<800	—	—	189
Ir5	465, 575	2	0.58	<800	—	—	189
Ir6	470, 575	1	0.41	<800	—	—	189
Ir7	498/456	22	0.90	1048	104	—	191
Ir8	537/540	15	1.00	800	1.5	8.5	192
Ir9	642/645	80	1.31	—	6.1	1.5	192
Ir10	643	30	0.85	556	49	—	194
Pd1 ^a	637/—	89	0.97	726/589	9.2	1.1	200
Pt1 ^b	640/—	—	2.3	484	—	—	201

^a 5 wt% of **Pd1** doped polymethyl methacrylate (PMMA). ^b 0.1 wt% of **Pt1** in Zeonex[®] films.



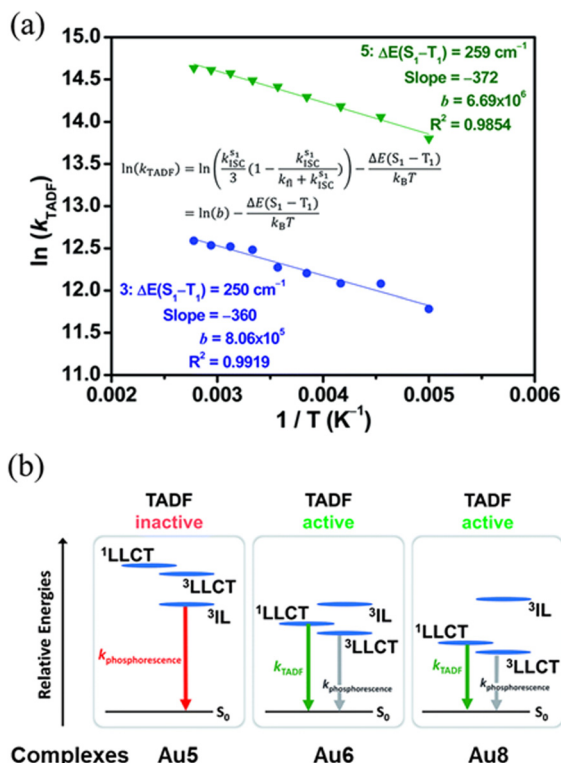


Fig. 11 (a) Plot of $\ln(k_{\text{TADF}})$ vs. $1/T$ of **Au6** (●) and **Au7** (▲) in 5 wt% doped *m*-*N,N'*-dicarbazolyl-3,5-benzene (mCP) thin-films monitored at 560 and 570 nm, respectively, and the fits of the temperature-dependent lifetime data from 200 to 360 K. (b) Qualitative state diagram depicting the relative energies of the ¹LLCT states and the ³IL state of **Au5**, **Au6** and **Au8** in the solid state at 298 K. The trend of the relative energies of the states is based on the results from the emission studies. Printed with permission from ref. 217.

In fact, the stability of metal complexes can be improved by increasing the chelating behavior ligands. The use of rigid tetradentate ligands involving C-donor atom(s) is known to strengthen the metal–ligand bond character, resulting in higher thermal stabilities and restricted excited state structural

distortions. Onda and coworkers recently suggested that such rigid structures can also reduce the activation energy barrier for rISC and favor efficient TADF.²²² Consequently, Che and others started to work on tetradentate ligand frameworks for Au(III) complexes.²²³ First, Che's group implemented a microwave-assisted C–H activation step leading to a new synthetic pathway toward tetradentate (C[∧]C[∧]N[∧]C) Au(III) complexes – **Au9–10**; Scheme 2 and Table 2.

The introduction of the alkoxy group in the 3-position of the phenyl ring of the C[∧]N[∧]C moiety of the C[∧]C[∧]N[∧]C ligand scaffold was considered as key to obtain a superior rigidity as 5-5-6 membered chelating rings are formed. In terms of design rules toward TADF, the incorporation of a donor group, *e.g.* DMA, **Au9**, or phenoxazine, **Au10**, in the phenyl ring *trans* to the pyridine unit was proven to be paramount for spatially well-separated HOMO and LUMOs and thus, small ΔE_{ST} values. Indeed, $\Delta E_{\text{ST}} = 686$ cm⁻¹ and excited states of ¹/₃LLCT [$\pi(\text{donor unit}) \rightarrow \pi^*(\text{C}^{\wedge}\text{N}^{\wedge}\text{C})$] character confirmed the presence of TADF. These findings agree well with the lifetimes of *ca.* 2 μs associated with PLQYs up to 82%, **Au9**, and radiative decay rates up to 3.94×10^5 s⁻¹ in thin-film states. In 2023, Yam and co-workers demonstrated how to obtain low-energy emitting Au(III) complexes without sacrificing PLQYs and TADF behavior, **Au11–13** – Scheme 2.²²¹ The use of the more rigid tetradentate ligand scaffold (*e.g.*, C[∧]C[∧]N[∧]N) instead of the pincer-like ones in combination with strong donating acridinyl moieties resulted in (i) orange to deep-red emitting Au(III) complexes with PLQYs up to 76% and radiative decay rates in the range of 10⁵ s⁻¹, and (ii) decreased ΔE_{ST} owing to the stabilization of the S₁ states. The latter can be mainly rationalized by the increased energy difference between the IL and ILCT excited states, as already discussed above. In addition, the color tuning was shown to be more effective when introducing electron-withdrawing groups in the pyridine unit instead of incorporating electron-donating groups in the acridinyl moiety.

2.3.4. Cu-, Ag- and Zn-complexes. During the last decades, significant attention has been devoted to closed-shell TMCs configurations, since (i) non-radiative low-lying metal-centered

Table 2 Photophysical properties of Au-complexes showing TADF in the solid state

Complex	λ_{max} (298 K)/ λ_{max} (77 K) [nm]	PLQY [%]	$\tau_{\text{T}}/\tau_{\text{DF}}$ [μs]	ΔE_{ST} [cm ⁻¹]	$k_{\text{r}} \times 10^5$ [s ⁻¹]	$k_{\text{nr}} \times 10^5$ [s ⁻¹]	Ref.
Au1	523/530	4.5	—	—	—	—	213
Au2	523/532	8.3	—	—	—	—	213
Au3^a	577/—	88	—/0.85	—	10.35	—	216
Au4^b	567/—	65	—/1.46	—	4.45	—	216
Au5^c	528, 568, 616/—	57	69.1/—	—	0.059	0.045	217
Au6^c	562/—	87	—/5.7	250	1.56	42.1	217
Au7^c	585/—	70	—/0.6	259	5.38	2.31	217
Au8^c	636/—	40	—/0.4	—	1.00	15.0	217
Au9^d	520/—	82	—/2.08	686 ^e	3.94	—	220
Au10^d	568/—	71	—/2.54	—	2.80	—	220
Au11^c	595/—	73	—/1.2	1129	6.1	—	221
Au12^c	598/—	63	—/2.0	1129	3.2	—	221
Au13^c	650/—	12	—/1.4	—	0.86	—	221

^a PMMA thin-film samples, 4 wt% of the complex. ^b Tris(4-carbazolyl-9-ylphenyl)amine (TCTA): 1,3,5-tris(*N*-phenylbenzimidazol-2-yl)benzene (TPBi) thin-film samples, 4 wt% of the complex. ^c mCP thin-film with 5 wt% of the complex. ^d TCTA thin-film with 8 and 4 wt% for **Au9** and **Au10**, respectively. ^e Obtained from TD-DFT calculations.



excited states (d-d* transitions) are absent, (ii) they are cost-effective and more sustainable for potential up-scaling processes, (iii) they hold a large structural variety of their coordination sphere, (iv) their redox properties are easily tunable, and (v) the discovery of TADF emission mechanism.²²⁴

Over the last two decades, a large number and variety of Cu(I) complexes, including different geometries and nuclearities, have shown TADF. This can be rationalized by the spatially well-separated HOMO and LUMOs. In addition, owing to the energetically high-lying 3d orbitals of Cu(I), they strongly contribute to the nature of the frontier orbitals, and hence, the low-energy transitions are often of CT character, *e.g.* MLCT, (M+X)LCT or LLCT. In this context, the relatively small SOC of copper plays a key role therein as it is large enough to ensure efficient rISC to populate S_1 owing to the involvement of Cu(I) in the frontier orbitals but is small enough to hamper efficient transitions from T_1 to S_0 . However, the choice of ligands and coordination motifs can lead to scenarios, in which the SOC becomes large, and thus, the emission is not only ruled by TADF but also phosphorescence.¹⁸¹ Among mononuclear complexes, linear/two-coordinated and four-coordinated Cu(I) complexes display the most prominent classes, while less attention has been devoted to trigonal/three-coordinated complexes.

Among four-coordinated complexes, heteroleptic cationic as well as their neutral analogs display the most studied representatives. Heteroleptic cationic Cu(I) complexes, $[Cu(N^{\wedge}N)(P^{\wedge}P)]^+$, typically feature chelating diphosphine ligands ($P^{\wedge}P$) – *e.g.* dppbz, POP (= bis[2-(diphenylphosphino)phenyl]ether), xantphos = 4,5-bis-(diphenylphosphino)-9,9-dimethylxanthene, and modifications thereof – and bidentate diimine ligands ($N^{\wedge}N$), *e.g.* diimines, phenanthroline – Fig. 12.

The HOMO is predominantly of 3d-nature of the Cu(I) orbitals with minor contributions of the P atoms of $P^{\wedge}P$, while the LUMO is solely located on the π^* system of the diimine ligand ($N^{\wedge}N$).^{172,225,226} As confirmed by various in-depth TD-DFT/DFT calculations, the lowest excited states are mainly of MLCT character, and in combination with the distinct spatial separation of the HOMO and LUMO, a small energy splitting is obtained, resulting in efficient TADF. In terms of color tunability, the emission colors are adjusted by de-/stabilizing the LUMO energy, since chemical modifications of the diimine ligands are more straightforward compared to diphosphines. The resulting large variety of diimine ligands, *e.g.* bipyridines, phenanthroline, pyridine/pyrazine-pyrazole, biquinolines, dipyrindylamines, and derivatives thereof, gave access to emission colors of the corresponding Cu(I) complexes covering the whole visible and NIR regions – Fig. 12.²²⁷

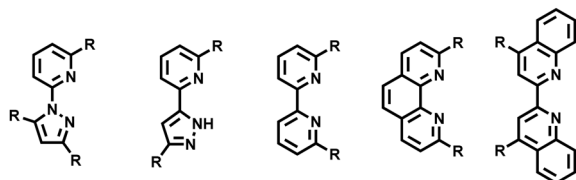


Fig. 12 Diimine ligands used in Cu-complexes for color tuning.

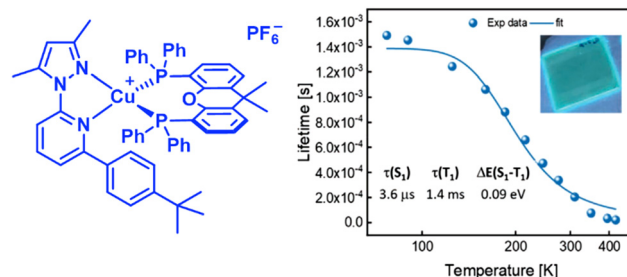


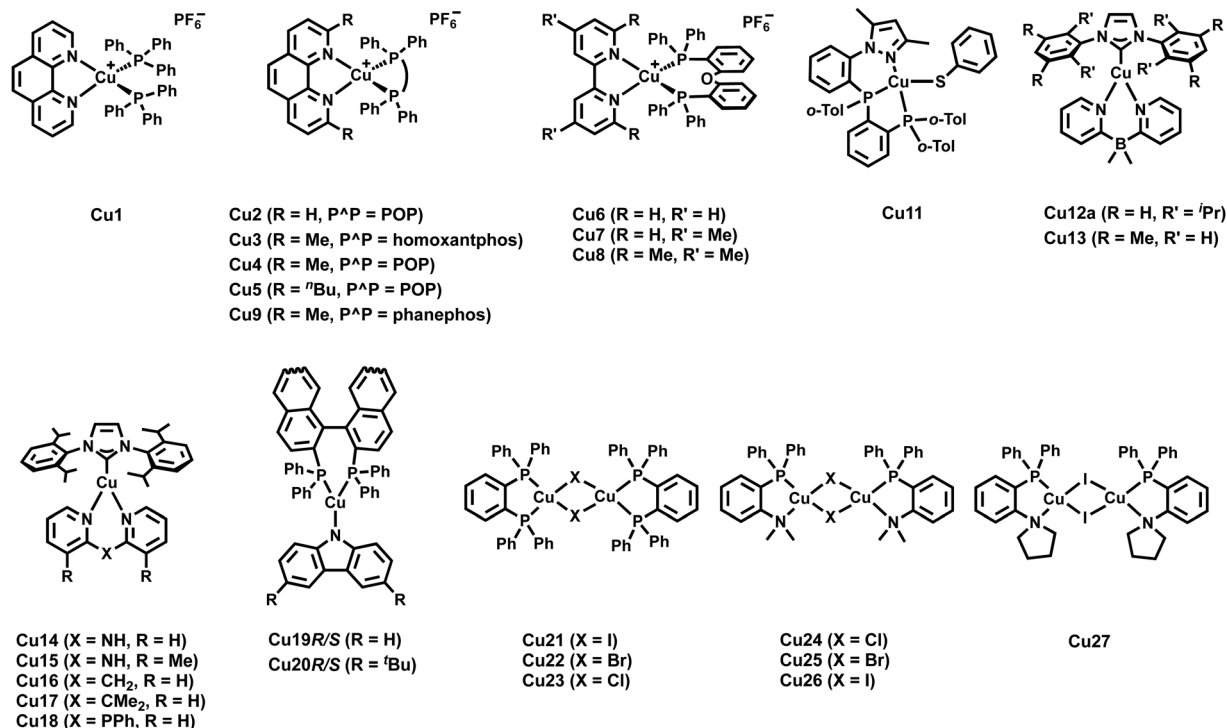
Fig. 13 Left: Structural representation of a highly emissive blue-emitting Cu(I) complex. Right: $\langle \tau \rangle$ vs. temperature plot the corresponding thin-film fitted with eqn (6), thin-film under UV irradiation ($\lambda_{\text{ex}} = 305 \text{ nm}$) is depicted as inset. Reproduced with permission from ref. 228.

In this context, Costa and coworkers developed a multivariate analysis tool to predict photoluminescent and electroluminescent key parameters, such as PLQYs and λ_{em} , for a given molecular structure. This was exploited to refine a highly blue emissive Cu(I) complex for LECs – Fig. 13 and Section 3.²²⁸

As a tremendous number of four-coordinated Cu(I) complexes have been explored over the last two decades, this section mainly focus on the design strategies to unlock TADF emission in these complexes combined with the most prominent examples. Interested readers are highly recommended to refer to the excellent previous reviews targeting emissive Cu(I) complexes as a complement to this review.^{90,128,172,226,229,230}

As noted above, lifetimes in the sub-microsecond range and high PLQYs are paramount for efficient TADF emitters and display a crucial requirement for the validity of the fitting procedures – Section 2.1. In this regard, major attention has been devoted to strategies to minimize the undesired flattening distortion of Cu(I) complexes upon excitation.²³¹ In detail, upon excitation a weakening of the Cu-P σ -bond and a geometrical change from (pseudo)-tetrahedral to square-planar, *e.g.* Jahn-Teller distortion, due to the partial oxidation of Cu(I), is typically noted. As a consequence, fast non-radiative decay rates are reflected in drastically decreased PLQYs. First, in-depth studies on heteroleptic $[Cu(P^{\wedge}P)(N^{\wedge}N)]^+$ complexes revealed the importance of using chelating and large bite-angle diphosphines like POP and xantphos ligands due to (i) the prevention of ligand redistribution processes and the formation of undesired homoleptic complexes and (ii) improved photophysical properties, especially increased PLQYs – Cu1–2, Scheme 3 and Table 3.^{232–234} In this regard, Zysman-Colman and coworkers recently studied the influence of large bite angles diphosphines, *e.g.* POP (102°), xantphos (112°), homoxantphos (102°), as well as their flexibility range on the photophysical and EL properties. The heteroleptic $[Cu(\text{homoxantphos})(\text{dmp})]^+$ complex, Cu3 – Scheme 3, displays the highest PLQYs and is the most interesting candidate in terms of electroluminescence – Section 3.²³⁵ Further improvements can be obtained by using matrix materials like cages of rigid microenvironments^{236–238} or performing changes at the molecular level. For instance, the introduction of bulky groups, *e.g.* alkyl, methoxy, or phenyl groups, at the *ortho* position of the diimine ligands leads to a



Scheme 3 Molecular structures of **Cu1–27**.

5-fold increase of the PLQYs, *e.g.* **Cu2–8** – Scheme 3, since the increased bulkiness of the N^{*}N ligands drastically suppresses structural distortions upon excitation.²³⁹ Among others, Constable and Housecroft further expanded the library of substituted diimine ligands – *e.g.* including alkenyls, alkynyls, and thioethers.^{240–242}

Yersin and coworkers presented a design strategy to increase the overall rigidity of the coordination sphere. In short, the bulky diphosphine, phanephos, was employed to build a rigid “semicage” around the Cu(I) center in combination with dmp, **Cu9** – Scheme 3. Table 3 and Fig. 14. The mutual steric interactions between the P⁺P and dmp drastically minimize radiationless relaxations that result in high PLQYs up to 80% and record small non-radiative decay rates of $1.4 \times 10^4 \text{ s}^{-1}$ without exceeding the required ΔE_{ST} of 1000 cm^{-1} . In addition, the authors noted that the emission scenario at ambient temperature is characterized by a mixture of TADF and phosphorescence. The ratio of S_1/T_1 was then estimated to be 20 by applying the following equation:²⁴⁶

$$\frac{I(S_1)}{I(T_1)} = \frac{k_r(S_1)}{3k_r(T_1)} \times e^{\frac{\Delta E_{\text{ST}}}{k_B T}} \quad (21)$$

However, **Cu9** already demonstrates the challenge of achieving high radiative rates, without sacrificing small ΔE_{ST} values to obtain efficient TADF. In this context, a neutral heteroleptic, four-coordinated TADF Cu(I) emitters, **Cu10** – Scheme 3, with a relatively small ΔE_{ST} of 370 cm^{-1} and short excited state lifetimes of $\tau = 3.3 \text{ } \mu\text{s}$ was presented.²⁴⁷ The small ΔE_{ST} value

originates from a small overlap of the HOMO and the LUMO. The former features a 3d metal character with significant contribution from the nitrogen atoms of the anionic pyrazole-substituted phenyl borate ligand and the phosphorous atoms of dppbz. The LUMO is solely localized on the phenyl backbone ring of the dppbz ligand. As a consequence of the small HOMO–LUMO overlap and the related small exchange interactions, the $S_1 \rightarrow S_0$ transition is less favorable. Indeed, this is reflected in the calculated oscillator strength of $f = 0.0016$ and the relatively small fluorescence decay rate of $3.9 \times 10^6 \text{ s}^{-1}$ obtained from the three-state Boltzmann-type fitting – eqn (6).^{128,247,255}

An alternative strategy to obtain high PLQYs, short τ_{TADF} while maintain a small ΔE_{ST} was also presented by Yersin and coworkers. They designed a new rigid tridentate N,P,P-ligand, 3,5-dimethyl-1-(2-((di-*o*-tolyl)phosphanyl)(*o*-tolyl)phosphanyl)phenyl-1*H*-pyrazole, to achieve a TADF Cu(I) complex with small freedom for distortion in the excited states.²³¹ Further rigidity was achieved by employing the anionic thiophenolate ligand. The resulting TADF Cu(I) complex **Cu11** (Scheme 3) exhibits PLQYs up to 90% in the solid state with high TADF decay rates of $1.8 \times 10^5 \text{ s}^{-1}$ without the expected increase of ΔE_{ST} . The calculated small ΔE_{ST} of 600 cm^{-1} is favored by (i) the spatially well-separated HOMO (Cu(I) center + thiophenolate) and LUMO (phenyl backbone of the N,P,P ligand) and (ii) the MLCT character of the lowest excited states.

Concerning tri-coordinating Cu(I) complexes, Yersin, Gailard, and Costa introduced a new family of neutral and cationic



Table 3 Photophysical properties of Cu-complexes featuring TADF in the solid state

Complex	λ_{\max} (298 K)/ λ_{\max} (77 K) [nm]	PLQY [%]	$\tau_{\text{ph}}/\tau_{\text{DF}}$ [μs]	ΔE_{ST} [cm^{-1}]	$k_{\text{r}} \times 10^4$ [s^{-1}]	$k_{\text{nr}} \times 10^4$ [s^{-1}]	Ref.
Cu1	541/—	13	—/8.2	—	1.58	10.6	243
Cu2	556/—	15	—/4.5	—	3.33	18.9	243
Cu3	576/—	35	—	—	—	—	235
Cu4	527/—	49	—/13.2	—	—	—	244
Cu5	519/—	69	—/20.3	—	—	—	244
Cu6	580/—	3.0	—/1.5	—	—	—	245
Cu7	535/—	43	—/10.5	—	—	—	239
Cu8	555/575	55	87/11	720	5.0	4.1	239
Cu9	530/562	80	240/14	1000	5.7	—	246
Cu10	535/535	70	1200/3.3	370	21	—	247
Cu11	540/540	90	680/5	600	18	2.0	231
Cu12a	475/490	76	34/11	710	6.9	2.2	248
Cu13	575/585	73	18/21	—	4.1	1.5	248
Cu14	463/—	22	45/13	2823	1.7	6.0	249
Cu15	458/—	86	81/44	—	1.9	0.3	249
Cu16	473/483	15	32/6	565	2.5	14.2	250
Cu17	474/482	73	38/14	—	5.2	1.9	250
Cu18	503/519	86	87/13	484	6.6	1.1	250
Cu19S/R ^a	579/580	55	900/2.5	680	22	18	251
Cu20S/R ^a	606/603	53	1600/1.7	490	31	27	251
Cu21	502/505	80	211/4	—	—	—	252
Cu22	520/524	60	2300/4.3	—	—	—	252
Cu23	533/537	60	2400/4.2	—	—	—	252
Cu24	506/513	45	220/6.6	460	6.8	—	253
Cu25	490/498	65	930/4.1	510	16	—	253
Cu26	464/472	65	270/4.6	570	14	—	253
Cu27	465/465	65	250/5.6	630	12	—	253
Cu28 ^{mono}	548/—	58	2450/6.0	490	180	7.0	254
Cu28 ^{dimer}	577/—	80	2300/1.2	390	1130	67	254

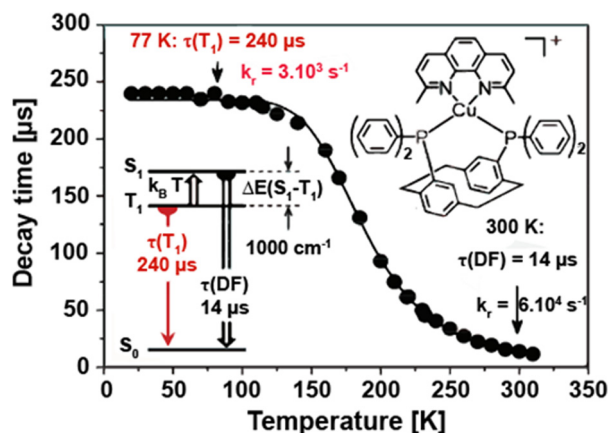
^a Ground powder sample.

Fig. 14 Emission decay time of Cu9 in powder state vs. temperature. The sample was excited with a pulsed UV laser at $\lambda_{\text{ex}} = 355$ nm (pulse width 7 ns). The emission was detected at $\lambda_{\text{det}} = 550$ nm. The solid line represents a fit of eqn (6) to the experimental data with the phosphorescence decay time $\tau(T_1) = 240$ μs measured at 77 K. The resulting fit parameters are $\Delta E_{\text{ST}} = 1000$ cm^{-1} and $\tau(S_1) = 40$ ns, representing the magnitude of the singlet–triplet splitting and the decay time of the spontaneous $S_1 \rightarrow S_0$ fluorescence, respectively. The spontaneous fluorescence is not observed directly due to much faster intersystem crossing. $\tau(\text{DF}) = 14$ μs is the decay time of the delayed fluorescence at ambient temperature. Reproduced with permission from ref. 246. Copyright 2013, Royal Society of Chemistry.

three-coordinated Cu(i) complexes bearing bidentate nitrogen-based ligands, e.g. bis-pyridyl, dipyridylamine, phenanthroline,

bipyridine, and modifications thereof, and N-heterocyclic carbene (NHC) ligands.^{248,256,257} The (i) good σ -donating and π -accepting properties of carbene ligands and (ii) the possibility to introduce bulky substituents in the carbene backbone strongly contribute to the high stability of the resulting NHC–Cu(i) complexes.

While the first neutral NHC–Cu(i) complexes that bear bidentate nitrogen-based ligands solely displayed phosphorescence,^{256,257} Yersin and coworkers shed light on the crucial parameters that rule the TADF behavior in these complexes.²⁴⁸ In short, it was found that ΔE_{ST} is marginally affected by electronic substitution on the NHC ligands, but strongly impacted by steric modifications (e.g. ⁱPr vs. Me) – of the phenyl groups bound to the nitrogen atoms of the NHC ligand. For instance, Cu12a shows TADF, while Cu13 only emits from T_1 . Based on these findings, in-depth TD-DFT/DFT calculations of a model complex, Cu12b, without any substituents in the phenyl group revealed a significant relation between the torsion angle, N–C–Cu–N, and ΔE_{ST} – Scheme 3, Fig. 15 and Table 3. In detail, it was found that a planar configuration (torsion angle of 0°) leads to a delocalization of the HOMO – without affecting the LUMO – which then resulted in a better spatial separation of the HOMO and LUMO and a small ΔE_{ST} of 540 cm^{-1} . This is in good agreement with the experimentally found value of 740 cm^{-1} for Cu12a – Table 3. The authors also noted SOC is effective in Cu12a as the phosphorescent lifetime of 34 μs is only three times longer than the one obtained at ambient conditions that correspond to TADF.

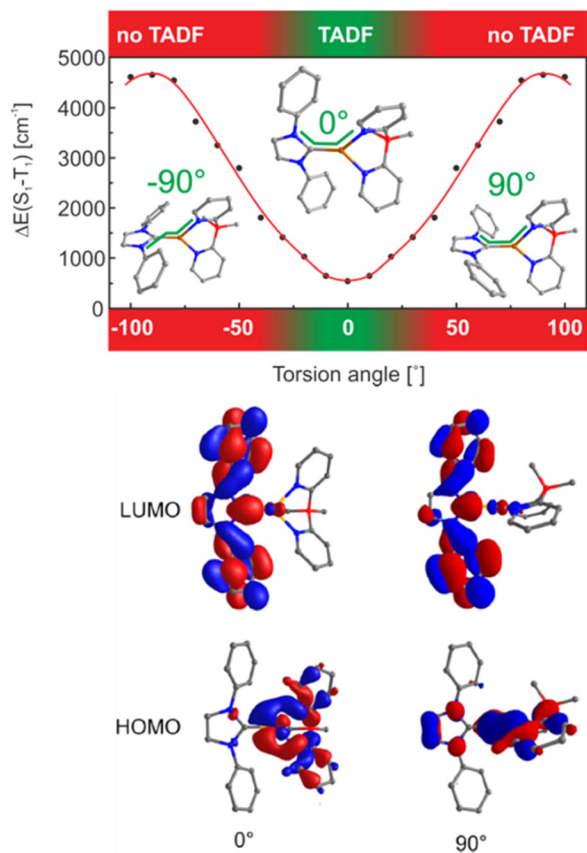


Fig. 15 Top: Singlet–triplet splitting $\Delta E(S_1-T_1)$ in dependence of the torsion angle N–C–Cu–N (marked by the green line) as obtained from DFT and TD-DFT calculations on the B3LYP/def2-SVP level of theory. Bottom: HOMOs and LUMOs of model compound **Cu12b** displayed for a torsion angles of 0° and 90° , respectively. Reproduced with permission from ref. 248.

Gaillard, Costa and coworkers studied the cationic NHC–Cu(I) analogs that feature – instead of the anionic dipyrrolyl borate ligand – neutral bis-pyridyl ligands with different bridging groups – Table 3. As the change of the ligand as well as the presence of the anion and its interactions with the cationic counterpart can change the electronic situation in the NHC–Cu(I) complex significantly, the findings from Yersin *et al.* cannot be extrapolated to these systems. However, certain trends have been established. At first, electronic modifications of the NHC ligands were found to marginally impact the photoluminescent properties as well as the nature of lowest excited states. In contrast, they are much more sensitive to electronic and steric changes in the bis-pyridyl ligands.^{249,257} For instance, the emission color is adjusted by modifying the dpa ligands, since the LUMO is located on the pyridine rings of the dpa, while the HOMO is mainly of metal and N- p_z character of the dpa ligand. Further, it was found that (i) shorter Cu–C_{carbene} bond distances, (ii) certain substitution patterns in the bis-pyridyl ligand, and (iii) high symmetry breaks, typically lead to higher PLQYs. The latter is related to (i) CH– π interactions between the phenyl group of the NHC ligand and the hydrogen

atoms of the bis-pyridyl ligand, (ii) changes of the bridging atom in the bis-pyridyl ligand, *e.g.* from NH to CMe₂ or PPh, and (iii) H–F interaction between the PF₆[–] anion and the hydrogen atoms of the bis-pyridyl ligand. As indicated above, the HOMO and LUMO are spatially well separated and according to DFT/TD-DFT calculations, **Cu14** and **Cu15** (Scheme 3) display TADF, but with a relatively large energy splitting of 2823 cm^{–1} (0.35 eV). This value was, indeed, defined as the upper limit for NHC–Cu(I) complexes by Yersin. In a subsequent work, the influence of the bridging group, *e.g.* CH₂, CMe₂ or PPh, on the TADF properties was studied, showing a much higher ΔE_{ST} values of 4839 cm^{–1} (0.6 eV) – **Cu16–18**; Scheme 3.²⁵⁰

The relatively long emission decay times in TADF Cu(I) complexes displays still a challenge in designing efficient TADF emitters suitable for LECs and OLEDs, since roll-off effects on the efficiency are expected to occur already at low current densities.^{167,252,258–261} In this context, Steffen, Pflaum, and coworkers designed the neutral Cz-based TADF Cu(I) complexes bearing the chiral diphosphine, *S*- and *R*-BINAP, **Cu19S/R** and **Cu20S/R**, that show record short τ_{TADF} in the range of 1.7–2.5 μ s and k_r constants up to 3.1×10^5 s^{–1} in the ground state – Scheme 3 and Fig. 16.²⁵¹ The TADF originates from LLCT states with the carbazolate unit as donor and the (*S*/*R*)-BINAP as accepting moiety with admixtures of MLCT. The authors noted a strong dependency of the PLQYs, emission maxima, and TADF properties on environmental changes since strong C–H··· π interactions in the crystalline state – confirmed by

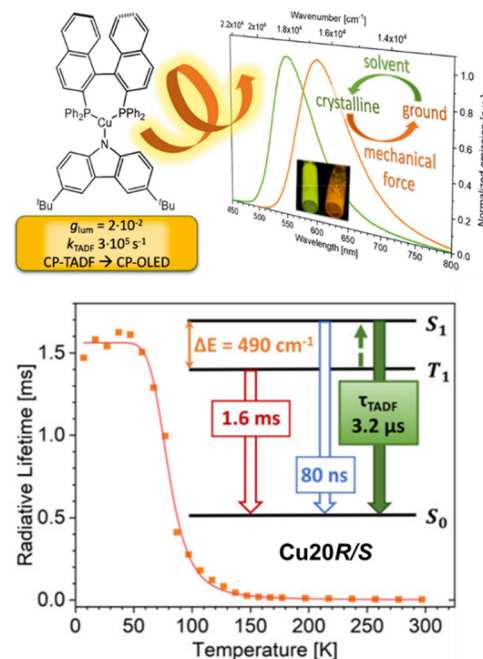


Fig. 16 Top: Structural presentation of **Cu20R/S** and the corresponding emission spectrum of the crystalline and ground powder sample, as well as their UV irradiation, is shown as inset. Bottom: Temperature dependence of the radiative lifetimes of **Cu20R/S** in the ground solid state and the state diagram visualizing the TADF processes. Reproduced with permission from ref. 251.

single crystal X-ray and powder X-ray diffraction (PXRD) analysis – were found. Upon grinding of the crystalline samples, the intermolecular C–H... π interactions were disrupted with a concomitant reduction of the number of surrounding dipoles. This results in a decreased energy splitting of the $^1/3$ LLCT states with a concomitant increase of the energetic separation between $^1/3$ LLCT and 3 LC (BINAP) states (ΔE_{ST} of 600 cm^{-1} (Cu20S/R) in crystalline to 490 cm^{-1} (Cu20S/R) in the ground state). Consequently, TADF becomes more efficient. In addition, Cu19S/R and Cu20S/R show circularly polarized luminescence (CPL) behavior with dissymmetry factors, g_{lum} , of up to $\pm 6.0 \times 10^{-3}$ in THF and $\pm 2.1 \times 10^{-2}$ in the solid state – Scheme 3.

TADF can also be achieved in dinuclear Cu(I) complexes as well as in Cu-based clusters.^{253,262–265} One prominent class displays halogen-bridged Cu(I) complexes, namely $[\text{Cu}(\mu\text{-X})(\text{L}^{\wedge})]_2$ with $\text{L} = \text{P}^{\wedge}\text{P}$ or $\text{P}^{\wedge}\text{N}$ and $\text{X} = \text{Cl}, \text{Br}, \text{I}$.²⁶⁶ Among others, Ueno, Yersin, and coworkers reported a series of blue to green-emitting dinuclear TADF Cu(I) complexes bearing the chelating dppbz or aminophosphine ligands with $\text{X} = \text{I}^-, \text{Br}^-, \text{Cl}^-$, – Cu21–27; Scheme 3 and Fig. 17 and Table 3.^{252,253} While TADF originates from spatially well-separated HOMO and LUMO with the lowest excited states of (M+X)LCT character, the choice of the halogen ion marginally influence TADF properties but the emission color. The ligand field strength increases in the order

of $\text{I}^- < \text{Br}^- < \text{Cl}^-$ and leads to a stabilization of the HOMO energy – without drastically affecting the LUMO, resulting in red-shifted emission maxima – Table 3. Interestingly, the TADF decay times are relatively short for Cu(I) complexes, ranging between 4.1 and 6.6 μs at ambient conditions. Still, no clear dependence of the choice of the bridging halogen atom was noted.^{252,253}

In a following study, Yersin *et al.* demonstrated how to overcome the close relation between a small ΔE_{ST} and the related less favorable $\text{S}_1 \rightarrow \text{S}_0$ – *vide infra*.²⁵⁴ In detail, the Davidov model was applied to TADF molecules for the first time. It is based on coupling two symmetry-related transition dipole moments of the same molecule. The resulting combinations of the transition dipoles, that is, parallel or antiparallel alignment that could cancel out or double and thus, give a twice as large transition dipole moment as the monomeric unit – Fig. 18. This concept was realized by combining twice the quasi-Cu(I) TADF monomer, Cu28^{mono}, resulting in the Cu(I) dimer Cu28^{dimer} (Scheme 3 and Fig. 18 and Table 3) that displays landmark high radiative rates of $1.13 \times 10^7 \text{ s}^{-1}$ ($f_{cal} = 0.0499$) and record short τ_{TADF} of 1.2 μs without the expected concomitant increase of ΔE_{ST} . Indeed, ΔE_{ST} was reduced to an unusually small value of 390 cm^{-1} since the energy of the lowest singlet excited state was lowered for the dimer as well.

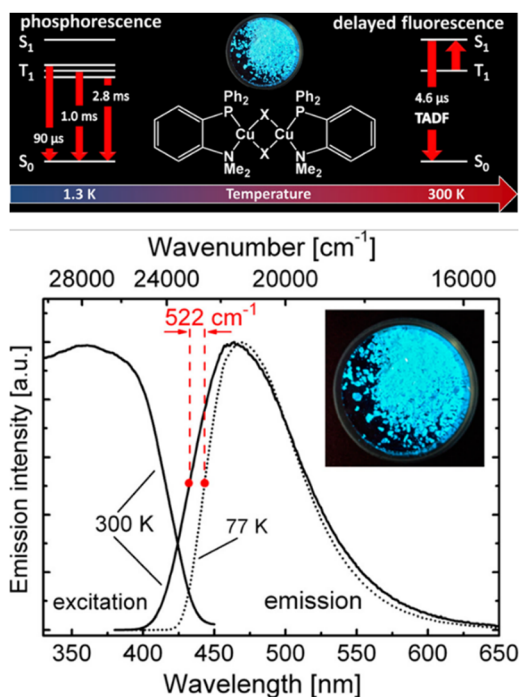


Fig. 17 Top: Structural representation of Cu24–26 ($\text{X} = \text{Cl}, \text{Br}, \text{I}$) and corresponding state diagram visualizing the emission mechanisms at 1.3 K and 300 K. Bottom: Emission and excitation spectra of compound Cu26 ($\text{X} = \text{I}$) (powder) at ambient temperature (solid line) and 77 K (dotted line). The emission spectra were recorded under excitation at $\lambda_{exc} = 360 \text{ nm}$, and the excitation spectra were detected at $\lambda_{det} = 470 \text{ nm}$. The inset shows a photo of the powder sample of compound Cu26 excited at 365 nm. Printed with permission from ref. 253.

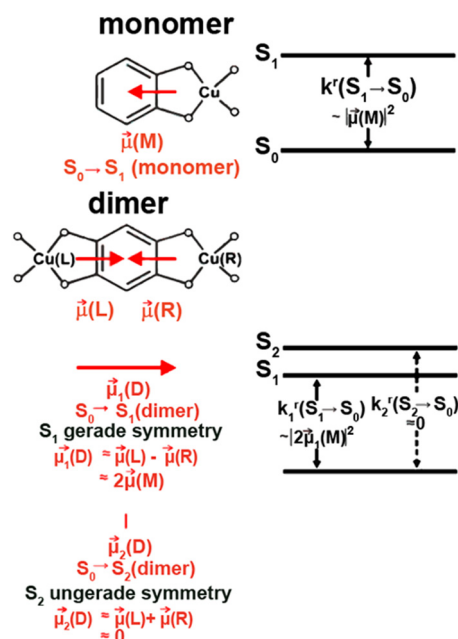
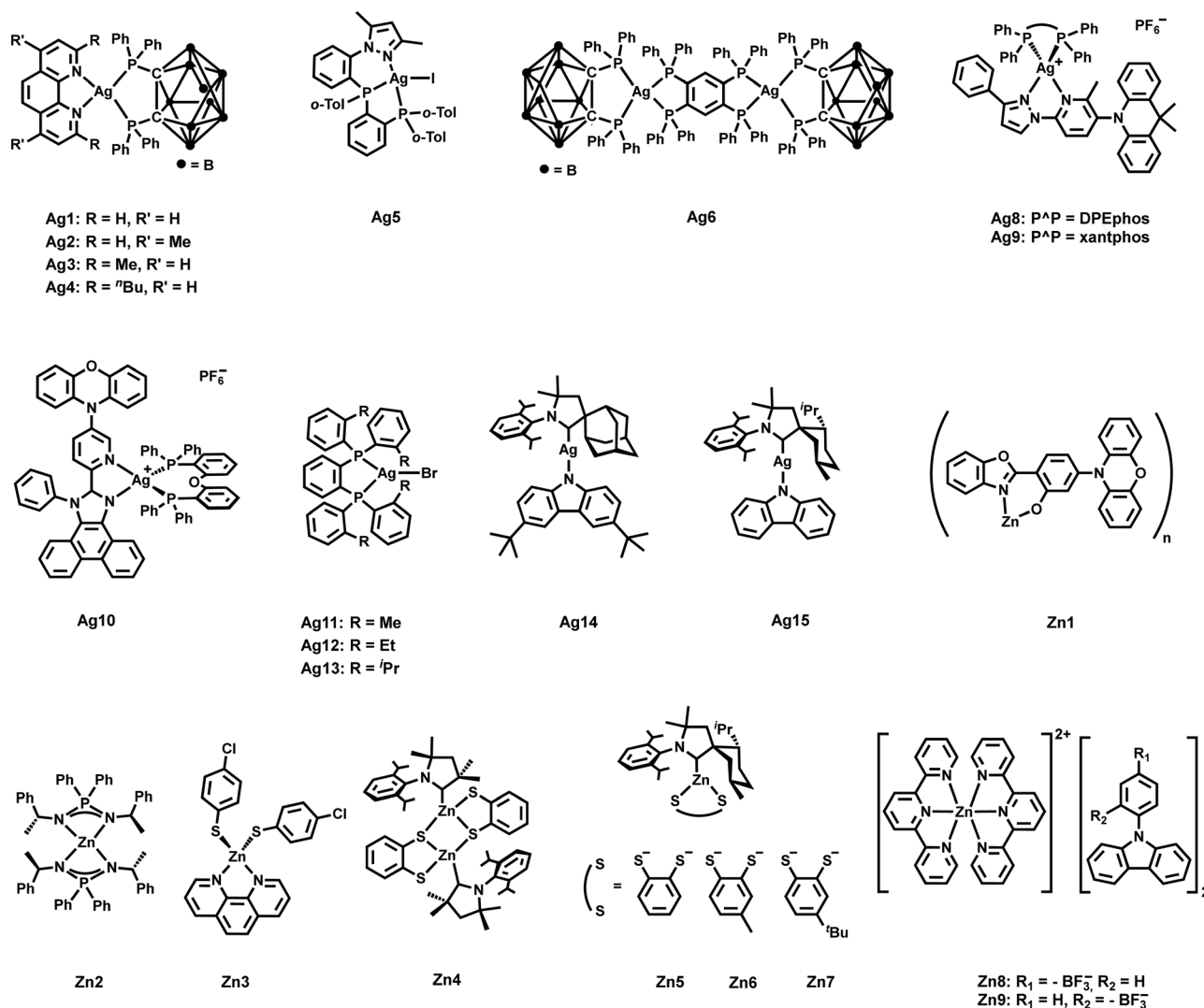


Fig. 18 Schematic guiding model for Cu28^{dimer} with a left (L) – right (R) inversion symmetry relation. For this dimer, one finds a distinctly faster rate of the $\text{S}_1 \rightarrow \text{S}_0$ transition than for the related monomer, Cu28^{monomer}, however, maintaining a small ΔE_{ST} energy gap. The model does not provide the sequence of the two singlet states S_1 and S_2 of the dimer. However, TD-DFT calculations show that the $\text{S}_1(^1\text{MLCT})$ dimer state will be the lower in energy. The triplet states are not discussed in this guiding model. TD-DFT calculations place them energetically below but near to the singlets. k_r is the radiative rate that is proportional to the squared transition dipole moment. Reproduced with permissions from ref. 254. Copyright 2019, American Chemical Society.





Scheme 4 Molecular structures of Ag1–15 and Zn1–9.

While Cu(I) complexes have been extensively investigated over the last two decades, significant attention has recently started to be devoted to Ag(I) complexes. Many factors, like the higher oxidation potential of Ag(I) beneficial for possible LEC or OLED applications, and their higher PLQYs trigger the research in this direction.²⁶⁷ However, compared to Cu(I) complexes, the design of efficient TADF Ag(I) complexes is more challenging due to the higher oxidation potential of Ag(I). The related energetically low-lying 4d-orbitals of Ag(I) barely contribute to the frontier orbitals, and thus, the lowest energy electronic transitions are scarcely of ¹/₃ MLCT character. Instead, they are often characterized by LC excited states of ³ ππ* (³LC) nature causing long-lived phosphorescence with even slow ISC rates. Therefore, only a few examples of Ag(I) complexes as efficient TADF emitters are known so far.

In 2017, Yersin *et al.* reported a breakthrough TADF Ag(I) series, [Ag(phen*)(P₂-*n*CB)] **Ag1–Ag4** (λ_{em} = 575–526 nm), displaying PLQYs up to 100% and record short radiative TADF

decay times, τ_{TADF}, of 1.4 μs (**Ag4**) – Scheme 4 and Table 4.^{268,269}

This was achieved by a rational design strategy based on several parameters. A highly electron-donating ligand, the anionic bis(diphenylphosphine)-*nido*-carborane (P₂-*n*CB), was chosen to destabilize the energetically low-lying metal 4d-orbitals. DFT/TD-DFT calculations confirmed the success of this strategy as the silver contribution to the HOMO was increased to up to 13%. This resulted in lowest excited state transitions of MLL'/CT, while the spatial separation of the HOMO and LUMO with L and L' being different ligands was maintained. Indeed, a relatively small energy separation of 650 cm⁻¹ was found for **Ag4** – Fig. 19.

Second, the rigidity of this molecular structure turned out to be crucial for high PLQYs and a high radiative decay rate, k_r(S₁ → S₀). This was proven by four phenanthroline derivatives modified either in the 2,9- or 4,7-position, **Ag1–4** – Table 4. First, the increasing bulkiness of the phenanthroline ligands from **Ag1** to **Ag4** resulted in increased oscillator strength of



Table 4 Photophysical properties of Ag(I) complexes showing TADF in the solid state

Complex	λ_{max} (298 K)/ λ_{max} (77 K) [nm]	PLQY [%]	$\tau_{\text{ph}}/\tau_{\text{DF}}$ [μs]	ΔE_{ST} [cm^{-1}]	$k_{\text{r}} \times 10^4$ [s^{-1}]	$k_{\text{nr}} \times 10^4$ [s^{-1}]	Ref.
Ag1	575/—	36	270/2.0	—	18	32	269
Ag2	562/—	45	310/1.7	—	26	32	269
Ag3	537/—	78	804/2.8	650	28	7.9	269
Ag4	526/—	100	1300/1.4	650	71	<2.1	269
Ag5	479/484	70	—/270, 470	—	5.4	—	231
Ag6	555/—	70	1845/1.9	480	37	—	270
Ag7	527/529	76	—/0.65	403	—	—	271
Ag8^a	472/469	87.6	24 400/6.3	1371	—	—	272
Ag9^a	471/469	89.4	26 100/6.5	1210	—	—	272
Ag10^b	573/557	62 ^b	4650/3.5	645	—	—	273
Ag11	487/500	56	—/7.38	850	—	—	274
Ag12	463/482	70	—/8.22	890	—	—	274
Ag13	463/479	98	—/8.03	800	—	—	274
Ag14^c	514/— ^c	45	—/0.42	—	110	130	275
Ag15^d	472/472 ^d	100	—/0.5	150	200	<2	169

^a In doped PMMA films (15 wt%). ^b In DPEPO films. ^c In a poly(9-vinylcarbazone) (PVK) matrix. ^d In doped polystyrene (PS) films (1 wt%).

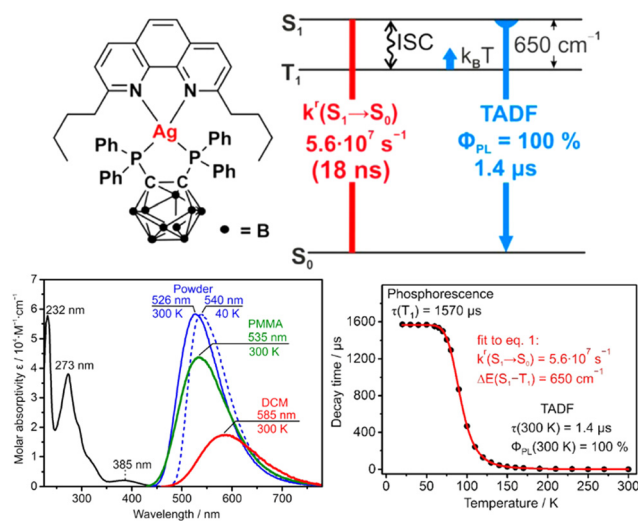


Fig. 19 Top: Structural representation of **Ag4** and the state energy diagram visualizing the TADF process. Bottom left: Absorption spectrum of the **Ag4** measured in dichloromethane (DCM) at 300 K (black) and emission spectra of the **Ag(dbp)(P₂-nCB)** complex shown as colored lines ($\lambda_{\text{exc}} = 410$ nm) measured under different conditions. The DCM solutions had a concentration of $\approx 10^{-5}$ M. The PMMA film was doped with ≈ 1 wt % complex. Bottom right: Luminescence decay times (τ) of **Ag4** powder measured at different temperatures (left) and plotted vs temperature (right). The $k_{\text{r}}(S_1 \rightarrow S_0)$ of $5.6 \times 10^7 \text{ s}^{-1}$ (18 ns) and the ΔE_{ST} of 650 cm^{-1} result from a fit of eqn (6) to the experimental $\tau(T)$ values, with $\tau(T_1)$ fixed to $1570 \mu\text{s}$ as determined directly for temperatures below 60 K (plateau). Printed with permission from ref. 268.

$S_1 \rightarrow S_0$ transitions ($f(S_1 \rightarrow S_0) = 0.0258$ for **Ag1** to $f(S_1 \rightarrow S_0) = 0.0536$ for **Ag4**), while maintaining a relatively small energy separation of ΔE_{ST} of 650 cm^{-1} . The obtained radiative decay rates, e.g. $k_{\text{r}}(S_1 \rightarrow S_0) = 7.1 \times 10^5 \text{ s}^{-1}$ for **Ag4**, is one order of magnitude higher than usually found for Cu(I) complexes with similar ΔE_{ST} values.²⁶² Third, the high rigidity also results in strongly increased PLQYs from 36% for **Ag1** to 100% for **Ag4**. Theoretical calculations and single X-ray analysis further confirms this design strategy, since steric interactions between the *n*-butyl groups in the 2,9-positions of the phenanthroline and

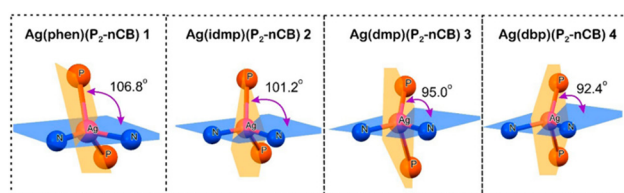


Fig. 20 Coordination core geometries of complexes **Ag1**, **Ag2**, **Ag3** and **Ag4** as found by single-crystal X-ray diffraction analysis. The given interplanar angles characterize the deviations from the tetrahedral geometry ($\varphi = 90^\circ$) (not to be confused with the valence angle of 109° in a tetrahedral molecule such as methane). Represented with permission from ref. 269.

the phenyl groups of the P_2 -nCB ligand are present, minimizing geometrical distortion in the excited state – Fig. 20. Overall, this study presented the first example of an efficient TADF Ag(I) complex, displaying high PLQY with a moderately small ΔE_{ST} of 650 cm^{-1} and high radiative rate, reflected in record short TADF decay times of $1.4 \mu\text{s}$.

The same strategy was also applied to a neutral, mono-nuclear Ag(I) complex **Ag5** – Scheme 4. Similar to Cu(I) analogous, Yersin and coworkers designed a rigid, tridentate N,P,P-ligand, 3,5-dimethyl-1-(2-((2-(di-*o*-tolyl)-phosphanyl)-(o-tolyl)-phosphanyl)phenyl)-1*H*-pyrazole, to minimize structural distortions upon excitation which resulted in PLQYs up to 70% – Table 4. TADF was achieved by a distinct spatial separation of the HOMO (metal halide moiety) and the LUMO (N,P,P-ligand). The silver contribution to the HOMO enabled MLCT transitions.²³¹ In 2018, Yersin and coworkers reported a neutral, dinuclear complex bearing the tetradentate ligand, 1,2,4,5-tetrakis(diphenylphosphino) benzene (tpbz), as a bridging ligand and two terminal P_2 -nCB ligands, $[\text{Ag}_2(\text{tpbz})(P_2\text{-nCB})_2]$ **Ag6** – Scheme 4 and Table 4. This complex design is similar to the one employed for **Ag1**–**Ag4**, namely, destabilizing the d-orbitals by using the same strongly donating ligand, P_2 -nCB. Thus, **Ag6** shows also efficient TADF with a small ΔE_{ST} of 480 cm^{-1} and PLQY up to 70%. Moreover, **Ag6** displays another example of an Ag(I) TADF emitter with an outstanding short TADF decay time of $1.9 \mu\text{s}$.²⁷⁰



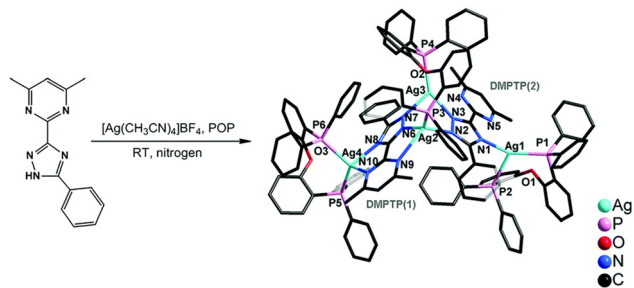


Fig. 21 Synthesis and structural presentation of **Ag7** (anions, hydrogen atoms and included solvent molecules have been omitted for clarity). Printed with permission from ref. 271.

Lu *et al.* demonstrated that this strategy can also be applied to a neutral, tetranuclear Ag(I) complexes. In this case, four Ag(I) centers coordinate to two 4,6-dimethyl-2-(5-phenyl-4*H*-1,2,4-triazol-3-yl)pyrimidine (DMPTP) and three POP moieties, **Ag7** – Scheme 4 and Fig. 21.²⁷¹ The combination of the large bite-angle bis(diphosphine), the two methyl groups as well as the phenyl group at the pyrimidine-triazole ligand introduced a highly rigid environment giving rise to PLQYs of 76%. Moreover, this design leads to a substantial silver metal anion contribution to the HOMO, and thus, the lowest-excited states are of MLCT and LLCT character. The spatial separation of the HOMO and the LUMO, which is mainly located on the DMPTP unit, benefits the small ligand field splitting energy of 403 cm^{-1} , while maintaining a fast decay time of 0.65 μs .

A second strategy towards TADF Ag(I) complexes was presented by Lu *et al.* in 2020 as a coordination-induced TADF mechanism.²⁷² In short, the usually “undesired” LC character of the excited states of Ag(I) complexes was exploited by the coordinating the non-TADF D–A molecule with a large ΔE_{ST} of 3791 cm^{-1} to a silver ion. The corresponding heteroleptic complexes, bearing POP (**Ag8**) or xantphos (**Ag9**) as the second chelating ligand – Scheme 4, Fig. 22 and Table 4, show a deep blue emission at 462 nm with PLQYs of 65.9%. The coordination of DMAC-MPyPz to Ag(I) leads to the planarization of the DMAC unit. Thus, the increased molecular rigidity forces a larger twisting in the D–A emitter, resulting in smaller energy splitting between the triplet and the singlet excited states ($\Delta E_{\text{ST}} = 1371\text{ cm}^{-1}$ and 1210 cm^{-1} for **Ag8** and **Ag9**) and minimizing flattening distortions upon excitation. According to TD-DFT calculations, the $S_1 \rightarrow S_0$ transition is mainly of ILCT character, which explains the negligible Jahn–Teller distortion upon excitation and thus the small non-radiative decay rates and the high PLQY. Again, such high radiative decay rates of $1.9 \times 10^7\text{ s}^{-1}$ (**Ag8**) display record values for TADF Ag(I) complexes so far. The potential of this strategy was further confirmed by using different D–A molecule, *e.g.* a spiro-type diimine ligand.²⁷⁶

Inspired by these findings, Yang's group applied this strategy to cationic Ag(I) complexes.²⁷³ Again, a D–A moiety as diimine, in which the pyridine-substituted 1-phenyl-1*H*-phenanthro[9,10-*d*]imidazole (PI) accepting moiety was functionalized with the 10*H*-phenoxazine (PXZ) donor unit, was combined with POP to yield the orange-emitting Ag(I) complex

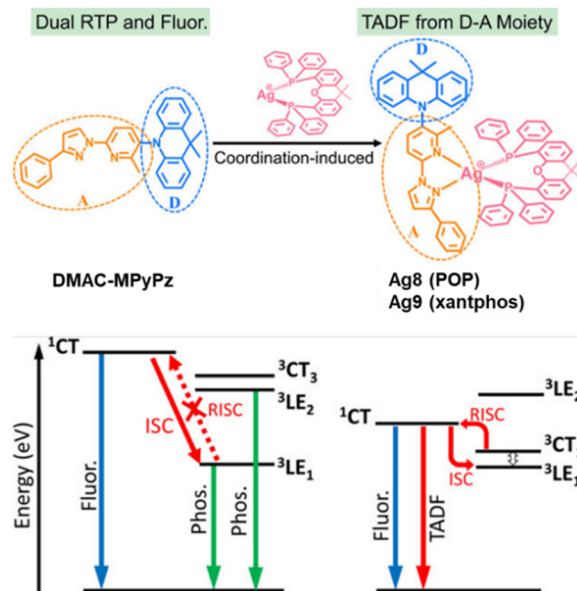


Fig. 22 Top: Molecular design strategies for the realization of TADF including the molecular structure of **Ag8** and **Ag9**. Bottom: PL processes for the free DMAC-MPyPz ligand (left) and the corresponding Ag(I) complexes (right). Printed with permission from ref. 272.

Ag10 (Scheme 4) with PLQYs up to 62%. Based on temperature-dependent excited state lifetime measurements, the typical TADF behavior for **Ag10** in a bis[2-(di(phenyl)phosphino)-phenyl]ether oxide (DPEPO) film with a relatively small ΔE_{ST} of 645 cm^{-1} and τ_{DF} of 3.5 μs was found. DFT/TD-DFT aided in assigning the nature of the excited states S_1 and T_1 to $^1/3\text{ILCT}$. The HOMO and LUMO are located on the PXZ and PIPy units. While Lu and coworkers report the coordination of the D–A unit to the Ag(I) center and its concomitant twisting as a key feature to obtain efficient TADF, Yang *et al.* claim that the coordination of the silver ion stabilizes the $^1\text{ILCT}$ and $^3\text{ILCT}$ states which leads to an increased ILCT character of the T_1 state and thus, ΔE_{ST} decreases.

Hoshino and coworkers prepared a series of blue-emitting three-coordinated Ag(I) bromide complexes, **Ag11–Ag13**, bearing modified 1,2-bis(bis(2-alkylphenyl)phosphino)benzene ligands – Scheme 4 and Table 4.²⁷⁴ The increased steric hindrance of the alkyl groups gives the binuclear-bridge complex **Ag11**, while the bulky ethyl- and isopropyl-substituted bis(diphosphines) form the mononuclear species, **Ag12** and **Ag13**. The bulkiness of the alkyl groups directly affects the PLQYs, increasing from 56% for **Ag11** to 98% for **Ag13** – Table 4. This trend was ascribed to the restricted geometrical distortions owing to increased steric hindrance in the peripheral phenyl groups. All three complexes show TADF behavior with energy splittings around $800\text{--}890\text{ cm}^{-1}$ Table 4. Based on DFT/TD-DFT calculations, the TADF emission mainly stems from $(\sigma + X) \rightarrow \pi^*$ transitions.

As a final note in both families of Cu(I) and Ag(I) complexes, linear complexes have evolved as substantial alternatives without sacrificing the TADF properties when rational ligand



combinations are employed. In detail, Romanov, Bochmann, Credgington, and Thompson *et al.* found that replacing the halogen ligand with a strong donating ligand, *e.g.* anionic secondary amines, in carbene metal complexes changes the dominant emissive pathway from phosphorescence to TADF. In this work, we are focusing briefly on the design rules for linear coinage carbene-metal-amide (CMA) complexes showing TADF as they are of particular interest due to their (i) high PLQYs (up to 90–100%), (ii) good color tunability, (iii) fast k_{ISC} rates (iv) and short excited state lifetimes in the sub-/microsecond regime.²⁷⁷ For deeper insights, the interested reader is recommended to refer to Thompson's recent review.¹²²

In short, the metal ion serves as a linker between the π -donating amide, *e.g.* diaryl- or dialkylamines or Cz and derivatives thereof, and the π -accepting carbene unit, *e.g.* NHCs, MAC, CAAC = cyclic (alkyl)(amino)-carbene, CCArC, BZI derivatives. The HOMO is mainly located on the amide unit with small to minor metal contributions (less than 15%) – decreasing in the following order: Cu(I) > Au(I) > Ag(I), while the LUMO is mainly of p-orbital character of the carbon atom of the carbene ligand.¹⁶⁹ Despite the minor contribution of the metal ion to the frontier orbitals, it still holds a key position as (i) its d-orbitals serve as a bridge for the CT from the amide to the carbene, and (ii) its high SOC constant increases the efficiency of the ISC/rISC processes ($k_{\text{ISC}} = 10^{10}$ – 10^{11} s^{−1}) and thus favors TADF. Moreover, the choice of the metal becomes more evident for the extinction coefficients, oscillator strengths, excited state lifetimes, and ΔE_{ST} values. While the oscillator strength and extinction coefficients decline in the following order: Au(I) > Cu(I) > Ag(I), τ and ΔE_{ST} increase in the order of Ag(I) < Au(I) < Cu(I). The latter tendency correlates well with the C^{carbene}–metal–N^{amide} distance: Ag: 4.15 Å, Cu: 3.7 Å, Ag: 4.0 Å, which is a consequence of the decreasing atomic radii: Ag > Au > Cu. In this context, Bochmann and Thompson reported two examples of Ag(I)-based CMA complexes, **Ag14** and **Ag15** – Scheme 4, with record short lifetimes of 420 and 500 ns and singlet–triplet energy splitting down to 645 cm^{−1} (**Ag14**).^{169,275} As mentioned before, fast radiative TADF decay times are crucial for optoelectronic applications, which are ideally obtained with large oscillator strength $f(S_1 \rightarrow S_0)$ (and thus fast $k_r(S_1 \rightarrow S_0)$) and small ΔE_{ST} . However, a small ΔE_{ST} results from a small overlap of the frontier orbitals but lowers $k_r(S_1 \rightarrow S_0)$ and thus the TADF decay time. In this context,

Thompson *et al.* established a relationship between the degree of spatial overlap between the hole and electron wave functions that describe the excited states and the TADF key parameters.²⁷⁸ In this study, twelve CMA-TADF emitters were prepared – including Cu(I), Ag(I), and Au(I) ions – with high PLQYs (<50%) and short lifetimes (>2 μ s). Natural transition orbitals were used to evaluate this overlap, A_{NTO} . Both $k_r S_1$ and ΔE_{ST} were found to increase exponentially with increasing NTO overlap. The optimal range of the NTO overlap to obtain the best compromise of $k_r(S_1 \rightarrow S_0)$ and ΔE_{ST} was found to range between 0.25–0.3.

As the last representative in this family, Zn(II) displays the most common oxidation state for Zn with excellent redox stability and a substantial variety of different coordination modes. While high-coordination numbers (>4) are well established, low-coordination complexes are less explored due to their high reactivity, but they are of high interest due to the increased Lewis acidity, the atypical reactivity, and the planar geometric configuration. Recently, different design strategies toward such low-coordinated Zn(II) complexes were introduced. In short, strong σ -donating groups combined with sterically demanding ligands can compromise its highly electron-deficient character and protect the metal center from further attachment/coordination of ligands/solvent molecules. Due to the d¹⁰ electron configuration of Zn(II) and consequently, the lack of metal-centered excited states, Zn(II) emitters are of high interest for photoluminescent applications. However, the high oxidation potential of Zn(II) leads to the absence of d-orbital contributions in the excited states and hampers the access of MLCT lowest excited states. Thus, the heavy-atom effect of Zn(II) is almost negligible and disfavors efficient the spin-orbit coupling. As a result, most of the emission mechanisms reported for Zn(II) so far, are fluorescent decay pathways, and only a few, but an increasing number of phosphorescent and TADF scenarios are known.

The first Zn(II)-based TADF emitter was introduced by Adachi *et al.* in 2015.²⁷⁹ A monomeric, homoleptic four-coordinated Zn(II) complex, **Zn1**, bearing the D-A ligand, PX-BOX-X = bis(2-(benzo[d]oxazol-2-yl)-5-(10H-phenoxazin-10-yl)phenolate), with excited states of ILCT nature shows characteristic TADF features – Table 5. Through the coordination of the D-A ligands, the angle between the donor and acceptor unit was changed with a concomitant decrease of ΔE_{ST} from 2500 cm^{−1} of the free ligand to 484 cm^{−1} – **Zn1**; Scheme 4.

Table 5 Photophysical properties of Zn-complexes with TADF in the solid state

Complex	λ_{max} (298 K)/ λ_{max} (77 K) [nm]	PLQY [%]	$\tau_{\text{ph}}/\tau_{\text{DF}}$ [μ s]	ΔE_{ST} [cm ^{−1}]	$k_r \times 10^5$ [s ^{−1}]	$k_{\text{nr}} \times 10^5$ [s ^{−1}]	Ref.
Zn1 ^a	542/—	78.4	—/37.8	485	—	—	279
Zn2	480/—	3	4500/24.5	1000	—	—	280
Zn3	452, 540	50	828/—	242	—	—	281
Zn4 ^b	577/558	10	5900/0.74	637	1.4×10^5	1.2×10^6	282
Zn5	560/556	28	1940/0.63	—	4.5×10^5	—	283
Zn6	583/568	13	46/0.17	—	7.5×10^5	—	283
Zn7	580/553	49	346/0.49	452	1.2×10^6	—	283
Zn8	468/—	12	—	2662	—	—	284
Zn9	508/—	33	—	484	—	—	284

^a 6 wt% emitter in 3,3'-di(9H-carbazol-9-yl)-1,1'-biphenyl (mCBP) doped films. ^b Photophysical data of **Zn5** (10 wt%) in a PMMA matrix.



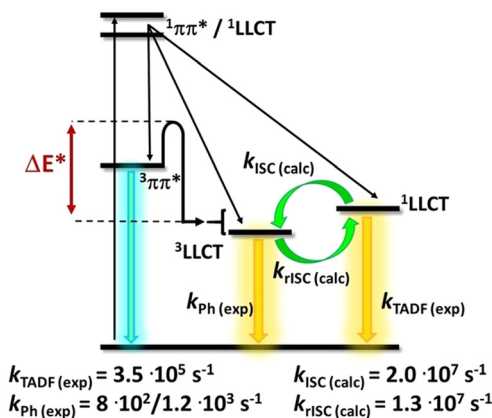


Fig. 23 Proposed excited-state decay mechanism upon photoexcitation of **Zn3**. Printed with permission from ref. 281.

In 2021, Roesky's group reported a tetrahedral, blue-emitting Zn(II) iminophosphonamide (NPN) complex, **Zn2** – Scheme 4, showing TADF in the solid state – Table 5.²⁸⁰ In detail, the twisting of the NPN moiety in the lowest triplet state T_1 enables an efficient thermally driven spin-flip from the triplet to the singlet state with an energy splitting of 1000 cm^{-1} which was obtained from fitting the temperature-dependent excited state lifetimes from 5 to 298 K.

Back in 1985, Crosby *et al.* reported a series of four-coordinated $[\text{Zn}(\text{SC}_6\text{H}_4\text{-4-R})_2(\text{phen})]$ complexes, *e.g.* **Zn3** ($\text{R} = \text{Cl}$, Scheme 4), showing a dual emission character.^{285–287} While the vibrationally structured high-energy band was assigned to phosphorescence from locally excited $^3\pi\text{-}\pi^*$ states centered on the phenanthroline ligand, the broad and unstructured emission band was reported to stem from interligand thiolate \rightarrow phen LLCT transitions. Steffen, Marian and coworkers revisited the proposed kinetic scheme by temperature-dependent and time-resolved luminescent measurements. The obtained high k_r constant $k_r = 3.5 \times 10^5 \text{ s}^{-1}$ in combination with high-level DFT/multireference configuration interaction (MRCI) calculations reveals efficient reverse intersystem crossing by up-conversion from $^3\text{LLCT}$ to the $^1\text{LLCT}$ state – Fig. 23. This leads to efficient population of the $^1\text{LLCT}$ state and to TADF as major emission channel.²⁸¹

In 2023, Steffen and Marian *et al.* followed the strategy of a donor-Zn(II)-acceptor molecular system to enter $^1/3\text{LLCT}$ states and thus to obtain high radiative rates.²⁸² The presented dimeric Zn(II) carbene complex bearing two electron-rich, chelating benzene-1,2-dithiolate ligands combined with electrophilic carbene ligands – **Zn4**; Scheme 4, shows moderate brightness (up to 10% in a PMMA matrix with 10 wt%) in the green-yellow range of the electromagnetic spectrum – Table 5. Excited state lifetimes in the range of 472–741 ns in the solid state reveal unprecedented high radiative rates for Zn(II) complexes up to $1.4 \times 10^5 \text{ s}^{-1}$. Variable temperature studies in conjunction with DFT/MRCI calculations disclose TADF as main emission pathway at room temperature origination from the LLCT state. The energy splitting, ΔE_{ST} , was estimated to

637 cm^{-1} . The high stability towards moisture, air and irradiation stems from the μ_2, κ^2 -bonding mode of the dithiolate ligand that is a key feature for the steric stabilization and protection of the Zn–carbene bond and combined with long-lived triplet states makes **Zn4** an ideal candidate for Dexter energy transfer photocatalysis.

Based on a theoretical study on monomeric carbene–zinc–dianionic complexes that focused on the influence of the π -accepting and σ -donor character of different carbenes (NHC, CAAC, CAACrC) on the photoluminescent properties – including TADF behavior,²⁸⁸ Steffen and coworkers introduced a new generation of monomeric carbene–zinc–dithiolate complexes displaying characteristic TADF behavior.²⁸³ In detail, menthyl-substituted cAAC ($^{\text{Menth}}$ cAAC) ligand and derivatives of dithiolate ligands gave three monomeric Zn(II) complexes, **Zn5** ($\text{R} = \text{H}$), **Zn6** ($\text{R} = \text{Me}$) and **Zn7** ($\text{R} = \text{t-Bu}$) in Scheme 4, while the latter one shows polymorphism. The bright yellow to orange photoluminescence with PLQs up to 49% in the crystal state and lifetimes in the range of 170–630 ns result in unprecedented high k_r constants up to $7.5 \times 10^5 \text{ s}^{-1}$ – Table 5. Time-resolved variable temperature studies reveal a change of the emitting state below 50 K, accompanied by two orders of magnitude decreased radiative rates ($k_r = 2.5 \times 10^3 \text{ s}^{-1}$). The TADF behavior was finally confirmed by fitting the temperature-dependent excited state lifetime measurements with the Boltzman-type equation (Section 2) yielding an ΔE_{ST} of 452 cm^{-1} for **Zn7**. According to high-level DFT/MRCI calculations the relative orientation of the two ligands involved in the $^1/3\text{LLCT}$ states displays a key parameter to control the TADF properties. For instance, a dihedral angle of $33\text{--}36^\circ$ in **Zn7** gives rise to a very efficient rISC rate in the range of 10^9 s^{-1} owing to efficient SOC mediated by the sulfur atom.

He *et al.* presented an alternative approach toward Zn(II)-TADF emitter involving an intracomplex D–A ion pair that forms an exciplex with TADF behavior. The cationic $[\text{Zn}(\text{tpy})_2]^{2+}$ complex displays the accepting group and was combined with a Cz-type counter anion, (4-(9H-carbazol-9-yl)phenyl)-trifluoroborate ($\text{CAZ-}p\text{-BF}_3^-$), or (2-(9H-carbazol-9-yl)-phenyl)trifluoroborate ($\text{CAZ-}o\text{-BF}_3^-$), that serves as donor, **Zn8** and **Zn9** – Scheme 4 and Table 5.²⁸⁴ Single X-ray analysis show stronger $\pi\text{-}\pi$ interactions between the donor and acceptor ions for **Zn9**. They rule the photophysical properties since only **Zn9** emits *via* TADF at room temperature. ΔE_{ST} was estimated to 484 cm^{-1} in the crystalline state for **Zn9**, while **Zn8** exhibits a six-fold larger ΔE_{ST} (*i.e.*, 2662 cm^{-1}).

3. TADF d^x-metal complexes in solid-state lighting

3.1. OLEDs

TADF technology rapidly developed in recent years, and several companies invested high-cost budget to develop red, green and yellow TADF emitters that can offer a cost-effective substitute to phosphorescent organic light-emitting diodes (PHOLEDs) mainly supplied by Universal Display Corporation (UDC) For



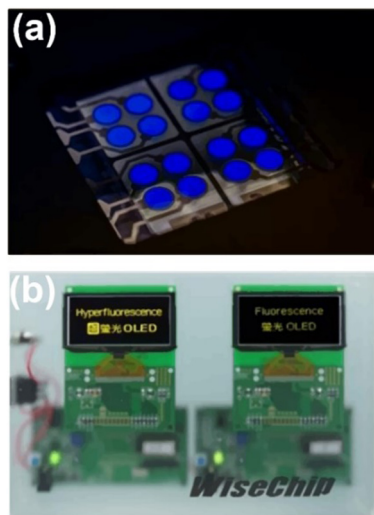


Fig. 24 Examples of TADF OLEDs for (a) blue and (b) yellow. Reproduced with permissions from ref. 289.

instance, Cynora company is developing new emitter materials for SSLDs, as shown for its initial marketable product based on TADF fluorescent blue emitter exhibiting a 15% efficiency improvement over existing blue emitters on the market – Fig. 24a. Kyulux Inc., a world leader in the development of OLED Hyper fluorescence™/TADF technology, announced that WiseChip launches world's first commercial Hyperfluorescence™ OLED demonstrate based on TADF materials designed by Kyulux Inc. The 2.7-inch, 128 × 64-pixel array, yellow type Hyper fluorescence™ OLED can reach up to 220 nits–2.5 times brighter than using general fluorescence materials. Surprisingly, the lifetime of the product is more than 50 000 h – Fig. 24b.

Recent reviews summarized the progresses of OLEDs based on TADF organic compounds.^{125,290–294} To complement these reviews, our work aims to show the latest progress achieved in the field OLED based on metal complex based TADF emitters. Accordingly, the following sections will summarize the most relevant complexes applied to OLEDs, highlighting their device performance as well as their photoluminescence features as a complement of Section 2.

3.1.1. Ir-complexes. The use of Ir(III) complexes in TADF OLEDs has been almost focused on the developing of hyper-fluorescent and hyperphosphorescent schemes as explained in Section 2. For instance, homoleptic iridium(III) metal complexes containing cyclometalating chelates based on 5-(trifluoromethyl)imidazo[4,5-*b*]pyridin-2-ylidene and 6-(trifluoromethyl)imidazo[4,5-*b*]pyridin-2-ylidene, *f*-tpb1 and *f*-tpb2 were used as sensitizers with t-DABNA as the TADF terminal emitter. Hyper-OLEDs were developed with high efficiency reaching 29.6%, FWHM (full width at half maximum) of 30 nm, and *x,y* CIE (Commission internationale de l'éclairage) color coordinates of 0.13, 0.11, demonstrating efficient FRET processes.²⁹⁵ Likewise, this approach was also applied to TADF dendrimers with *fac*-tris[2-phenylpyridyl]iridium(III) [Ir(ppy)₃] cores with dendrons based on

TADF.²⁹⁶ In this line, a promising approach was proposed involving the covalent attachment of TADF groups to phosphorescent iridium(III) complexes with the TADF units acting as light-harvesting components and iridium phosphor as the emission core. By integrating TADF groups into the designed TriTADF-Ir (dFppy)₃ complex, energy transfer from the TADF units to the phosphorescent core enhances device performance and mitigates efficiency roll-off by reducing triplet exciton annihilation. Consequently, PLQY of blend films containing TriTADF-Ir (dFppy)₃ can reach an impressive level of almost 73%. The inclusion of peripheral TADF dendrons enables the versatile use of TriTADF-Ir (dFppy)₃ in manufacturing solution-processed OLEDs emitting a greenish-blue light with an EQE exceeding 20% and maintain approximately 16% efficiency at 1000 cd m⁻², showing the substantial improvement in device performance.²⁹⁷ Just a few more works on hyper-OLEDs with Ir(III) complexes have been also reported by Chou *et al.*²⁹⁸ and Yan *et al.*²⁹⁹

To provide a comprehensive view, a final approach to merge TADF and Ir(III) complexes is the integration of TADF interfacial exciplex and phosphorescent ultrathin emitting layers (Ph-UEMs) made of Ir(III) complexes. In short, monochrome/WOLEDs were structured by directly incorporating single or complementary Ph-UEMs at the interface of the TADF interfacial exciplex ((mCP)/2,4,6-tris[3-(diphenylphosphinyl)phenyl]-1,3,5-triazine (PO-T2T)) using a simple doping-free technique. The hole-transporting donor layer (mCP) and electron-transporting acceptor layer (PO-T2T) effectively confine carrier recombination to the interface of the mCP/PO-T2T exciplex. Simultaneously, optimizing the thickness of the hole-transporting layer promotes a well-balanced distribution of electrons and holes at the mCP/PO-T2T interface. Additionally, the Ph-UEMs are sensitized by the TADF interfacial exciplex of mCP/PO-T2T which enables complete exciton utilization through multi-channel energy transfer from the TADF interfacial exciplex to the Ph-UEMs. These factors significantly contribute to the exceptional performance of the suggested monochrome/WOLEDs. As a result, all monochrome OLEDs in blue, green, orange, and red colors demonstrated a low turn-on voltage of 2.4–2.5 V and achieved outstanding device performance with maximum EQE (EQE_{max}) exceeding 20%. Particularly, the blue OLED based on bis[2-(4,6-difluorophenyl)pyridinato-C2,N] (picolinato)iridium(III) (FIRpic) achieved a remarkable forward-viewing EQE of 30.21%, which stands among the highest values reported in literature. Furthermore, the fabricated two-, three-, and four-color WOLEDs also delivered exceptional performance with a low turn-on voltage of 2.5 V and high EQEs of 23.47, 22.70, and 23.88% (equivalent to 78.80, 76.70, and 70.89 lm W⁻¹). All white devices exhibited remarkable color stability across a practical luminance range from approximately 5000 to 12 000 cd m⁻², indicating significant potential for real-world applications. Overall, this study shows that complete exciton utilization can be achieved through multi-channel energy transfer. In this case, Ph-UEMs sensitized by TADF interfacial exciplex were employed.



The proposed scheme is believed to open a new pathway for developing ultra-simple and high-performance monochrome/WOLEDs.³⁰⁰

Besides the above scenario, Pander *et al.* have recently presented compelling evidence of TADF as discussed in Section 2. dinuclear, $[\text{Ir}(\text{N}^{\wedge}\text{C})_2]_2(\text{m-L})$, displays deep-red luminescence ($\lambda_{\text{em}} = 643 \text{ nm}$) and a TADF with k_r of $3.5 \times 10^5 \text{ s}^{-1}$ associated to a modest ΔE_{ST} of around 403 cm^{-1} . An OLED fabricated by incorporating 1 as a dopant in the emitting layer (EML) at 5 wt% exhibits red electroluminescence centered at 625 nm with an EQE value of 5.5% and a maximum brightness of 6300 cd m^{-2} .¹⁹⁴ This represents the first work on using TADF based Ir(III) complexes and, in turn, much more needs to be studied to determine the limitations and challenges.

3.1.2. Pd-, Pt-, and Au-complexes. Tetradentate cyclometalated Pd(II) and Pt(II) complexes were designed and prepared in which tzpPh (3-phenyl-[1,2,4]triazolo[4,3-*a*]pyridine) acts as strong electron-withdrawing unit and an acceptor – Fig. 25.¹⁹⁸ They show bright green TADF emission – Table 6. Moreover, by modifying tetradentate ligand with σ -donating groups in Pd(II) complexes, the PLQY improved more than 8-fold. Complex the Pd(tzp-3) (**Pd4**; Scheme 5) shows strong typical metal-assisted delayed fluorescent (MADF) in PMMA film, due to a little ΔE_{ST} of 1840 cm^{-1} . The OLED device fabricated with Pt(tzp-2) (**Pt2**; Scheme 5) showed an EQE of 8.7% and a L_{max} of $28\,280 \text{ cd m}^{-2}$ – Table 6.

Li *et al.* present a novel development of TADF Pd(II) complexes that show ILCT excited states perturbed by small metal contribution. They have successfully developed two complexes (**Pd7** and **Pd8**; Scheme 5) emitting orange and red light with efficiencies of 82% and 89% and lifetimes of 2.19 and 0.97 μs ,

respectively – Table 7. Through mixed transient spectroscopic and theoretical analyses on one complex, they have identified a metal-perturbed rapid ISC process. OLEDs utilizing these Pd(II) complexes exhibit remarkable EQE_{max}, ranging from 27.5% to 31.4% – Table 6, with minimal roll-offs down to 1% at 1000 cd m^{-2} . Additionally, the operational stability of the Pd(II) complexes is exceptional, with LT95 values exceeding 220 hours at 1000 cd m^{-2} . This stability stems from the strong σ -donating ligands, the presence of multiple intramolecular noncovalent interactions and in addition from their short emission lifetimes. This research highlights a favorable strategy for creating effective and durable luminescent complexes without using third-row transition metals.²⁰⁰

Two solid-state near-infrared (NIR) emitting Pt(II) complexes that appear yellow and green in solution, namely PBSNND (**Pt3**) and AtFNND (**Pt4**) – Scheme 5, were successfully utilized alongside the classical blue fluorescent *N,N'*-di-1-naphthalenyl-*N,N'*-diphenyl-[1,1':4',1'':4'',1''':4''',1''''-quaterthiophene]-4,4'''-diamine (4P-NPD) to create hybrid WOLEDs. By employing an ultra-thin EML technique, dual emission in yellow and deep red/NIR EL was effectively achieved in **Pt3**-based hybrid WOLEDs. The most optimal EL performance was observed in a hybrid WOLED configuration with a 1.0 nm ultra-thin phosphorescent emitting layer, and a 4P-NPD layer (2.5 nm) positioned in front of TPBi, the ETL of the device (Hyb W1). Hyb W1 displayed warm white EL with a color coordinate of *x,y* CIE color coordinates of (0.41, 0.31), a high CRI of 86, and an EQE reaching 12.9% – Table 6. In contrast, by using a singly doped phosphorescent emitting layer, dual emission in green and deep red/NIR emission was achieved in **Pt4**-based hybrid WOLEDs. With an **Pt4** dopant concentration of 5% or

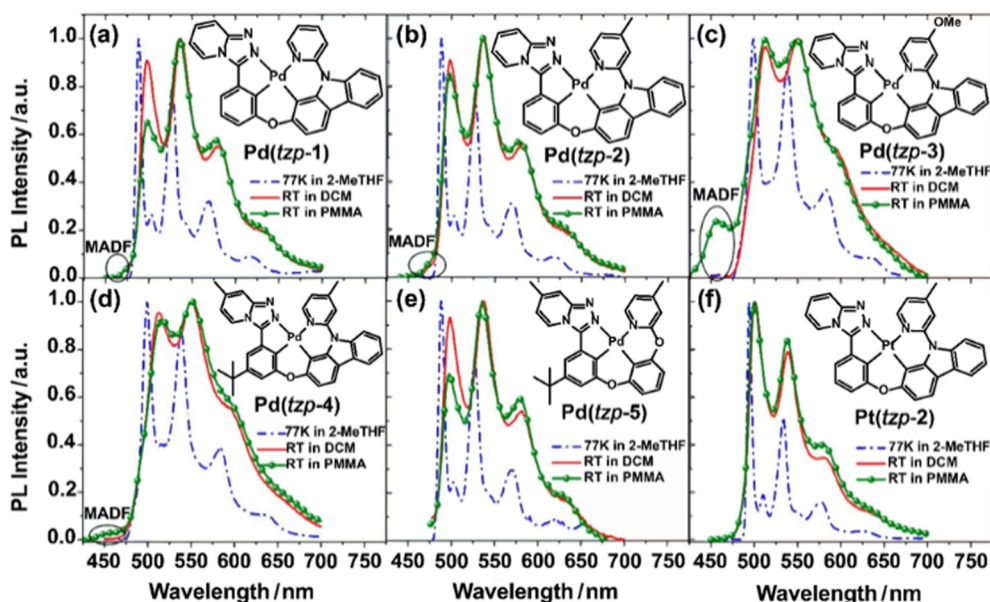


Fig. 25 Luminescence spectra of (a) Pd(tzp-1) (**Pd2**), (b) Pd(tzp-2) (**Pd3**), (c) Pd(tzp-3) (**Pd4**), (d) Pd(tzp-4) (**Pd5**), (e) Pd(tzp-5) (**Pd6**), and (f) Pt(tzp-2) (**Pt2**) at 77 K in 2-MeTHF (dash-dotted lines), at room temperature in CH_2Cl_2 solution (solid lines) and at room temperature in PMMA film (solid-ball lines). The chemical structure of each emitter is shown in the inset. The peaks in the black circles are MADF emissions. Reproduced with permissions from ref. 198. Copyright 2019, American Chemical Society.



Table 6 The OLED characteristics based on Pd-, Pt- and Au-based TADF complexes

Complex	OLED Structure	Device	Concentration [%wt]	EL _{max} [nm]	CIE [x,y]	V _{on} [V]	CE _{max} [cd A ⁻¹]	η _p [lm W ⁻¹]	L _{max} [cd m ⁻²] at V _{app}	η _{ext} [%]	Ref.
Pt2	HAT-CN/NPD/TCTA/mCBP/ Pt2 :mCBP/DPPS/Bepp2:Li ₂ CO ₃ /Li ₂ CO ₃ /Al	—	—	508, 545	0.31, 0.61	—	—	—	28 280	8.7	198
Pd8	ITO/HAT-CN (5 nm)/TAPC (30 nm)/TCTA (15 nm)/mCBP (10 nm)/DMIC-TRZ: Pd8 (40 nm)/PO-T2T (20 nm)/ANT-BIZ (30 nm)/LiQ (2 nm)/Al (100 nm).	—	1	576	(0.49, 0.50)	—	79.1	76.4	150 300	28.8	200
Pd8	ITO/HAT-CN (5 nm)/TBBD (30 nm)/o-SFAF (15 nm)/DMIC-TRZ: Pd8 (45 nm)/ANT-BIZ (40 nm)/LiQ (2 nm)/Al (100 nm)	—	3	583	(0.51, 0.48)	—	62.7	56.3	103 100	25.1	200
Pd8	ITO/HAT-CN (5 nm)/TBBD (30 nm)/o-SFAF (15 nm)/DMIC-TRZ: Pd8 (45 nm)/ANT-BIZ (40 nm)/LiQ (2 nm)/Al (100 nm)	—	1	575	(0.49, 0.50)	—	75.2	98.5	124 800	27.5	200
Pd7	ITO/HAT-CN (5 nm)/TBBD (30 nm)/o-SFAF (15 nm)/DMIC-TRZ: Pd7 (45 nm)/ANT-BIZ (40 nm)/LiQ (2 nm)/Al (100 nm)	—	1	636	(0.62, 0.38)	—	32.1	42.0	70 230	31.4	200
Pd7	ITO/HAT-CN (5 nm)/TAPC (30 nm)/TCTA (15 nm)/mCBP (10 nm)/DMIC-TRZ: Pd7 (40 nm)/PO-T2T (20 nm)/ANT-BIZ (30 nm)/LiQ (2 nm)/Al (100 nm)	—	1	640	(0.63, 0.37)	—	29.6	27.5	92 000	30.1	200
Pt3	ITO/NPB/ultrathin layer of Pt3 /mCP/4P-NPD/TPBi/LiF/Al	Ulth1	—	602	(0.54, 0.44)	3.0	—	10.6	1651	13.6	301
		Ulth2	—	654	(0.55, 0.44)	3.5	—	11.3	2093	15.5	
		Ulth3	—	664	(0.57, 0.42)	6.5	—	7.8	826	21.9	
Pt4	ITO/NPB/a dopant of Pt4 in CBP/mCP/4P-NPD/TPBi/LiF/Al	Dop1	—	526	(0.33, 0.61)	4.0	—	33.5	5448	18.7	301
		Dop2	—	528	(0.36, 0.59)	5.0	—	25.7	4186	20.2	
		Dop3	—	676	(0.47, 0.48)	4.5	—	6.1	3093	8.6	
		Dop4	—	654	(0.35, 0.28)	7.0	—	4.8	1459	13.7	
		Dop5	—	658	(0.64, 0.36)	9.0	—	3.1	707	15.1	
		Dop6	—	674	(0.64, 0.36)	6.0	—	1.6	1162	9.1	
Pt3	—	Hyb W1	—	654	(0.41, 0.31)	9.0	—	4.0	1778	12.9	301
Pt4	—	Hyb W2	—	532	(0.30, 0.31)	7.0	—	6.3	1541	10.5	
Pt4	—	Hyb W3	—	654	(0.35, 0.32)	9.5	—	5.0	1412	13.7	
Pt1	ITO PEDOT:PSS Al4083 (30 nm) mCP: PO-T2T (n: m) co x% 2 (y nm) PO-T2T (50 nm) LiF (0.8 nm) Al (100 nm)	1	5	637, 730	—	—	—	—	—	2.64	204
Pt5	—	2	20	651, 787	—	—	—	—	—	0.99	
Pt6	—	3	33	805	—	—	—	—	—	0.51	
Pt1	ITO/HIL 1.3N (45 nm)/PVKH (10 nm)/TPD: PBD (60:40 w/w) co 5% 5 (30 nm)/TPBi (50 nm)/LiF (0.8 nm)/Al (100 nm)	—	—	607	(0.62, 0.37)	7	—	—	11 000	7.4	201
Pt12	ITO/PEDOT:PSS (50 nm)/Poly-TPD (15 nm)/47% mCP:47% OXD-7: 6% PtAu ₂ complex Pt12 (50 nm)/ETL (40 nm)/LiF (1 nm)/Al (100 nm)	—	6	525	(0.27, 0.69)	4.0	80.6	42.8	10 865	20.8	302
Pt9	ITO/PEDOT:PSS (50 nm)/Poly-TPD (15 nm)/host materials:PtAu ₂ complex (50 nm)/BmPyPb (40 nm)/LiF (1 nm)/Al (100 nm)	—	—	557	(0.46, 0.54)	3.2	76.2	45.2	8368	21.6	302
Pt12	—	—	—	525	(0.29, 0.66)	4.0	80.6	42.8	10 865	20.8	
Pt13	ITO/(PEDOT:PSS):PFI (54 nm)/mCPBC:PIM-TRZ: Pt13 2 wt% (50 nm)/DMFBD-TRZ (10 nm)/(Na-An-BI):LiQ (30 nm)/LiQ (2 nm)/Al (80 nm)	D1	2	507	(0.22, 0.63)	3.3	41.0	32.5	7765	13.5	303
		D2	—	503	(0.13, 0.63)	3.0	46.9	41.9	4892	16.6	
		D3	—	528	(0.38, 0.57)	3.3	32.7	25.8	3759	9.7	
Au15	—	—	—	—	—	2.6	76.3	62.7	44 700	26.3	304
Au16	—	—	—	—	—	3.0	45.2	33.6	39 540	17.9	
Au17	—	—	—	—	—	2.6	87.1	75.1	73 100	27.5	
Au18	ITO/HAT-CN (5 nm)/TAPC (40 nm)/mCBP (10 nm)/Au-emitter:mCBP (20 nm)/PPF (10 nm)/TmPyPb (40 nm)/LiF(1.2 nm)/Al (100 nm)	—	4	566	(0.47, 0.52)	—	60.3	72.1	198 000	21.3	305
Au19	—	—	10	502	(0.21, 0.51)	—	76.7	79.3	236 000	26.9	



Table 6 (continued)

Complex	OLED Structure	Device	Concentration [%wt]	EL _{max} [nm]	CIE [x,y]	V _{on} [V]	CE _{max} [cd A ⁻¹]	η _p [lm W ⁻¹]	L _{max} [cd m ⁻²] at V _{app}	η _{ext} [%]	Ref.
Au20			2	483	(0.15, 0.26)		34.7	29.2	12 500	23.6	
Au21			6	503	(0.20, 0.50)		72.0	63.7	147 000	25.9	
Au22			10	517	(0.25, 0.58)		78.2	62.3	230 000	24.5	
Au23			6	487	(0.18, 0.33)		32.6	33.2	93 000	15.1	
Au24			2	632	(0.61, 0.39)		18.8	22.3	68 800	17.4	
Au25			10	705	(0.69, 0.30)		0.58	0.61	3200	9.96	
Au21 (6 wt%):BN2 (1 wt%)			6	535	(0.29, 0.65)		92.2	90.0	265 000	25.3	
Au26	ITO/60 nm PEDOT:PSS/20 nm TAPC/10 nm PCZAC/25 nm PBICT: DBTTP1: Au(i) complex/	—	3	539	(0.36, 0.59)	4.5	85.7	76.7	—	24.4	306
Au27	5 nm TSPO1/40 nm TPBi/1.5 nm LiF/200 nm Al			551	(0.41, 0.56)	4.8	77.5	67.7		23.3	
Au28				650	(0.63, 0.36)	7.3	7.9	5.3		10.7	
Au29				655	(0.63, 0.36)	7.0	7.8	5.9		11.6	
Au30				680	(0.62, 0.36)	8.2	2.8	2.1		7.0	
Au32	(ITO)/10 nm p-doped (3 wt% NDP series, Novaled AG) (BCFA)/40 nm BCFA/10 nm (HT host): (ET host) (6: 4, v/v):20 wt% Au(i) complex:emitter/(mCP-2CN)/30 nm (DBFPO): (LiQ)/LiQ/Al	—	20 wt%: 1.5 wt%	475	(0.108, 0.160)	4.5	—	36.1	—	30.2	307
Au33				494	(0.156, 0.496)	4.6		58.4		22.8	
Au34	ITO/HAT-CN (10 nm)/FSFA (120 nm)/FSF4A (5 nm)/(NHC)AuBN: DMIC-Cz: DMIC-TRZ (30 nm)/ANT-BIZ (5 nm)/ANT-BIZ: Liq (1: 1, 25 nm)/Liq (2 nm)/Al (100 nm).	2	0.5	511	(0.20, 0.69)	—	86.1	—	2.53 × 10 ⁵	24.8	308
Au35		—	0.5	509	(0.16, 0.66)		74.0		1.17 × 10 ⁵	24.0	
Au36		1	2	540	(0.16, 0.68)		97.1		2.16 × 10 ⁵	30.3	
Au37		—	4	515	(0.22, 0.67)		82.8		1.92 × 10 ⁵	24.0	
Au38		—	1	512	(0.18, 0.69)		93.5		1.51 × 10 ⁵	27.6	
Au40	ITO/HAT-CN (5 nm)/TAPC (30 nm)/TCTA (15 nm)/mCBP (10 nm)/DMIC-TRZ: emitter (45 nm)/PO-T2T (20 nm)/ANT-BIZ (30 nm)/Liq (2 nm)/Al (100 nm)	—	1	531	(0.37, 0.57)	2.8	75.7	63.2	3000	23.9	309
Au5	ITO/PEDOT:PSS; 40 nm/emissive layer (30 nm)/3TPyMB; 5 nm/TmPyPB; 30 nm/LiF (0.8 nm)/Al (100 nm)	—	10	528	(0.37, 0.60)	—	37.0	18.2	—	10.0	217
Au43			20	532	(0.42, 0.56)		30.1	18.5		8.9	
Au6			20	572	(0.49, 0.50)		22.2	12.4		8.0	
Au44			20	588	(0.53, 0.48)		12.3	5.2		5.2	
Au7			20	616	(0.60, 0.40)		7.9	4.4		5.3	
Au46	ITO/PEDOT:PSS/PVK:OXD-7: Au(III) complex/TPBi/LiF/Al	—	4	509	(0.29, 0.52)	—	24.0	12.7	27 400	8.3	310
			8	—	(0.30, 0.53)		36.9	20.9	34 200	12.5	
			12	—	(0.31, 0.54)		43.9	22.5	53 840	14.6	
			16	—	(0.32, 0.55)		44.9	23.6	57 340	14.8	
Au49	ITO/PEDOT:PSS/PVK:OXD-7: Au(III) complex/TPBi/LiF/Al	A	4	500	(0.25, 0.47)	—	34.9	22.5	11 450	12.7	310
			8	—	(0.26, 0.49)		60.3	43.0	22 750	20.6	
			12	—	(0.26, 0.50)		60.2	41.1	27 900	20.9	
			16	—	(0.27, 0.51)		70.4	47.3	33 740	23.8	



Table 6 (continued)

Complex	OLED Structure	Device	Concentration [%wt]	EL _{max} [nm]	CIE [x,y]	V _{on} [V]	CE _{max} [cd A ⁻¹]	η _p [lm W ⁻¹]	L _{max} [cd m ⁻²] at V _{app}	η _{ext} [%]	Ref.
Au10	ITO/HAT-CN(5 nm)/TaPc (50 nm)/TCTA: AuIII emitter (10 nm)/TmPyPb (50 nm)/LiF (1.2 nm)/Al (100 nm)	—	4	—	0.38, 0.56	—	65.59	91.98	7300	20.84	223
			8		0.40, 0.55		70.82	81.73	16 500	22.72	
			16		0.43, 0.54		77.78	94.00	22 700	25.03	
Au60	ITO/HAT-CN (5 nm)/TAPC (50 nm)/TCTA (10 nm)/Au ^{III} emitter: DPEPO: TCTA (20 nm)/DPEPO (10 nm)/TmPyPB (40 nm)/LiF (1 nm)/Al (100 nm)	—	4	540	(0.38, 0.57)	—	82.9	91.1	31 000	24.9	311
Au61			8	529	(0.31, 0.60)		89.0	87.7	35 100	26.2	
Au63			8	537	(0.34, 0.60)		92.5	104	43 200	27.3	
Au60	ITO/HAT-CN (5 nm)/TAPC (40 nm)/mCBP (10 nm)/BN2:complex Au60 :mCBP (20 nm)/PPF (10 nm)/TmPyPB (40 nm)/LiF (1.2 nm)/Al (100 nm)	A: Au60 (6 wt%); BN2 (1 wt%)	Au60 (6 wt%); BN2 (1 wt%)	538	(0.33, 0.65)	—	120.7	122.5	170 000	29.4	311
Au3	ITO/HAT-CN(5 nm)/TAPC (40 nm)/TCTA(10 nm)/TCTA:TPBi: Au(III) emitter(10)/TPBi(10 nm)/TmPyPb (40 nm)/LiF (1.2 nm)/Al (100 nm)	—	2	—	(0.32, 0.56)	—	67.0	81.0	32 000	21.6	216
Au3			4		(0.34, 0.56)		71.9	87.0	37 000	23.1	
Au3			8		(0.35, 0.56)		76.0	99.4	37 500	23.1	
Au4			2		(0.38, 0.56)		59.9	72.3	21 300	19.5	
Au4			4		(0.41, 0.55)		57.5	86.9	26 300	19.7	
Au4			8		(0.43, 0.53)		53.8	65.0	17 200	19.5	
Au67			2		(0.33, 0.56)		55.5	69.5	30 900	18.2	
Au67			4		(0.40, 0.55)		70.6	82.8	70 300	23.4	
Au67			8		(0.41, 0.54)		66.3	79.6	59 100	22.2	
Au70	Solution-processed devices, ITO/PEDOT:PSS; 40 nm/x% Au(III):mCP (30 nm)/3TPyMB; 5 nm/TmPyPB; 40 nm/LiF (1 nm)/Al (150 nm)	—	20	612	(0.61, 0.39)	—	8.3	4.1	—	5.5	221
Au71				604	(0.59, 0.41)		22.9	16.9		12.2	
Au72				608	(0.60, 0.40)		12.6	7.8		7.8	
Au75				628	(0.64, 0.36)		5.0	3.2		4.5	
Au70	Vacuum-deposited devices, ITO/α-NPD; 40 nm/TCTA; 5 nm/x% Au70-Au75 : m-CBP; 20 nm/Tm3PyP26PyB; 50 nm/LiF (1 nm)/Al (150 nm)	—	5	608	(0.58, 0.41)	—	14.1	12.6	1483	9.3	221
Au71			8	600	(0.57, 0.43)		23.4	21.0	2522	12.7	
Au72			5	600	(0.56, 0.44)		17.8	16.0	1507	9.9	
Au73			8	612	(0.60, 0.40)		15.8	16.6	1867	10.8	
Au74			11	612	(0.60, 0.40)		13.7	12.9	1604	9.2	
Au75			2	616	(0.59, 0.40)		10.5	8.3	706	7.8	
Au77			14	528	(0.32, 0.61)	—	43.9	38.8	—	12.6	312
Au78			5	552	(0.42, 0.56)		34.8	31.2		10.3	
Au79			14	532	(0.33, 0.61)		55.5	58.1		15.7	
Au80			8	544	(0.39, 0.58)		53.0	41.6		15.4	
Au81			2	612	(0.59, 0.40)		10.3	9.2		7.0	
Au83	ITO/PEDOT:PSS (40 nm)/ Au83-85 :mCP (30 nm)/3TPyMB (5 nm)/TmPyPB (30 nm) LiF (1 nm)/Al (120 nm)	—	20	548	(0.40, 0.57)	—	40.0	15.7	689	11.9	313
Au84				560	(0.43, 0.54)		27.1	10.4	—	8.7	



Table 6 (continued)

Complex	OLED Structure	Device	Concentration [%wt]	EL _{max} [nm]	CIE [x,y]	V _{on} [V]	CE _{max} [cd A ⁻¹]	η _p [lm W ⁻¹]	L _{max} [cd m ⁻²] at V _{app}	η _{ext} [%]	Ref.
Au85				540	(0.38, 0.57)		52.6	41.3	850	15.8	
Au86	Solution-processed device, ITO/PEDOT:PSS (40 nm)/ Au86-91 : mCP (30 nm)/3TPyMB (5 nm)/TmPyPB (40 nm) LiF Al	—	20	500, 528	(0.29, 0.56)	—	26.2	13.7	—	8.4	314
Au87				520	(0.29, 0.58)		38.0	17.1		11.7	
Au88				584	(0.51, 0.48)		15.4	6.3		6.1	
Au89				576	(0.49, 0.50)		27.7	11.4		10.0	
Au90				560	(0.44, 0.54)		36.6	18.7		11.4	
Au91				556	(0.42, 0.55)		34.8	15.6		10.9	
Au87	Vacuum-deposited device, ITO/PEDOT:PSS (40 nm)/ Au87 , Au89 , Au90 and Au91 : mCP (30 nm)/3TPyMB (5 nm)/TmPyPB (40 nm) LiF Al	—	14	528	(0.33, 0.56)	—	36.6	38.3	3314	12.0	314
Au89			5	564	(0.45, 0.52)		33.7	30.3	4321	12.2	
Au90			11	564	(0.46, 0.53)		42.6	41.5	4442	14.9	
Au91			8	544	(0.40, 0.55)		46.4	41.6	2110	15.0	

A: by using a higher band-gap material PYD2 (2,6-bis(9H-carbazol-9-yl)pyridine) to replace PVK: OXD-7 as the host, the emission peak maxima of the device with **60** further blue-shifts to 486 nm with CIE coordinates of (0.21, 0.42). The EQE_{max} of this device is 15.7% which slightly decreased to 14.4% at 1000 cd m⁻². **HAT-CN**: 1,4,5,8,9,11-hexaazatriphenylenehexacarbonitrile. **DMIC-TRZ**: {5-(3-(4,6-diphenyl-1,3,5-triazin-2-yl)phenyl)-7,7-dimethyl-5,7-dihydroindeno[2,1-b]carbazole}. **ANT-BIZ**: {1-(4-(10-([1,10-biphenyl]-4-yl)anthracen-9-yl)phenyl)-2-ethyl-1H-benzo[d]imidazole}. **Al**: aluminum. **Liq**: 8-hydroxyquinolinolito-lithium. **TBBD**: N₄N₄N₄N₄-tetra(4-biphenyl)-biphenyl-4,4'-diamine. **o-SFAF**: N-([1,1'-biphenyl]-2-yl)-N-(9,9-dimethyl-9H-fluoren-2-yl)-9,9'-spirobifluoren-2-amine. **NPB**: 4,4'-bis[N-(1-naphthyl)-N-phenylamino]-biphenyl. **PVKH**: poly(9-vinylcarbazole). **TPD**: N,N'-bis(3-methylphenyl)-N,N'-bis(phenyl)-benzidine. **PBD**: {2-(4-biphenyl)-5-(4-tert-butylphenyl)-1,3,4-oxadiazole}. **PFI**: perfluorinated ionomer. **mCPBC**: 9-(3-(9H-carbazol-9-yl)phenyl)-9H-3,9'-bicarbazole. **PIM-TRZ**: di-[4-(N,N-ditolyamino)-phenyl]cyclohexane. **DMFBD-TRZ**: 2-(3'-(9,9-dimethyl-9H-fluoren-2-yl)-[1,1'-biphenyl]-3-yl)-4,6-diphenyl-1,3,5-triazine. **PCZAC**: 9,9-dimethyl-10-(9-phenyl-9H-carbazol-3-yl)-9,10-dihydroacridine. **PBIC**: 2-phenyl-4,6-bis(12-phenylindolo[2,3-a]carbazole-11-yl)-1,3,5-triazine. **DBTTP1**: 4-(3-(triphenylene-2-yl)phenyl)dibenzo[b,d]thiophene. **TSPO1**: diphenyl-4-triphenylsilylphenylphosphineoxide. **BCFA**: N-([1,1'-biphenyl]-4-yl)-9,9-dimethyl-N-(4-(9-phenyl-9H-carbazol-3-yl)phenyl)-9H-fluoren-2-amine. **HT host**: 9-[1,1'-diphenyl]-3-yl-9H-3,9'-bicarbazole. **ET host**: 9-(3'-(9H-carbazol-9-yl)-6-cyano-[1,1'-biphenyl]-3-yl)-9H-carbazole-3-carbonitrile. **mCP-2CN**: 9-(3-(9H-carbazol-9-yl)phenyl)-9H-carbazole-3,6-dicarbonitrile. **DBFPO**: dibenzo[b,d]furan-2,8-diylbis(diphenylphosphineoxide). **LiQ**: 8-hydroxyquinoline lithium. **FSFA**: N-([1,1'-biphenyl]-2-yl)-N-(9,9-dimethyl-9H-fluoren-2-yl)-9,9'-spirobifluoren-2-amine. **FSF4A**: N-([1,1'-biphenyl]-2-yl)-N-(9,9-dimethyl-9H-fluoren-2-yl)-9,9'-spirobifluoren-4-amine. **DMIC-Cz**: 7,7-dimethyl-5-phenyl-2-(9-phenyl-9H-carbazol-3-yl)-5,7-dihydroindeno[2,1-b]carbazole. **3TPyMB**: tris(2,4,6-trimethyl-3-(pyridin-3-yl)phenyl)borane. **TmPyPB**: 1,3,5-tris[(3-pyridyl)phen-3-yl]benzene. **PPF**: (2,8-bis(diphenyl-phosphoryl)-dibenzo[b,d]furan). **Tm3PyP26PyB**: 1,3,5-tris(6-(3-(pyridin-3-yl)phenyl)pyridine-2-yl)benzene.

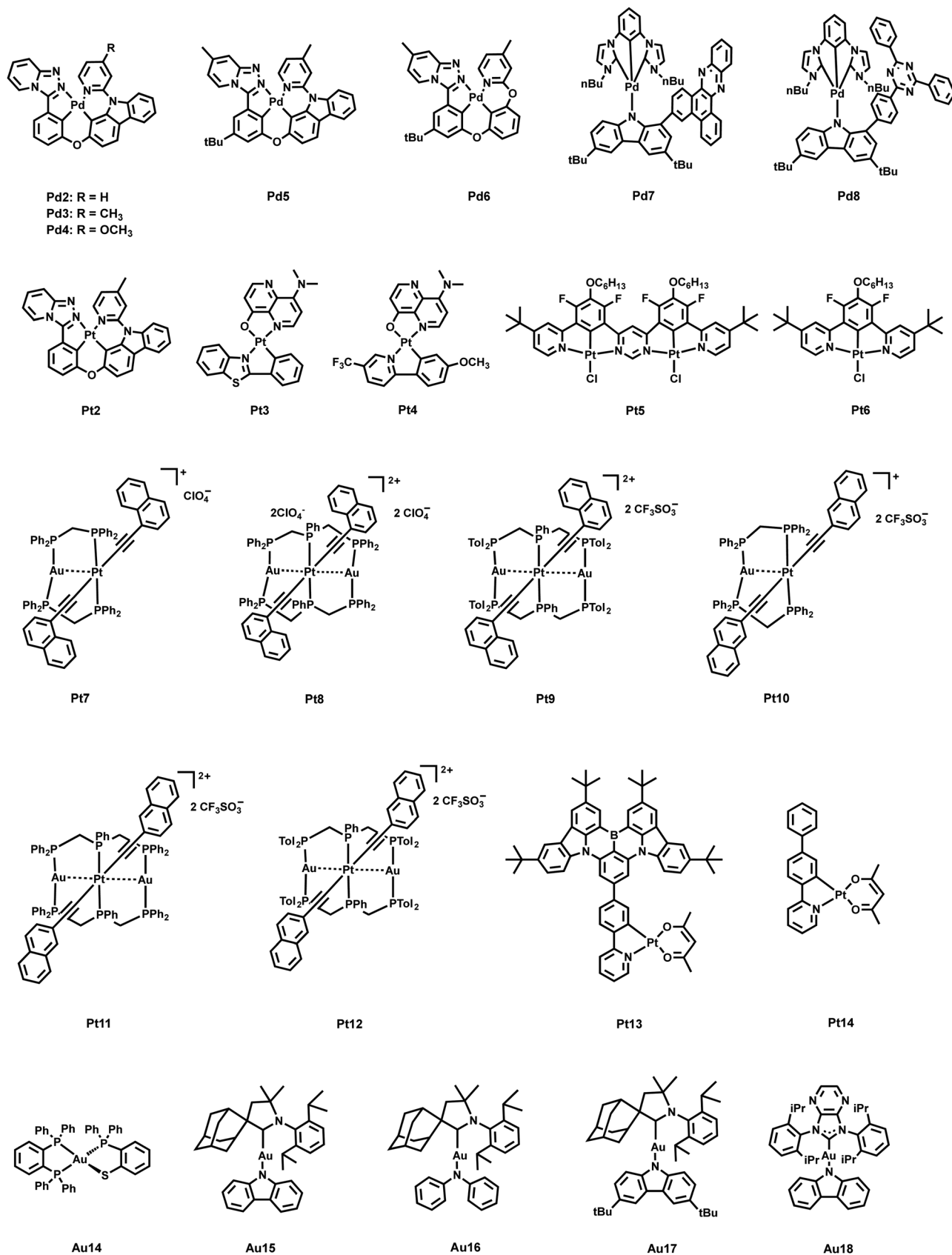
7% by weight, a purplish blue white electroluminescence with x,y CIE color coordinates of 0.30, 0.31, a CRI of 84, and an EQE reaching 10.5% (Table 6). For devices Hyb W3, an authentic white EL was achieved with x,y CIE color coordinates (0.35, 0.32), an exceptional CRI of 88, and a high EQE of 13.7% – Table 6.³⁰¹

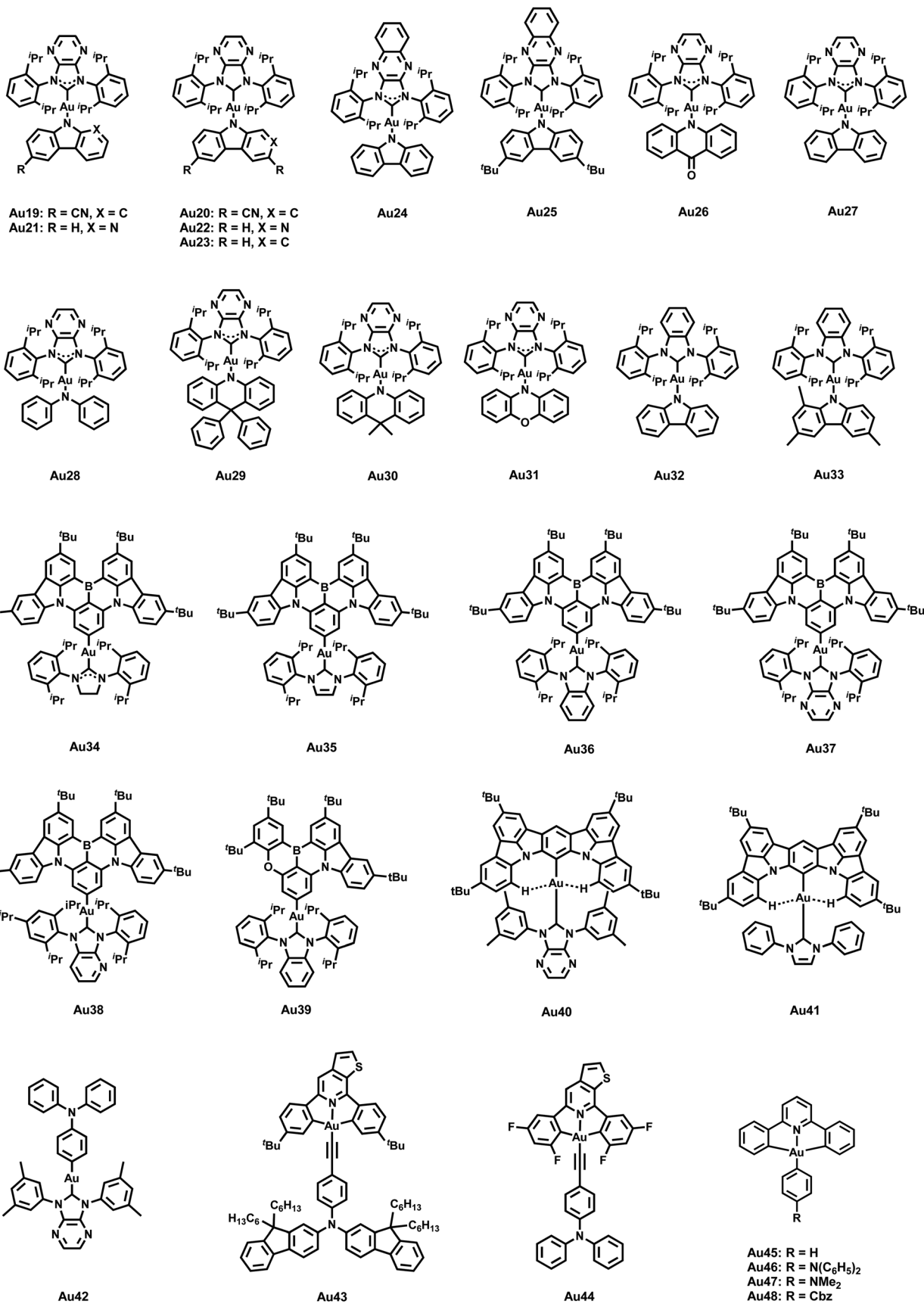
Pander and co-workers conducted the preparation and comprehensive photophysical analysis of a di-Pt(II) complex featuring a ditopic bisN⁺C⁻N ligand (**Pt1**, **Pt5** and **Pt6**) – Scheme 5. This complex demonstrates dual luminescent behavior, emitting both delayed fluorescence and phosphorescence simultaneously. Through a comparison with the mono-Pt(II) counterpart, they establish that the di-Pt(II) complex activates TADF owing to three primary differences when compared to the mono-Pt(II) form: a higher singlet radiative rate constant (*k*_r^S), a reduced Δ*E*_{ST}, and an extended phosphorescence decay lifetime (τ_{PH}). Their observations align with similar trends observed in other di-Pt(II) complexes, indicating that bimetallic structures create favorable conditions for TADF. Additionally, the diPt(II) complex (**Pt5**) exhibits a long-wavelength-emissive excimer,

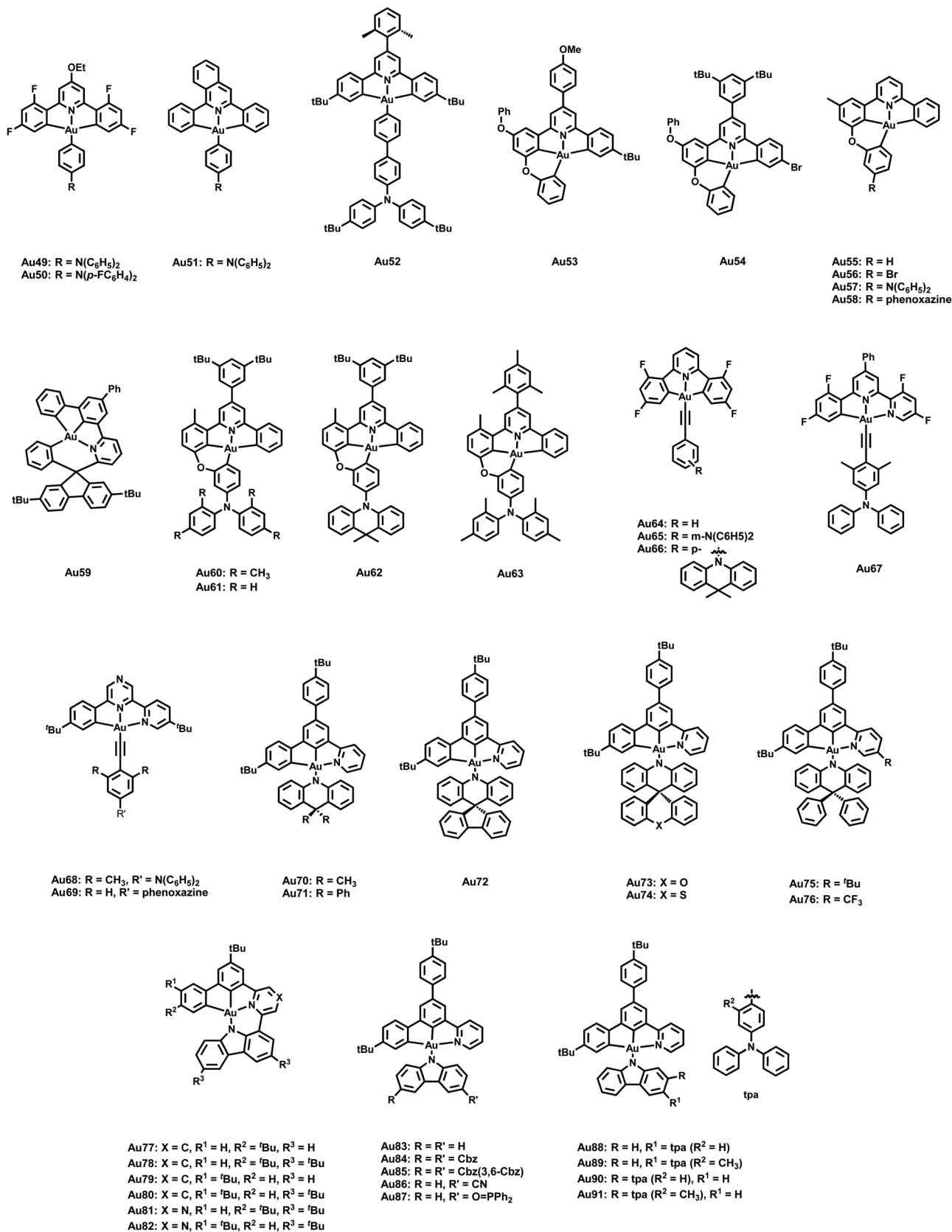
leading to NIR electroluminescence at 805 nm in a solution-processed OLED device with a remarkable EQE_{max} of 0.51% – Table 6.²⁰⁴

A new dinuclear Pt(II) complex (**Pt1**; Scheme 5) has been synthesized, featuring a ditopic, bis-tetradentate ligand. This ligand provides a planar O⁻N⁺C⁻N coordination environment for each metal ion, with both metals bound to the nitrogen atoms of a bridging pyrimidine group. The complex exhibits strong red luminescence with a PLQY of 83% in deoxygenated methycyclohexane solution at room temperature, along with a notably short, excited state lifetime of 2.1 ms – Table 7. These exceptional properties stem from an impressively high *k*_r constant of approximately 4 × 10⁵ s⁻¹ – Table 7, and small FWHM of 75 nm in OLED host and outstanding 22 nm in methycyclohexane. This unique behavior results from efficient thermally activated rISC, facilitated by a small Δ*E*_{ST} of just 556 ± 24 cm⁻¹. In OLED applications, the complex was successfully integrated into solution-processed devices, achieving EQE_{max} of 7.4% – Table 6. This development marks the well-documented instance of a Pt(II) complex exhibiting TADF at









Scheme 5 Molecular structures of Pd2–8, Pt2–14 and Au14–91.



Table 7 Photophysical and TADF characteristics of OLED based on Pd, Pt and Au complexes

Complex	Medium	λ_{em} [nm]	PLQY [%]	τ_{exp} [μs]	k_{r} [s^{-1}]	k_{nr} [s^{-1}]	k_{ISC} [s^{-1}]	k_{rISC} [s^{-1}]	ΔE_{ST} [cm^{-1}]	Ref.
Pd2	At RT in DCM	498, 537, 582	0.21	30.5	—	—	—	—	1202	198
Pd3		498, 536, 580	0.52	26.7	—	—	—	—	1153	
Pd4		513, 551	1.34	152.9	—	—	—	—	1839	
Pd5		513, 550	1.72	118.5	—	—	—	—	1887	
Pd6		499, 538, 582	2.88	44.4	—	—	—	—	—	
Pt2	At RT in PMMA	501, 539, 576	50.1	15.8	—	—	—	—	—	198
Pd2		461, 498, 536, 580	—	89.4	—	—	—	—	—	
Pd3		462, 498, 536, 579	—	79.9	—	—	—	—	—	
Pd4		457, 513, 548	—	109.9	—	—	—	—	—	
Pd5		456, 515, 551	—	57.0	—	—	—	—	—	
Pd6	In 5 wt% doped PMMA at 298 K and (77 K)	498, 536, 597	—	109.5	—	—	—	—	—	200
Pt2		500, 537, 579	—	12.2	—	—	—	—	—	
Pd7		637 (634)	89	0.97 (70.6)	9.2×10^5	1.1×10^5	—	—	—	
Pd8		598 (594)	82	2.19 (336)	3.7×10^5	8.2×10^4	—	—	—	
Pt5		579, 617	0.16	1.2	1.3×10^5	7.1×10^5	—	—	—	204
Pt6	Toluene Chlorobenzene CH_2Cl_2	578, 635	0.51	5.0	1.0×10^5	1.0×10^5	—	—	—	
		568, 641	0.34	3.9	0.9×10^5	1.7×10^5	—	—	—	
		495, 514	0.82	5.3	1.6×10^5	0.3×10^5	—	—	—	204
Pt1	MCH	514	0.85	5.7	1.5×10^5	0.3×10^5	—	—	—	
		512	0.73	6.4	1.1×10^5	0.4×10^5	—	—	—	
		602, 654	0.83 ± 0.090	2.1 ± 0.1	$4.0 \pm 0.6 \times 10^5$	$0.8 \pm 0.5 \times 10^5$	—	—	—	201
Pt7	Toluene	612	0.68 ± 0.08	1.2 ± 0.1	$5 \pm 1 \times 10^5$	$2.6 \pm 0.9 \times 10^5$	—	—	—	
			0.04 ± 0.01	0.11 ± 0.01	$4 \pm 2 \times 10^5$	$92 \pm 9 \times 10^5$	—	—	—	
			0.02 ± 0.01	0.055 ± 0.002	$4.0 \pm 0.6 \times 10^5$	$0.8 \pm 0.5 \times 10^5$	—	—	—	302
Pt7	CH_2Cl_2 (2×10^{-5} M)	556	<0.5	7.7	—	—	—	—	—	
Pt8		557	4	4.3	—	—	—	—	—	
Pt9		555	52	14.8	—	—	—	—	—	
Pt10		524	<0.5	7.9	—	—	—	—	—	302
Pt11		525	46	4.9	—	—	—	—	—	
Pt12		525	81	4.0	—	—	—	—	—	
Pt7	Solid	556	<0.5	8.3	—	—	—	—	—	302
Pt8		553	11	9.9	—	—	—	—	—	
Pt9		553	14	11.2	—	—	—	—	—	
Pt10		521	<0.5	10.6	—	—	—	—	—	
Pt11		530	3	11.4	—	—	—	—	—	302
Pt12	PMMA film	520	8	10.9	—	—	—	—	—	
Pt7		552	20	26.2	—	—	—	—	—	
Pt8		553	46	15.6	—	—	—	—	—	
Pt9		551	84	23.8	—	—	—	—	—	
Pt10		516	33	13.9	—	—	—	—	—	302
Pt11	mCP film	522	86	12.3	—	—	—	—	—	
Pt12		520	90	19.4	—	—	—	—	—	
Pt7		553	52	28.4	—	—	—	—	—	
Pt8		554	93	14.5	—	—	—	—	—	
Pt9		552	94	20.4	—	—	—	—	—	302
Pt10	Toluene solution (1×10^{-5} M, 298 K)	519	59	19.1	—	—	—	—	—	
Pt11		524	96	8.8	—	—	—	—	—	
Pt12		521	97	17.2	—	—	—	—	—	
Pt13		497, 536, 578	75	—	—	—	—	—	—	
Pt14		527, 564, 612	35	—	—	—	—	—	—	303
Au18	Toluene (2×10^5 M)	617	0.17	0.17	10.0	8.3	3.1×10^{10}	0.8×10^9	565	
Au19		550	0.73	0.33	22.1	8.2	—	—	—	
Au20		485	0.72	0.36	20.0	7.8	—	—	—	
Au21		550	0.53	0.45	11.7	10.4	4.3×10^{10}	3.0×10^9	323	
Au22		570	0.60	0.36	16.6	11.1	3.9×10^{10}	1.2×10^9	484	305
Au23	Toluene solution (1×10^{-5} M, 298 K)	500	0.76	0.45	16.9	5.3	9.9×10^{10}	1.7×10^9	645	
Au24		728	0.10	<0.1	—	—	9.2×10^{10}	3.5×10^9	484	
Au25		768	0.02	<0.1	—	—	—	—	—	



Table 7 (continued)

Complex	Medium	λ_{em} [nm]	PLQY [%]	τ_{exp} [μs]	k_{r} [s^{-1}]	k_{nr} [s^{-1}]	k_{ISC} [s^{-1}]	k_{rISC} [s^{-1}]	ΔE_{ST} [cm^{-1}]	Ref.
Au18	6 wt% mCBP	554	0.99	0.39	25.4	0.3	3.1×10^{10}	0.8×10^9	565	305
Au19		504	0.99	0.31	31.9	0.3	—	—	—	
Au20		468	0.75	1.1	6.8	2.2	—	—	—	
Au21		509	0.91	0.35	26.0	2.6	4.3×10^{10}	3.0×10^9	323	
Au22		525	0.99	0.32	30.9	0.3	3.9×10^{10}	1.2×10^9	484	
Au23		466	0.82	0.66	12.4	2.7	9.9×10^{10}	1.7×10^9	645	
Au24		644	0.83	0.28	29.6	6.1	9.2×10^{10}	3.5×10^9	484	
Au25		666	0.63	0.21	30.0	17.6	—	—	—	
Au26	Thin-films	533	0.84	0.84	26×10^5	5.0×10^5	21×10^8	6.6×10^8	323	306
Au27		553	0.87	0.87	27×10^5	2.4×10^5	22×10^8	4.5×10^8	444	
Au28		663	0.26	0.26	8.7×10^5	25×10^5	7.9×10^8	1.5×10^8	395	
Au29		666	0.22	0.22	8.5×10^5	30×10^5	25×10^8	2.6×10^8	516	
Au30		705	0.10	0.10	6.3×10^5	56×10^5	3.8×10^8	4.7×10^8	419	
Au31		750	—	—	—	—	—	—	—	
Au32	Zeonex films	444	0.92	1.6	$> 3.9 \times 10^7$	$> 0.034 \times 10^7$	$> 370 \times 10^7$	$> 65 \times 10^7$	565/661	307
Au33		466	0.95	0.38	$> 13 \times 10^7$	$> 0.066 \times 10^7$	$> 180 \times 10^7$	$> 45 \times 10^7$	645/476	
Au34	THF solution (2×10^{-5} M)	511	0.88	7.9	—	—	—	—	—	308
Au35	(298 K)	511	0.83	7.2	—	—	—	—	—	
Au36		511	0.86	6.9	—	—	—	—	—	
Au37		510	0.78	6.5	—	—	—	—	—	
Au38		511	0.93	7.3	—	—	—	—	—	
Au39		471	0.89	27.0	—	—	—	—	—	
Au34	2% PMMA (298 K)	515	0.92	5.5	—	—	—	—	—	308
Au35		514	0.90	5.8	—	—	—	—	—	
Au36		513	0.91	5.5	—	—	—	—	—	
Au37		514	0.87	5.6	—	—	—	—	—	
Au38		514	0.88	5.9	—	—	—	—	—	
Au39		473	0.84	22.8	—	—	—	—	—	
Au40	10 wt% DPEPO film at 300 K (77 K)	525 (477)	66	2.9 (48.5)	2.3×10^5	1.2×10^5	—	—	561	309
Au41		478 (478)	51	704 (966)	7.2×10^2	7×10^2	—	—	—	
Au42		529 (529)	66	1.2 (23.4)	5.5×10^5	2.8×10^5	—	—	506	
Au5	Toluene (298 K)	524, 564, 606	0.029	5.7	5.14×10^3	1.70×10^5	—	—	—	217
Au43		525, 563, 609	0.083	3.9	2.12×10^4	2.35×10^5	—	—	—	
Au6		606	0.066	0.3	2.19×10^5	3.11×10^6	—	—	—	
Au44		660	0.022	< 0.1	2.20×10^5	9.78×10^6	—	—	—	
Au7		656	0.028	2.8	1.01×10^4	3.47×10^5	—	—	—	
Au8		740	0.012	1.6	7.25×10^3	6.18×10^5	—	—	—	
Au5	Thin-film (298 K) 5 wt% in mCP	528, 568, 616	0.57	96.1	5.93×10^3	4.47×10^3	—	—	—	217
Au43		528, 568, 616	0.52	79.3	6.56×10^3	6.05×10^3	—	—	—	
Au6		562	0.87	5.7	1.53×10^5	2.28×10^4	—	—	—	
Au44		559	0.53	13.5	3.93×10^4	3.48×10^4	—	—	—	
Au7		585	0.70	1.3	5.38×10^5	2.31×10^5	—	—	—	
Au8		636	0.40	0.4	1.00×10^6	1.50×10^6	—	—	—	
Au45	In Toluene, room temperature	(468, 503, 534)	0.14	61.5	2×10^3	—	—	—	—	310
Au46		534	0.74	1.03	7.2×10^5	—	—	—	—	
Au47		596	0.18	0.32	5.6×10^5	—	—	—	—	
Au48		(469, 503, 532)	0.13	43.5	3×10^3	—	—	—	—	
Au49		524	0.79	0.71	11.1×10^5	—	—	—	—	
Au50		511	0.68	0.75	9.1×10^5	—	—	—	—	
Au51		(591, 641, 702)	0.68	29.4	2×10^3	—	—	—	—	
Au52		527	0.065	1.10	6.8×10^5	—	—	—	—	
Au45	4 wt% in PMMA thin-film, room temperature	(471, 504, 534)	0.75	61.5	2×10^3	—	—	—	—	310
Au46		523	0.14	51	3×10^3	—	—	—	—	
			0.66	1.35	4.9×10^5	—	—	—	209	



Table 7 (continued)

Complex	Medium	λ_{em} [nm]	PLQY [%]	τ_{exp} [μs]	k_{r} [s^{-1}]	k_{nr} [s^{-1}]	k_{ISC} [s^{-1}]	k_{rISC} [s^{-1}]	ΔE_{ST} [cm^{-1}]	Ref.
Au47		564	0.42	0.74	5.7×10^5				393	
Au48		(471, 504, 534)	0.13	34	4×10^3				—	
Au49		517	0.84	0.72	11.7×10^5				318	
Au50		513	0.78	0.85	9.2×10^5				—	
Au51		(593, 642, 701)	0.031	16.5	2×10^3				—	
Au52		521	0.67	1.10	6.1×10^5				—	
Au53	In toluene	495, 526, 565 498,	0.54	93.1	5.8×10^3	—	—	—	—	223
Au54		526, 567 524, 550	0.40	77.1	5.2×10^3				—	
Au9		612 493, 521 485,	0.77	94.3	8.2×10^3				—	
Au10		518, 552 533 580	0.47	0.62	758×10^3				—	
Au55		480, 513, 557	0.28	225	1.2×10^3				—	
Au56			0.26	152	1.7×10^3				—	
Au57			0.94	1.61	584×10^3				—	
Au58			0.74	0.79	937×10^3				—	
Au59			0.003	1.04	2.88×10^3				—	
Au53	In thin-films	492, 523, 560	0.20	43.8	4.57×10^3	—	—	—	—	223
Au54		490, 522, 562	0.04	90.1	0.44×10^3				—	
Au9		550	0.47	56.8	8.27×10^3				—	
Au10		568	0.89	1.69	527×10^3				—	
Au55		489, 519, 555	0.06	147	0.41×10^3				—	
Au56		486, 518, 555	0.06	90.4	0.66×10^3				—	
Au57		520	0.82	2.08	394×10^3				—	
Au58		568	0.71	2.54	280×10^3				—	
Au59		482, 515, 552	0.06	36.01	1.67×10^3				—	
Au53		492, 523, 560	0.20	43.8	4.57×10^3				—	
Au54		490, 522, 562	0.04	90.1	0.44×10^3				—	
Au9		550	0.47	56.8	8.27×10^3				—	
Au10		568	0.89	1.69	527×10^3				—	
Au55		489, 519, 555	0.06	147	0.41×10^3				—	
Au56		486, 518, 555	0.06	90.4	0.66×10^3				—	
Au57		520	0.82	2.08	394×10^3				—	
Au58		568	0.71	2.54	280×10^3				—	
Au60	Toluene	547	80	0.56	1.43×10^6	0.36×10^6	1.52×10^{11}	—	—	311
Au61		537	77	0.67	1.15×10^6	0.34×10^6	7.14×10^{10}	—	—	
Au62		528	73	19	0.038×10^6	0.014×10^6	4.88×10^{10}	—	—	
Au63		532	88	0.69	1.28×10^6	0.17×10^6	1.00×10^{11}	—	—	
Au60	4 wt% in DPEPO/TCTA	530	98	0.56	1.75×10^6	0.036×10^6	—	—	—	311
Au61		521	93	0.51	1.82×10^6	0.14×10^6	—	—	—	
Au63		528	99	0.54	1.83×10^6	0.019×10^6	—	—	—	
Au64	In toluene	466, 495, 530	0.002	0.34	0.06×10^5	—	—	—	—	216
Au3		574	0.60	0.78	7.69×10^5				—	
Au65		545	0.21	1.25	1.68×10^5				—	
Au66		562	0.49	0.80	6.13×10^5				—	
Au4		603	0.57	0.84	6.79×10^5				—	
Au67		594	0.25	0.33	7.58×10^5				—	
Au68		632	0.02	0.20	1.00×10^5				—	
Au69		625	0.08	0.25	3.20×10^5				—	
Au64	In thin-films	468, 496, 530	0.028	22.4	0.01×10^5	—	—	—	—	216
Au3		577	0.88	0.85	10.35×10^5				—	
Au65		546	0.29	3.78	0.77×10^5				—	
Au66		560	0.67	1.43	4.69×10^5				—	
Au4		567	0.65	1.46	4.45×10^5				—	
Au67		568	0.80	1.19	6.72×10^5				—	
Au68		595	0.56	0.77	7.27×10^5				—	
Au69		527, 570, 640	0.09	0.33	2.73×10^5				—	
Au70	Toluene (298 K)	638	0.06	1.5	4.0×10^4	6.3×10^5	—	—	—	221
Au71		615	0.08	1.0	8.0×10^4	9.2×10^5			1048	
Au72		625	0.11	1.3	8.5×10^4	6.8×10^5			968	
Au73		621	0.08	0.8	1.0×10^5	1.2×10^6			—	
Au74		628	0.05	0.5	1.0×10^5	2.0×10^6			—	
Au75		650	0.07	1.3	5.4×10^4	7.2×10^5			—	
Au76		714	4.4×10^{-3}	0.2	2.2×10^4	5.0×10^6			—	
Au77	Toluene (298 K)	532	0.23	8.1	2.8×10^4	9.5×10^4	—	—	1290	312
Au78		550	0.19	7.2	2.6×10^4	1.3×10^5			—	



Table 7 (continued)

Complex	Medium	λ_{em} [nm]	PLQY [%]	τ_{exp} [μ s]	k_r [s^{-1}]	k_{nr} [s^{-1}]	k_{ISC} [s^{-1}]	k_{rISC} [s^{-1}]	ΔE_{ST} [cm^{-1}]	Ref.
Au79		534	0.20	10.5	1.9×10^4	7.6×10^4			1290	
Au80		549	0.21	4.8	4.4×10^4	1.7×10^5			—	
Au81		635	0.09	5.3	1.7×10^4	1.7×10^5			1452	
Au82		630	0.11	5.6	2.0×10^4	1.6×10^5			—	
Au77	Thin-film (298), in mCP	531	0.77	1.9, 22.1	—	—	—	—	1290	312
Au78		546	0.75	2.9, 18.8					—	
Au79		534	0.74	2.3, 20.6					1290	
Au80		546	0.67	2.4, 20.9					—	
Au81		604	0.30	1.6, 8.2					1452	
Au82		608	0.24	2.4, 9.7					—	
Au83	Toluene (298 K)	607	0.040	0.5	8.0×10^4	1.9×10^6	—	—	—	313
Au84		624	0.036	0.2	1.8×10^5	4.8×10^6				
Au85		584	0.091	0.5	1.8×10^5	1.8×10^6				
Au83	Thin flm (298 K), 20 wt% in mCP	547	0.82	3.5	2.3×10^5	5.1×10^4	—	—	—	313
Au84		543	0.68	1.1	6.2×10^5	2.9×10^5				
Au85		525	0.58	1.6	3.6×10^5	2.6×10^5				
Au86	Toluene (298 K)	540	0.15	2.0	7.50×10^4	4.25×10^5	—	—	—	314
Au87		570	0.14	0.6	2.33×10^5	1.43×10^6				
Au88		659	0.003	0.04	6.98×10^4	2.32×10^7				
Au89		637	0.01	0.1	1.00×10^5	9.90×10^6				
Au90		600	0.05	0.5	1.00×10^5	1.90×10^6				
Au91		599	0.07	0.5	1.20×10^5	1.88×10^6				
Au86	Thin flm (298 K), 20 wt% in mCP	498, 526	0.34	62.9	5.41×10^3	1.05×10^4	—	—	—	314
Au87		501, 524	0.59	54.7	1.08×10^4	7.50×10^3				
Au88		580	0.27	0.8	3.38×10^5	9.13×10^5				
Au89		564	0.52	1.3	4.00×10^5	3.69×10^5				
Au90		548	0.66	4.8	1.38×10^5	7.08×10^4				
Au91		543	0.68	3.2	2.13×10^5	1.00×10^5				

room temperature, as well as being the incorporation of a Pt(II)-based delayed fluorescence emitter into an OLED system.²⁰¹

Achieving narrow-band emission is essential for enhancing color purity in panel displays. However, this goal presents a significant challenge due to the broad bandwidths typically associated with TADF or phosphorescence in organic and metal-organic materials, arising from multiple CT transitions. In this study, a novel strategy is suggested to realize effective narrow-band emission through the sensitization of LC phosphorescence by significant intermetallic interactions. Compared to the weak phosphorescence observed in mononuclear Pt(II) precursors, the introduction of Pt(II)-Au(I) heteronuclear structures (**Pt7–12**, Scheme 5) results in a remarkable activation of highly efficient LC phosphorescence through significant d⁸-d¹⁰ interaction, achieving PLQYs of up to 81% in solution and 97% in doped films – Table 7. Through this approach, high-efficiency solution-processed OLEDs producing narrow-band emission have been developed. These OLED devices exhibit impressive EQE of 21.6% and FWHM of 36 nm for yellow electroluminescence, as well as EQE = 20.8% and FWHM = 32 nm for green electroluminescence – Table 6. The incorporation of Pt-Au heteronuclear structures not only enhances ISC from singlet to triplet states but also mitigates non-radiative thermal relaxation processes, leading to a substantial sensitization of LC phosphorescence. Notably, PtAu₂ complexes supported by double triphosphine ligands exhibit superior protection against non-radiative deactivation of triplet states compared to PtAu complexes linked by double diphosphine ligands, thereby yielding significantly stronger

phosphorescence. The comparison of the absorption and emission features of the Pt(II) precursor and the related Pt-Au heteronuclear complexes suggest that the Pt-Au clusters function effectively as sensitizers to capture light. Finally, this can then be effectively transferred to the naphthalene-acetylide ligands.³⁰²

In following, Xu *et al.* propose a viable molecular development approach to create an organic electroluminescent emitter with narrowband emission. This approach involves incorporating an innovative multiple resonance TADF fragment into the traditional Pt(II) complex. The solution-processed OLED, utilizing the designed Pt(II) complex BNCz-PPy-Pt-acac (BNCPPt) (**Pt13**, Scheme 5) as the dopant emitter, demonstrates light green emission with a peak wavelength of 507 nm and a narrow FWHM of 35 nm. This system achieves a EQE_{max} of 13.5% with minimal efficiency roll-off of just 4.4% at an illumination intensity of 1000 cd m⁻² – Table 6. This complex not only incorporates the advantageous features of the multiresonant design, but also preserves the remarkable traits of short lifetime and minimal efficiency reduction of heavy metal complexes. The impressive electroluminescent characteristics exhibited by **Pt13** were the foundation for a practical and insightful molecular model in materials research for cutting-edge display technologies. Significantly, this novel design approach bridges the multiresonant strategy with heavy metal atoms, establishes a definitive molecular structure design principle, and introduces a fresh strategy for developing heavy metal complexes with narrowband emission tailored for ultra-high definition displays.³⁰³



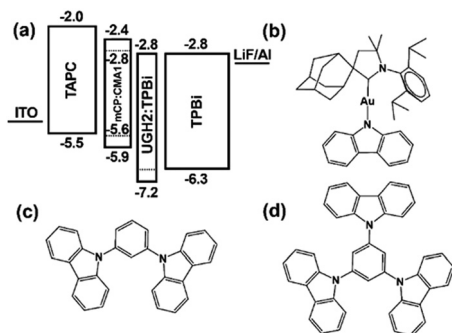


Fig. 26 (a) Device architecture of CMA1 OLEDs ITO/1,1'-bis[(di-4-tolylamino)phenyl]cyclohexane (TAPC) (40 nm)/mCP:CMA1(20 nm, varying wt%)/UGH2:TPBi(10 nm, 10 wt% TPBi)/TPBi (40 nm)/LiF(1 nm)/Al (100 nm) HOMO and LUMO energy levels are indicated in eV. (b)–(d) Complex (CAAC)AuCz **Au15** (b), mCP (c), and TCP (d). Reproduced with permissions from ref. 304. Copyright 2018, Wiley-VCH.

Despite the fact that the first Au(I) TADF emitter Au(PP)(PS) (**Au14**, Scheme 5) (PP = 1,2-bis(diphenylphosphino)benzene and PS = 2-diphenylphosphinobenzenethiolate) was developed by Osawa *et al.* in 2013, the presence of rapid ligand exchange in solution precluded its implementation in OLEDs.³¹⁵ However, very recently, examples of TADF Au(I) complexes have been employed in OLEDs. Here, Credgington, Bochmann, Linnolahti *et al.* demonstrated that the new linear donor-bridge-acceptor design that produced very effective rISC to singlets in Cu(I) complexes was also applicable for the design of the first examples of TADF in Au(I) chemistry.³¹⁶ In this respect, Table 6 list the most important Au(I) complexes reported in literature, together with the OLED structure in which they have been used, as well as the corresponding device metrics. Photo-physical and TADF properties of OLED utilizing Au(I) complexes are summarized in Table 7.

Specifically, the complexes (CAAC)AuCz (**Au15**, Scheme 5), (CAAC)AuNPh₂ (**Au16**, Scheme 5) and (CAAC)AuDTBCz (**Au17**, Scheme 5) (Cz anion, DTBCz = 3,6-di-*tert*-butylcarbazole anion) were implemented in all-organic multi-layer OLEDs. The devices consist on a ~180 nm polymeric hole-transport/electron-blocking layer, poly(9,9-dioctylfluorene-*N*-(4-butylphenyl)diphenylamine) (TFB), deposited on poly(3,4-ethylenedioxythiophene) polystyrene sulfonate (PEDOT:PSS) from toluene solution, a ~20 nm LEL comprising the corresponding complex, is deposited on PVK host from a dimethylformamide solution. Simultaneously, a layer of about 70 nm thickness comprising bathophenanthroline (BPhen), which acts as an electron-transport/hole-blocking layer, is deposited.

They were also able to implement complex (CAAC)AuCz (**Au15**, Scheme 5) in a thermal evaporation fabrication routine and demonstrated the viability of these complexes for industrial application. A device with lesser device-to-device variation compared with the solution-processed devices and a champion $\eta_{\text{EQE,EL}} = 26.9\%$ is reported.³⁰⁴ The authors explore mCP (Fig. 26c) and TCP (Fig. 26d) as host materials and found a critical effect on varying the host and the dopant concentration on the properties of the device, so a careful device optimization is mandatory.

Lam *et al.* present a group of structurally straightforward and operationally robust two-coordinate CMA(Au) TADF materials, **Au18–25** (Scheme 5), leveraging a CMA molecular framework incorporating sterically bulky pyrazine/pyridine/quinoxaline-fused NHC ligands.

These CMA(Au) emitters exhibit thermal stability, establish coplanar or orthogonal alignment between the carbene and amide ligands. They exhibit blue to deep red TADF emissions (466–666 nm) that are characterized by singlet ligand-to-ligand-charge-transfer excited states with emission quantum yields ranging from 0.63 to 0.99 – Table 8, short emission decay lifetimes (below 1.1 μs), and radiative decay rate constants of 0.68 to $3.2 \times 10^6 \text{ s}^{-1}$ in thin-film configurations at ambient temperature.

Investigations using ultrafast spectroscopy on compounds **Au18**, **Au21**, **Au22**, **Au23**, and **Au24** (Scheme 5) unveil a highly effective ISC mechanism exhibiting k_{ISC} ranging from 3.1 to $9.9 \times 10^{10} \text{ s}^{-1}$, alongside a rapid rISC process characterized by k_{rISC} between 8 and $35 \times 10^8 \text{ s}^{-1}$ – Table 9. The impact of extending the π -conjugation and adopting an orthogonal molecular geometry is evident in diminishing both the $\Delta E(S_1-T_1)$ and S_1 transition dipole moment. The OLEDs in blue to NIR spectral range showed exceptional performance metrics, achieving EQE/CE/PE of up to 26.9%, 76.7 cd A^{-1} , and 79.3 lm W^{-1} , respectively – Table 6. Noteworthy electroluminescent properties are observed in vacuum-deposited Au(I) complex based OLEDs, showing exceptionally high brightness levels at $300\,000 \text{ cd m}^{-2}$, EQEs reaching up to 26.2% with minimal roll-offs down to 2.6% at 1000 cd m^{-2} . Detailed investigations conducted in their laboratory revealed the operational lifetimes of these devices, reaching impressive LT₉₅ values (at L_0 , of 1000 cd m^{-2}) of up to 2082, 239, 126, and 30.5 h for yellow, green, red, and blue OLEDs, respectively. Furthermore, the NIR OLED demonstrated a LT₉₅ of 768 hours under a consistent driving current density of 30 mA cm^{-2} . Utilizing complex **Au21** as the sensitizer and BN2 as the emitter, they successfully developed narrowband TADF-sensitized fluorescence OLEDs. These OLEDs showed remarkable performance, achieving a high EQE of 19% at a luminance of 1000 cd m^{-2} with minimal efficiency roll-offs ranging from 12% to 25%. Furthermore, ultrapure-green TADF-enhanced fluorescent OLEDs using the CMA(Au) emitter as a sensitizer and a multiresonance terminal emitter achieve impressive EQEs of up to 25.3% – Table 6.³⁰⁵

To tackle the issue of efficient red-emitting TADF OLEDs, researchers are exploring molecular design strategies focused on enhancing the PLQY of two-coordinate Au(I) complex through the manipulation of amido ligands, namely [Au(^{Dipp}PZI)-(ACD)] (**Au26**), [Au(^{Dipp}PZI)(Cz)] (**Au27**), [Au(^{Dipp}PZI)(DPA)] (**Au28**), [Au(^{Dipp}PZI)(DPAC)] (**Au29**), [Au(^{Dipp}PZI)(DMAC)] (**Au30**), and [Au(^{Dipp}PZI)(PXZ)] (**Au31**) [1,3-bis(2,6-diisopropylphenyl)pyrazinoimidazolium (DippPZI), acridin-9-onide (ACD), cabazolid (Cz), *N,N*-diphenylamide (DPA), 9,9-diphenylacridinide (DPAC), 9,9-dimethylacridinide (DMAC), and phenoxazinide (PXZ)] – Scheme 5. They demonstrated photoluminescence peak wavelengths spanning 533–750 nm and PLQY values of up to 10% even in the NIR emission region, surpassing energy gap



Table 8 The OLED characteristics based on Cu, Ag–TADF complexes

Complex	OLED structure	Device	Concentration [wt%]	EL _{max} [nm]	CIE [x,y]	V _{on} [V]	CE _{max} [cd A ⁻¹]	η _p [lm W ⁻¹]	L _{max} [cd m ⁻²] at V _{app}	EQE [%]	Ref.
Cu29	ITO/PEDOT:PSS (40 nm)/20 wt% of A	—	—	519 (0.24,0.36)	6.9	8.82	—	—	1116	3.18	317
Cu30	Cu29 , Cu30 or Cu31 :host (30 nm)/	A	—	504 (0.21,0.30)	6.9	4.07	—	—	502	1.59	
Cu31	DPEPO (50 nm)/LiF (0.7 nm)/Al	A	—	508 (0.21,0.33)	6.1	23.68	—	—	2033	8.47	
Cu29	(100 nm)	B	—	500 (0.20,0.29)	8.7	5.15	—	—	309	1.98	
Cu30		B	—	484 (0.17,0.21)	9.3	8.37	—	—	194	3.72	
Cu31		B	—	496 (0.18,0.25)	11.5	3.53	—	—	139	1.42	
Cu32	ITO/PEDOT:PSS/PVK/10 wt% of Cu32 : host 3TPyMB LiF:Al	C	—	550 (0.40,0.52)	6.4	9.7	—	—	—	3.6	315
		D	—	560 (0.40,0.52)	5.0	17.5	—	—	—	6.3	
		E	—	560 (0.40,0.53)	5.0	21.3	—	—	—	7.8	
Cu33	ITO/PEDOT:PSS/PLEXCORE UT-314/ Cu33 :PYD2/3TPyMB/LiF:Al (ITO)/TAPC/mCP+10% Cu34 – Cu38 /3TPyMB/LiF/Al	—	—	—	2.6	73	—	—	10.000 (10)	23	318
Cu34		—	—	527 (0.30,0.55)	3.3	67.7	—	—	—	21.1	319
Cu35		—	—	517 (0.29,0.4)	3.0	65.3	—	—	—	21.3	
Cu36		—	—	513 (0.26,0.51)	3.1	62.4	—	—	—	21.2	
Cu37		—	—	529 (0.32,0.54)	3.3	69.4	—	—	—	22.5	
Cu38		—	—	515 (0.26,0.51)	3.3	55.6	—	—	—	18.6	
Cu40	ITO/HAT-CN(5 nm)/TAPC (40 nm)/	—	2	521 (0.33,0.52)	—	41.9	43.8	—	9260	16.4	231
Cu40	TCTA (10 nm)/TCTA:DPEPO: Cu40	—	4	521 (0.35,0.52)	—	39.5	41.4	—	8080	13.9	
Cu40	or Cu11 (10 nm)/DPEPO (40 nm)/	—	8	521 (0.35,0.52)	—	38.7	40.5	—	7600	13.7	
Cu11	LiF (1.2 nm)/Al (100 nm)	—	2	535 (0.35,0.51)	—	30.5	28.2	—	760	10.8	
Cu11		—	4	535 (0.36,0.52)	—	36.5	31.8	—	433	12.8	
Cu11		—	8	535 (0.37,0.52)	—	33.5	29.2	—	304	11.6	
Cu42	ITO/PEDOT:PSS/ Cu42 (20 wt%):czpzy/DPEPO/TPBi/LiF/Al	F ^a	—	514 (0.259,0.49)	5.6	17.34	—	—	2939 (14.1)	6.34	320
		G	—	516 (0.252,0.49)	5.6	17.53	—	—	3251 (14.3)	6.36	
Cu43	ITO/PEDOT:PSS/ Cu43 or	—	—	490 (0.17,0.37)	5.3	14.01	—	—	6563	5.83	321
Cu44	Cu44 :mCP/3TPyMB/LiF:Al	—	—	501 (0.21,0.43)	7.4	20.24	—	—	5579	7.42	
Cu45	ITO/PEDOT:PSS/TCTA/ Cu45 , Cu46 , D1	—	—	544 (0.37,0.55)	5.2 ^b	47.03	21.62	—	11010 (11.0)	14.81	322
Cu46	or Cu47 (10 wt%):mCP/TmPyPb/	D2	—	544 (0.38,0.55)	5.6 ^b	35.61	14.48	—	5152 (11.0)	11.17	
Cu47	LiF/Al	D3	—	544 (0.38,0.54)	5.3 ^b	21.33	12.07	—	5242 (9.0)	6.67	
Cu48	ITO/MoO ₃ /TAPC/TCTA/mCP:10%	—	—	550 (0.31,0.54) ^c	5.1	32.9	19.9	—	2339 (17.1)	10.1	323
Cu49	Cu48 –50/TmPyP/LiF/Al	—	—	520 (0.31,0.50) ^c	5.4	20.4	11.2	—	2399 (15.9)	7.3	
Cu50		—	—	550,610 (0.38,0.51) ^c	3.9	22.9	16.0	—	3256 (15)	8.3	
Cu53	ITO/MoO ₃ , 10 nm/TAPC, 40 nm/ 2,6DCzppy: 5 wt% Cu53 (20 nm)/ TmPyPB, 50 nm/LiF (1 nm)/Al (100 nm)	R/S-D	—	542 (0.34,0.53)	4.1	78	57	—	1990	21.7	324
Cu54	ITO/PEDOT:PSS/EML TPBi /LiF/Al	A-1	—	553 —	3.7	24.4	15.3	—	42 000	8.0	325
		A-2	—	553	3.5	24.9	15.9	—	40 000	7.8	
		A-3	—	553	3.8	24.5	15.6	—	40 000	7.8	
		A-4	—	552	3.4	24.6	16.6	—	35 000	7.9	
		B-1	—	550	4.0	7.3	4.5	—	1600	2.1	
		B-2	—	550	3.7	15.2	8.7	—	3000	4.7	
		C-1	—	552	3.7	36.4	21.8	—	34 000	11.4	
Cu55	ITO/MoO ₃ /TAPC/mCP: Cu55 –57 (10 wt%)/TPBi/LiF/Al	—	—	≈ 584 (0.473,0.495)	—	24.7	21.4	—	—	9.6	326
Cu56		—	—	≈ 584 (0.466,0.495)	—	32.7	28.8	—	—	12.4	
Cu57		—	—	≈ 584 (0.475, 0.493)	—	40.8	35.9	—	—	16.3	
Cu58	ITO (135 nm)/PEDOT:PSS (40 nm)/	1	—	523 (0.30,0.54)	8.5	24.8	—	—	2342 (22.9)	7.6	327
Cu59	20 wt% Cu58 , Cu59 or Cu60 :80	2	—	526 (0.30,0.54)	7.7	20.4	—	—	2012 (17.7)	6.2	
Cu60	wt% PYD2 (30 nm)/3TPyMB (50 nm)/LiF (0.8 nm)/Al (100 nm)	3	—	522 (0.29,0.53)	7.3	27.1	—	—	2012 (17.7)	8.3	
Cu61	ITO/PEDOT:PSS/PYD2: Cu(i) complex/DPEPO (10 nm)/TPBi (40 nm)/LiF/Al	—	4	526 (0.36,0.55)	—	48.12	18.68	—	7350	15.17	328
Cu61		—	8	531 (0.36,0.56)	—	51.52	21.29	—	8640	16.25	
Cu61		—	12	535 (0.37,0.56)	—	58.50	22.97	—	8650	18.46	
Cu61		—	20	540 (0.37,0.56)	—	45.27	17.43	—	9310	14.31	
Cu62		—	4	570 (0.48,0.51)	—	24.51	8.21	—	10 210	8.99	
Cu62		—	8	578 (0.50,0.49)	—	32.00	9.57	—	17 238	12.41	
Cu62		—	12	582 (0.51,0.48)	—	35.27	10.00	—	17 600	14.30	
Cu62		—	20	589 (0.53,0.47)	—	23.67	5.99	—	12 110	8.69	
Cu63		—	4 ^d	614 (0.54,0.38)	—	8.44	2.76	—	4880	5.95	
Cu63		—	8 ^d	622 (0.57,0.38)	—	12.74	8.17	—	5280	8.96	
Cu63		—	12 ^d	627 (0.59,0.38)	—	3.53	1.12	—	4040	2.97	
Cu63		—	20 ^d	634 (0.61,0.37)	—	2.36	0.69	—	1690	2.27	
Cu63		—	4 ^e	631 (0.61,0.38)	—	11.26	4.10	—	4630	10.17	
Cu63		—	8 ^e	638 (0.62,0.37)	—	6.67	2.47	—	4390	6.82	
Cu63		—	12 ^e	641 (0.63,0.37)	—	3.72	1.12	—	5260	4.14	
Cu63		—	20 ^e	647 (0.64,0.36)	—	1.48	0.42	—	2660	1.85	
Cu66		—	—	~ 530 (0.32,0.53)	4	—	—	—	12 800 (14.0 V)	10.5	238



Table 8 (continued)

Complex OLED structure	Device	Concentration [wt%]	EL _{max} [nm]	CIE [x,y]	V _{on} [V]	CE _{max} [cd A ⁻¹]	η _p [lm W ⁻¹]	L _{max} [cd m ⁻²] at V _{app}	EQE [%]	Ref.
Cu4 ITO/PEDOT:PSS/85% BCPO:15% Cu complex/TPBi/LiF/Al			~ 530	(0.33,0.54)	4			7740 (14.5 V)	9.5	
Cu69 70 nm ITO/5 nm HA-TCN/40 nm (TAPC/10 nm mCP/25 nm Cu69/65 nm TPBi/1.5 nm LiQ/100 nm Al)	—	10	537	—	3.0 ^f	—	—	41 000	17.0	329
		40	543	—	2.5 ^f	—	—	54 000	19.4	
		100	555	—	2.5 ^f	—	—	41 000	16.3	
Cu77 ITO/HAT-CN (5 nm)/NPB (30 nm)/Tris-pcz (15 nm)/CCP (6 nm)/Cu77/PPF (10 nm)/BPPB(25 nm)/LiQ (2 nm)/Al (120 nm)	A	5	453	(0.19,0.22)	3.9	—	—	910	11.2	330
	B	20	459	(0.20,0.25)	3.4	—	—	1730	20.6	
	C	40	468	(0.20,0.26)	3.4	—	—	1570	16.6	
	D	20	457	(0.18,0.19)	4.6	—	—	1540	18.1	
	E	—	477	(0.22,0.31)	3.0	—	—	940	10.3	
Cu78 ITO/MoO ₃ (2 nm)/TAPC (80 nm)/mCP (10 nm)/emissive layer (20 nm)/TPBi (10 nm)/3TPyMB (60 nm)/LiF (1 nm)/Al (140 nm)	A	1.0	622	(0.56,0.44)	2.9	30.2	30.1	16 894	20.7	331
	B	1.5	628	(0.58,0.42)	3.1	31.2	28.9	17 706	21.1	
	C	3.0	629	(0.57,0.43)	3.1	19.9	18.4	9233	17.6	
Cu79 ITO/HAT-CN (5 nm)/TAPC (50 nm)/TCTA (10 nm)/Cu ¹ complex:host	—	6	582	(0.51,0.48)	—	44.7	46.2	222 200	18.7	332
Cu80 (20 nm)/hole-blocking layer (HBL)	—	4	521	(0.27,0.57)	—	67.6	60.7	208 000	20.6	
Cu81 (10 nm)/TPBi (40 nm)/LiF (1 nm)/Al (100 nm)	—	2	619	(0.58,0.42)	—	22.1	22.0	155 000	14.4	
Cu83 (10 nm)/TPBi (40 nm)/LiF (1 nm)/Al (100 nm)	—	4	474	(0.14,0.22)	—	36.4	32.6	15 600	23.6	
Cu84 ITO/PEDOT:PSS/TAPC/TAPC:[Cu84][BarF ₄]/B3PYMPM/LiF/Al	—	—	—	(0.305,0.637)	2.4	—	—	8900 (15 V)	11.2	333
ITO/PEDOT:PSS/TAPC/CBP:[Cu84][BarF ₄]/B3PYMPM/LiF/Al	—	—	—	—	4.2	—	—	19 000	—	
Cu86 ITO/PEDOT:PSS/complex Cu86/TPBi/LiF/Al	—	—	564	(0.43,0.51)	—	—	—	234	7.74	334
Cu92 ITO/PEDOT:PSS (50 nm)/OTPD (4 nm)/PYD2:emitter Cu92 and Cu93(60 nm)/DPEPO (10 nm)/TPBi (40 nm)/LiF (1.2 nm)/Al (100 nm)	—	24	~ 560	(0.43,0.54)	6.4	18.23	9.98	6800	5.91	335
Cu93 (4 nm)/PYD2:emitter Cu92 and Cu93(60 nm)/DPEPO (10 nm)/TPBi (40 nm)/LiF (1.2 nm)/Al (100 nm)	—	16	~ 560	(0.51,0.49)	—	19.74	8.86	2520	7.96	
Cu101 ITO/TAPC (35 nm)/TCTA (5 nm)/mCBP doped with a certain weight percent of compound Cu101 or Cu102 (25 nm)/TmPyPB (50 nm)/LiF (1.5 nm)/Al (150 nm)	A1	1	—	(0.30,0.41)	3.8	22.7	19.8	13 542	10.3	336
	A2	5	—	(0.36,0.42)	3.6	25.9	22.3	17 839	13.7	
	A3	10	494,590	(0.38,0.42)	3.5	34.1	27.1	44 215	16.5	
	A4	20	—	(0.43,0.46)	3.7	26.0	20.2	41 695	15.7	
Cu102 LiF (1.5 nm)/Al (150 nm)	B1	1	494	(0.25,0.42)	3.7	31.5	25.4	35 947	12.9	
	B2	5	—	(0.26,0.45)	3.6	31.9	26.0	42 773	12.2	
	B3	10	—	(0.30,0.45)	3.8	21.7	15.5	36 478	9.2	
	B4	20	—	(0.36,0.48)	3.8	14.8	9.4	37 183	5.9	
Cu103 ITO/HAT-CN (10 nm)/NPB (10 nm)/TCTA (20 nm)/Host (aza-SBFs):8% CuI (20 nm)/Cz35PyDCb (5 nm)/TmPyPB (50 nm)/LiQ (1 nm)/Al (100 nm)	A	—	552	—	4.1	16.8	13.2	4342	6.6	337
	B	—	588	—	4.5	16.5	11.3	6740	7.6	
Cu105 CuI (20 nm)/Cz35PyDCb (5 nm)/TmPyPB (50 nm)/LiQ (1 nm)/Al (100 nm)	C	—	552	—	4.2	21.7	17.9	7600	8.8	
Cu106 TmPyPB (50 nm)/LiQ (1 nm)/Al (100 nm)	D	—	540	—	4.2	41.9	32.9	6180	16.8	
Cu107 ITO/PEDOT:PSS/PYD2: Cu107/DPEPO (10 nm)/TPBi (40 nm)/LiF (1.2 nm)/Al (100 nm)	—	2	—	(0.38,0.45)	—	6.48	3.39	1160	2.61	338
	—	4	—	(0.38,0.48)	—	8.39	4.01	1880	3.14	
	—	8	—	(0.38,0.49)	—	10.5	4.25	2500	3.80	
Ag10 ITO/PEDOT:PSS (50 nm)/OTPD (4 nm)/PYD2:emitter Ag10 (60 nm)/DPEPO (10 nm)/TmPyPb (40 nm)/LiF (1.2 nm)/Al (100 nm)	—	4	—	(0.44,0.52)	6.1	23.85	9.37	3300	8.46	273
	—	8	—	(0.45,0.52)	6.4	23.11	9.22	3015	8.76	
	—	12	—	(0.46,0.52)	6.8	19.41	7.28	1211	6.78	

^a To simplify the process, we directly spin-coated a mixture of czpzy and the starting material [Cu(CH₃CN)₂(POP)]BF₄ as emitting layer, expecting they form the emitter 14 during the solution process. For comparison, we planned to prepare the same EML as Device F by controlling the ratio of two materials (see Experimental section for details), and the resulting device is named as Device G. Other layers of Device G are identical to those of Device F. ^b Turn-on voltage recorded at a luminance of 1 cd m⁻². ^c Measured at 1000 cd m⁻². ^d PYD2 host. ^e CBP host. ^f Defined at brightness of 0.1 cd m⁻². **A,B**: hole-transporting 2,6-mCPy and electron-transporting DPEPO with high triplet energy levels (2.93 eV and 3.0 eV, respectively) are used as hosts, which are named as Device A and Device B, respectively. **C**: CDBP. **D**: 30 wt% of TAPC:CDBP. **E**: 30 wt% of TAPC: mCP. **A-1** SC, neat EML chlorobenzene g/g. **A-2** SC, neat EML chlorobenzene a/a. **A-3** SC, neat EML *o*-xylene g/g. **A-4** SC, neat EML *o*-xylene a/a. **B-1** IJP, neat EML indane a/a. **B-2** IJP, neat EML indane/mesitylene a/a. **C-1** SC, doped EML toluene g/g. (* SC: spincoated, IJP: inkjet printed; ** first letter indicates conditions for processing, second for drying; g: glovebox, a: air). **2,6-mCPy** = 2,6-bis(*N*-carbazolyl)pyridine. **2,6DCzppy**: (2,6-bis(3-(9*H*-carbazol-9-yl)phenyl)pyridine). **B3PYMPM**: (4,6-Bis(3,5-di(pyridin-3-yl)phenyl)-2-methylpyrimidine). **OTPD**: *N,N'*-bis(4-(6-(3-ethyloxy-3-yl)methoxy)-hexylphenyl)-*N,N'*-diphenyl-4,4'-diamine. **Cz35PyDCb**: 5-(5-(3-(9*H*-carbazol-9-yl)phenyl)pyridin-3-yl)-5*H*-pyrido[3,2-*b*]indole.

limitations. The λ_{em} was observed to correlate with the E_{ox} , a relationship affected by the amido ligand, aligning with the nature of the LLCT transition. As λ_{em} increased, the PLQY exhibited a sharp decline, suggesting nonradiative processes

dictated by the energy gap law. Quantum chemical calculations and photophysical analyses elucidate the role of radiative control, which enhances significantly as the overlap between hole and electron distributions ($S_r(r)$) in the excited state



Table 9 Photophysical and TADF characteristics of OLED based on Cu, Ag complexes

Complex	Medium	λ_{em} [nm]	PLQY [%]	τ_{exp} [μs]	k_{r} [s^{-1}]	k_{nr} [s^{-1}]	k_{ISC} [s^{-1}]	k_{rISC} [s^{-1}]	ΔE_{ST} [cm^{-1}]	Ref.
Cu29	In degassed CH_2Cl_2 , $T = 298$ K	590	2.1	1.6	—	—	—	—	—	317
Cu30		536	45	11.9						
Cu31		540	30	13.3						
Cu29	Crystalline powder, $T = 298$ K	490	56	20.4	—	—	—	—	1452	317
Cu30		465	87	12.2					1371	
Cu31		492	75	22.8					1452	
Cu32	In the solid state $T = 293$ K	521 ^a	52 ^a	1.73, 0.33	—	—	—	—	309 ^{cal}	315
Ag16		505 ^a	32 ^a	2.22, 0.56					199 ^{cal}	
Au14		610 ^a	12 ^a	1.66, 0.47					405 ^{cal}	
Cu32	In the solid state $T = 77$ K	534 ^a	73 ^a	847	—	—	—	—	309 ^{cal}	315
Ag16		530 ^a	72 ^a	574					199 ^{cal}	
Au14		630 ^a	18 ^a	52					405 ^{cal}	
Cu33	—	—	92	3.6	—	—	—	—	726	318
Cu34	In the solid state $T = 293$ K	517 ^b	38 ^c	4.6 ^b	—	—	—	—	680 ^d	319
Cu35		512 ^b	55 ^c	8.0 ^b					810 ^d	
Cu36		473 ^b	59 ^c	7.1 ^b					830 ^d	
Cu37		487 ^b	80 ^c	6.5 ^b					600 ^d	
Cu38		486 ^b	95 ^c	8.9 ^b					710 ^d	
Cu34	In the solid state $T = 77$ K	507 ^b	56 ^c	2500 ^b	2.2×10^2	1.8×10^2	—	—	—	319
Cu35		500 ^b	85 ^c	360 ^b	2.4×10^3	4.2×10^2				
Cu36		456 ^b	85 ^c	100 ^b	8.5×10^3	1.5×10^3				
Cu37		477 ^b	85 ^c	520 ^b	1.6×10^3	2.9×10^2				
Cu38		487 ^b	95 ^c	910 ^b	1.0×10^3	5.5×10				
Cu19	Ground Solid State, 295 K	579	55	2.5	22×10^4	18×10^4	—	—	—	251
Cu19	mCP (1 wt%), 295 K	534	64	14.3	4.5×10^4	2.5×10^4	—	—	—	251
Cu19	CzSi (10 wt%), 295 K	575	47	2.2	21×10^4	24×10^4	—	—	—	251
Cu19	UGH-3 (10 wt%), 295 K	575	30	2.4	13×10^4	30×10^4	—	—	—	251
Cu19	PMMA (1 wt%), 295 K	553	47	12.0	3.9×10^4	4.4×10^4	—	—	—	251
Cu20	Ground Solid State, 295 K	606	53	1.7	31×10^4	27×10^4	—	—	—	251
Cu20	mCP (1 wt%), 295 K	538	51	149	0.34×10^4	0.33×10^4	—	—	—	251
Cu20	CzSi (10 wt%), 295 K	595	14	1.3	11×10^4	68×10^4	—	—	—	251
Cu20	UGH-3 (10 wt%), 295 K	590	18	1.2	15×10^4	68×10^4	—	—	—	251
Cu20	PMMA (1 wt%), 295 K	540	46	116	0.40×10^4	0.47×10^4	—	—	—	251
Cu39	Powder at 300 K/77 K	541/ 551	83/85	9/3300	$9.2 \times 10^4/2.6 \times 10^2$		—	—	—	231
Cu40	Powder at 300 K/77 K	530/ 530	82/85	7/ \approx 420	$12 \times 10^4/20 \times 10^2$		—	—	—	231
Cu11	Powder at 300 K/77 K	540/ 540	90/70	5/680	$18 \times 10^4/10 \times 10^2$		—	—	—	231
Cu11	Powder at 300 K/50 K	540/ 540	90/70 (77 K)	5/700	$18 \times 10^4/10 \times 10^2$	$2.0 \times 10^4/4.3 \times 10^2$	—	—	600	231
Cu11	Doped in PMMA (≈ 1 wt%)	544	56	7	8.0×10^4	6.3×10^4	—	—	—	231
Cu11	Fluid DCM Solution ($c \approx 10^{-5}$ M)	544	1	4	0.25×10^4	25×10^4	—	—	—	231
Cu41	In the solid state $T = 293$ K	495	45	134	3.4×10^3	4.1×10^3	—	—	1452	320
Cu42		518	98	23	4.3×10^4	8.7×10^2			1048	
Cu41	In the solid state $T = 77$ K	507	71	671	1.1×10^3	4.3×10^2	—	—	—	320
Cu42		521	39	521	9.5×10^2	1.5×10^3				
Cu43	In CH_2Cl_2 , $T = 77$ K	—	—	—	—	—	—	—	—	321
Cu43	In powder, $T = 77$ K	501	—	593	—	—	—	—	—	321
Cu43	In CH_2Cl_2 , $T = 293$ K	518	16	4.6	—	—	—	—	—	321
Cu43	In powder, $T = 293$ K	493	60.9	145	—	—	—	—	968	321
Cu44	In CH_2Cl_2 , $T = 77$ K	—	—	—	—	—	—	—	—	321
Cu44	In powder, $T = 77$ K	516	—	496	—	—	—	—	—	321
Cu44	In CH_2Cl_2 , $T = 293$ K	518	19	7.2	—	—	—	—	—	321
Cu44	In powder, $T = 293$ K	475	40.7	51	—	—	—	—	968	321
Cu45	Solution (in degassed CH_2Cl_2)	(616 ^e , 543 ^f)	—	—	—	—	—	—	—	322
Cu46		(616 ^e , 538 ^f)	—	—	—	—	—	—	—	
Cu47		(616 ^e , 546 ^f)	—	—	—	—	—	—	—	
Cu45	Powder, 300 K	550	22.4	5.7	—	—	—	—	645 ^g	322
Cu46		549	18.5	5.7	—	—	—	—	726 ^g	
Cu47		556	20.0	5.7	—	—	—	—	323 ^g	
Cu45	Powder, 77 K	568	19.3	343	—	—	—	—	—	322
Cu46		560	16.2	317	—	—	—	—	—	
Cu47		564	19.4	363	—	—	—	—	—	
Cu45	PMMA film	528	33.1	—	—	—	—	—	—	322
Cu46		525	31.7	—	—	—	—	—	—	
Cu47		528	31.5	—	—	—	—	—	—	



Table 9 (continued)

Complex	Medium	λ_{em} [nm]	PLQY [%]	τ_{exp} [μs]	k_{r} [s^{-1}]	k_{nr} [s^{-1}]	k_{ISC} [s^{-1}]	k_{rISC} [s^{-1}]	ΔE_{ST} [cm^{-1}]	Ref.
Cu48	In the solid state $T = 298 \text{ K}$	498	32^h	2.5^i	1.28×10^5	—	—	—	968^{cal}	323
Cu49		511	28^h	12.5^i	0.22×10^5	—	—	—	968^{cal}	
Cu50		527	29^h	4.8^i	0.60×10^5	—	—	—	1129^{cal}	
Cu48	In the solid state $T = 77 \text{ K}$	500	—	103^i	—	—	—	—	—	323
Cu49		517	—	714^i	—	—	—	—	—	
Cu50		532	—	818^i	—	—	—	—	—	
Cu51	CH_2Cl_2 ($1 \times 10^{-5} \text{ mol L}^{-1}$) at room temperature	505	—	—	—	—	—	—	121	324
Cu52	CH_2Cl_2 ($1 \times 10^{-5} \text{ mol L}^{-1}$) at room temperature	502	—	—	—	—	—	—	153	324
Cu53	CH_2Cl_2 ($1 \times 10^{-5} \text{ mol L}^{-1}$) at room temperature	500	—	—	—	—	—	—	32	324
Cu54	In the solid state as neat powder at room temperature	550	75 ± 5	$6.9^j/21.4^k$	0.11×10^{-6}	0.03×10^{-6}	—	—	—	325
Cu54	Neat film at room temperature	550	57 ± 5	6.2	0.09×10^{-6}	0.07×10^{-6}	—	—	—	325
Cu54	50% in PMMA at room temperature	550	56 ± 5	7.7	0.07×10^{-6}	0.06×10^{-6}	—	—	—	325
Cu54	40% in PYD2 at room temperature	550	62 ± 5	6.8	0.10×10^{-6}	0.04×10^{-6}	—	—	—	325
Cu54	20% in PYD2 at room temperature	550	60 ± 5	6.7	0.09×10^{-6}	0.06×10^{-6}	—	—	—	325
Cu55	In film $T = 300 \text{ K}$	530	76	19	4.0×10^4	1.3×10^4	—	—	$(798^l, 40.3^m)$	326
Cu56		523	79	16	4.9×10^4	1.4×10^4	—	—	$(758^l, 290^m)$	
Cu57		521	83	11	7.5×10^4	1.6×10^4	—	—	$(-^l, 363^m)$	
Cu55	In film $T = 77 \text{ K}$	531	82	1778	4.6×10^2	1.0×10^2	—	—	—	326
Cu56		531	83	1611	5.2×10^2	1.0×10^2	—	—	—	
Cu57		531	85	294	2.9×10^3	5.0×10^2	—	—	—	
Cu58	$T = 77 \text{ K}$	509	43 ± 5	5.5 ± 1	8.0×10^4	1.0×10^5	—	—	—	327
Cu59		519	29 ± 5	16 ± 1	1.8×10^4	4.4×10^5	—	—	—	
Cu60		503	79 ± 5	5.5 ± 1	1.4×10^5	3.8×10^4	—	—	—	
Cu58	$T = 298$	523	67 ± 5	158 ± 1	4.2×10^3	2.1×10^3	—	—	718^n	327
Cu59		546	54 ± 5	356 ± 1	1.5×10^3	1.3×10^3	—	—	1065^n	
Cu60		516	82 ± 5	209 ± 1	3.9×10^3	8.4×10^2	—	—	758^n	
Cu61	—	—	—	—	—	—	—	—	1121	328
Cu62		—	—	—	—	—	—	—	1621	
Cu63		—	—	—	—	—	—	—	2073	
Cu64	CH_2Cl_2 at 298 K	560	$28.4^o/0.84^p$	$10.9^o/0.26^p$	$2.61 \times 10^4^o/3.23 \times 10^4^p$	$6.56 \times 10^4^o/381 \times 10^4^p$	—	—	976^{cal}	238
Cu65		568	$19.7^o/0.68^p$	$9.0^o/0.26^p$	$2.26 \times 10^4^o/2.62 \times 10^4^p$	$8.86 \times 10^4^o/382 \times 10^4^p$	—	—	879^{cal}	
Cu66		568	$22.9^o/0.73^p$	0.26^p	$2.30 \times 10^4^o/3.32 \times 10^4^p$	$7.70 \times 10^4^o/451 \times 10^4^p$	—	—	—	
Cu4		565	22.6	$10.0^o/0.22^p$	2.09×10^4	6.65×10^4	—	—	895^{cal} 1081^{cal}	
Cu64	CH_2Cl_2 at 77 K	546	—	321	—	—	—	—	—	238
Cu65		525	—	173	—	—	—	—	—	
Cu66		525	—	178	—	—	—	—	—	
Cu4		518	—	211	—	—	—	—	—	
Cu64	PMMA (1% wt) at 298 K	532	57	18.0, 36.5	—	—	—	—	—	238
Cu65		520	51	22.8, 57.9	—	—	—	—	—	
Cu66		520	53	24.0, 63.0	—	—	—	—	—	
Cu4		520	65	25.3, 75.1	—	—	—	—	—	
Cu64	Powders at 298 K	553	41	16.3	—	—	—	—	—	238
Cu65		548	15	14.9^q	—	—	—	—	—	
Cu66		538	32	17.1	—	—	—	—	—	
Cu4		527	37	27.5	—	—	—	—	—	
Cu67	Solution in 2-MeTHF, RT	448	24	2.3	1.0×10^5	3.3×10^5	—	—	—	329
Cu68		492	100	1.2	8.3×10^5	$<0.083 \times 10^5$	—	—	—	
Cu69		542	55	1.1	5.0×10^5	4.1×10^5	—	—	500	
Cu70		602	5	0.080	6.2×10^5	119×10^5	—	—	—	
Cu71		666	2	0.052	3.8×10^5	180×10^5	—	—	—	
Cu72		—	—	—	—	—	—	—	—	
Cu67	Solution in 2-MeTHF, 77 K	424	—	9300	—	—	—	—	—	361
Cu68		428	—	2200	—	—	—	—	—	
Cu69		432	—	2100 (62%) and 345 (38%) @430 nm, 181 @520 nm	—	—	—	—	—	
Cu70		492	—	18	—	—	—	—	—	
Cu71		536	—	210	—	—	—	—	—	
Cu72		—	—	—	—	—	—	—	—	



Table 9 (continued)

Complex	Medium	λ_{em} [nm]	PLQY [%]	τ_{exp} [μs]	k_{r} [s^{-1}]	k_{nr} [s^{-1}]	k_{ISC} [s^{-1}]	k_{rISC} [s^{-1}]	ΔE_{ST} [cm^{-1}]	Ref.
Cu67	1 wt% in PS film, RT	432	80	2.6 (47%), 14 (53%)	0.9×10^5	0.23×10^5	—	—	—	329
Cu68		468	100	1.3	7.7×10^5	$<0.077 \times 10^5$				
Cu69		506	90	1.4	6.4×10^5	0.71×10^5				
Cu70		548	78	1.2	6.5×10^5	1.8×10^5				
Cu71		616	30	0.75	4.0×10^5	9.3×10^5				
Cu72		704	3	0.19	1.6×10^5	51×10^5				
Cu67	1 wt% in PS film, 77 K	424	—	3200	—	—	—	—	—	361
Cu68		464	—	100						
Cu69		502	—	140						
Cu70		544	—	150						
Cu71		612	—	410						
Cu72		682	—	150						
Cu67	Neat solid, RT	438	5	0.37 (33%), 1.8 (67%)	0.38×10^5	7.2×10^5	—	—	—	329
Cu68		474	76	0.75	10.0×10^5	3.2×10^5				
Cu69		492	53	0.84	6.3×10^5	5.5×10^5				
Cu70		550	68	1.0	6.8×10^5	3.2×10^5				
Cu71		616	15	0.33	4.5×10^5	26×10^5				
Cu72		658	12	0.39	3.1×10^5	22×10^5				
Cu67	Neat solid, 77 K	438	—	7100	—	—	—	—	—	329
Cu68		468	—	90						
Cu69		482	—	160						
Cu70		558	—	280						
Cu71		598	—	180						
Cu72		634	—	310						
Cu73	1 wt% doped PS film at RT	505	19	0.55	3.5×10^5	15×10^5	—	—	—	330
Cu74		560	5	0.19	2.6×10^5	50×10^5				
Cu75		560	8	0.18	4.4×10^5	51×10^5				
Cu76		555	12	0.82	1.5×10^5	11×10^5				
Cu77		458	74	1.9	3.9×10^5	1.4×10^5				
Cu78	Toluene (1×10^{-4} M, 300 K)	638	12	0.11	6.9×10^5	3.9×10^5	—	—	444	331
Cu78	PS-doped film (with a 5 wt% doping concentration)	609	24	0.42	6.9×10^5	3.9×10^5	—	—	444	331
Cu78	CBP:TPBi-doped film (with a 1.5 wt% doping concentration)	599	65	0.93	6.9×10^5	3.9×10^5	—	—	444	331
Cu79	Toluene ([Cu] = 1×10^{-4} M)	624	29	0.18	16.1×10^5	39.4×10^5	—	—	—	332
Cu80	Toluene ([Cu] = 5×10^{-5} M)	555	58	0.36	16.1×10^5	11.6×10^5			—	
Cu81	Toluene ([Cu] = 1×10^{-4} M)	660	14	0.11	12.7×10^5	78.2×10^5			81	
Cu82	Toluene ([Cu] = 5×10^{-5} M)	635	15	0.12	12.5×10^5	70.8×10^5			—	
Cu83	Toluene ([Cu] = 5×10^{-5} M)	502	74	0.55	13.5×10^5	4.7×10^5			81	
[Cu84][BAF₄]	Powdered solid, 298 K	518	50	—	5.1×10^4	5.1×10^4	—	—	581 ± 32	333
[Cu84][BF₄]		518	—	9.8	—	—				
[Cu84][BAF₄]	Powdered solid, 77 K	—	71	—	7.1×10^3	2.9×10^3	—	—	—	333
[Cu84][BF₄]		—	—	100	—	—				
[Cu84][BAF₄]	DCM solution, 298 K	—	78	—	—	—	—	—	—	333
[Cu84][BF₄]		—	—	—	—	—				
[Cu84][BAF₄]	DCM solution, 77 K	—	93	—	—	—	—	—	—	333
[Cu84][BF₄]		—	—	—	—	—				
[Cu84][BAF₄]	THF solution, 298 K	—	79	—	7.2×10^4	1.9×10^4	—	—	—	333
[Cu84][BF₄]		525	—	—	—	—				
[Cu84][BAF₄]	THF solution, 77 K	—	82	—	—	—	—	—	—	333
[Cu84][BF₄]		—	—	—	—	—				
Cu85	In powder state, 297 K	485	0.41	36.4	1.13×10^4	—	—	—	850 (476')	334
Cu86		506	0.52	48.9	1.06×10^4					
Cu87		535	0.29	20.8	1.39×10^4				807 (1031')	
Cu88		515	0.18	9.0	2.04×10^4				940 (1035')	
									528 (464')	
Cu89		535	0.07	10.0	0.65×10^4				644 (841')	
Cu90		516	0.03	4.2	0.62×10^4				492 (848')	
Cu85	In powder state, 77 K	473	—	73.9	—	—	—	—	—	334
Cu86		498	0.87	595						
Cu87		536	—	772						
Cu88		499	—	108						
Cu89		502	—	469						
Cu90		508	—	462						
Cu91	10 wt% doped DPEPO film 298 K/77 K	534/544	62	21.4	—	—	—	—	887	335



Table 9 (continued)

Complex	Medium	λ_{em} [nm]	PLQY [%]	τ_{exp} [μs]	k_r [s^{-1}]	k_{nr} [s^{-1}]	k_{ISC} [s^{-1}]	k_{rISC} [s^{-1}]	ΔE_{ST} [cm^{-1}]	Ref.
Cu92		533/ 545	71	24.1					645	
Cu93		565/ 582	48	5.8					565	
Cu94		564/ 575	42	4.3					403	
Cu95	Toluene solution	511	37	0.58	6.4×10^5	10.9×10^5	—	—	—	336
Cu96		517	42	0.75	5.6×10^5	7.7×10^5				
Cu97		507	41	0.36	11.4×10^5	16.4×10^5				
Cu98		513	79	0.85	9.3×10^5	2.5×10^5				
Cu99		521	39	0.46	8.5×10^5	13.3×10^5				
Cu100		527	23	0.41	5.6×10^5	18.8×10^5				
Cu101		549	73	0.72	10.1×10^5	3.6×10^5				
Cu102		554	76	0.76	10.0×10^5	3.2×10^5				
Cu95	PMMA films (5 wt%)	471	74	2.6	2.8×10^5	1.0×10^5	—	—	—	336
Cu96		478	82	1.9	4.3×10^5	0.9×10^5				
Cu97		467	68	1.9	3.6×10^5	1.6×10^5				
Cu98		474	84	2.1	4.0×10^5	0.8×10^5				
Cu99		479	71	2.1	3.4×10^5	1.4×10^5				
Cu100		484	78	1.6	4.9×10^5	1.4×10^5				
Cu101		499	73	1.6	4.6×10^5	1.7×10^5				
Cu102		509	89	1.2	7.2×10^5	1.2×10^5				
Cu103	aza-SBFs: CuI of 1.00:0.08 in DMF was measured at 77 K	517/ 556/ 615	4.6	0.6/5.8/55.8	—	—	3.18×10^8	7.95×10^4	242–1936	337
Cu104		625	52.6	18.1			4.65×10^8	1.78×10^5	1290	
Cu105		580	60.4	21.1			5.05×10^8	3.20×10^5	1290	
Cu106		550	92.2	40.6			6.18×10^8	2.84×10^5	807	
Cu107	Thin-film doped in PYD2 (8 wt%)	544	27	3.1	—	—	—	—	—	338
Cu107	Thin-film doped in mCP (8 wt%)	535	20	5.5	—	—	—	—	—	338
Cu107	Thin-film doped in PVK (8 wt%)	545	11	3.2	—	—	—	—	—	338
Cu107	Thin-film doped in TCTA (8 wt%)	542	10	4.3	—	—	—	—	—	338
Cu107	Thin-film doped in CBP (8 wt%)	537	13	2.8	—	—	—	—	—	338
Ag17	DPEPO film at 298 and (77 K)	520/ 536	0.48	4.7	—	—	—	—	1694	273
Ag18		524/ 535	0.34	7.4					1694	
Ag10		573/ 585	0.62	3.5					1290	
Ag19		535/ 557	0.50	3.7					1774	

^a $\lambda_{\text{exc}} = 310 \text{ nm}$. ^b $\lambda_{\text{exc}} = 355 \text{ nm}$. ^c Absolute PL quantum yield in the solid state (error $\pm 8\%$). ^d Energy gap between S_1 and T_1 levels obtained by temperature dependence of decay time. ^e $T = 300, 77 \text{ K}$, respectively. ^f $T = 300, 77 \text{ K}$, respectively. ^g Calculated from S_1 and T_1 of complexes as powders. ^h Absolute emission quantum in the solid state. Experimental errors are $\pm 5\%$. ⁱ Emission lifetime. Experimental errors are $\pm 5\%$. ^j $T = 298, 77 \text{ K}$. ^k $T = 298, 77 \text{ K}$. ^l Energy gap between S_1 and T_1 determined from the emission spectra at 77 K and 298 K. ^m Data are given in parentheses is Φ_F . ⁿ Energy gap between S_1 and T_1 determined from the emission spectra at 77 K and 298 K. ^o Double entries for each complex refer to oxygen free (o) and airequilibrated samples (p). ^p Double entries for each complex refer to oxygen free (o) and airequilibrated samples (p). ^q This compound exhibits a biexponential decay with a short component of 7.29 μs . ^r The S_1 and T_1 energy levels were estimated according to the emission peak onsets at 297 K and 77 K.

increases. It is revealed that $S_1(r)$ increases with the distance between the hole-distribution centroid and the nitrogen atom ($d_{\text{h-N}}$) in an amido ligand. Notably, multilayer OLEDs incorporating the Au(i) complex emitters demonstrate superior performance, pushing the boundaries of the electroluminescence wavelength–EQE space established by previous coinage metal complex devices. These Au(i) complex-based OLEDs achieved a EQE_{max} of 7.0% at λ_{EL} of 680 nm – Table 6, which could be extended up to 706 nm at high concentrations. This study is expected to inform future molecular design approaches aimed at enhancing the efficiency of OLEDs emitting long-wavelength light.³⁰⁶

Likewise, the development of organic blue-emitting devices has encountered challenges in achieving high EQEs, narrow bandwidths, and extended operational lifetimes under intense luminance. A novel material approach has been demonstrated to address these crucial requirements. This innovative strategy leverages linear heteroleptic Au(i) complex exciton harvesters $[\text{Au}(\text{D}^{\text{ip}}\text{PBZI})(\text{Cz})]$ (**Au32**) and $[\text{Au}(\text{D}^{\text{ip}}\text{PBZI})(\text{TMCz})]$ (**Au33**) in conjunction with multiresonant emitters – Scheme 5. The resultant organic electroluminescence devices deliver blue emissions x/y CIE color coordinates of 0.108, 0.160 and exhibit a notably narrow FWHM value of 20 nm. These devices achieve an impressive EQE_{max} of up to 30.2% – Table 6. Noteworthy is



the sustained EQE performance of 22.2% even at high luminance levels of 2000 cd m^{-2} , surpassing conventional devices using organic exciton harvesters plagued by significant quantum efficiency roll-offs. The mitigation of EQE roll-off is credited to the expeditious transformation of dark triplet excitons into luminescent singlet excitons facilitated by the Au(I) complexes. The investigations, rooted in photophysical assessments and quantum chemical computations, elucidate that the swift capture of triplet excitons is a result of the synergistic interaction between the highly effective triplet-to-singlet conversion aided by the robust SOC within the Au 5d orbitals and the minimal $\Delta E(\text{ICT}^3\text{LE})$ due to the well-separated natural transition orbital distributions. Furthermore, the advanced device exhibits a substantial tenfold enhancement in operational lifetime compared to control devices. The research attributes these improvements to the distinctive capability of Au(I) complexes in rapidly capturing triplet excitons. Additionally, these complexes facilitate Förster energy transfer to the emitter, effectively curtailing hazardous triplet-triplet Dexter energy transfer. The findings of this study hold promise for driving the commercialization of high-efficiency and stable blue electroluminescence devices, marking a significant leap in the advancement of organic optoelectronics technologies.³⁰⁷

Acceleration of singlet-triplet ISC plays a crucial role in enhancing triplet exciton utilization in emitters, such as (SiPr)AuBN (**Au34**), (IPr)AuBN (**Au35**), (BzIPr)AuBN (**Au36**), (PzIPr)AuBN (**Au37**), (PyIPr)AuBN (**Au38**) and (BzIPr)AuBNO (**Au39**) – Scheme 5. In contrast to their organic parent counterparts, Au(I) emitters achieved approximately a two-fold increase in ISC and rISC rates due to improved SOC. This study outlines a straightforward Au(I) coordination approach to amplify the SOC of green and blue BN(O)-based TADF emitters, leading to a significant increase in the rate constants of the spectroscopically observed ISC process to $3 \times 10^9 \text{ s}^{-1}$ with nearly complete ISC quantum yields. Consequently, the resulting thermally-stable Au^I emitters achieved substantial values of delayed fluorescence k_r constant, up to $1.3 \times 10^5/1.7 \times 10^5 \text{ s}^{-1}$ in THF/PMMA films, while maintaining narrowband emissions (FWHM = 30–37 nm) and high PLQYs (0.9). Vapor-deposited ultrapure-green OLEDs doped with (BzIPr)AuBN (**Au36**) demonstrated high luminance of up to $2.53 \times 10^5 \text{ cd m}^{-2}$, along with EQE_{max} of up to 30.3% – Table 6, narrowband electroluminescence with FWHM of 34 nm and minimal roll-offs at 0.8%, accompanied by extended device lifetimes (LT₆₀) of 1210 h at 1000 cd m^{-2} . This work propose that this uncomplicated and readily applicable metal coordination technique aimed at enhancing triplet exciton utilization could be expanded to various TADF compounds beyond TADF emitters. This expansion opens up a new avenue for practical TADF OLEDs.³⁰⁸

The practical utility of luminescent mononuclear Au(I) complexes as optoelectronic materials has been constrained by their poor stability. In this study, Li *et al.* present a novel approach to enhance the stability of several novel Au(I) complexes (IPzIDCz (**Au40**), ImIDCz (**Au41**) and IPzTPA (**Au42**) exhibiting TADF – Scheme 5). By employing a highly rigid and groove-like σ -donating aryl ligand, they have fostered the

formation of dual Au⁺...H C hydrogen bonds, thereby fortifying the stability of the complex. The existence of secondary metal-ligand interactions has been confirmed through single-crystal structure analysis, nuclear magnetic resonance (NMR) spectroscopy, and theoretical simulations. In conjunction with the steric influences of the ligands, the metal ion is enveloped within a highly congested coordination environment. They exhibit notably augmented thermal stability and PLQY values of around 76%. Thus, OLEDs fabricated *via* vacuum deposition demonstrate promising electroluminescence, achieving EQE_{max} exceeding 23% and minimal 3.3% efficiency roll-off even at luminance levels of $10\,000 \text{ cd m}^{-2}$ – Table 6. The estimated LT₅₀ surpassing 77 000 h at an initial luminance of 100 cd m^{-2} underscores the impressive operational stability of the system. This research offers a pathway for designing stable luminescent Au(I) complexes with remarkable potential for practical applications in optoelectronic devices.³⁰⁹

The first TADF Au(III) emitter was developed by Fernandez-Cestau *et al.* in 2015.²¹³ Remarkably, the utilization of Biscyclometallated aryl Au(III) complexes integrated with TADF has enabled the development of solution-processed OLEDs. These OLEDs exhibit impressive figures of merit, including EQEs, CEs, and luminance reaching as far as 23.8%, 70.4 cd A^{-1} , and $57\,340 \text{ cd m}^{-2}$, respectively. This indicates that Au(III)-TADF emitters demonstrate competitiveness with the top-performing Pt(II) and Ir(III) phosphorescent emitters in terms of EQE and luminance for OLED applications.³¹⁰

Chan and co-workers present the design and synthesis of a novel group of Au(III) complexes, that is, **Au5–8** and **Au43–44** featuring fused heterocyclic alkynyl ligands – Scheme 5, exhibiting adjustable emission colors from yellow to red in solid form and demonstrating TADF characteristics. These complexes show notable PLQY of up to 0.87 – Table 10. The increased energy gap between the higher-lying ³IL excited state and the lower-lying LLCT excited state in the complexes results in reduced involvement of the long-lived ³IL state in the emission process of **Au6–8** and **Au44** – Scheme 5. Consequently, these complexes exhibit heightened emission intensity as the temperature rises, with a rate constant (k_r) reaching up to 10^6 s^{-1} , attributed to TADF. Upon elevating the temperature from 200 to 360 K, a substantial rise in emission intensity is observed without significant alterations in excited-state lifetime, suggesting an escalation in the radiative decay rate. Au(III) complex-based OLEDs fabricated through solution processing have achieved EQE_{max} of up to 10.0% – Table 6. These devices utilize TADF Au(III) complexes to significantly decrease efficiency roll-offs from around 60% to approximately 17% at a luminance level of 1000 cd m^{-2} . Notably, the ΔE_{ST} is estimated to be as small as 242 cm^{-1} , aligning with computational predictions at 403 cm^{-1} . The meticulous selection of the cyclometalating ligand and fused heterocyclic ligand plays a pivotal role in inducing TADF by regulating the energy levels of ILCT and LLCT. This study marks a milestone in fabricating TADF Au(III) complex based OLEDs with fused heterocyclic alkynyl ligands capable of emitting yellow to red light.²¹⁷



Table 10 The LEC characteristics based on Cu–TADF complexes

Complex	LEC structure	EL _{max} [nm]	CIE [x,y]	CE _{max} [cd A ⁻¹]	η _p [lm W ⁻¹]	L _{max} [cd m ⁻²] at V _{app}	EQE [%]	Ref.
Cu109	ITO/PEDOT:PSS/[Cu(P [^] P) [^] N [^] N][PF ₆]:[Emim][PF ₆]	595	—	0.7	0.2	65	0.4	339
Cu110		589	(0.449, 0.532)	1.1	0.4	109	0.5	
Cu117		593	—	1.3	0.4	131	0.6	
Cu118	ITO/EDOT:PSS (80 nm)/EML (100 nm):[Emim][PF ₆]/Al	—	—	0.3	—	17	—	340
Cu119	(100 nm)	—	—	1.3	—	63	—	
Cu120		—	—	0.7	—	37	—	
Cu121		—	—	0.6	—	32	—	
Cu122		—	—	0.2	—	14	—	
Cu123		—	—	0.4	—	22	—	
Cu124		—	—	0.9	—	45	—	
Cu125		—	—	1.6	—	79	—	
Cu126		—	—	1.6	—	80	—	
Cu127		—	—	0.9	—	44	—	
Cu128		—	—	0.8	—	39	—	
Cu129		—	—	1.1	—	56	—	
Cu130		—	—	1.1	0.2	53	0.2	341
Cu131		—	—	1.5	0.5	77	0.7	
Cu132	ITO/PEDOT:PSS(90 nm)/Cu132: [EMIM][PF ₆] 4:1 (100 nm)/Al (70 nm)	557	—	5.2	—	53	—	245
Cu133	ITO/PEDOT:PSS(80 nm)/Cu133(90 nm)/Al (90 nm)	580	—	0.4	—	54	—	342
Cu117	ITO/PEDOT:PSS(80 nm)/Cu117: [EMIM][PF ₆] 4:1 (120 nm)/Al (90 nm)	593	—	1.3	—	131	—	339
Cu140	ITO/PEDOT:PSS/[Cu(P [^] P)(N [^] N)][PF ₆]:[Emim][PF ₆]	582	—	4.5	2.3	451	1.8	343
Cu134	4:1 molar ratio/Al L	588	—	0.7	0.4	33	0.30	
Cu139		570	—	4.6	2.0	462	1.7	
Cu135		589	—	1.3	0.9	130	1.20	
Cu138		571	—	1.8	0.6	92	0.6	
Cu136		585	—	0.1	0.1	13	0.05	
Cu141		580	—	1.7	0.7	87	1.1	
Cu137		586	—	0.3	0.2	34	0.15	
Cu142	ITO/PEDOT:PSS (40 nm)/EML:LiBF ₄ (80 nm)/Al	—	—	1.7	—	169	0.65	235
Cu143		—	—	2.2	—	223	0.84	
Cu3		—	—	4.5	—	452	1.85	
Cu145		—	—	N/A	—	2	N/A	
Cu146		—	—	1.1	—	108	0.45	
Cu148	ITO/PEDOT:PSS (70 nm)/active layer (80–100 nm)/Al	523	(0.26, 0.38)	0.02	0.03	6	0.01	344
Cu149	(90 nm)	562	(0.38, 0.53)	0.35	0.11	117	0.13	
Cu151		577	(0.49, 0.49)	0.04	0.03	10	0.02	
Cu152	ITO/PEDOT:PSS(80 nm)/CBP (25 nm)/Cu152(90 nm)/Al	500	—	1.2	—	160	—	345
	(90 nm)	—	—	—	—	—	—	

In 2017, several highly luminescent cyclometalated Au(III) complexes (**Au45–52**; Scheme 5), containing aryl ligand were reported by Che *et al.*, so that among Au(III) complexes, these complexes exhibit the highest PLQY both in solution and thin-films (0.79 and 0.84 respectively).³¹⁰ Furthermore, the origination of TADF in some of them that attributed to small ΔE_{ST} of 200–500 cm⁻¹ which was confirmed by variable temperature-emission lifetime measurements and DFT calculations, were attributed to the existence of amino group on the ancillary aryl ligand. A plausible explanation for the detection of ³IL emission rather than TADF in **Au50** (Scheme 5) could be attributed to the significantly lower energy level of the ³IL excited state compared to the ¹LLCT and ³LLCT excited states. This disparity in energy levels is attributed to the substantial exchange energy for the localized IL excited state, thereby leading to emission originating from the ³IL state. When Au(III) aryl emitters (**Au46** and **Au49**; Scheme 5) were tested in solution-processed OLEDs, the sky-blue to green electroluminescence with EQEs, luminance and current efficiencies up to 23.8%, 57 340 cd m⁻² and 70.4 cd A⁻¹ respectively, were obtained – Fig. 27.

It has been shown that increasing the chelating features of the ligands can improve the stability of metal complexes and metal–ligand bond strength. Therefore, tetradentate ligands

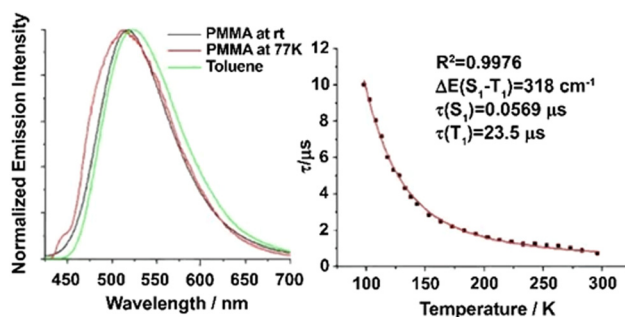


Fig. 27 Emission spectra and lifetime data of **Au49**. (left) Emission spectra of the complex (4 wt%) in PMMA thin-film at rt and 77 K, and in toluene at rt. (right) Plot of emission lifetime monitored at 517 nm against temperature and fitting of the data (red line) to the equation for TADF. Reproduced with permissions from ref. 310. Copyright 2017, Wiley-VCH.



are thought to have the ability to induce greater thermal stability and to inhibit structural distortion of complex in the excited state.

The increasing the rigidity of emitters can repress the structural distortion of complex during S_1 - T_1 transformation. Thus, it decreases the activation energy barrier for reverse rISC, resulting in effective TADF. To this end, Zhou *et al.* reported tetradentate $[C^{\wedge}C^{\wedge}N^{\wedge}C]$ Au(III) complexes containing 5-5-6 membered chelate rings *via* microwave-induced C-H bond activation – **Au53–59**; Scheme 5.²²³ These Au(III) complexes showed robust PL with Φ of 0.94, which is attributed to three emission origins 3IL , 3ILCT and TADF, adjusted by modifying the nature and positions of substituents on the $C^{\wedge}C^{\wedge}N^{\wedge}C$ ligand. The emission mechanism of Au(III) complexes is TADF due to large k_r and short τ . The OLED devices constructed with these TADF emitters indicated EQEs of up to 25% and LT_{95} of up to 5280 h at 100 cd m^{-2} , which is 10 times more effective than tridentate emitters – Table 6.

Key parameters for the commercialization of OLEDs include high EQE_{\max} , minimal efficiency roll-offs, and extended operational lifetime at practical luminances. To meet these criteria simultaneously, maximizing the radiative decay rate constant (k_r) is essential. For a TADF emitter, achieving a large $S_1 \rightarrow S_0$ radiative decay rate constant (k_r^S) alongside a reduced $\Delta E(S_1-T_1)$ is crucial. Several new tetradentate TADF Au(III) complexes (**Au60–63**; Scheme 5) has been designed to narrow the $\Delta E(S_1-T_1)$ while maintaining a high k_r^S . They exhibit green emission with nearly unity PLQY and a k_r approaching $2 \times 10^6\text{ s}^{-1}$ in thin-films. Green OLEDs fabricated *via* vacuum deposition using complexes **Au60** and **Au63** achieved impressive EQE_{\max} of up to 24% and 27% with efficiency roll-offs of 5.5% and 2.2% at 1000 cd m^{-2} , respectively – Table 6. The EQE remain high even at $10\,000\text{ cd m}^{-2}$, reaching 19% (**Au60**) and 24% (**Au63**). Complex **Au60** demonstrates a remarkable long operational lifetime (LT_{90}) of 1820 hours at 1000 cd m^{-2} , representing one of the most stable TADF-OLEDs to date. The incorporation of a multiresonant-TADF emitter into the OLEDs has led to the realization of high-color-quality displays in the **Au60**-based device. This integration preserves the inherent narrowband emission of the multiresonant-TADF emitter while significantly enhancing the electroluminescent performance. Notably, these devices exhibit an impressive EQE_{\max} of up to 29.4%, reduced efficiency roll-offs, a maximum luminance of $170\,000\text{ cd m}^{-2}$, and a PE_{\max} of 122.5 lm W^{-1} – Table 6. The exceptional performance of these tetradentate Au(III)-TADF emitters highlights their potential as leading contenders for the development of high-efficiency and operationally stable OLEDs, driving sustainable advancements in display technologies.³¹¹

A rare example of Au-complexes, which can be used in next-generation displays and lighting technologies, are donor-acceptor Au(III) acetylide emitters with strong thermal stability and luminescence – **Au64–69**; Scheme 5.²¹⁶ Owing to the stabilized LUMO of the 2,6-bis(4-(*tert*-butyl)phenyl)pyrazine in complex **Au68**, their absorption bands are red-shifted compared with those including di-deprotonated 2,6-bis(2,4-difluorophenyl)pyridine. Moreover, amino-substituted **Au3**

and **Au65–69** complexes showed wide emission band with color from green to red emission and high PLQYs of up to 60% relative to complex **Au64** – Table 11. The investigation in thin-film and DFT/TD-DFT proved that decay occurs through TADF mechanism with PLQY up to 88% and emission $\tau \approx 1\text{--}2\text{ }\mu\text{s}$ at ambient temperature. OLED based on device fabricated with **Au67** indicated an EQEs reaching 23.4% and luminance of $70\,300\text{ cd m}^{-2}$ – Table 6.

Several novel Au(III) complexes (**Au70–76**; Scheme 5) have been successfully developed and prepared, featuring tetradentate $C^{\wedge}C^{\wedge}N^{\wedge}N$ ligands with acridinyl groups that exhibit TADF. These complexes emit in orange-red to deep-red hues through incorporation of different substituents onto the acridinyl and pyridine units, exhibiting high PLQYs of up to 0.76 in thin-films. Notably, they demonstrate short τ of $\leq 2.0\text{ }\mu\text{s}$ and significant k_r on the order of 10^5 s^{-1} – Table 7. High-performance OLEDs have been successfully fabricated using these complexes, both through solution processing and vacuum deposition. The resulting devices show exceptional EQE_{\max} of 12.2% and 12.7%, respectively – Table 6, ranking among the highest reported values for red-emitting Au(III)-based OLEDs. Moreover, these red-emitting devices exhibit satisfactory operational half-lifetime (LT_{50}) values reaching up to 34 058 hours. The operational lifetimes of these devices is strongly influenced by the functional groups attached to the acridinyl units. Incorporating –O– and –S– linkers has been shown to significantly extend the LT_{50} value by an order of magnitude. The TADF characteristics of the complexes are further supported by the blue shifted emission band and the notable increased emission intensity as the temperature rises. Estimates suggest that there are small ΔE_{ST} , with values of approximately 1000 cm^{-1} observed in toluene and the solid state, respectively. Temperature-dependent ultrafast TA investigations have confirmed the TADF of these complexes, revealing rISC and providing the activation parameters for the first time, shedding light on their excited-state dynamics.²²¹

Several novel Au(III) complexes with tetradentate $C^{\wedge}C^{\wedge}N^{\wedge}N$ ligands containing pyridine and pyrazine have been formulated and prepared (**Au77–82**; Scheme 5) to exhibit TADF. These complexes featured high PLQYs of up to 0.77 in thin-films – Table 7. In toluene and doped mCP thin-films, their enhanced thermal emissions revealed hypsochromic spectral shifts of approximately $403\text{--}1371\text{ cm}^{-1}$ along with significantly reduced τ values. Utilizing TA spectroscopy, the direct observation of rISC processes enabled the determination of activation parameters. In the solution state, the k_r was analyzed using the Boltzmann two-level model, yielding estimated ΔE_{ST} of approximately $1290\text{--}1452\text{ cm}^{-1}$ for **Au77**, **Au79**, and **Au81**. By altering the electron-donating –*t*Bu substituent in the cyclometalating ligand to influence the host-guest interactions and molecular anisotropy, the permanent dipole moments of the complexes in **Au77–80** (Scheme 5) were adjusted to increase the TDMVs' θ_h enhancing the out-coupling efficiency (η_{out}) in the OLEDs. Consequently, more horizontal-orientated complexes **Au79** and **Au80** were applied in vacuum-deposited OLEDs reaching promising electroluminescent performance of EQE_{\max} of up to



Table 11 Photophysical and TADF characteristics of LEC based on Cu complexes

Complex	Medium	λ_{em} [nm]	Φ_{PLQY} [%]	τ_{exp} [μs]	k_{r} [s^{-1}]	k_{nr} [s^{-1}]	ΔE_{ST} [cm^{-1}]	Ref.
Cu6	Powder ^a	581 ^b	3.0 ^b	1.5 ^b	—	—	—	339
Cu108		587 ^b	1.7 ^b	1.3 ^b				
Cu109		575 ^b	6.2 ^b	2.9 ^b				
Cu110		581 ^b	11.1 ^b	2.9 ^b				
Cu111		648	0.5 ^c	0.185 ^c				
Cu112		647	0.5 ^c	0.251 ^c				
Cu113		664 ^c	0.5 ^c	0.096 ^c				
Cu114		632 ^c	0.9 ^c	0.579 ^c				
Cu117		517 ^b	50.3 ^b	12 ^b				
Cu115		547 ^b	33.8	9.6 ^b				
Cu116		539 ^b	37.3 ^b	11.4 ^b				
Cu6	Me-THF at 77 K	610	—	16	—	—	—	339
Cu108		613		11				
Cu109		610		45				
Cu110		595		31				
Cu111		656		—				
Cu112		646		—				
Cu113		650		3				
Cu114		652		5				
Cu117		604		42				
Cu115		567		46				
Cu116		551		88				
Cu6	CH ₂ Cl ₂ ^d solution	618, 649 ^d	0.4/0.5	43/46	—	—	1428	339
Cu108		620, 650 ^d	0.5/0.5	75/104			1492	
Cu109		618, 646 ^d	0.7/0.7	95/119			968–1613	
Cu110		622, 647 ^d	0.6/0.6	84/99			968–1613	
Cu111		—	—/—	—/—			968–1613	
Cu112		—	—/—	—/—			968–1613	
Cu113		667, 697 ^a	—/—	—/—			1524	
Cu114		667, 705 ^a	—/—	—/—			1589	
Cu117		612, 637 ^d	0.5/0.5	39/39			887	
Cu115		605, 635 ^d	1.0/1.8	27/78			968–1613	
Cu116		606, 635 ^d	1.6/10.0	451/3406			968–1613	
Cu118	Solution	613, 640 ^e	<1	0.204	—	—	—	340
Cu119		613, 641 ^f	<1	0.253				
Cu120		610, 641 ^g	1	0.277				
Cu121		613, 639 ^e	<1	0.334				
Cu122		605, 635 ^e	<1	0.259				
Cu123		606, 630 ^h	<1	0.258				
Cu124		609, 637 ^h	<1	0.231				
Cu125		610, 633 ^g	1	0.279				
Cu126		608, 635 ^e	<1	0.313				
Cu127		608, 632 ^e	1	0.315				
Cu128		605, 630 ^e	<1	0.280				
Cu129		603, 629 ^e	1	0.30				
Cu118	Solution at 77 K	599	5	21	—	—	—	340
Cu119		596	6	28				
Cu120		613	3	16				
Cu121		563	10	48				
Cu122		598	9	31				
Cu123		600	7	33				
Cu124		593	11	23				
Cu125		594	15	23				
Cu126		610	11	13				
Cu127		588	20	38				
Cu128		575	20	38				
Cu129		576 ^b	23	44				
Cu118	Powder	565	17	3.3	—	—	—	340
Cu119		570	9	2.7				
Cu120		585	5	1.5				
Cu121		549	30	10.2				
Cu122		564	22	6.5				
Cu123		566	20	6.2				
Cu124		566	19	4.7				
Cu125		566	22	4.0				
Cu126		572	12	2.7				
Cu127		557	21	6.0				
Cu128		552	32	6.5				
Cu129		552 ^b	38	9.1				



Table 11 (continued)

Complex	Medium	λ_{em} [nm]	Φ_{PLQY} [%]	τ_{exp} [μs]	k_{r} [s^{-1}]	k_{nr} [s^{-1}]	ΔE_{ST} [cm^{-1}]	Ref.
Cu118	Film	—	4	—	—	—	—	340
Cu119			5					
Cu120			5					
Cu121			5					
Cu122			5					
Cu123			7					
Cu124			6					
Cu125			7					
Cu126			6					
Cu127			5					
Cu128			6					
Cu129			7					
Cu134	CH_2Cl_2 solution ⁱ (non-deaerated/deaerated)	622, 643	0.5/0.7 ^k	0.057/ 0.108 ^k	$8.8 \times 10^4/6.5 \times 10^4$	$1.7 \times 10^7/9.2 \times 10^6$	—	343
Cu135		616, 642	0.4/0.9 ^k	0.153/ 0.338 ^k	$2.6 \times 10^4/2.7 \times 10^4$	$6.5 \times 10^6/2.9 \times 10^6$		
Cu136		614, 648 ^j	0.5/0.5 ^k	0.039/ 0.045 ^k	$1.3 \times 10^5/1.1 \times 10^5$	$2.6 \times 10^7/2.2 \times 10^7$		
Cu137		615, 632 ^j	0.4/0.5 ^k	0.076/ 0.093 ^k	$5.3 \times 10^4/5.4 \times 10^4$	$1.3 \times 10^7/1.1 \times 10^7$		
Cu138		598, 630	1.0/1.5 ^k	0.202/ 0.730 ^k	$5.0 \times 10^4/2.1 \times 10^4$	$4.9 \times 10^6/1.3 \times 10^6$		
Cu139		582, 627	0.9/3.3 ^k	0.228/ 1.595 ^k	$3.9 \times 10^4/2.1 \times 10^4$	$4.3 \times 10^6/6.1 \times 10^5$		
Cu140		597, 629	0.8/6.0 ^k	0.240/ 2.401 ^k	$3.3 \times 10^4/2.5 \times 10^4$	$4.1 \times 10^6/3.9 \times 10^5$		
Cu141		583, 626	0.9/9.6 ^k	0.262/ 4.987 ^k	$3.4 \times 10^4/1.9 \times 10^4$	$3.8 \times 10^6/1.8 \times 10^5$		
Cu134	Powder ^k	585	2.7	2.3	11.7×10^9	423.0×10^9	—	343
Cu135		571	6.3	5.1	12.4×10^9	183.7×10^9		
Cu136		602	1.1	0.4	27.5×10^9	2472.5×10^9		
Cu137		556	9.6	3.3	29.1×10^9	273.9×10^9		
Cu138		518	42.7	9.3	45.9×10^9	61.6×10^9		
Cu139		529	58.8	9.8	60.0×10^9	42.0×10^9		
Cu140		558	27.5	8.7	31.6×10^9	83.3×10^9		
Cu141		550	9.8	10.2	9.6×10^9	88.4×10^9		
Cu142	Dilute degassed solutions (<i>ca.</i> 10^{-5} M)	550	71	—	—	—	1532	235
Cu143		549	40				1452	
Cu3		567	60				1613	
Cu144		547	<1				1532	
Cu145		543	1				1532	
Cu146		541	98				1613	
Cu147		431	<1				1452	
Cu148	Powder 298 K (77 K)	480 (490) ^l	17	24.7 (198.4) ^l	0.7×10^4	3.4×10^4	951	386
Cu149		551 (549) ^l	14	7.31 (982.4) ^l	1.9×10^4	11.8×10^4	773	
Cu150		546 (537) ^l	<1	11.2 (155.6) ^l	0.1×10^4	8.8×10^4	588	
Cu151		574 (584) ^l	38	3.0 (244.1) ^l	12.7×10^4	20.7×10^4	500	
Cu148	Thin-film 298 K (77 K)	497 (493) ^l	8	15.2 (177.0) ^l	0.5×10^4	6.0×10^4	—	344
Cu149		540 (537) ^l	10	61.9 (781.0) ^l	0.2×10^4	1.5×10^4	—	
Cu150		546 (537) ^l	<1	7.5 (160.3) ^l	0.1×10^4	1.3×10^4	—	
Cu151		580 (571) ^l	21	47.6 (944.0) ^l	0.4×10^4	1.7×10^4	—	

^a Solution concentration = 5.0×10^{-5} mol dm⁻³. ^b λ_{exc} = 365 nm. ^c λ_{exc} = 405 nm. Deaeration was by flow of argon. ^d Solution concentration = 2.5×10^{-5} mol dm⁻³. ^e λ_{exc} = 420 nm. ^f λ_{exc} = 400 nm. ^g λ_{exc} = 410 nm. ^h λ_{exc} = 390 nm. ⁱ Solution concentration = 2.5×10^5 mol dm⁻³. ^j Solution concentration = 5.0×10^5 mol dm⁻³. ^k λ_{exc} = 365 nm. ^l At 298 K (77 K).

15.7% and strongly improved η_{out} by $\sim 30\%$, compared to their regioisomers, **Au77** and **Au78** – Table 6 the based on the more horizontal-orientated complexes **Au79** and **Au80** showed improvements in η_{out} by $\sim 30\%$, compared to their regioisomers, **Au77** and **Au78** and exhibited promising electroluminescent performance, achieving EQE_{max} of up to 15.7% – Table 6. Introducing a *-t*Bu substituent to the carbazoyl groups not only enhanced the operational stability of the OLEDs, but also facilitated horizontal molecular orientation. This study shows the potential of the *-t*Bu substituent in optimizing Au(III) C[∧]C[∧]N[∧]N systems for the advancement of efficient

Au(III)-based OLEDs, offering valuable insights for further development efforts.³¹²

Several novel carbazoyl Au(III) dendrimers containing C[∧]C[∧]N ligands (**Au83–85**; Scheme 5) has been developed and synthesized. Exceptionally high PLQY reaching up to 82% in thin-films, along with large radiative decay rate constants on the order of 10^5 s⁻¹, have been observed – Table 7. These Au(III) dendrimers demonstrate TADF, supported by time-resolved photoluminescence decay and computational investigations, with estimated ΔE_{ST} values of *ca.* 32 cm⁻¹. OLEDs based on these Au(III) dendrimers were successfully fabricated *via*



solution processing. These OLEDs achieved current efficacies of 52.6 cd A^{-1} , EQE_{max} of 15.8%, and substantial power efficiency of 41.3 lm W^{-1} – Table 6. Furthermore, the operational stability of these OLEDs was evaluated, revealing remarkable results. The devices utilizing zero- and second-generation dendrimers showed maximum half-lifetimes of 1305 and 322 h at 100 cd m^{-2} , respectively. This pioneering work demonstrates the application of Au(III) dendrimers in operationally stable solution-processed OLEDs.³¹³

Several new carbazolyl ligands have been synthesized by incorporating various electron-donating and electron-accepting group at the 2- and 3-positions of the ancillary ligand, such as 4-(diphenylamino)aryl, cyano, and diphenylphosphine oxide, to create a novel class of Au(III) complexes (**Au86–91**; Scheme 5). They are designed to tune the energies of their triplet intraligand and LLCT excited states to enable TADF. This can effectively reduce the τ in the Au(III) complexes by more than two orders of magnitude from $\sim 80 \text{ ms}$ to 0.8 ms . Upon excitation, these complexes exhibit high PLQYs of up to 80% in thin-films, with short τ as low as 1 ms . OLEDs based on these complexes, fabricated using both vacuum deposition and solution processing methods, display promising electroluminescent performance – Table 6. These devices achieve EQE_{max} of 15.0% and 11.7%, respectively. Importantly, the suppression of the roll-off in solution-processed devices can be notably reduced when TADF is utilized. Specifically, the roll-off decreases from 65% in phosphorescence-based devices (**Au86**) to just 1% in TADF-based devices (**Au89**), achieving this improvement at a practical brightness level of 1000 cd m^{-2} . The superior electroluminescent characteristics are attributed to the presence of multichannel radiative decay pathways through both phosphorescence and TADF mechanisms, which effectively reduce emission lifetimes and mitigate the adverse effects of triplet–triplet annihilation in the Au(III) complexes.³¹⁴

3.1.3. Cu- and Ag-complexes. As explained in Section 2, the photophysical properties of heteroleptic heteroleptic Cu(I) complexes have been widely studied and thus, they constitute the most representative family of OLEDs based on metal complex TADF emitters.^{180,249–252,258–262} Not surprising, the $\text{EQE} > 23\%$ for OLEDs with TADF Cu(I) complexes is close to the efficiency of OLEDs based on Ir(III) complex emitters, highlighting the interest of this family of emitters.³¹⁸ In this respect, Table 8 summarizes the most important Cu(I) complexes reported in literature, including the OLED device architecture, in which they have been used, as well as the corresponding device metrics. As a complement to Section 2, the photophysical and TADF properties of OLEDs with all the discussed complexes is also summarized in Table 9.

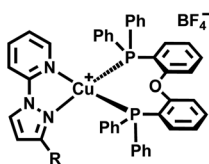
Due to the importance of developing blue-emitting OLEDs, a number of cationic Cu(I) complexes with excellent greenish-blue to blue emission based on POP and N-linked 2-pyridyl pyrazolate diimine ligands, *e.g.*, $[\text{Cu}(\text{pypz})(\text{POP})]\text{BF}_4$ (**Cu29**), $[\text{Cu}(\text{pympz})(\text{POP})]\text{BF}_4$ (**Cu30**), and $[\text{Cu}(\text{pytfmpz})(\text{POP})]\text{BF}_4$ (**Cu31**) (pypz = 1-(2-pyridyl)pyrazole, pympz = 3-methyl-1-(2-pyridyl)pyrazole, and pytfmpz = 3-trifluoromethyl-1-(2-15 pyridyl)pyrazole) were synthesized and characterized – Scheme 6.³¹⁷

The HOMO–LUMO energy gap is adjustable to obtain blue light emission.³⁴⁶ The electron donating capability of the pypz ligand led to the increase of the HOMO–LUMO energy gap and the shift of the emissions to the blue region through the instability of the LUMO level of the luminescent dopant substances. In addition, different substituents such as CH_3 and CF_3 on the pyrazole ring of 2-pyridyl pyrazolate ligands were used to adjust the emission efficiencies and colors of the related Cu(I) complexes. The dependence of emission decay time on spectroscopic properties under different temperature was an interesting phenomenon in these complexes.³¹⁷ The application of these complexes as dopants with various hosts in solution-processed OLEDs showed the values of 23.68 cd A^{-1} for efficiency and 2033 cd cm^{-2} for peak brightness for **Cu31** as dopant and 2,6-mCpy as host – Table 8.³¹⁷ Effective confinement of triplet excitons and charge carriers led to these performances. Conversely, the nearly equal LUMO level of the 2,6-mCpy host and dopants of **Cu29** or **Cu30** results in relatively low efficiencies of OLEDs made of **Cu29** and **Cu30**.³¹⁷

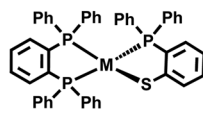
Several neutral d^{10} metal complexes containing tetrahedral structures, $[\text{Cu}(\text{PP})(\text{PS})]$ (**Cu32**), $[\text{Ag}(\text{PP})(\text{PS})]$ (**Ag16**), and $[\text{Au}(\text{PP})(\text{PS})]$ (**Au14**), containing two bidentate ligands [PS^- = 2-diphenylphosphinobenzenethiolate] and [PP = 1,2-bis(diphenylphosphino)benzene] have been also investigated – Scheme 6.³¹⁵ In accordance with molecular orbital calculations, the electron-donating property of the PS ligand decreases the participation of metal orbitals in the HOMOs, impeding an efficient MLCT of their excited states and the TADF of metal(I) complexes associated with LLCT transition. Despite the high thermal stability of **Cu32**, **Ag16** and **Au14**, (decomposition temperatures above 300°C), the negligible vapor pressure up to thermal decomposition of mentioned complexes hampers their vacuum deposition for the realization of emitting films. Thus, the latter have been realized through wet processes. Fig. 28 illustrates the emission spectra of complexes **Cu32**, **Ag16** and **Au14** at 77 and 293 K as well as the electroluminescence spectra and dependence of the EQE on the current density for OLEDs containing **Cu32** as a dopant. According to these data, **Cu32** exhibits an efficient green TADF that was successfully exploited in OLEDs. Contrary to **Cu32**, the rapid ligand exchange reaction in case of **Au14** causes its instability in solution, while the low solubility of **Ag16** in organic solvents restricts its use as luminescent guest molecules.

Binuclear Cu(I) complexes based on N-heterocyclic phosphine were also applied to OLEDs. They consist of a Cu_2I_2 moiety with a butterfly-like structure as shown in **Cu33** – Scheme 6, featuring two ancillary phosphine ligands and an N,P-ligand bridge.³¹⁸ Air stability and lower ΔE_{ST} (200 meV) than similar green emitting Cu-compounds are the most relevant features.³⁴⁷ Four-fold bridged Cu(I) centers in this dinuclear Cu(I) complex led to its high thermal stability ($T_d = 290^\circ\text{C}$), which was another advantage of this dinuclear complex. The use of this multi-bridge dinuclear Cu(I) complex as a TADF emitters in OLEDs with an EQE of 23% (Table 8), due to its distinct structure, high processability, high PLQY in PYD2-doped films and low ΔE_{ST} . This value is close to the

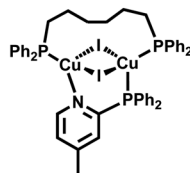




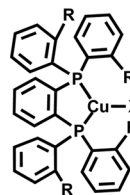
Cu29: R = H
Cu30: R = CH₃
Cu31: R = CF₃



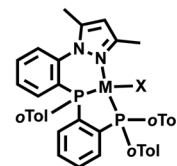
Cu23
Ag16



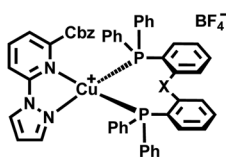
Cu33



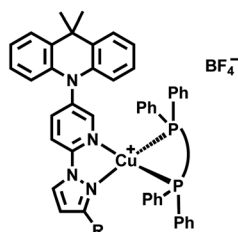
Cu34: R = CH₃, X = Cl
Cu35: R = CH₃, X = Br
Cu36: R = CH₃, X = I
Cu37: R = Et, X = Br
Cu38: R = ⁱPr, X = Br



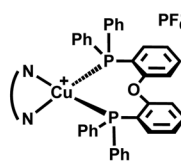
Cu39: X = Br
Cu40: X = I



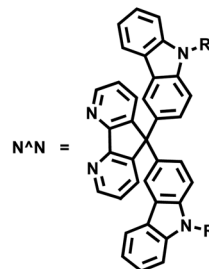
Cu41: X = H
Cu42: X = O



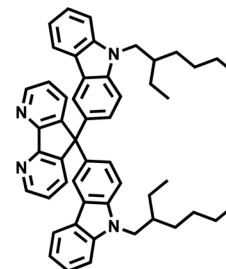
Cu43: P^P = DPEphos
Cu44: P^P = xantphos



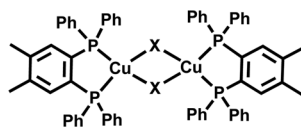
Cu45: N^N = 1
Cu46: N^N = 2
Cu47: N^N = 3



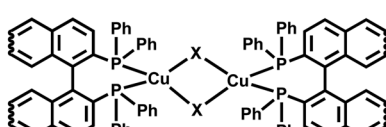
1: R = Et
3: R = Ph



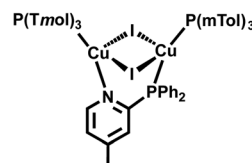
2



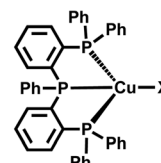
Cu48: X = I
Cu49: X = Br
Cu50: X = Cl



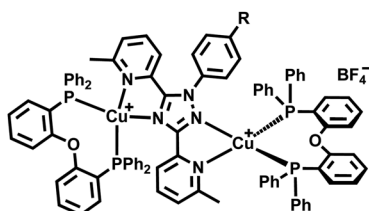
Cu51: X = Cl
Cu52: X = Br
Cu53: X = I



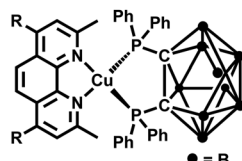
Cu54



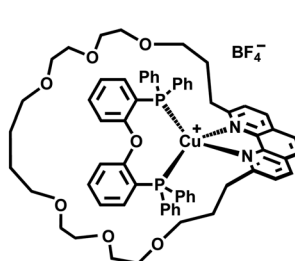
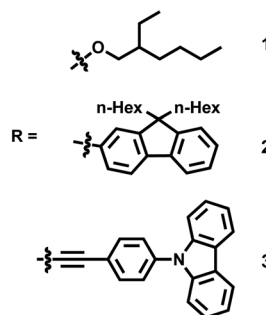
Cu55: X = Cl
Cu56: X = Br
Cu57: X = I



Cu58: R = H
Cu59: R = CF₃
Cu60: R = Cbz

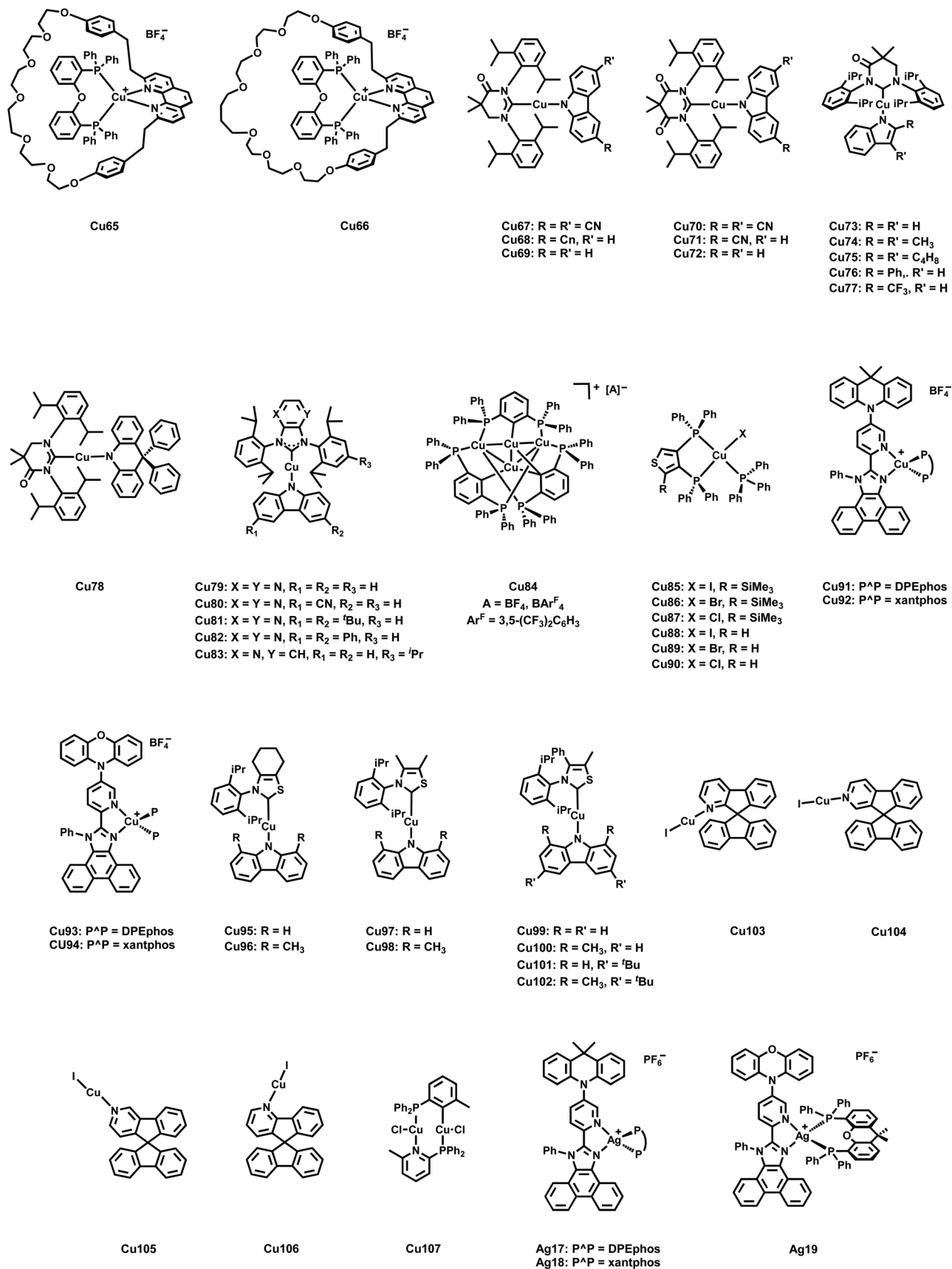


Cu61: R = 1
Cu62: R = 2
Cu63: R = 3



Cu64





Scheme 6 Molecular structures of Cu29–107 and Ag16–19.



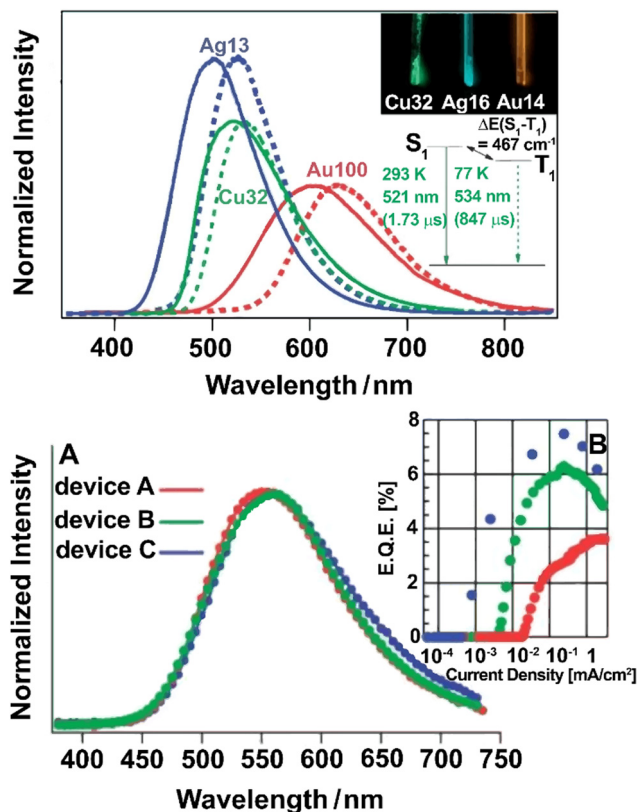


Fig. 28 (a) Corrected emission spectra of **Cu32** (green), **Ag16** (blue), and **Au14** (red) in the solid state at 293 (solid lines) and 77 (dashed lines) K; $\lambda_{\text{ext}} = 310$ nm. The upper inset shows luminescence images of **Cu32**, **Ag16** and **Au14** at 293 K; $\lambda_{\text{ext}} = 354$ nm. The lower inset shows a two-state model for **Cu32**. (b) Properties of OLEDs [device A (red), B (green), and C (blue)] containing **Cu32** as a dopant. (A) electroluminescence spectra, (B) dependence of EQE on current density. Reproduced with permissions from ref. 315. Copyright 2013, Royal Society of Chemistry.

high-performance EQE of devices under vacuum made of Ir(III) complexes. For the sake of completeness, **Cu33**-based OLEDs are demonstrated that the device indicates a pronounced roll-off of the current efficiency as luminance increases. Imbalance of charge leads to this behavior because hole transport occurs through the emitter itself rather than through the host material. In general, the progression of a novel generation of TADF-based OLEDs using the concept of multi-bridged binuclear Cu(I) complex is being explored as a new paradigm shift.

By considering the dependence of k_{nr} and PLQYs on the structural distortions of tetrahedral Cu(I) complexes in the excited state – Section 2, several highly luminescent Cu(I) complexes with a three-coordinate structure without any structural modification in the excited state, $(\text{L}_{\text{Me}})\text{CuX}$ [$\text{X} = \text{Cl}$ (**Cu34**), Br (**Cu35**), I (**Cu36**)], $(\text{L}_{\text{Et}})\text{CuBr}$ (**Cu37**), and $(\text{L}_{\text{IPr}})\text{CuBr}$ (**Cu38**) with bidentate bisphosphine ligands [$\text{L}_{\text{Me}} = 1,2$ bis[bis(2-methylphenyl)phosphino]benzene, $\text{L}_{\text{Et}} = 1,2$ -bis[bis(2-ethylphenyl)phosphino]benzene, and $\text{L}_{\text{IPr}} = 1,2$ -bis[bis(2-isopropylphenyl)phosphino]benzene] were introduced – Scheme 6.³¹⁹ In these complexes, the molecular motions were limited by the presence of varied *ortho*-substituents on the peripheral phenyl moieties.

Furthermore, in complexes **Cu34–38** – Scheme 6, the emission arises from $(\sigma + \text{X}) \rightarrow \pi^*$ (diphosphine ligand) transition. The presence of alkyl substituents at the *ortho* positions of the peripheral phenyl moieties was determined to have a marginal impact on the electronic excited states. Since the emission of complexes **Cu34–38** is associated to a $(\sigma + \text{X}) \rightarrow \pi^*$ (diphosphine ligand) transition, the photoluminescent characteristics of these complexes are predominantly determined by the diphosphine ligands. Fig. 29 shows their electroluminescence characteristics. The TADF-type OLEDs based on complexes **Cu34–38** exhibited a green luminescence with high EQE values ranging from 18.6 to 22.5% – Table 8.

In this line, Pflaum and colleagues recently presented the synthesis of enantiomerically pure $\text{Cu}(\text{CbzR})[(S/R)\text{-BINAP}]$ [$\text{R} = \text{H}$ (**Cu19**), 3,6-*t*Bu (**Cu20**)] as highly effective TADF emitters (Scheme 3) with impressive radiative rate constants (k_{DF}) close to $3.1 \times 10^5 \text{ s}^{-1}$ originating from $^1/3\text{LLCT}$ states, as confirmed by temperature-dependent time-resolved luminescence experiment as well as CPL signal. They exhibit strong C–H $\cdots\pi$ interactions between the ligands and neighboring molecules. For instance, in single crystalline solid state, a dominant phosphorescent component was observed from $^3\text{LLCT/Cbz}$ states with maximum peak wavelengths of 564 nm for (**Cu19**) and 549 nm for (**Cu20**). However, highly efficient TADF was achieved by grinding complexes. As a result, k_{r} to $3.1 \times 10^5 \text{ s}^{-1}$ and a shift in the emitting $^1/3\text{LLCT}$ states to $\lambda_{\text{max}} = 579$ (**Cu19**) and 606 (**Cu20**) nm was gained – Table 9. The choice of matrix

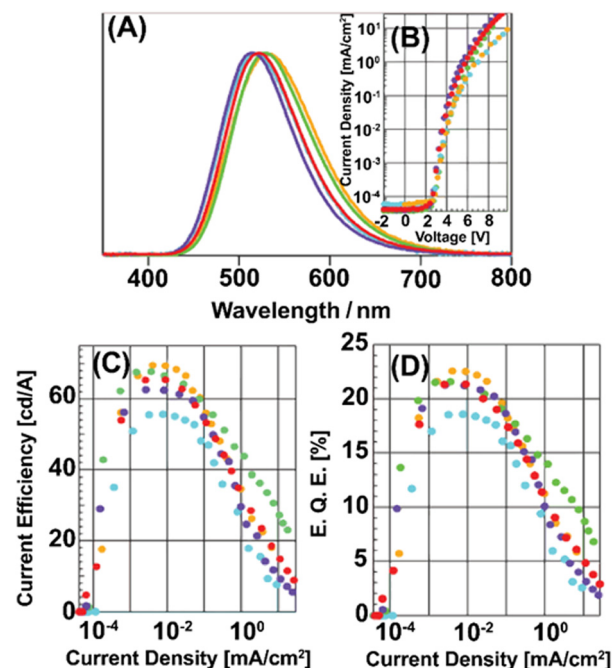


Fig. 29 Properties of OLEDs containing complex **Cu34** (green line), complex **Cu35** (red line), complex **Cu36** (purple line), complex **Cu37** (orange line) and complex **Cu38** (blue line). (A) Electroluminescence spectra; (B) the dependence of the EQE on the current density; (C) I – V characteristics; (D) the dependence of the current efficiency on the current density. Reproduced with permissions from ref. 319. Copyright 2015, Royal Society of Chemistry.

material for fabrication of device is strongly influenced by intermolecular hydrogen bonding on excited state energies. The emission shift to the green region of the electromagnetic spectrum by polar and sterically unprotected mCP or PMMA results in significant decline in k_r to $<5 \times 10^4$ for **Cu19** and $<0.5 \times 10^4 \text{ s}^{-1}$ for **Cu20** – Table 9. Retention of outstanding TADF characteristics of Cu(i) complexes at lower emission energies is achieved by using nonpolar UGH-3 or bulk CzSi. The asymmetry values (g_{lum}) for CPL of $\pm 6 \times 10^{-3}$ (**Cu19**) and $\pm 5 \times 10^{-3}$ (**Cu20**) in solution, and $\pm 1.7 \times 10^{-2}$ (**Cu19**) and $\pm 2.1 \times 10^{-2}$ (**Cu20**) in the solid state are due to the notable rotational strength of the electronic transitions arising from the chirality of the emitter molecules. These findings highlight the importance of careful device design in achieving efficient generation of Circularly Polarized Electroluminescence (CP EL).²⁵¹

Neutral Cu(i) and Ag(i) complexes have also been synthesized using a novel rigid tridentate N,P,P ligand called dmpzpp, 3,5-dimethyl-1-(2-((2-(di-*o*-tolyl)-phosphanyl) (*o*-tolyl)-phosphanyl)phenyl)-1*H*-pyrazole. The complexes include Cu(dmpzpp)Br (**Cu39**), Cu(dmpzpp)I (**Cu40**), Cu(dmpzpp)SPh (**Cu11**) (SPh refers to thiophenylato) – Scheme 6. **Cu11**, which has bulky ligands and shows PLQY = 90% – Table 9, was specifically studied for emission properties in the range of 1.7 to 300 K. At temperatures up to approximately 70 K, **Cu11** exhibits only long-lived phosphorescence with a $\tau = 1 \text{ ms}$, attributed to weak SOC. The zero-field splitting of T_1 in the three substrates are less than 1 cm^{-1} . The phosphorescence is primarily caused by spin-vibronic mechanisms, as indicated by estimated individual decay times of 2400, 2250, and 292 μs . As the temperature increases up to 300 K, the significantly reduction in radiative decay time by more than two orders of magnitude to $\tau_{\text{DF}} = 5.6 \mu\text{s}$ was observed. This was attributed to TADF. This rapid decay time is influenced by the small ΔE_{ST} of 600 cm^{-1} or 74 meV and a fast radiative S_1 to S_0 transition rate = $1.1 \times 10^7 \text{ s}^{-1}$ (equivalent to 91 ns). To fabricate OLEDs, **Cu40** and **Cu11** were used in cohost device structures. For instance, a green emitting OLED with 2 wt% concentration of **Cu40** was constructed which showed values of (0.33, 0.52) for CIE coordinates, 16.4% for EQE and nearly $10\,000 \text{ cd m}^{-2}$ – Table 8.²³¹

Two highly efficient complexes, [Cu(czpzy)(PPh₃)]BF₄ (**Cu41**) and [Cu(czpzy)(POP)]BF₄ (**Cu42**) – Scheme 6, were prepared through the use of a novel diamine ligand based on Cz (czpzy) and two different types of phosphine-based ligand (PPh₃ and POP), in which czpzy = 2-(9*H*-carbazolyl)-6-(1*H*-pyrazolyl)pyridine, PPh₃ = triphenylphosphine.³²⁰ The Oak Ridge Thermal Ellipsoid Plot (ORTEP) diagrams of **Cu41** and **Cu42** are displayed in Fig. 30. The grafting the functional Cz group into the diamine ligand improves the light-emitting and hole-transporting properties of cuprous complexes. The TADF along with high PLQY close to 100% was achieved for **Cu42** at ambient temperature in thin-film – Table 9. In this approach, czpzy ligand has a dual role, *i.e.*, acting as a ligand to create the luminescent complex as well as a host for the formed emitter in OLEDs due to its effective hole-transporting capability and elevated triplet energy level. The associated

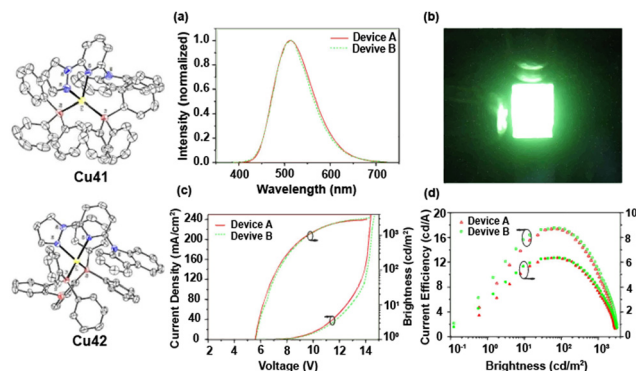


Fig. 30 ORTEP diagrams of **Cu41** and **Cu42** with thermal ellipsoids at 30% probability level. Solvent molecules, the anion, and H atoms are omitted for clarity. (a) Electroluminescence spectra (device a = **Cu41**, device b = **Cu42**); (b) photo of Device B; (c) current density–brightness (J – V – B) curves; (d) plots of EQE and current efficiency vs. brightness. Reproduced with permissions from ref. 320. Copyright 2015, Royal Society of Chemistry.

electroluminescence properties and quantitative results of **Cu42** are presented in Fig. 30.

Preparation of two bluish-green Cu(i) complexes [Cu(PNNA)-(POP)]BF₄ (**Cu43**) and [Cu(PNNA)(xantphos)]BF₄ (**Cu44**), (PNNA = 9,9-dimethyl-10-(6-(3-phenyl-1*H*-pyrazol-1-yl)pyridin-3-yl)-9,10-dihydroacridine) with a functionalized diimine and phosphine ligands were reported as TADF emitters – Scheme 6.³²¹ Here, the use of the donor segment, 9,9-dimethylacridan, on the diimine ligand was due to its excellent hole-transporting ability. Devices with **Cu44** as dopant showed the highest efficiency of $20.24 \text{ (cd A}^{-1}\text{)}$, brightness (5579 cd m^{-2}) and the bluest electroluminescence due to the properties of its rigid and bulky ligands – Table 8.

In classical tetrahedral heteroleptic Cu(i) complexes, three yellowish-green emitting cationic cuprous complexes [Cu(POP)-(ECAf)]PF₆ (**Cu45**), [Cu(POP)(EHCAF)]PF₆ (**Cu46**), and [Cu(POP)-(PCAF)]PF₆ (**Cu47**), based on POP along with the very bulky and bipolar ancillary ligands 9,9-bis(9-ethylcarbazol-3-yl)-4,5-diazafluorene (ECAf), 9,9-bis(9-ethylhexylcarbazol-3-yl)-4,5-diazafluorene (EHCAF), and 9,9-bis(9-phenylcarbazol-3-yl)-4,5-diazafluorene (PCAF), were investigated by the group of Zhang – Scheme 6.³²² Typically, ionic Cu(i) complexes must be processed using solution-based techniques. However the ancillary ligands decreases the lattice energies and weaken the electrostatic interaction, allowing the preparation of vacuum-evaporated OLEDs. In addition, the introduction of the 4,5-diazafluorene as electron-transporting and Cz moieties as hole-transporting causes bipolar charge-transporting abilities, balancing the charge carrier transport in the LEL, increasing the OLED performance. Due to the singlet harvesting, triplet harvesting and good thermal stabilities, the OLEDs exhibited a high electroluminescence brightness – $5152\text{--}11\,010 \text{ cd m}^{-2}$; Table 8.^{255,326,348,349}

Three novel effective blue-green neutral halogen-bridged dinuclear Cu(i) complexes constructed from a new bidentate 1,2-bis(diphenylphosphino)-4,5-dimethylbenzene (dpmb)



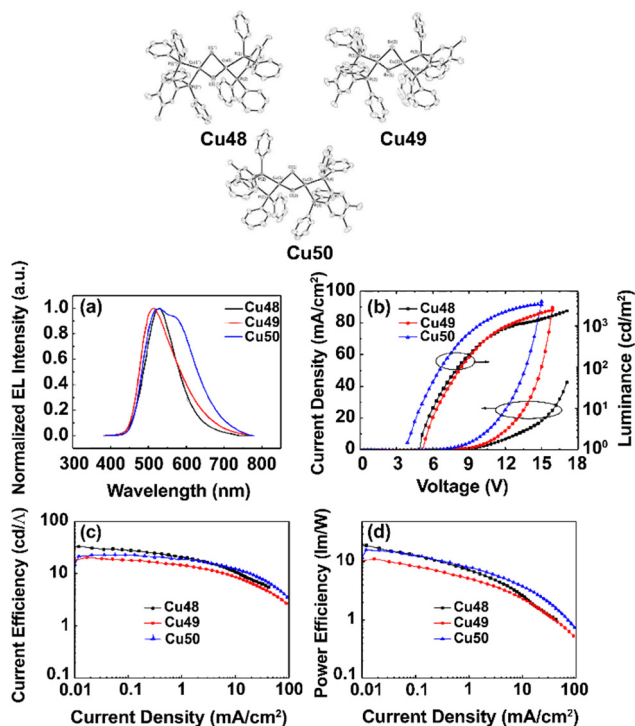


Fig. 31 ORTEP diagrams of complexes **Cu48–50**. (a) Electroluminescence spectra of devices **Cu48–50**; (b) current density–voltage–luminance characteristics (J – V – L) of devices **17–A3**; (c) EQE versus current density curves for devices **Cu48–50**; (d) power efficiency versus current density for devices **Cu48–50**. Reproduced with permissions from ref. 323. Copyright 2016, Elsevier.

ligand, $[\text{Cu}(\mu\text{-X})\text{dpmb}]_2$ ($\text{X} = \text{I}$ (**Cu48**), Br (**Cu49**), Cl (**Cu50**)) – Scheme 6, and possessing small ΔE_{ST} energy gaps ($954\text{--}1120\text{ cm}^{-1}$), were recently reported to investigate the impact of two *ortho*-methyl electron-donating groups on the diphosphine.³²³ Fig. 31 shows the ORTEP diagrams of complexes **Cu48–50**. The origin of the emission in **Cu48–50** are attributed to the $(\sigma + \text{X}) \rightarrow \pi^*$ transition, (σ is the Sigma bond between P and Cu). The methyl groups of these complexes significantly create a blue shift of the above transition energy, leading to a blue emission. When these complexes were used as the luminescent dopants with optimum concentration of 10% in TADF-type OLED devices fabricated by vacuum processes, bright green luminescence with EQE_{max} of 10.1% and current efficiencies of 32.9 cd A^{-1} were obtained for the case of complexes **Cu48** – Table 8. Fig. 31 shows the device characteristics of based on three complexes. The λ_{max} follow the sequence **Cu48** < **Cu49** < **Cu50**, aligning with the expected ligand field strengths of the halogen ions in the complexes ($\text{I}^- < \text{Br}^- < \text{Cl}^-$).³⁵⁰ Indeed, a slight blue shift for the electroluminescent peak wavelength of device **Cu48** compared to devices **Cu49** and **Cu50** was observed. In addition, the order of **Cu48** < **Cu49** < **Cu50** for the FWHM of the devices with each dopant is in line with the ligand field strength order of the halogen ions in the complexes. Probably, the improved electron injection to the EML causing a significant diminish in the turn-on and driving voltage of the device with **Cu50**. Furthermore, the relatively low efficiency of devices

with **Cu49** and **Cu50** indicates complete confinement of holes and electrons in the EML as well as effective suppression of current-induced exciton quenching because of the rather strong ligand field strength of the halogen ions in the complexes.

Similar to Pflaum *et al.* Zhou and co-workers successfully prepared three chiral Cu(I) chloro-bridged dimers, namely R/S -(BINAP) $_2\text{Cu}(\mu\text{-X})_2$ ($\text{X} = \text{Cl}$ (**Cu51**), Br (**Cu52**), and I (**Cu53**)) – Scheme 6, at room temperature within a short time of 10 min, with yields exceeding 95%. These dimers were based on R/S -2,2'-bis(diphenylphosphino)-1,1'-binaphthalene (R/S -BINAP) ligands showing high dissymmetry factors (g) surpassing 1×10^{-2} . Additionally, the small ΔE_{ST} and the overlap of theoretical frontier molecular orbitals led to TADF emission mechanism. Notably, when circularly polarized organic light-emitting diodes (CP-OLEDs) were fabricated using the evaporation method with R/S -(BINAP) $_2\text{Cu}(\mu\text{-I})_2$ (**Cu53**), a remarkable EQE_{max} of 21.7% was achieved – Table 8. Intriguingly, these CP-OLEDs also exhibited mirror-imaged CP EL with $|g_{\text{EL}}|$ close to 3.0×10^{-3} .³²⁴

As a final asset of this family of dinuclear Cu(I) complexes is the possibility to fabricate efficient inkjet-printed OLEDs. As leading example, a highly soluble Cu(I)-NHetPHOS TADF emitter was proposed.³²⁵ As for the case of dinuclear NHetPHOS-complexes, **Cu54** (Scheme 6) comprises a butterfly-shaped Cu_2I_2 moiety, a bridging N,P-ligand containing a nitrogen-with heterocycle (NHet), and two extra monodentate P-donors with tris-*m*-tolylphosphine, $\text{P}(m\text{Tol})_3$. The OLED with this complex yielded up to 11% EQE in large areas – Table 8.

In a related family of heteroleptic halogen-based Cu(I) complexes, the use of different halogens clearly allowed to balance dual emissions mechanisms (phosphorescence and TADF). In short, a set of mononuclear Cu(I) complexes TTPPCuX ($\text{X} = \text{Cl}$, Br , I); TTPP = tridentate phosphine ligand 2,2' (phenylphosphine-diyl)bis(2,1-phenylene) bis(diphenylphosphine) (**Cu55–57**; Scheme 6) with stable and rigid tetrahedral geometry were studied.³²⁶ The emission spectra of TTPPCuX at ambient temperature gradually blue-shifted by decreasing the ligand-field strength for X , from Cl , Br to I .²⁵³ Significantly, by considering the ΔE_{ST} and heavy atom effect for SOC improvement at ambient temperature, the activation of the $\text{T}_1 \rightarrow \text{S}_0$ transition, the balanced dual emissions with a significant phosphorescence fraction of 39%, PLQY of 85%, and ten-fold smaller triplet lifetime and about 50% larger k_{r} were obtained by TTPPCuI – Table 9. This lead to a EQE_{max} of 16.3% – Table 8, which is among the top values developed for OLEDs with yellow-emitting Cu(I) complexes^{248,318,348,349,351–355} was achieved with TTPPCuI . Fig. 32 reports the electroluminescence performance of TTPPCuX -based OLEDs.

In 2017, three cationic green emissive binuclear copper complexes containing various groups were systematically studied by Lin *et al.*³²⁷ The cationic copper complexes were $[\text{Cu}_2(\text{pytzph})(\text{POP})_2](\text{BF}_4)_2$ (**Cu58**), $[\text{Cu}_2(\text{pytzphcf})(\text{POP})_2](\text{BF}_4)_2$ (**Cu59**) and $[\text{Cu}_2(\text{pytzphcz})(\text{POP})_2](\text{BF}_4)_2$ (**Cu60**) with tetraimine derivatives and bisphosphine ligands, (pytzph = 6,6'-(1-phenyl-



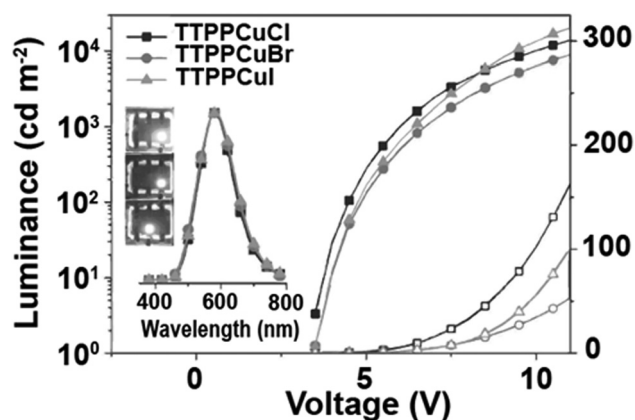


Fig. 32 Electroluminescence performance of TTPPCuX-based OLEDs. Current density (J) (hollow)–luminance (solid)–voltage curves, electroluminescence spectra at 1000 cd m^{-2} and device photos at 5 V (inset). Reproduced with permissions from ref. 326. Copyright 2016, Europe PMC.

1,2,4-triazole-3,5-diyl)bis(2-methylpyridine), pytzphcf = 6,6'-(1-(4 (trifluoromethyl)phenyl)-1,2,4-triazole-3,5-diyl)bis-(2-methylpyridine), pytzphcz = 9-(4-(3,5-bis(6-methylpyridin-2-yl)-1,2,4-triazol-1-yl)phenyl)-carbazole and POP) – Scheme 6. The small ΔE_{ST} $718\text{--}1064 \text{ cm}^{-1}$ led to highly efficient green TADF. However, among all these complexes, the highest efficiency in OLEDs was noted for those with **Cu60**, reaching an EQE of 8.3% – Table 8. Its high PLQY and superior Cz group's hole-conducting properties, and high rigidity led to this excellent device. In the same line, Gary *et al.* demonstrated excellent properties for rigid ligands, such as: (i) thermal stability,³⁵⁶ (ii) intermolecular interactions, (iii) capability to modulate HOMO and LUMO, (iv) high PLQY,^{357–360} (v) hydrophilicity,^{361–365} and (vi) concentration quenching behavior.^{366–368} As example, the synthesis of three cationic TADF Cu(I) complexes (**Cu61–63**; Scheme 6)³²⁸ using dppnc (7,8-bis(diphenylphosphino)-7,8-dicarba-*nido*-undecaborate) and neocuproine ligands were reported, highlighting how the neocuproine ligand structure rules the emission color change from green to dark red and, as such, the position of the T_1 state.³²⁸ Thus the difference between the T_1 of the complex and the energy levels of the host material was used to rationalized the decrease of EQE from 18.46% (**Cu61**) to 10.17% (**Cu63**) – Table 8. In addition, there was a significant effect of dopant concentrations at different levels between 4 and 20 wt% on the performance of these devices – Table 8. The best device made of 4 wt% Cu(dppnc)-R emitter and CBP showed pure red emission with a value of 10.17% for EQE.

Ligand rigidity has exerted a strong impact on heteroleptic Cu(I) complexes comprising biphosphines and macrocyclic phenanthroline ligands.^{369,370} In detail, synthesis and investigations of a series of heteroleptic Cu(I) pseudorotaxanes developed by macrocyclic phenanthroline ligands with various ring sizes and POP, $[\text{Cu}(\text{mXX})(\text{POP})]^+$ (mXX = m30 (**Cu64**), m37 (**Cu65**) and m42 (**Cu66**)), was published by Mohankumar and co-workers²³⁸ and compared with the standard material $[\text{Cu}(\text{dmp})(\text{POP})]^+$, (**Cu4**), (dmp = 2,9-dimethyl-1,10-phenanthroline) – Scheme 6.^{371–373} Due to

gradual suppression of steric congestion caused by a rise in the macrocycle size, the Cu(I) pseudorotaxane with the largest macrocycle (**Cu66**) exhibited a higher electrochemical stability compared to small counterparts. However, all of them showed similar TADF parameters – Table 8. Eventually, to get a high-performance OLEDs, **Cu66** was chosen as emitter due to its straightforward preparation, high PLQY in PMMA (53%, Table 9) and excellent electrochemical stability, while providing intense bright green electroluminescence that is comparable or even superior to those already reported for green OLEDs containing $[\text{Cu}(\text{dnbp})(\text{DPEPhos})]^+$ (dnbp = 2,9-di-*n*-butylphenanthroline) by Adachi and coworkers.³⁴⁹ Fig. 33 shows the electroluminescence spectra of the OLEDs based on **Cu66**.

The design and development of a series of two-coordinate Cu complexes with exceptional luminescence efficiency, comprising nonconventional cyclic amidocarbenes^{374–377} containing: (MAC*)Cu(CzCN₂) (**Cu67**); (MAC*)Cu(CzCN) (**Cu68**); (MAC*)Cu(Cz) (**Cu69**); (DAC*)Cu-(CzCN₂) (**Cu70**); (DAC*)-Cu(CzCN) (**Cu71**, Scheme 6) and (DAC*)Cu(Cz) (**Cu72**), in which MAC = cyclic monoamido-aminocarbene, DAC = cyclic diamidocarbene and “*” exhibits that 2,6-diisopropylphenyl is an aryl group bonded to N, have been also reported – Scheme 6.³²⁹ By selecting thre carbene (acceptor) and carbazolyl (donor), the emission color was systematically tuned from violet ($\lambda_{\text{max}} = 432 \text{ nm}$) to deep red ($\lambda_{\text{max}} = 704 \text{ nm}$), as shown in Fig. 34 and Table 9. Highly effective TADF, high PLQY (until 100%) and short decay lifetimes ($\tau \approx 1 \mu\text{s}$) were obtained (Table 9). As illustrated in Fig. 34, small ΔE_{ST} of 500 cm^{-1} and $10^5\text{--}10^6 \text{ s}^{-1}$ for k_r of these complexes are analogous to those of highly effective emitters containing noble metal, such as Pt and Ir.¹²⁷ Vapor-deposited OLEDs based on (MAC*)Cu(Cz), **Cu69** as the green emissive dopants provided a high EQE (19.4%) and brightness ($54\,000 \text{ cd m}^{-2}$) with modest roll-off at high currents – Table 8 and Fig. 35. In addition, the host-free devices containing **Cu69** presented highly efficient OLEDs with EQE of 16.3% – Table 8. This result highlights the capability of these complexes as neat emitters for OLED devices.

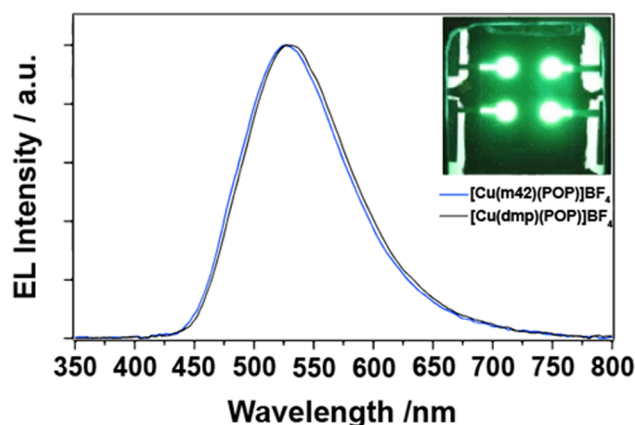


Fig. 33 Electroluminescence spectra at 10 V of OLEDs based on **Cu66** and **Cu4**. In the inset is reported a photograph of OLEDs based on **Cu66**. Reproduced with permissions from ref. 238. Copyright 2018, American Chemical Society.

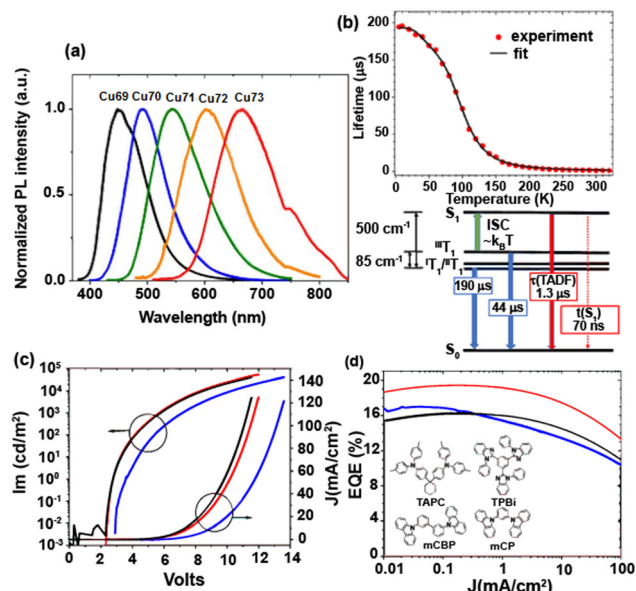


Fig. 34 (a) Emission spectra of complexes **Cu67–71** in 2-MeTHF at room temperature. Reproduced from ref. 329. (b) Emission lifetime versus temperature of complex **Cu69** in the PS film (top). Energy level diagram for complex **Cu69** derived from fit to eqn (1) (bottom). Reproduced from ref. 329. (c) EL device characteristics containing complex **Cu69** at doping concentrations of 10% (blue), 40% (red), and 100% (black). (d) Current density–voltage–luminance (*J*–*V*–*L*). (e) EQE. Inset: Molecular structures of materials used in the devices. Reproduced from ref. 329. Copyright 2019, American Chemical Society.

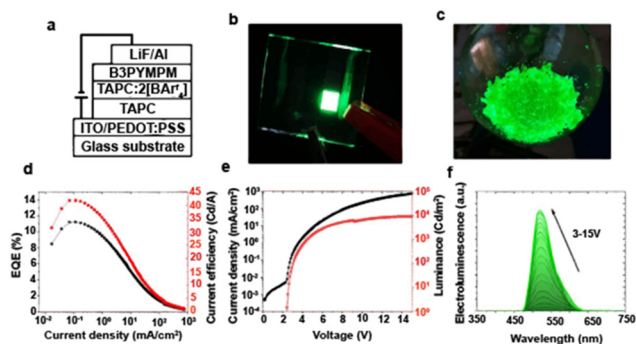


Fig. 35 (a) Schematic architecture of the OLEDs structure. (b) Emission from an OLED prototype with $[2]^+$ as a luminophore. (c) Green emission of crystalline $[\text{Cu84}][\text{BAR}_4\text{F}]$ under UV (254 nm) light exposure. (d) EQE and current efficiency vs. current density. (e) Current density–luminance–voltage characteristics of the electroluminescence device. (f) Electroluminescence spectra for various driving voltages. Reproduced from ref. 333. Copyright 2019, American Chemical Society.

In particular, TADF in linear two-coordinate coinage metal complexes is greatly influenced by the geometric ligand arrangement. Liu *et al.* developed a series of CMA CuI TADF emitters (**Cu73–77**; Scheme 6) and achieved the gradual tuning of configuration from coplanar to orthogonal by introducing various substituents on the indolyl ligands. The inclusion of a 2- CF_3 -indolyl substituent resulted in a confined twist configuration, characterized by a dihedral angle of approximately 45° ,

which can be attributed to the combined effects of intra-molecular steric hindrance and electronic repulsion. Its blue emission, with a peak at 458 nm, demonstrates a high PLQY value of 0.74 and a short τ value of 1.9 μs . These characteristics indicate a sufficiently fast $k_r = 3.9 \times 10^5 \text{ s}^{-1}$ and a suppressed $k_{nr} = 1.4 \times 10^5 \text{ s}^{-1}$ – Table 9. These exceptional luminescent characteristics can be assigned to the optimal overlap of the HOMO and LUMO on Cu^{I} d orbitals. This overlap ensures not only a small ΔE_{ST} , but also a significant transition oscillator strength, facilitating rapid k_r . Both doped and host-free emissive layer designs achieve EQEs above 20% and 10%, respectively – Table 8. These results highlight the potential of the configurationally confined approach in the development of efficient linear CuI TADF emitters in OLEDs.³³⁰

In addition, the development of effective red-emitting Cu(I) complexes is a major problem in OLEDs due to weak SOC and a significant excited-state reorganization effect in Cu(I) complexes. Wu *et al.* successfully developed a red Cu(I) complex known as MAC*-Cu-DPAC (**Cu78**; Scheme 6), by employing the nonconjugated MAC* ligand and a rigid donor ligand namely, 9,9-diphenyl-9,10-dihydroacridine. The Cu(I) complex demonstrated excellent red emission characteristics with a PLQY of 70% and a sub- μs lifetime. This was made possible by the linear geometry and coplanar conformation of the acceptor and donor ligands, resulting in a high value of 77% for horizontal dipole ratio in the host matrix. The resulting OLEDs incorporating MAC*-Cu-DPAC (**Cu78**) displayed impressive EQEs, reaching 21.1% at maximum (Tables 8) and 20.1% at 1000 nits. Furthermore, the OLEDs show emission bands peaking around 630 nm and remarkable performances representing the state-of-the-art for red-emitting OLEDs based on coinage metal complexes.³³¹

As a final work, Lam and coworkers focused on addressing the challenges associated with achieving high efficiency and long-term stability in OLEDs with stable two-coordinate CMA-type CuI-TADF emitters (**Cu79–83**, Scheme 6) with bulky pyrazine-(PzIPr) or pyridine-fused N-heterocyclic carbene (PyIPr*) and Cz ligands. These emitters feature improved bonding interactions of amide-Cu-carbene and exhibit TADF arising from the $^1\text{LL}'/\text{CT}(\text{Cz} \rightarrow \text{PzIPr}/\text{PyIPr}^*)$ excited states, which extends across the blue to red regions of the electromagnetic spectrum, with exceptionally high k_r ranging from 1.1 to $2.2 \times 10^6 \text{ s}^{-1}$. They exhibited impressive PLQYs, reaching up to 0.89. Notably, these complexes achieved high value of $2.2 \times 10^6 \text{ s}^{-1}$ for k_r at ambient temperature, which was attributed to their narrow ΔE_{ST} gap (ranging from 407 to 511 cm^{-1}) and fast $k_r(\text{S}_1)$ (2.6 to $3.1 \times 10^7 \text{ s}^{-1}$). Moreover, the OLEDs were fabricated using these CuI emitters through vapor deposition techniques and demonstrated outstanding EQE, reaching up to 23.6%, and high luminance levels of up to 222 200 cd m^{-2} – Table 8. Notably, these devices exhibited practical operational stability, with LT90 values of 1300 h at 1000 cd m^{-2} under laboratory conditions. These findings highlight the potential of CuI-TADF emitters as replacements for precious metal phosphors in the OLED industry.³³²

Olaru and co-workers³³³ presented highly photo- and electro luminescent clustered structure $[\text{Cu}_4(\text{PCP})_3][\text{A}]$ (**Cu84**; Scheme 6), ($\text{A} = \text{BF}_4^-$ or BAR_4F^- and $\text{PCP} = 2,6\text{-(PPh}_2)_2\text{C}_6\text{H}_3$ and

$\text{Ar}^{\text{F}} = 3,5\text{-(CF}_3)_2\text{C}_6\text{H}_3$), comprising a Cu_4 -core along with bulky tridentate carbanionic diphosphine, ligands. This rare cationic organocopper cluster geometry suppressed the non-radiative decays, resulting in a high PLQY in both solution and solid state with narrow emission bands (FWHM of 60 nm and 58 nm, respectively). According to PL decay kinetics and DFT calculations, the complex emission mechanism involves contributions of two phenomena, phosphorescence and TADF over a wide temperature range. The analysis suggests that at 300 K 94% of the total photoluminescence can be attributed to single harvesting, indicating a significant contribution from TADF, whereas the partial TADF involvement decreases to 0.5% at low temperature (77 K), at which phosphorescence prevails. The use of cationic tetranuclear organo-copper cluster $[\text{Cu}_4(\text{PCP})_3]^+$ in OLEDs resulted in bright green emission (8900 cd m^{-2} at 15 V) with 65 nm FWHM, a relatively high EQE_{max} (11.2% at 42 cd m^{-2}) and low turn-on voltage (2.4 V at 1 cd m^{-2}) – Table 8. Fig. 35 shows the optoelectronic properties of OLEDs made of the aforementioned complexes. By using a bipolar host material named as CBP, the OLED featured high brightness ($19\,000 \text{ cd m}^{-2}$) with a further increase of the turn-on voltages (4.2 V) – Table 8. This was ascribed to the deeper CBP HOMO level in comparison to TAPC, di-[4-(*N,N*-di-*p*-tolyl-amino)-phenyl]cyclohexane, (6.0 eV vs. 5.5 eV) where the hole injection is instead deteriorated.

Recently, Guo *et al.*³³⁴ developed the first efficient TADF-OLEDs based on ultra-soluble Cu(I) halide complexes comprising non-symmetrically substituted bidentate phosphine and PPh_3 ligands, $[\text{CuX}(\text{PPh}_3)(\text{dppts})]$, in which $\text{dppts} = 2\text{-trimethylsilyl-3,4-bis(diphenylphosphine)thiophene}$, $\text{X} = \text{I}$ for (**Cu85**), Br for (**Cu86**), Cl for (**Cu87**) and $[\text{CuX}(\text{PPh}_3)(\text{dppt})]$, in which $\text{dppt} = 3,4\text{-bis(diphenylphosphino)thiophene}$, $\text{X} = \text{I}$ for (**Cu88**), Br for (**Cu89**), Cl for (**Cu90**) – Scheme 6. Since the insolubility of neutral TADF materials often impedes the fabrication of solution processed devices *via* spin coating techniques, the insertion of flexible and bulky trimethylsilyl group into diphosphine ligand served to dramatically increases the solubility, as well as the PLQY (owing to the limitation of nonradiative processes induced by Jahn-Teller distortion of emissive excited states) of Cu(I) halide complexes. Consequently, ultra-soluble TADF materials were proposed for the manufacture of solution-processed devices as well as emitting material inks that are customizable for different print heads through the use of solvent blends with specifically engineered viscosity and surface tension characteristics. All the new four-coordinate mononuclear Cu(I) halide complexes demonstrated deep blue-green to yellowish green emissions in the range of 485–535 nm in powder state at ambient temperature – Table 9; **Cu85–87**, $\lambda_{\text{ex}} = 360$ and for **Cu88–90** $\lambda_{\text{ex}} = 373$ nm. Fig. 36b shows the emission spectra and x/y CIE coordinates for **Cu85–90** in powder state at 297 K. They provided high PLQYs ranging from 29 to 55% compared to **Cu88–90** (PLQY = 3–18%; Table 9). The emission of the complexes predominantly arises from MLCT, XLCT and intra-ligand transitions. The estimated $\Delta E_{\text{ST}} = 464\text{--}1035 \text{ cm}^{-1}$ were supported by calculations (492–940 cm^{-1}), revealing that they can exhibit efficient TADF.³⁷⁸

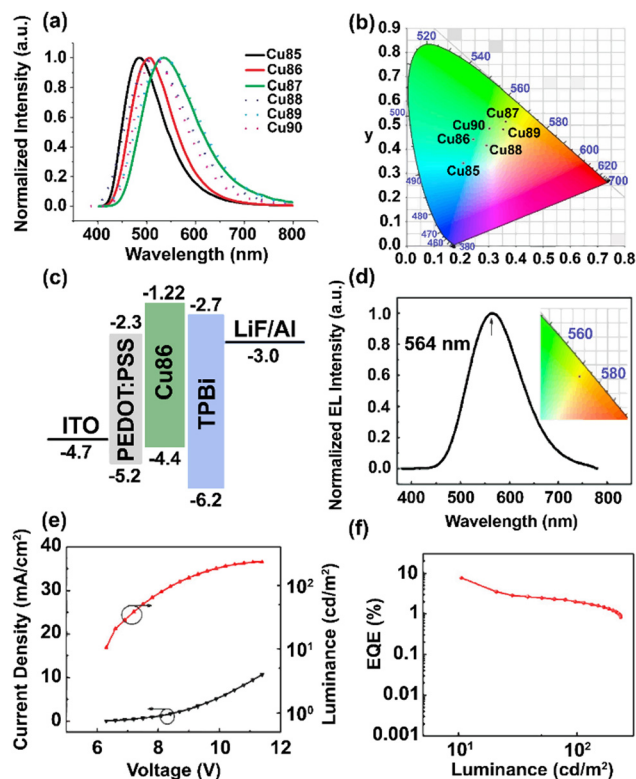


Fig. 36 (a) Normalized emission spectra and (b) CIE graph of complexes **Cu85–90** in powder state at 297 K. Reproduced from ref. 334. (c) Energy-level diagram of the device based on the complex **Cu86**; (d) electroluminescence spectra, and the inset is the CIE of electroluminescence spectra; (e) current density–voltage–luminance (J – V – L) characteristics; (f) EQE–luminance characteristics. Reproduced from ref. 334. Copyright 2020, Elsevier.

Solution-processed undoped and doped OLEDs containing **Cu86** displayed yellow green emission (564 nm) (Fig. 36). Devices doped with CBP and using mCP as host materials exhibited inferior performance compared to the non-doped device, probably because of the inadequate energy level compatibility between CBP, mCP and **Cu86**. Meanwhile, the undoped device indicated maximum brightness and EQE of 234 cd m^{-2} and 7.74% respectively (Table 8).

As explained in Section 2, TADF Cu(I) complexes have been prepared utilizing basic D–A type $\text{N}^{\wedge}\text{N}$ ligands and auxiliary phosphine ligands. The coordination of the metal ion induces a reduction in the energy gap for the LC excited states, leading to a switch from fluorescence in the free $\text{N}^{\wedge}\text{N}$ ligands to TADF in the complexes (**Cu91–94**; Scheme 6). Remarkably high PLQYs reaching up to 0.71 at room temperature in doped films (Table 9) have been achieved. Through DFT calculations, the complexes have been found to possess intraligand charge-transfer excited states that primarily localize on the $\text{N}^{\wedge}\text{N}$ ligands. The energy level of the excited state of intra-ligand CT is significantly influenced by the $\text{N}^{\wedge}\text{N}$ ligand donating strength, thereby dictating the energetic ordering of the ^3CT and ^3LE states. Consequently, the emission lifetimes of the Cu(I) complexes exhibit substantial variation, exceeding four-fold differences. Furthermore, solution-processed OLEDs



fabricated from one of these novel emitters exhibit EQE_{max} as high as 7.96% (Table 8). It has been observed that a shorter emission lifetime is advantageous for attaining higher EQEs. The promising outcomes of this study, integrated with logical design approaches may serve as a valuable guidance for the progress of Cu-complexes and OLEDs.³³⁵

Lately, luminescent complexes of CMA containing group 11 metals (Cu, Ag, Au) have gained significant interest for their remarkable emission efficiency and high radiative decay rates (k_r). Chang *et al.* investigate a set of eight Cu(I) complexes (**Cu95–102**; Scheme 6) with previously unexplored 1,3-thiazoline carbenes, analyzing their light emission properties for OLEDs. They demonstrated the high-performance EL excimers, whose prevalence of EL can be adjusted from either the monomer (bluish green) or the excimer (orange-red) by altering the emitter's steric hindrance or concentration within vacuum-deposited emissive layers. The radiative rates of the materials exhibit high values, ranging from $(2.8\text{--}7.2) \times 10^5 \text{ s}^{-1}$ – Table 9. By optimizing the emitter structure and mass fraction, devices based on emitter **Cu101** achieved both monomer and excimer electroluminescence, enabling the development of a single-emitter WOLED with high EQE of 16.5% and L_{max} exceeding $40\,000 \text{ cd m}^{-2}$ (Table 8). The broad emission bands of the monomer and excimer contributed to a CRI > 80. These results emphasize the potential of cost-effective copper complexes for lighting devices, offering reduced expenses and simplified device architecture.³³⁶

The direct co-deposition of copper halide and organic materials is considered a promising and straightforward approach for manufacturing OLEDs, compared to using pre-synthesized complexes Zhang *et al.* co-deposited four host aza-9,9-Spirobifluorenes (aza-SBFs) ligands with varying positions of the nitrogen atom in the azafluorene moiety along with Cu(I) iodide (CuI) to make emissive complexes, called α -aza-SBF:CuI (**Cu103**), β -aza-SBF: CuI (**Cu104**), γ -aza-SBF:CuI (**Cu105**) and δ -aza-SBF:CuI (**Cu106**) – Scheme 6. Interestingly, these co-deposited Cu(I) complexes exhibited both phosphorescent and TADF. Notably, by modifying the situation of the nitrogen atom, the TADF was successfully improved, leading to a high PLQY of 92.2% (**Cu106**; Table 9). As a result, green emission at 540 nm along with values of 41.9 cd A^{-1} for current efficiency, value of 32.9 lm W^{-1} for power efficiency and value of 16.8% for EQE of OLED device fabricated with **Cu106** compound as emitter were achieved – Table 8. This study highlight the future potential of utilizing the co-deposition strategy for manufacturing cost-effective and highly efficient OLED devices.³³⁷

Cheng and co-workers investigated the luminescent Cu(I) dimer complex $\text{Cu}_2\text{Cl}_2(\text{P}\cap\text{N})_2$ (**Cu107**; Scheme 6) ($\text{P}\cap\text{N}$ = diphenylphosphanyl-6-methyl-pyridine) as a potential emitter material for OLEDs. This complex exhibits TADF and phosphorescence even at room temperature. By using a solution-processable approach, we fabricated an OLED with the configuration of ITO/PEDOT:PSS/PYD2:**Cu107**/DPEPO (10 nm)/TPBi (40 nm)/LiF (1.2 nm)/Al (100 nm) that emits warm white light (CIE coordinates (0.38, 0.49)) with a moderate EQE = 3.80 – Table 8. The EQE value obtained for a material doped with

Cu107 is lower than predicted, despite the considerable PLQY of 92% for the powder state. The lower EQE value is attributed to the less rigid host materia PYD2l, which enhances unique geometric reorganization upon excitation compared to the powder medium. Consequently, the host material with a doping concentration of 8 wt% shows a PLQY of 27%. When the EQE is normalized to PLQY = 100%, the normalized EQE is found to be 14%. This suggests that designing the molecular structure of the emitter and the host environment more distinctly rigidly can lead to high-performance Cu(I) emitter devices.³³⁸

As a final remark for designing TADF OLEDs with Cu-complexes, Wang and co-workers proposed to use Cu(II) acetate as a spin sensitizer to simplify rISC and enhance electroluminescence in TADF-excimer OLEDs. Notable alterations in the intensity and lifetime of photoluminescence were observed due to the coordination interaction of Cu(II) acetate with exciplex molecules involving intermolecular CT properties. Additionally, the addition of copper acetate as a spin sensitizer was evidenced by magneto-photoluminescence data to promote spin transition in the rISC process, resulting in an approximately 80% enhancement of electroluminescence in spin-sensitized TADF-based OLEDs. These findings demonstrate that utilizing a spin sensitizer such as copper acetate can dominate the spin-forbidden limitation and minimizing the ΔE_{ST} in the engineering of TADF materials to promising improve performance of OLED device. This discovery opens up possibilities for developing efficient OLEDs and paves the way to advance the next-generation organic electronics.³⁷⁹

In stark contrast to Cu(I) complexes, Ag(I) complexes have been relatively unexplored yet. Here, Li *et al.* introduce several new $[\text{Ag}(\text{N}^{\wedge}\text{N})(\text{P}^{\wedge}\text{P})]\text{-PF}_6$ complexes (**Ag10** and **Ag17–19**; Scheme 6) that indicate highly effective TADF utilizing usable neutral diamine ligands and readily accessible auxiliary diphosphine chelates. The coordination of the metal ion leads to a reduction in ΔE_{ST} , facilitating the effective TADF from the excited state centered on the ligand. PLQY values of up to 62% in doped films were achieved – Table 9. Their high PLQYs in combination with significant delayed fluorescence ratio, allowed the development of solution-processed OLEDs with a remarkable EQE_{max} of 8.76% – Table 8.²⁷³

3.2. LECs

LECs are the simplest and cheapest SSL concept as they combine air-stable electrodes with solution-based fabrications techniques. Over the last years, ionic Cu(I) complexes gained much attention as electroluminescent emitters due to their well-adjustable photophysical properties, such as TADF, emission color, rich molecular design. So far, the best Cu(I) complex-based LECs achieve brightness of up to 452 d m^{-2} , efficiencies up to 4.5 cd A^{-1} and EQEs of 1.85% for the mid-energy emitting region,²³⁵ while blue-emitting Cu(I) complex-based LECs have been close performing with efficiencies of 3.6 cd A and EQE of 1.2%.²²⁸ Finally, red Cu(I) complex-based LECs have also led to interesting performances with irradiances of $130 \mu\text{W cm}^{-2}$ and day stabilities.³⁸⁰ Recently, the LEC community started to



consider Ag(I) complex-based LECs. Although clear design rules for TADF in Ag-complexes are missing and TADF is rarely observed in Ag-complexes, considerably device performance were achieved – especially in the low-energy region ($\lambda_{\text{exc}} = 645 \text{ nm}$, $\text{Irr}_{\text{max}} = 36 \mu\text{W cm}^{-2}$, $t_{1/2} = 5 \text{ h}$).^{381,382} Finally, very recently, He *et al.* introduced the first TADF-LEC with Ir-complexes as dopant as reported in OLEDs. Accordingly, the following will summarize the most relevant complexes applied to LECs, highlighting their device performance (Table 10) as well as their photoluminescence features as a complement of Section 2 (Table 11).

3.2.1. Ir-complex. Over the last 15 years, high-performance blue LECs for white LEC applications is still a challenge.³⁸³ Recently, He *et al.* proposed an ionic exciplex host to create color-stable, efficient, and bright blue LECs.³⁸⁴ This host features a bipolar charge transport and efficient energy transfer to the guest dopant. The cationic donor molecule, tBuCAZ-ImMePF₆, and cationic acceptor molecule, TRZ-ImEtPF₆, are engineered to form the ionic exciplex host. The combined film of tBuCAZ-ImMePF₆ and TRZ-ImEtPF₆ generates a blue exciplex with high singlet/triplet energy levels, a small ΔE_{ST} rapid rISC and TADF. Energy transfer from the exciplex to a blue-emitting iridium(III) complex is efficient in the doped film. Host-guest LECs utilizing this active layer exhibit stable blue emission color and high current efficiencies of up to 25.8 cd A^{-1} and EQE at 11.5%. Notably, they achieve both high efficiency and brightness simultaneously ($14.1/17.4/16.8 \text{ cd A}^{-1}$ at 705/872/1680 cd m^{-2}). The exceptional efficiency and brightness were attributed to the effective energy transfer from the exciplex host to the Ir(III) complex, which minimized phosphorescence concentration-quenching. In addition, the p-type/n-type doping is efficient leading to the establishment of a p-i-n junction through the utilization of the ionic exciplex host. Finally, the primary host-guest LEC displays promising operational stability. This research emphasizes that employing an ionic exciplex host offers a promising pathway for the development of high-performance blue LECs.³⁸⁴

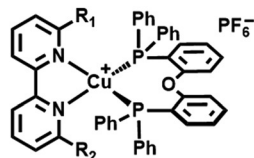
3.2.2. Cu- and Ag-complexes. As described in Section 2, TADF has been found in different emitting families, such as heteroleptic tetrahedral $[\text{Cu}(\text{N}^{\wedge}\text{N})(\text{P}^{\wedge}\text{P})]^+$, and the tri-coordinated $[\text{Cu}(\text{IPr})(\text{dpa})]^+$, in which IPr is 1,3-bis-(2,6-di-isopropylphenyl)imidazole-2-ylidene and dpa is 2,2'-bispyridylamine. Though the first reports in LECs based on Cu(I) complexes did not disclose any impact of the TADF process on the device performance as well as the photophysical behavior in thin-films,^{233,371,385} the relevance of TADF was firstly disclosed by Costa *et al.*³⁸⁶ in Cu(I) complexes. They reported a counterintuitive yellow electroluminescence from a Cu(I) complex $[\text{Cu}(\text{impy})(\text{POP})][\text{PF}_6]$, in which impy is 3-(2-methoxyphenyl)-1-(pyridine-2-yl)imidazo[1,5-*a*]pyridine, which showed blue photoluminescence. This was ascribed to absence of the TADF process that led to photoluminescence emission from S₁ and a yellow electroluminescence from T₁ lacking the possibility of TADF even when the devices were operated at high temperatures. This was ascribed to the exclusively LC nature of the excited states. Consequently, the device exhibited

moderate low performances with maximum brightness of 13.9 cd m^{-2} at a driving current of 7.5 mA and an efficacy of 0.03 cd A^{-1} .

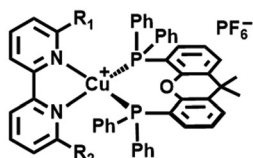
Along the evolution of LECs based on $[\text{Cu}(\text{N}^{\wedge}\text{N})(\text{P}^{\wedge}\text{P})]^+$ family, Constable and Housecroft systematically studied the effect of the substituent in N[^]N ligands on both the photo- and electro-luminescence behaviors. In detail, the family $[\text{Cu}(\text{P}^{\wedge}\text{P})(\text{N}^{\wedge}\text{N})][\text{PF}_6]$ with P[^]P = POP or xantphos, N[^]N = 2,2'-bipyridinebpy (bpy) ligands with methyl and CF₃ moieties as substitute in various positions of the bpy ligand, (6,6'-(CF₃)₂bpy, 6-CF₃bpy, 5,5'-(CF₃)₂bpy, 4,4'-(CF₃)₂bpy, 6,6'-Me₂-4,4'-(CF₃)₂bpy) (**Cu6**, **Cu108–116**; Scheme 7).³³⁹ While the TADF in powder was not affected with a ΔE_{ST} of 968–1613 cm^{-1} (TD-DFT calculations), the highest PLQY (50.3%) in powder sample (Table 11) were achieved by $[\text{Cu}(\text{xantphos})(4,4'-(\text{CF}_3)_2\text{bpy})][\text{PF}_6]$. Among them, only $[\text{Cu}(\text{POP})(6\text{-CF}_3\text{bpy})][\text{PF}_6]$, $[\text{Cu}(\text{xantphos})(6\text{-CF}_3\text{bpy})][\text{PF}_6]$ and $[\text{Cu}(\text{xantphos})(6,6'\text{-Me}_2\text{-4,4'-(CF}_3)_2\text{bpy})][\text{PF}_6]$ were used in LECs devices due to their high PLQY values because of dependency of the efficacy as well as the luminance of the LECs with the PLQY value in thin-film and exhibit yellow electroluminescence in wavelength rang 589–595 nm with maximum EQEs of 0.4%–0.6% were obtained – Table 10. However, CF₃-free bpy-based $[\text{Cu}(\text{P}^{\wedge}\text{P})(\text{N}^{\wedge}\text{N})][\text{PF}_6]$ complexes have better performance in comparison with their incorporating CF₃ counterparts due to their lower PLQY in films. By adding CF₃ units, the $E_{1/2\text{ox}}$ value for the Cu⁺/Cu²⁺ process in $[\text{Cu}(\text{POP})(\text{bpy})]^+$ and $[\text{Cu}(\text{xantphos})(\text{bpy})]^+$ complexes increases to higher potentials (+0.85 to +0.96 V). These identified trends in $E_{1/2\text{ox}}$ align with the findings obtained from DFT calculations. The properties of the N[^]N ligand remarkably modifies the HOMO–LUMO separation, and the largest redshift in the MLCT band is observed in $[\text{Cu}(\text{P}^{\wedge}\text{P})(5,5'-(\text{CF}_3)_2\text{bpy})]^+$ complex, which is also supported by DFT calculations. The emission energies of $[\text{Cu}(\text{P}^{\wedge}\text{P})(\text{bpy})]^+$ complexes with groups at the 6,6'-position of bpy do not align with the predicted values based on electronic requirements, such as MO analysis or electrochemical and optical absorption gaps. This is due to the introduction substituents inhibiting tetrahedron flattening distortions related to T₁ relaxation and prevents its stabilization. As a result, the T₁ state remains at higher energies in complexes with substituents at 6,6'-positions.

In this line, the same authors reported another large series of twelve heteroleptic $[\text{Cu}(\text{P}^{\wedge}\text{P})(\text{N}^{\wedge}\text{N})][\text{PF}_6]$ complexes – Scheme 7, (**Cu118**) $[\text{Cu}(\text{POP})(\text{MeObpy})][\text{PF}_6]$, (**Cu119**) $[\text{Cu}(\text{POP})(\text{EtObpy})][\text{PF}_6]$, (**Cu120**) $[\text{Cu}(\text{POP})(\text{PhObpy})][\text{PF}_6]$, (**Cu121**) $[\text{Cu}(\text{POP})(\text{MeSbpy})][\text{PF}_6]$, (**Cu122**) $[\text{Cu}(\text{POP})(\text{EtSbpy})][\text{PF}_6]$, (**Cu123**) $[\text{Cu}(\text{POP})(\text{Phsbpy})][\text{PF}_6]$ as well as (**Cu124**) $[\text{Cu}(\text{xantphos})(\text{MeObpy})][\text{PF}_6]$, (**Cu125**) $[\text{Cu}(\text{xantphos})(\text{EtObpy})][\text{PF}_6]$, (**Cu126**) $[\text{Cu}(\text{xantphos})(\text{PhObpy})][\text{PF}_6]$, (**Cu127**) $[\text{Cu}(\text{xantphos})(\text{MeSbpy})][\text{PF}_6]$, (**Cu128**) $[\text{Cu}(\text{xantphos})(\text{EtSbpy})][\text{PF}_6]$, (**Cu129**) $[\text{Cu}(\text{xantphos})(\text{PhSbpy})][\text{PF}_6]$, in which P[^]P = POP or xantphos, and N[^]N = (MeObpy) = 6-methoxy-2,2'-bipyridine, (EtObpy) = 6-ethoxy-2,2'-bipyridine, (PhObpy) = 6-phenyloxy-2,2'-bipyridine, (MeSbpy) = 6-methylthio-2,2'-bipyridine, (EtSbpy) = 6-ethylthio-2,2'-bipyridine and (PhSbpy) = 6-phenylthio-2,2'-bipyridine, through the addition of different moieties into the 6-substituted site of bpy ligand was performed to investigate the

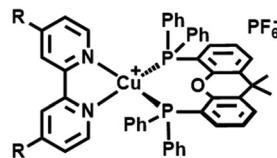




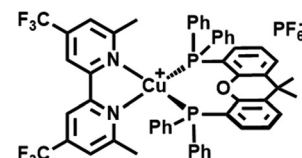
Cu108: $R_1 = R_2 = H$
 Cu109: $R_1 = CF_3$, $R_2 = H$
 Cu130: $R_1 = Et$, $R_2 = H$
 Cu132: $R_1 = Me$, $R_2 = H$
 Cu136: $R_1 = tBu$, $R_2 = H$



Cu110: $R_1 = CF_3$, $R_2 = H$
 Cu115: $R_1 = CH_3$, $R_2 = H$
 Cu116: $R_1 = R_2 = CH_3$
 Cu131: $R_1 = Et$, $R_2 = H$
 Cu137: $R_1 = tBu$, $R_2 = H$



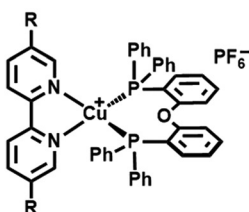
Cu114: $R = CF_3$
 Cu133: $R = OMe$



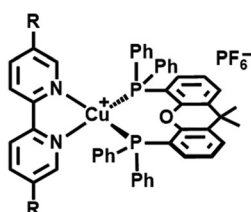
Cu117

Cu118: $R_1 = OMe$, $R_2 = H$
 Cu119: $R_1 = OEt$, $R_2 = H$
 Cu120: $R_1 = OPh$, $R_2 = H$
 Cu121: $R_1 = SMe$, $R_2 = H$
 Cu121: $R_1 = SEt$, $R_2 = H$
 Cu122: $R_1 = SPh$, $R_2 = H$
 Cu153: $R_1 = R_2 = OMe$

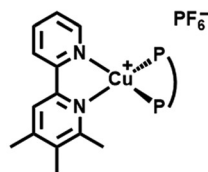
Cu124: $R_1 = OMe$, $R_2 = H$
 Cu125: $R_1 = OEt$, $R_2 = H$
 Cu126: $R_1 = OPh$, $R_2 = H$
 Cu127: $R_1 = SMe$, $R_2 = H$
 Cu128: $R_1 = SEt$, $R_2 = H$
 Cu129: $R_1 = SPh$, $R_2 = H$



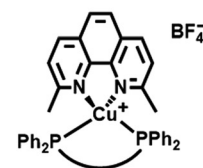
Cu111: $R = CF_3$
 Cu134: $R = CH_3$



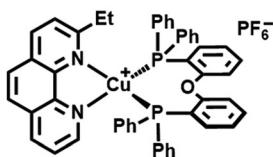
Cu112: $R = CF_3$
 Cu135: $R = CH_3$



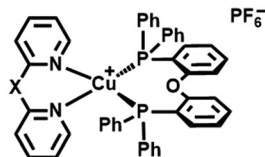
Cu138: $P^*P = DPEphos$
 Cu139: $P^*P = xantphos$



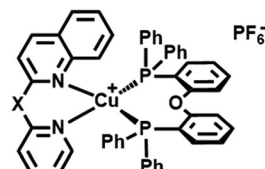
Cu124: $P^*P = DPEphos$
 Cu143: $P^*P = xantphos$
 Cu144: $P^*P = isopropoxantphos$
 Cu145: $P^*P = nixantphos$
 Cu146: $P^*P = thixantphos$
 Cu147: $P^*P = benzoxantphos$



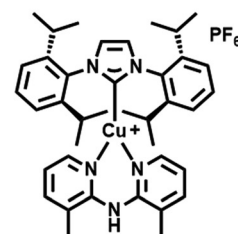
Cu140: $P^*P = DPEphos$
 Cu141: $P^*P = xantphos$



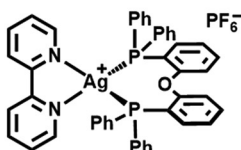
Cu148: $X = NH$
 Cu150: $X = S$



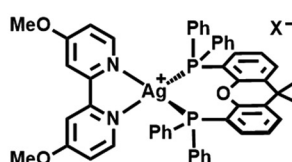
Cu149: $X = NH$
 Cu151: $X = S$



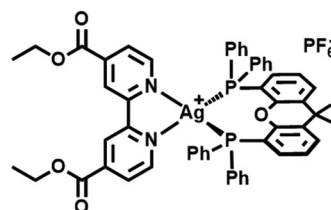
Cu152



Ag20



Ag21: $X = BF_4$
 Ag22: $X = PF_6$
 Ag23: $X = ClO_4$



Ag24

Scheme 7 Molecular structures of Cu108–152 and Ag20–24.



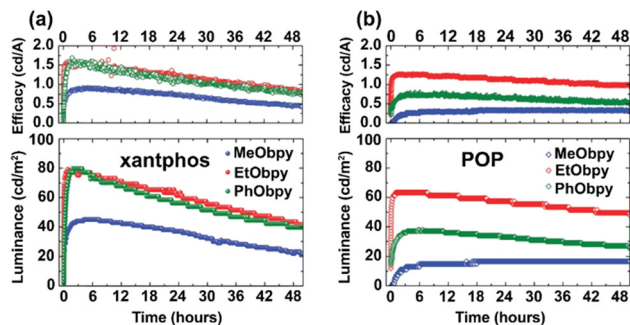


Fig. 37 Efficacy (top) and luminance (bottom) versus time for LECs employing Cu(I) complexes with RObpy and either (a) xantphos or (b) POP ligands. LECs were driven at an average current density of 50 A m². Reproduced from ref. 340. Copyright 2018, Royal Society of Chemistry.

potential of these compounds as emissive dopants for applications in LECs.³⁴⁰ The distorted tetrahedral geometry for Cu(I) and the chelating states for each N^N and P^P ligand in all compounds are established by single crystal structures. In the complexes containing xantphos, the asymmetric bpy ligand with a substituent group at position 6 is located on the “bowl” of xanthene. In addition, these materials are yellow emitters with a PLQY of 38% and an τ value of 10.2 ms in powder state – Table 11. Changing from powder to frozen Me-THF increases the τ value that could suggest the presence of TADF, but further studies were not provided. All of the twelve compounds have also been used in LECs and complexes with alkoxy- or phenyloxy- functionalized ligands showed stable and bright LEC devices that being extremely important for the later progression of electroluminescent devices containing Cu(I) metal ion center. The time evolution of efficacy and luminance for devices using Cu(I) complexes with RObpy and either (a) xantphos or (b) POP ligands are presented in Fig. 37. Furthermore, LECs based on [Cu(P^P)(EtObpy)][PF₆] demonstrate boosted values of Lum_{max}, $t_{1/2}$, t_{on} and efficacy when compared to the state-of-the-art LECs with Cu(I) which include [Cu(P^P)(Etbpy)][PF₆] (**Cu130** and **Cu131**; Scheme 7).³⁴¹

The above examples mainly emphasized the preparation of Cu(I) complexes by attaching one moiety at the *ortho* and *para* positions of the bipyridine ligand. However, a few reports have shown the benefits of (i) the substitution at the *para* position and (ii) a fully substitution at the *ortho* position. On one hand, Costa *et al.* conducted a thorough investigation on the impact of electron donor and electron acceptor moieties at the 4-positions of bpy in [Cu(bpy)(xantphos)] complexes.³⁴² They found that the LEC efficiency improved with increasing negativity of the σ -Hammett parameter (σ_p), which characterizes the σ -donation capability of the substituents. The best performing complex, namely the TADF [Cu(4,4'-dimethoxy-2,2'-bipyridine)(POP)]BF₄ (**Cu133**; Scheme 7), achieved 54 cd m⁻² at 10 mA of pulsed driving current – Table 10. Very recently, Keller *et al.* proved that also the *para* substitution with electron-withdrawing fluorinated groups can lead to improved figures-of-merit.³³⁹ As an example, [Cu(6,6'-Me₂-4,4'-(CF₃)₂bpy)(xantphos)]PF₆ (**Cu117**; Scheme 7) exhibited a maximum luminance of 131 cd m⁻² as well as a lifetime stability of 2 h – Table 10.

The τ value of 12 μ s at room temperature and of 42 μ s at 77 K along with a S₁-T₁ energy separation of 1613 cm⁻¹ suggest a TADF emission mechanism – Table 11. On the other hand, the substitution with the methyl moieties at the *ortho* position relative to the N bipyridine atoms brought to a substantial improvement of the performances when compared to the non-substituted bipyridine. LECs based on [Cu(6,6'-dimethyl-2,2'-bpy)(POP)]PF₆ (**Cu132**; Scheme 7) and the ionic liquid 1-ethyl-3-methylimidazolium hexafluorophosphate [EMIM][PF₆] in molar ratio 4:1 achieved 53 cd m⁻² at a current density of 10 A m⁻², thus achieving 5.2 cd A⁻¹ for copper-based LECs – Table 10.²⁴⁵

The impact of the P^P ligand was also disclosed by several groups. Constable and Housecroft group synthesized and characterized eight heteroleptic [Cu(POP)(N^N)][PF₆] and [Cu(xantphos)(N^N)][PF₆] complexes (**Cu134–141**; Scheme 7), [N^N is 5,5'-dimethyl-2,2'-bipyridine (5,5'-Me₂bpy), 4,5,6-trimethyl-2,2'-bipyridine (4,5,6-Me₃bpy), 6-(*tert*-butyl)-2,2'-bipyridine (6-*t*Bubpy) and 2-ethyl-1,10-phenanthroline (2-Etphen) and P^P is either bis(2-(diphenylphosphino)phenyl)ether (POP, PIN [oxydi(2,1-phenylene)]bis(diphenylphosphane)) or 4,5-bis(diphenylphosphino)-9,9-dimethylxanthene (xantphos, PIN (9,9-dimethyl-9*H*-xanthene-4,5-diyl)bis(diphenylphosphane))]. This study shows that electronic and steric impacts can result in a remarkable enhancement of PLQY values and the L_{max} of the device. Methyl or ethyl units in the 6-position of the bpy ligand improved the PLQY and device performance, while a *tert*-butyl substitution has a negative impact, leading to lower PLQY and shorter τ values of the complexes. The study found that incorporating 5,5'-Me₂bpy leads to inefficient emitters than 6-Mebpy, indicating that stabilizing the tetrahedral complex geometry with a group in the 6-site of the bpy is more beneficial than the electron-donating impact of two methyl moieties. Replacing the ligand with the analogous phenanthroline, 2-Etphen resulted in high values of luminance but only the complex with xantphos showed longer lifetimes for device. The study also showed that the device with the similar POP complex was significantly less stable with 2-Etphen compared to 6-Etbpy. These yellow to green emitters exhibit tunable photophysical properties, such as emission maxima in the range of 518–602 nm and PLQYs about 1.1–58.8% – Table 11. They also displayed TADF and have shown promising performance in LECs with value of 462 cd m⁻² for L_{max} and a value of 98 h for half-lifetimes of device – Table 10. The research provides understanding about the effects of alkyl substitution on the photophysical and device characteristics of the complexes, highlighting the importance of a systematic approach to improve the design of the complexes for enhanced device brightness and lifetime.³⁴³ Zysman-Colman *et al.* investigated on the photophysics, electrochemistry, and electroluminescence of seven cationic heteroleptic Cu(I) complexes, namely [Cu(P^P)(dmphen)]BF₄ (**Cu142–147**; Scheme 7) (dmphen = 2,9-dimethyl-1,10-phenanthroline and P^P represents a diphosphine chelate in homoxantphos, isopropoxantphos, nioxantphos, thioxantphos, and benzoxantphos). The main goal was to investigate the influence of the diphosphine ligand's bite



angle on the photophysical characteristics of the complexes. Among these complexes, several displayed relatively high PLQYs both in solid-state (35%) and in solution (up to 98%, Table 11). There is a correlation between the powder PLQYs and the % V_{bur} of the P[^]P ligand. Among them, **Cu3** exhibited a longer device lifetime (L_{50} of *ca.* 17 h) compared to the reference Cu(i)-based LEC [Cu(dnbp)(DPEPhos)]⁺ (1.2 h). A high value for % V_{bur} results in PLQY values of 35% – Table 10, reaching EQE_{max} of 4.4% for the devices. Finally, **Cu3** exhibited superior ECL performance in comparison to the other complexes. This improvement can be assigned to the high stability of both the oxidized and reduced species, as evidenced by its voltammetric profile. Particularly, complexes with more reversible electrochemistry displayed higher annihilation ECL and exhibited improved LECs.²³⁵

To increase the efficiency and reach other colors in TADF-based Cu-complexes based LECs, several authors explored several N[^]N ligands. As far as we know, there are three mainly families of copper (i) complexes that have been tested in LECs devices: (i) homoleptic and heteroleptic Cu-iTMCs bearing diimine (N[^]N), diphosphine (P[^]P) and phosphine-amide (P[^]N) ligands, (ii) dinuclear Cu-iTMCs and (iii) NHC Cu-iTMCs in which NHC is N-heterocyclic carbene. For instance, the former have shown great performances in green- and yellow devices,^{172,232} while prior to 2022 blue LECs were only achieved with NHC-based Cu-iTMCs showing stabilities of <5 min at 0.17 cd A⁻¹ and 20 cd m⁻².³⁴⁵

This gap of knowledge was particular limiting the development of white LECs. In fact, more efforts were done toward the development of red-emitting Cu(i) complexes that they were mixed with high-energy emitting SMs (*e.g.*, using CBP). In the first report of Cu(i) white LECs, a combination of CBP and [Cu(dcbq)(xantphos)]⁺ in which dcbq is 4,4'-diethylester-2,2'-biquinoline, only moderate performance were achieved (*i.e.*, 4 cd m⁻² at 25 mA).³⁸⁰ In 2022, Costa and Galliard *et al.* improved the red-emitting component through the use of pyrazine and pyrimidyl ancillary N[^]N ligands.¹⁷¹ The best devices reached luminances of 12 cd m⁻² associated to an excellent white color quality (*i.e.*, *x/y* CIE coordinates of 0.31/0.32 and CRI of 90) that is stable over their lifetime.

Despite these encouraging reports, the lack of stable and efficient blue Cu(i) complexes was a huge bottleneck for the field of Cu(i) complex-based white LECs. However, in 2022, Costa *et al.*²²⁸ introduced a novel approach using a large dataset and multivariate analysis to predict the performance of copper complexes ([Cu(N[^]N)(P[^]P)]⁺) in thin-film lighting devices. This method breaks away from traditional trial-and-error approaches that focus on single variables at a time. The key to this approach lies in the correlation between simulated and experimental data based on a multivariate model using data from over 90 Cu-iTMCs applied in LECs, including their X-ray structures, electronic properties, and performance in thin-film devices (emission wavelength, efficiency, *etc.*). This research achieved two breakthroughs: (i) highly efficient blue LECs using were fabricated successfully, and (ii) the first single-layered white LEC using only Cu-iTMCs was achieved. In particular,

[Cu(N[^]N)(P[^]P)]⁺ in which N[^]N is 2-(4-(*tert*-butyl)phenyl)-6-(3,5-dimethyl-1*H*-pyrazol-1-yl)pyridine and P[^]P is 4,5-bis(diphenylphosphino)-9,9-dimethylxanthene (**Cu8**; Scheme 3) based LECs achieved a maximum efficiency of 3.6 cd A⁻¹, which is considered top-notch for copper-based LECs regardless of color and it is better than state-of-art blue Ir-iTMCs LECs.¹⁸⁷

Despite the first fully Cu(i) complex-based white LECs was achieved, the poor performance of the low-energy emitting Cu-iTMCs was still of concern. Thus, Galliard *et al.*³⁴⁴ focused on improving the performance of red-emitting complexes exploring conventional strategies: (i) extending the π -systems and (ii) introducing S-bridges between heteroaromatic rings. This resulted in the synthesis of two new heteroleptic Cu(i) complexes: 2-(pyridin-2-yl)-12-azanylquinoline (CuN2) (**Cu149**) and 2-(naphthalen-2-ylthio)-quinoline (CuS2) (**Cu151**) as N[^]N, with bis[(2-diphenylphosphino)phenyl] ether as the P[^]P ancillary ligand – Scheme 7. These complexes exhibited enhanced PLQY and TADF processes in comparison with their reference complexes: di(pyridin-2-yl)-12-azane (CuN1) (**Cu148**) and di(pyridin-2-yl)sulfane (CuS1) (**Cu150**) shown in Scheme 7. Notably, **Cu151** showed the highest PLQY (38% compared to 17%, 14%, and 1% for **Cu148**, **Cu149**, and **Cu150**, respectively, Table 11). However, only **Cu149**-LECs demonstrated superior performance, with a current density of 0.35 cd A⁻¹ at a luminance of 117 cd m⁻² – Table 10, whereas **Cu148**-LECs performed poorly (0.02 cd A⁻¹ at 6 cd m⁻²; Table 10), and **Cu151**-LECs had low performance (0.04 cd A⁻¹ at 10 cd m⁻²; Table 10). This indicated that traditional chemical engineering strategies did not effectively enhance device efficiency. Capitalizing on the acquired knowledge through the previously reported multivariate analysis, it has been proposed a non-obvious design consideration that takes into account the ligand polarization features (specifically, clogP and tPSA) governing ϵ and σ in thin-films and, consequently, the operation mechanism of LECs. This novel design insight was uncovered through a multivariate statistical analysis model that connects electronic parameters and X-ray structural of Cu(i) complexes with their photo/electro-luminescent behaviors in thin-films, in the context of their applications in lighting and electrochemical impedance spectroscopy (EIS) studies. These analyses revealed a new design rule: the polarizability of the ancillary ligand plays a key role in improving the efficiency of LECs. Thus, it is imperative to consider the polarizability of the ligands in addition to the well-known structural parameters.³⁴⁴ Overall, this methodology can also be applied to understand the limitations in the complex designs beyond the discovery of new examples for a desired color.

In 2016, Costa, Gaillard *et al.* published a study on a series of mononuclear Cu(i) complexes containing NHC and nitrogen bidentate ligands. These complexes displayed highly favorable luminescence characteristics, demonstrating blue or blue-green emission.^{249,250} All the complexes showed τ values ranging from 6 to 14 μ s at ambient temperature and from 32 to 87 μ s at 77 K. According to Thompson *et al.*, a 2- to 3-fold increase in the τ when changing ambient temperature to 77 K is a good indication of a TADF emission process rather than a



phosphorescence one.²⁴⁸ The best performing LEC was achieved with [Cu(IPr)(3-Medpa)]PF₆, (**Cu152**; Scheme 7) with a luminance of 20 cd m⁻², efficacy of 0.17 cd A⁻¹, and a total emitted energy (E_{tot}) of 4 mJ. This parameter refers to the radiant flux of the device over time, starting from $t = 0$ when bias was applied until the time it reaches a 1/5 of the maximum irradiance value. Thus, this stability parameters enables a reliable comparison of devices, regardless of their varying luminance levels, as recommended by Bard and colleagues.³⁸⁷ This value was recently improved in a following contribution by decoupling hole and electron transport in a multi-layered architecture, reaching 160 cd m⁻², an efficacy of 1.2 cd A⁻¹ and a total emitted energy of 32.7 mJ – Table 10.³⁴⁵

In 2018, Costa and coworkers performed an in-depth study on (i) the molecular design of Cu(i) complexes and their photophysical and electroluminescent properties and (ii) introduced a novel device architecture.³⁸⁸ First, the introduction of two methoxy groups at the 6,6'-position of the bpy ligand led to a two-fold increase of the PLQYs from 6% ([Cu(bpy)(POP)]PF₆) (**Cu108**) to 14% ([Cu(6,6'-(MeO)₂-bpy)(POP)]PF₆) (**Cu153**). This molecular modification was also noted in the performance of the pristine devices as the stabilities and efficiencies improved drastically from 0.6 to 1.1 h and 0.1 cd A⁻¹ to 0.3 cd A⁻¹, respectively. Second, the authors addressed the frequently observed issue of Cu(i) complex-based LECs namely the formation of irreversible oxidized species owing to the irreversible oxidation of the employed Cu(i) complexes. In detail, they introduced a multilayered device architecture incorporating 4,4'-bis(9-carbazolyl)-1,1'-biphenyl, 4,4'-N,N'-dicarbazole-1,1'-biphenyl as hole injection layer to decouple the hole injection, transport and exciton formation – Fig. 38. Finally, this resulted in 10-fold increased stabilities for both complexes without affecting brightness and efficiency. The success of this multi-layered device architecture was further confirmed by other works.^{171,380}

As an alternative strategy to the ones mentioned above (*e.g.* molecular modifications, device architecture) in order to overcome the drawbacks of Cu(i) complexes and Cu(i)-LECs, *e.g.* (i) Jahn–Teller distortion upon excitation, (ii) unforeseen changes from powder to thin-film and (iii) irreversible oxidation behavior of Cu(i) complexes and the related formation of oxidized species in the devices, (iv) lack of efficient blue-emitting Cu(i) complex-based LECs, the research community started to work on Ag(i) as the most natural alternative. This progression was

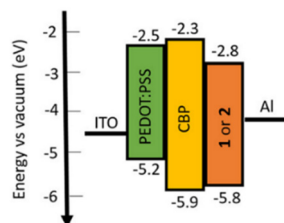


Fig. 38 Energy diagram of the multilayer device architecture (**1** = **Cu108**, **2** = **Cu153**, HOMO and LUMO levels were derived from cyclic voltammetry). Reproduced with permissions from ref. 388.

driven by the fact that Ag(i) complexes are known to exhibit (i) high PLQYs, (ii) a higher ligand field splitting energy of Ag compared to Cu(i) facilitating the design of efficient blue-emitting LECs and (iii) high oxidation potentials.²⁶⁷

In 2015, Moudam *et al.* reported the first ever Ag(i)-based LEC.³⁸⁹ In short, the heteroleptic, tetrahedral Ag(i) complex, [Ag(bpy)(POP)]BF₄ (**Ag20**), was applied in a LEC device (ITO/PEDOT:PSS/**Ag20**:[BMIM]PF₆/LiF:Ag) showing a very broad emission band peaking around 550 nm. A maximum efficacy of nearly 0.45 cd A⁻¹ (5.5 V) with a luminance efficiency of 54 cd m⁻² (9.4 V) was obtained without any notes about the device and complex stability itself. Inspired by this, Costa and coworkers performed an in-depth study of a similar Ag(i) complex, namely [Ag(4,4'-dimethoxy-2,2'-bipyridine)(xantphos)]X (X = BF₄ (**Ag21**), PF₆ (**Ag22**), and ClO₄ (**Ag23**)), to elucidate their electrochemical and electroluminescent behavior.³⁸² The pristine device of all three complexes (ITO/PEDOT:PSS/Ag(i)/Al) was found to show an unusual LEC profile with a continuously decreasing voltage profile associated with a luminance of 40 cd m⁻², efficacy of 0.2 cd A⁻¹, and very poor stability of 30 s – Fig. 39. A joint study of cyclic voltammetry in solution and EIS and X-ray diffraction (XRD) measurements of the fresh and the post-mortem devices revealed the presence of Ag(0) in solution and in post-mortem devices – Fig. 39. In detail, the authors claimed that upon reduction of the studied Ag(i) complexes, an irreversible decomposition to Ag nanoclusters/nanoparticles occurs in solution, but also in thin-films. Finally, the device stability was improved by using a double-layered device architecture to decouple electron injection and exciton formation giving rise to a 4 order of magnitude improved stability (> 80 h) and a brightness of 35 cd m⁻², but the broad whitish electroluminescent spectrum (*x/y* CIE color coordinates of 0.40/0.44) was assigned to an exciplex-like emission. However, both Moudam and Costa did not provide further experimental

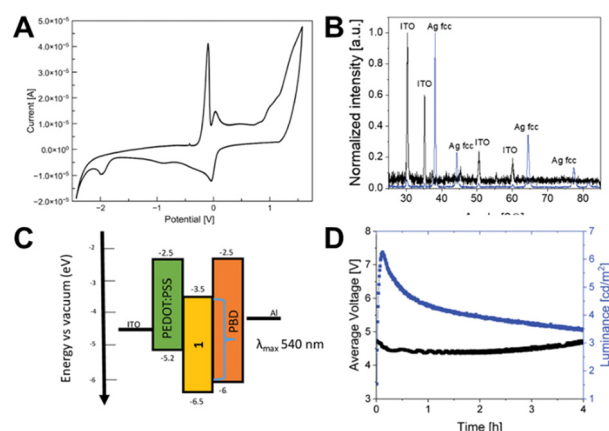


Fig. 39 (A) Second scan of the cyclic voltammetry measurement of **Ag21** in acetonitrile versus Fc/Fc⁺. (B) XRD measurements of fresh (blue) and used (black) **Ag21** pristine devices. The peaks related to ITO and to metallic silver (fcc crystalline silver) are marked above. (C) Schemes of a multilayered device architecture using PBD as electron injection layer. (D) Average voltage and luminance over time (bottom) of **Ag21**-LEC devices driven at pulsed current of 15 mA. Reproduced with permissions from ref. 382.



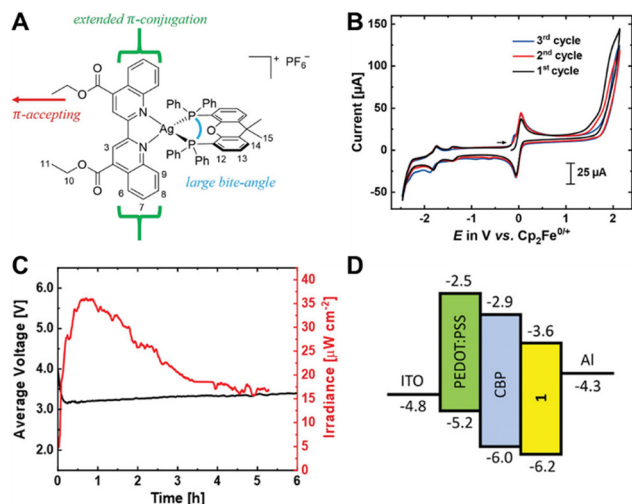


Fig. 40 (A) Chemical structure representation of **Ag₂₄** including the design strategy. (B) Cyclic voltammogram of **Ag₂₄** (10^{-4} M; 100 mV s^{-1}) in $\text{CH}_3\text{CN}/\text{NBu}_4\text{PF}_6$ (0.1 M), at room temperature using (i) working electrode: platinum, (ii) counter electrode: platinum, and (iii) reference electrode: Ag/AgNO₃. (C) Average voltage (black) and irradiance (red) versus time of **CBP-Ag₂₄-LEC**, driven at pulsed 20 mA. (D) Schematic representation of the energy levels for the multi-layered device (**1** = **Ag₂₄**). Reproduced with permissions from ref. 381.

studies to elucidate the emission mechanism of the employed Ag(I) complexes.

In 2023, a thoughtful complex design strategy to provide the first red-emitting Ag(I) complex, $[\text{Ag}(\text{debq})(\text{xantphos})]\text{PF}_6$ (**Ag₂₄**), with PLQYs up to 42%.³⁸¹ More intriguing, outstanding electrochemical stabilities under reductive conditions were obtained. The authors claimed that the high rigidity of the employed debq ligand combined with Xantphos as large bite-angle diphosphine are paramount for the greatly improved electrochemical stability – Fig. 40. Thus, the resulting first ever reported low-energy emitting Ag(I) complex-based LEC outperformed the state-of-the-art pristine reference by three orders of magnitude (2.5 h). EIS and cyclic voltammetry disclosed the oxidation/hole injection as detrimental process. Applying a multilayered device architecture, namely using CBP as hole transport material, to decouple hole injection/transport and exciton formation lead to a device stability of up to 5 h and irradiances of $35 \mu\text{W cm}^{-2}$.

4. Conclusion and outlook

This review provides a comprehensive summary of a hot topic in the design of TADF emitters. Although major efforts are devoted to organic-TADF materials, metal complexes with TADF are attracting an increasing interest in both OLEDs and LECs as shown in the summary provided in this review (Section 1). More importantly, Section 2 has provided a good overview about the design of metal complex based TADF compounds. They can be *ad hoc* engineered *via* chemical modification of coordinated ligand frameworks and/or the type of metal ion center, enabling the control of their photo- and electro-luminescence features in

crystalline powder and, ultimately, in thin-films.²²⁸ In general, a spatial separation between HOMO and LUMO is required to minimize the energy difference between singlet and triplet states. In particular, several design rules have been disclosed for each family of TADF emitters based on the metal ions. In Al-complexes a strong donor ligand coupled to β -diketone is required. The complexation with Al(III) ions is acting as an acceptor moiety. In contrast, in Ir-based complexes, a strong donor (carbene) is directly coordinated to the metal ions and thus, rISC competes with ISC, despite the high SOC due to the heavy atom effect. In the case of Pd-/Pt-based complexes showing TADF, there is a clear lack of design rules as only few examples are known so far. For instance, the coordination of a D–A ligand was found to unlock TADF in a Pd-complex. The introduction of a second metal center and thus, the formation of a dinuclear Pd-complexes led to the first Pd-complex showing TADF. The main strategy for Au-complexes is based on changing the nature of the lowest excited states from intra-ligand to LL'CT character. In this context, three strategies have been proposed: (i) increasing the energy of the ³IL states, (ii) increasing the energy difference between the ³IL and ³LLCT states and/or (iii) decreasing the energy of the ^{1/3}LLCT states. For instance, the first two aspects were realized by combining 2,6-bis(2,4-difluorophenyl)pyridine or 2,6-bis(2,4-diterbutylphenyl)pyrazine accepting-pincer ligands (C^NN^C) with alkynyl ligands bearing strong donor groups, *e.g.* *p*-NPh₂, *m*-NPh₂, phenoxazine.

For d¹⁰ transition metal complexes, the geometry must be taken into account when designing the TADF emitter. For example, in linear Cu-, Ag- and Au-based complexes TADF is mainly achieved through a donor–metal–acceptor system with lowest excited states of LL'CT character. Thus, negatively charged donor ligands (*e.g.*, carbazates) are often combined with strong acceptor ligand like carbenes (*e.g.* NHCs, MCAs). The TADF scenario in trigonal or tetrahedral Cu(I) complexes has been extensively explored and thus, clear design rules have been established. In short, the lowest excited states are mainly of MLCT character since the HOMO and LUMO are spatially well-separated resulting in small ΔE_{ST} . However, the opposing relationship between the HOMO–LUMO overlap, ΔE_{ST} and oscillator strength of the $S_1 \rightarrow S_0$ transition/ τ_{TADF} still displays a challenge in this context.

In contrast, the TADF scenario in Ag- and Zn-based complexes becomes much more challenging owing to energetically low-lying d-orbitals. In the case of Ag-complexes, fluorescence and multi-phosphorescence processes are more frequently noted and only a few examples of unambiguous TADF have been reported. In these cases, TADF was achieved by using a strongly donating ligands, *e.g.*, anionic diphosphines, to destabilize the low-lying d-orbitals resulting in the lowest excited state with a strong MLCT character. There are only a few examples of Zn-complex TADF emitters, but so far, no clear design rules have been established with the exception of the coordination of a D–A ligand that resulted in a TADF Zn-complex, in which the emission originates from LL'CT excited states. This was realized by designing a donor–Zn–acceptor



system including carbenes a acceptor and di-/thiolates as donor ligands.

Although clear design rules are lacking for several families, it has been successfully demonstrated that TADF can be achieved even in those with high SOC constants that are traditionally known as efficient phosphorescent emitters, *e.g.*, Ir-/Pd-/Pt-complexes. This encourages future work to establish clear structure–property relationships and eventually apply them in OLEDs/LECs.

It is also critical to pay attention to the protocols to measure TADF in these families. As discussed in Section 2, it is important to highlight that the assumptions that can be made depend on the systems studied. For instance, in the case of $k_{\text{ISC}} \gg k_{\text{r}}(\text{S}_1 \rightarrow \text{S}_0)$, which is the most common for TMCs, it is advisable to use Boltzmann's equation (eqn (6) and (7)) only if the complexes are highly emissive (PLQY > 50%). In the other cases (*e.g.*, TADF Al-based complexes) the assumption $k_{\text{ISC}} \cong k_{\text{r}}(\text{S}_1 \rightarrow \text{S}_0)$ holds true. Thus, it is better to describe the system using eqn (19).

In this regard, it is also imperative to determine the TADF behavior in powders and thin-films applied to devices to confirm the device trends with respect to EQE values. This is related to the changes in the coordination sphere around the metal ion as the films are mostly processed *via* solution-based techniques in technologies, such as LECs. Changes on the ligand coordination affect the energy and nature of the excited states, SOC, and the HOMO–LUMO overlap, altering ΔE_{ST} and k_{r} . This has been largely neglected in the literature, but it has been shown to be critical for Cu-complexes. For example, efficient and stable blue LECs have recently been achieved by exploiting the information obtained through multivariate analysis of a dataset of > 90 contributions.²²⁸ Here, not only first-order interactions but also their interplay (second order interactions) must be taken into account to chemically design Cu-complexes with the desired emission features (color and PLQY) in thin-films. Thus, it is highly necessary to get more information on these points to reach a more mature understanding, creating a larger data collection that will allow the application of predictive models based on artificial intelligence algorithms. Likewise, ion electrolytes are commonly used as additives in LECs, which could also affect the TADF behavior of the films due to strong internal electric fields and temperature generation,^{390–394} with detrimental effects on the TADF performance and device efficiencies. Thus, the design of these complexes and the active layer must be confirmed by spectroscopic studies of the TADF of the active layers applied to devices.

In terms of device performance, most of the effort over the past 20 years has been devoted to Cu(i) complexes, which basically cover two families of TADF emitters. Today, the best performing blue,²²⁸ yellow,³⁹⁵ and red³⁸⁰ Cu(i) complex-based LECs have brightness of 180/140/30 cd m^{−2} associated with stabilities of 25/0.2/20 h, respectively. While they are not competitive for the mid/low energy visible region, they have recently outperformed the Ir(III)-based counterpart in the blue region. OLEDs based on Cu(i) complexes with very high EQE of 23.6% and luminance of 222 200 cd m^{−2} have already been achieved,³³² while color tunability has been successfully

addressed. Finally, device stability is typically less addressed in OLEDs, while it is a major concern in LECs, in which the electrochemical reversibility of the TADF complexes is critical. This has strongly influenced the hole injection/transport and electron injection/transport processes, respectively, in Cu/Ag complex-based LECs. Here, the device architecture to decouple charge injection/transport and exciton recombination in LECs has successfully prevented device degradation. However, further efforts are needed to provide electrochemically reversible TADF complexes. In this context, Ir-based TADF complexes in LECs as well as the use of Cu-complexes as dopants for hyperfluorescent LECs need to be explored soon. Finally, the use of ionic additives, such as ionic liquids, is a controversial topic regarding their impact on the TADF mechanism in thin-films due to the lack of available data. Therefore, systematic studies are desirable.

Besides the above criticism on the metal complex based TADF emitters for SSL, we need to contextualize the above best performances for OLEDs and LECs with their respective devices with the best organic TADF emitters. In fact, we can conclude that metal complex based TADF emitters are indeed a competitive field. For example, the best EQE and luminance for OLEDs with inorganic TADF emitters have been achieved for Pd-complexes with 31.4% (**Pd7**) and 150 300 cd m^{−2} (**Pd8**).²⁰⁰ However, the record of luminance of 265 000 cd m^{−2} has been reported for the Au family (**Au25**) associated with an EQE of 25.3%.³⁰⁵ These values are very close to the average best OLEDs based on organic TADF emitters.³⁹⁶ Besides the fact that LECs are less performing than OLEDs, the interest in metal complex-based TADF emitters is even more attractive in this field, since LECs based on pristine ionic organic TADF emitters have only exhibited EQEs < 0.1%.³⁹⁷ As comparison, the best LECs with metal complex TADF emitters have shown EQEs of 1.85%.²³⁵ However, it is worth noting that recently ionic organic TADF emitters have been successfully stabilized in an ionic host matrix, reaching the unprecedented record value of 10% EQE.³⁹⁸ Thus, a fair comparison with ionic metal TADF compounds is currently lacking, as metal complexes have not been implemented in host:guest schemes. We believe that these outstanding results will soon have a ripple effect throughout the research community.

In light of the above, we hope that this review will help and motivate the community to further advance this exciting field, which is still full of challenges, toward a mature understanding.

Data availability

No primary research results, software or code have been included and no new data were generated or analysed as part of this review.

Conflicts of interest

There are no conflicts to declare.



References

- 1 F. Perera, *Int. J. Environ. Res. Public Health*, 2018, **15**, 16.
- 2 P. A. Owusu and S. Asumadu-Sarkodie, *Cogent Eng.*, 2016, **3**, 1167990.
- 3 D. Gielen, F. Boshell, D. Saygin, M. D. Bazilian, N. Wagner and R. Gorini, *Energy Strategy Rev.*, 2019, **24**, 38–50.
- 4 T. Güney, *Int. J. Sustainable Dev.*, 2019, **26**, 389–397.
- 5 A. Qazi, F. Hussain, N. A. Rahim, G. Hardaker, D. Alghazzawi, K. Shaban and K. Haruna, *IEEE Access*, 2019, **7**, 63837–63851.
- 6 Y.-H. Kim, H. Cho and T.-W. Lee, *Proc. Natl. Acad. Sci. U. S. A.*, 2016, **113**, 11694–11702.
- 7 B. Pashaei, S. Karimi, H. Shahroosvand, P. Abbasi, M. Pilkington, A. Bartolotta, E. Fresta, J. Fernandez-Cestau, R. D. Costa and F. Bonaccorso, *Chem. Soc. Rev.*, 2019, **48**, 5033–5139.
- 8 C. W. Tang, S. A. VanSlyke and C. H. Chen, *J. Appl. Phys.*, 1989, **65**, 3610–3616.
- 9 C. Adachi, M. A. Baldo, M. E. Thompson and S. R. Forrest, *J. Appl. Phys.*, 2001, **90**, 5048–5051.
- 10 Y.-L. Chang, Z. Wang, M. Helander, J. Qiu, D. Puzzo and Z. Lu, *Org. Electron.*, 2012, **13**, 925–931.
- 11 D. H. Kim, N. S. Cho, H. Y. Oh, J. H. Yang, W. S. Jeon, J. S. Park, M. C. Suh and J. H. Kwon, *Adv. Mater.*, 2011, **23**, 2721–2726.
- 12 Y. H. Kim, C. Wolf, H. Cho, S. H. Jeong and T. W. Lee, *Adv. Mater.*, 2016, **28**, 734–741.
- 13 D. Kabra, L. P. Lu, M. H. Song, H. J. Snaith and R. H. Friend, *Adv. Mater.*, 2010, **22**, 3194–3198.
- 14 H. Uoyama, K. Goushi, K. Shizu, H. Nomura and C. Adachi, *Nature*, 2012, **492**, 234–238.
- 15 Y. K. Chen, J. Jayakumar, C. M. Hsieh, T. L. Wu, C. C. Liao, J. Pandidurai, C. L. Ko, W. Y. Hung and C. H. Cheng, *Adv. Mater.*, 2021, **33**, 2008032.
- 16 V. L. Colvin, M. C. Schlamp and A. P. Alivisatos, *Nature*, 1994, **370**, 354–357.
- 17 H. Mattoussi, L. H. Radzilowski, B. O. Dabbousi, E. L. Thomas, M. G. Bawendi and M. F. Rubner, *J. Appl. Phys.*, 1998, **83**, 7965–7974.
- 18 M. Schlamp, X. Peng and A.-L. Alivisatos, *J. Appl. Phys.*, 1997, **82**, 5837–5842.
- 19 S. Coe, W.-K. Woo, M. Bawendi and V. Bulović, *Nature*, 2002, **420**, 800–803.
- 20 S. Coe-Sullivan, J. S. Steckel, W. K. Woo, M. G. Bawendi and V. Bulović, *Adv. Funct. Mater.*, 2005, **15**, 1117–1124.
- 21 J. Kwak, W. K. Bae, D. Lee, I. Park, J. Lim, M. Park, H. Cho, H. Woo, D. Y. Yoon and K. Char, *Nano Lett.*, 2012, **12**, 2362–2366.
- 22 X. Dai, Z. Zhang, Y. Jin, Y. Niu, H. Cao, X. Liang, L. Chen, J. Wang and X. Peng, *Nature*, 2014, **515**, 96–99.
- 23 Z.-K. Tan, R. S. Moghaddam, M. L. Lai, P. Docampo, R. Higler, F. Deschler, M. Price, A. Sadhanala, L. M. Pazos and D. Credgington, *Nat. Nanotechnol.*, 2014, **9**, 687–692.
- 24 Y. H. Kim, H. Cho, J. H. Heo, T. S. Kim, N. Myoung, C. L. Lee, S. H. Im and T. W. Lee, *Adv. Mater.*, 2015, **27**, 1248–1254.
- 25 H. Cho, S.-H. Jeong, M.-H. Park, Y.-H. Kim, C. Wolf, C.-L. Lee, J. H. Heo, A. Sadhanala, N. Myoung and S. Yoo, *Science*, 2015, **350**, 1222–1225.
- 26 K. Lin, J. Xing, L. N. Quan, F. P. G. de Arquer, X. Gong, J. Lu, L. Xie, W. Zhao, D. Zhang and C. Yan, *Nature*, 2018, **562**, 245–248.
- 27 Z. Chu, Q. Ye, Y. Zhao, F. Ma, Z. Yin, X. Zhang and J. You, *Adv. Mater.*, 2021, **33**, 2007169.
- 28 Y. Yang and Q. Pei, *J. Appl. Phys.*, 1997, **81**, 3294–3298.
- 29 S. Tang, A. Sandström, P. Lundberg, T. Lanz, C. Larsen, S. van Reenen, M. Kemerink and L. Edman, *Nat. Commun.*, 2017, **8**, 1–9.
- 30 M. S. Shur and R. Zukauskas, *Proc. IEEE*, 2005, **93**, 1691–1703.
- 31 I. L. Azevedo, M. G. Morgan and F. Morgan, *Proc. IEEE*, 2009, **97**, 481–510.
- 32 R. S. Cok, M. Meitl, R. Rotzoll, G. Melnik, A. Fecioru, A. J. Trindade, B. Raymond, S. Bonafede, D. Gomez and T. Moore, *J. Soc. Inf. Disp.*, 2017, **25**, 589–609.
- 33 H. Zhang and J. A. Rogers, *Adv. Opt. Mater.*, 2019, **7**, 1800936.
- 34 Q. Huang, Y. Zou, S. A. Bourelle, T. Zhai, T. Wu, Y. Tan, Y. Li, J. Li, S. Duham and T. Song, *Nanoscale Horiz.*, 2019, **4**, 924–932.
- 35 M. Kneissl, T. Kolbe, C. Chua, V. Kueller, N. Lobo, J. Stellmach, A. Knauer, H. Rodriguez, S. Einfeldt and Z. Yang, *Semicond. Sci. Technol.*, 2010, **26**, 014036.
- 36 T.-Y. Seong, J. Han, H. Amano and H. Morkoç, *III-Nitride based light emitting diodes and applications*, Springer, 2013.
- 37 C. Weisbuch, M. Piccardo, L. Martinelli, J. Iveland, J. Peretti and J. S. Speck, *Phys. Status Solidi*, 2015, **212**, 899–913.
- 38 H. Masui, S. Nakamura, S. P. DenBaars and U. K. Mishra, *IEEE Trans. Electron Devices*, 2009, **57**, 88–100.
- 39 L. Chen, C.-C. Lin, C.-W. Yeh and R.-S. Liu, *Materials*, 2010, **3**, 2172–2195.
- 40 H. Lin, T. Hu, Y. Cheng, M. Chen and Y. Wang, *Laser Photonics Rev.*, 2018, **12**, 1700344.
- 41 G. B. Nair and S. J. Dhoble, *The Fundamentals and Applications of Light-Emitting Diodes: The Revolution in the Lighting Industry*, Woodhead Publishing, 2020.
- 42 J. Li, J. Wang, X. Yi, Z. Liu, T. Wei, J. Yan and B. Xue, *III-Nitrides Light Emitting Diodes: Technology and Applications*, Springer, 2020, pp. 7–18.
- 43 G. Held, *Introduction to light emitting diode technology and applications*, Auerbach Publications, 2016.
- 44 X. Sun, J. Liu, L. C. Kimerling and J. Michel, *Opt. Lett.*, 2009, **34**, 1198–1200.
- 45 J. Jiang, M. Xue, C.-Y. Lu, C. S. Fenrich, M. Morea, K. Zang, J. Gao, M. Cheng, Y. Zhang and T. I. Kamins, *ACS Photonics*, 2019, **6**, 915–923.
- 46 M. Premkumar, M. Arun, S. Sathiya Priya, D. Kalaiarasi and R. Prathipa, *Mater. Today: Proc.*, 2023, **80**, 1932–1935.
- 47 H.-J. Yeh and J. S. Smith, *IEEE Photonics Technol. Lett.*, 1994, **6**, 706–708.
- 48 S. Tsintzos, N. Pelekanos, G. Konstantinidis, Z. Hatzopoulos and P. Savvidis, *Nature*, 2008, **453**, 372–375.



- 49 H. Morkoc and S. N. Mohammad, *Science*, 1995, **267**, 51–55.
- 50 D.-S. Shin, D.-P. Han, J.-Y. Oh and J.-I. Shim, *Appl. Phys. Lett.*, 2012, **100**, 153506.
- 51 W.-C. Chao, T.-H. Chiang, Y.-C. Liu, Z.-X. Huang, C.-C. Liao, C.-H. Chu, C.-H. Wang, H.-W. Tseng, W.-Y. Hung and P.-T. Chou, *Commun. Mater.*, 2021, **2**, 96.
- 52 Y. Ozen, T. Sertel, S. S. Cetin and S. Ozcelik, *J. Electron. Mater.*, 2018, **47**, 7129–7133.
- 53 W. C. Peng and Y. S. Wu, *Appl. Phys. Lett.*, 2004, **84**, 1841–1843.
- 54 E. Dupont, H. Liu, M. Buchanan, S. Chiu and M. Gao, *Appl. Phys. Lett.*, 2000, **76**, 4–6.
- 55 T. Khan, P. Bodrogi, Q. T. Vinh and H. Winkler, *LED lighting: Technology and perception*, John Wiley & Sons, 2015.
- 56 D. Zhu, D. Wallis and C. Humphreys, *Rep. Prog. Phys.*, 2013, **76**, 106501.
- 57 S. N. Mohammad and H. Morkoç, *Prog. Quantum Electron.*, 1996, **20**, 361–525.
- 58 M. S. Wong, S. Nakamura and S. P. DenBaars, *ECS J. Solid State Sci. Technol.*, 2019, **9**, 015012.
- 59 T. Ayari, S. Sundaram, C. Bishop, A. Mballo, P. Vuong, Y. Halfaya, S. Karrakhou, S. Gautier, P. L. Voss and J. P. Salvestrini, *Adv. Mater. Technol.*, 2019, **4**, 1900164.
- 60 M. A. Naeser, R. Zafonte, M. H. Krengel, P. I. Martin, J. Frazier, M. R. Hamblin, J. A. Knight, W. P. Meehan III and E. H. Baker, *J. Neurotrauma*, 2014, **31**, 1008–1017.
- 61 D. R. Opel, E. Hagstrom, A. K. Pace, K. Sisto, S. A. Hirano-ALi, S. Desai and J. Swan, *J. Clin. Aesthet. Dermatol.*, 2015, **8**, 36.
- 62 E. C. P. Leal-Junior, A. A. Vanin, E. F. Miranda, P. D. T. C. De Carvalho, S. Dal Corso and J. M. Bjordal, *Lasers Med. Sci.*, 2015, **30**, 925–939.
- 63 T. Müller, J. Skiba-Szymanska, A. Krysa, J. Huwer, M. Felle, M. Anderson, R. Stevenson, J. Heffernan, D. A. Ritchie and A. Shields, *Nat. Commun.*, 2018, **9**, 1–6.
- 64 C. Chow, C. Yeh, Y. Liu and Y. Liu, *IEEE Photon. Soc. Newslett.*, 2012, **26**, 9–13.
- 65 Y. H. Song, S. H. Choi, W. K. Park, J. S. Yoo, S. B. Kwon, B. K. Kang, S. R. Park, Y. S. Seo, W. S. Yang and D. H. Yoon, *Sci. Rep.*, 2018, **8**, 1–6.
- 66 H. A. Höppe, *Angew. Chem., Int. Ed.*, 2009, **48**, 3572–3582.
- 67 N. Guan, X. Dai, A. V. Babichev, F. H. Julien and M. Tchernycheva, *Chem. Sci.*, 2017, **8**, 7904–7911.
- 68 C. W. Tang and S. A. VanSlyke, *Appl. Phys. Lett.*, 1987, **51**, 913–915.
- 69 A. Salehi, X. Fu, D. H. Shin and F. So, *Adv. Funct. Mater.*, 2019, **29**, 1808803.
- 70 N. T. Kalyani and S. Dhoble, *Renewable Sustainable Energy Rev.*, 2012, **16**, 2696–2723.
- 71 T. Oyamada, C. Maeda, H. Sasabe and C. Adachi, *Jpn. J. Appl. Phys.*, 2003, **42**, L1535.
- 72 Y. Xu, P. Xu, D. Hu and Y. Ma, *Chem. Soc. Rev.*, 2021, **50**, 1030–1069.
- 73 G. M. Farinola and R. Ragni, *Chem. Soc. Rev.*, 2011, **40**, 3467–3482.
- 74 S. Ho, S. Liu, Y. Chen and F. So, *J. Photonics Energy*, 2015, **5**, 057611.
- 75 K. S. Yook and J. Y. Lee, *Adv. Mater.*, 2014, **26**, 4218–4233.
- 76 C. A. Zuniga, S. Barlow and S. R. Marder, *Chem. Mater.*, 2011, **23**, 658–681.
- 77 W. J. Hyun, S. H. Im, O. O. Park and B. D. Chin, *Org. Electron.*, 2012, **13**, 579–585.
- 78 K. M. Kuznetsov, M. I. Kozlov, A. N. Aslandukov, A. A. Vashchenko, A. Medved'ko, E. Latipov, A. S. Goloveshkin, D. Tsybarenko and V. V. Utochnikova, *Dalton Trans.*, 2021, **50**, 9685–9689.
- 79 J. Jeong, D. Mascaro and S. Blair, *Org. Electron.*, 2011, **12**, 2095–2102.
- 80 C. S. Buga and J. C. Viana, *Adv. Mater. Technol.*, 2021, 2001016.
- 81 J. Li, L. Xu, C. W. Tang and A. A. Shestopalov, *ACS Appl. Mater. Interfaces*, 2016, **8**, 16809–16815.
- 82 J.-C. G. Bünzli, S. Comby, A.-S. Chauvin and C. D. Vandevyver, *J. Rare Earths*, 2007, **25**, 257–274.
- 83 M. C. Gather, A. Köhnen and K. Meerholz, *Adv. Mater.*, 2011, **23**, 233–248.
- 84 A. L. Hicks, T. L. Theis and M. L. Zellner, *J. Ind. Ecol.*, 2015, **19**, 285–295.
- 85 D. F. de Souza, P. P. F. da Silva, L. F. A. Fontenele, G. D. Barbosa and M. de Oliveira Jesus, *Energy Rep.*, 2019, **5**, 409–424.
- 86 T. D. Little, P. Dib, K. Shah, N. Barraford and B. Gallagher, *IEEE*, 2008, 373–378.
- 87 A. Sabbar, S. Madhusoodhanan, S. Al-Kabi, B. Dong, J. Wang, S. Atcity, R. Kaplar, D. Ding, A. Mantooth and S.-Q. Yu, *Sci. Rep.*, 2019, **9**, 1–8.
- 88 S. M. Pawson and M.-F. Bader, *Ecol. Appl.*, 2014, **24**, 1561–1568.
- 89 B. K. Hawes, T. T. Brunyé, C. R. Mahoney, J. M. Sullivan and C. D. Aall, *Int. J. Ind. Ergon.*, 2012, **42**, 122–128.
- 90 H. Yersin, R. Czerwieniec, U. Monkowius, R. Ramazanov, R. Valiev, M. Z. Shafikov, W.-M. Kwok and C. Ma, *Coord. Chem. Rev.*, 2023, **478**, 214975.
- 91 R. Delorme and F. Perrin, *J. Phys. Radium*, 1929, **10**, 177–186.
- 92 G. N. Lewis, D. Lipkin and T. T. Magel, *J. Am. Chem. Soc.*, 1941, **63**, 3005–3018.
- 93 C. Parker and C. Hatchard, *Trans. Faraday Soc.*, 1961, **57**, 1894–1904.
- 94 S. Kim, H. J. Kwon, S. Lee, H. Shim, Y. Chun, W. Choi, J. Kwack, D. Han, M. Song and S. Kim, *Adv. Mater.*, 2011, **23**, 3511–3516.
- 95 B. A. Prabowo, L.-C. Su, Y.-F. Chang, H.-C. Lai, N.-F. Chiu and K.-C. Liu, *Sens. Actuators, B*, 2016, **222**, 1058–1065.
- 96 Y. Jeon, H. R. Choi, M. Lim, S. Choi, H. Kim, J. H. Kwon, K. C. Park and K. C. Choi, *Adv. Mater. Technol.*, 2018, **3**, 1700391.
- 97 Y. J. Song, J.-W. Kim, H.-E. Cho, Y. H. Son, M. H. Lee, J. Lee, K. C. Choi and S.-M. Lee, *ACS Nano*, 2020, **14**, 1133–1140.
- 98 N. Thejo Kalyani and S. J. Dhoble, *Renewable Sustainable Energy Rev.*, 2015, **44**, 319–347.



- 99 C. Zhang, R. Liu, D. Zhang and L. Duan, *Adv. Funct. Mater.*, 2020, **30**, 1907156.
- 100 S. B. Meier, D. Tordera, A. Pertegas, C. Roldan-Carmona, E. Orti and H. J. Bolink, *Mater. Today*, 2014, **17**, 217–223.
- 101 D. Tordera, S. Meier, M. Lenes, R. D. Costa, E. Ortí, W. Sarfert and H. J. Bolink, *Adv. Mater.*, 2012, **24**, 897–900.
- 102 S. Tang and L. Edman, *Photoluminescent Materials and Electroluminescent Devices*, Springer, 2017, pp. 375–395.
- 103 A. Sandström and L. Edman, *Energy Technol.*, 2015, **3**, 329–339.
- 104 S. Karimi, H. Shahroosvand, S. Bellani and F. Bonaccorso, *J. Phys. Chem. C*, 2021, **125**, 819–829.
- 105 Q. Zhang, Q. Zhou, Y. Cheng, L. Wang, D. Ma, X. Jing and F. Wang, *Adv. Funct. Mater.*, 2006, **16**, 1203–1208.
- 106 R. D. Costa, E. Orti, H. J. Bolink, F. Monti, G. Accorsi and N. Armadori, *Angew. Chem., Int. Ed.*, 2012, **51**, 8178–8211.
- 107 Q. Sun, Y. Li and Q. Pei, *J. Disp. Technol.*, 2007, **3**, 211–224.
- 108 Q. Pei, G. Yu, C. Zhang, Y. Yang and A. J. Heeger, *Science*, 1995, **269**, 1086–1088.
- 109 J.-K. Lee, D. Yoo and M. F. Rubner, *Chem. Mater.*, 1997, **9**, 1710–1712.
- 110 M. S. Lowry and S. Bernhard, *Chem. – Eur. J.*, 2006, **12**, 7970–7977.
- 111 J. D. Slinker, J. Rivnay, J. S. Moskowitz, J. B. Parker, S. Bernhard, H. D. Abruña and G. G. Malliaras, *J. Mater. Chem.*, 2007, **17**, 2976–2988.
- 112 E. Fresta and R. D. Costa, *J. Mater. Chem. C*, 2017, **5**, 5643–5675.
- 113 J. D. Slinker, J. Rivnay, J. A. DeFranco, D. A. Bernards, A. A. Gorodetsky, S. T. Parker, M. P. Cox, R. Rohl, G. G. Malliaras and S. Flores-Torres, *J. Appl. Phys.*, 2006, **99**, 074502.
- 114 F. Dumur, D. Bertin and D. Gigmes, *Internet J. Nanotechnol.*, 2012, **9**, 377–395.
- 115 J. E. Namanga, H. Pei, G. Bousrez, V. Smetana, N. Gerlitzki and A.-V. Mudring, *ACS Appl. Energy Mater.*, 2020, **3**, 9271–9277.
- 116 J. Zhang, L. Zhou, H. A. Al-Attar, K. Shao, L. Wang, D. Zhu, Z. Su, M. R. Bryce and A. P. Monkman, *Adv. Funct. Mater.*, 2013, **23**, 4667–4677.
- 117 A. Malewar, Light-emitting electrochemical cell (LECs) – now an efficient and bright device, <https://www.techexplorist.com/light-emitting-electrochemical-cell-lecs-now-efficient-bright-device/10428/>.
- 118 K. Youssef, Y. Li, S. O'Keeffe, L. Li and Q. Pei, *Adv. Funct. Mater.*, 2020, **30**, 1909102.
- 119 Y. Tang, M. Deng, Z. Zhou, C. Kang, J. Wang and Q. Liu, *Coord. Chem. Rev.*, 2024, **499**, 215490.
- 120 X.-K. Chen, D. Kim and J.-L. Brédas, *Acc. Chem. Res.*, 2018, **51**, 2215–2224.
- 121 X. Liang, Z.-L. Tu and Y.-X. Zheng, *Chem. – Eur. J.*, 2019, **25**, 5623–5642.
- 122 T.-Y. Li, S.-J. Zheng, P. I. Djurovich and M. E. Thompson, *Chem. Rev.*, 2024, **124**, 4332–4392.
- 123 A. Endo, M. Ogasawara, A. Takahashi, D. Yokoyama, Y. Kato and C. Adachi, *Adv. Mater.*, 2009, **21**, 4802–4806.
- 124 Y. Tao, K. Yuan, T. Chen, P. Xu, H. Li, R. Chen, C. Zheng, L. Zhang and W. Huang, *Adv. Mater.*, 2014, **26**, 7931–7958.
- 125 D. Volz and J. Photonics, *Energy*, 2016, **6**, 020901.
- 126 K. Goushi, K. Yoshida, K. Sato and C. Adachi, *Nat. Photonics*, 2012, **6**, 253–258.
- 127 H. Yersin, A. F. Rausch, R. Czerwieniec, T. Hofbeck and T. Fischer, *Coord. Chem. Rev.*, 2011, **255**, 2622–2652.
- 128 *Highly efficient OLEDs: Materials based on thermally activated delayed fluorescence*, ed. H. Yersin, John Wiley & Sons, 2019.
- 129 M. Y. Wong and E. Zysman-Colman, in *Light-Emitting Electrochemical Cells: Concepts, Advances and Challenges*, ed. R. D. Costa, Springer International Publishing, Cham, 2017, pp. 237–266.
- 130 G. Hong, X. Gan, C. Leonhardt, Z. Zhang, J. Seibert, J. M. Busch and S. Bräse, *Adv. Mater.*, 2021, **33**, 2005630.
- 131 C. Adachi, *Jpn. J. Appl. Phys.*, 2014, **53**, 060101.
- 132 A. Endo, K. Sato, K. Yoshimura, T. Kai, A. Kawada, H. Miyazaki and C. Adachi, *Appl. Phys. Lett.*, 2011, **98**, 42.
- 133 K. Sato, K. Shizu, K. Yoshimura, A. Kawada, H. Miyazaki and C. Adachi, *Phys. Rev. Lett.*, 2013, **110**, 247401.
- 134 H. Yersin, A. F. Rausch and R. Czerwieniec, *Phys. Org. Semicond.*, 2012, 371–424.
- 135 P. W. Atkins and R. S. Friedman, *Molecular quantum mechanics*, Oxford University Press, New York, 2011, 4th edn.
- 136 M. Montalti, A. Credi, L. Prodi and M. T. Gandolfi, *Handbook of photochemistry*, CRC Press, Boca Raton, 2006.
- 137 R. Ishimatsu, S. Matsunami, K. Shizu, C. Adachi, K. Nakano and T. Imato, *J. Phys. Chem. A*, 2013, **117**, 5607–5612.
- 138 Y. Im and J. Y. Lee, *Chem. Mater.*, 2014, **26**, 1413–1419.
- 139 L.-S. Cui, S.-B. Ruan, F. Bencheikh, R. Nagata, L. Zhang, K. Inada, H. Nakanotani, L.-S. Liao and C. Adachi, *Nat. Commun.*, 2017, **8**, 1–8.
- 140 E. Y.-T. Li, T.-Y. Jiang, Y. Chi and P.-T. Chou, *Phys. Chem. Chem. Phys.*, 2014, **16**, 26184–26192.
- 141 M. Baba, *J. Phys. Chem. A*, 2011, **115**, 9514–9519.
- 142 P. Ceroni, *Chem*, 2016, **1**, 524–526.
- 143 T. Tsuzuki and S. Tokito, *Adv. Mater.*, 2007, **19**, 276–280.
- 144 T.-Y. Li, J. Wu, Z.-G. Wu, Y.-X. Zheng, J.-L. Zuo and Y. Pan, *Coord. Chem. Rev.*, 2018, **374**, 55–92.
- 145 T. Nakagawa, S.-Y. Ku, K.-T. Wong and C. Adachi, *Chem. Commun.*, 2012, **48**, 9580–9582.
- 146 S. Y. Lee, T. Yasuda, H. Nomura and C. Adachi, *Appl. Phys. Lett.*, 2012, **101**, 093306.
- 147 G. Méhes, H. Nomura, Q. Zhang, T. Nakagawa and C. Adachi, *Angew. Chem., Int. Ed.*, 2012, **51**, 11311–11315.
- 148 S. Liu, B. Yang, J. Chen, D. Wei, D. Zheng, Q. Kong, W. Deng and K. Han, *Angew. Chem., Int. Ed.*, 2020, **59**, 21925–21929.
- 149 J. Adachi, H. Kakizoe, P. K. D. Tsang and A. Endo, *SID Symp. Dig. Tech. Pap.*, 2019, **50**, 95–98.
- 150 C. Adachi, *SID Symp. Dig. Tech. Pap.*, 2013, **44**, 513–514.
- 151 A. M. Polgar, C. M. Tonge, C. J. Christopherson, N. R. Paisley, A. C. Reyes and Z. M. Hudson, *ACS Appl. Mater. Interfaces*, 2020, **12**, 38602–38613.



- 152 H. Nakanotani, T. Higuchi, T. Furukawa, K. Masui, K. Morimoto, M. Numata, H. Tanaka, Y. Sagara, T. Yasuda and C. Adachi, *Nat. Commun.*, 2014, **5**, 4016.
- 153 K. Stavrou, L. G. Franca, A. Danos and A. P. Monkman, *Nat. Photonics*, 2024, **18**, 554–561.
- 154 S. K. Behera and R. D. Costa, *J. Mater. Chem. C*, 2023, **11**, 13647–13656.
- 155 F. B. Dias, T. J. Penfold and A. P. Monkman, *Methods Appl. Fluoresc.*, 2017, **5**, 012001.
- 156 P. W. Atkins, *Quanta: A Handbook of Concepts*, Oxford University Press, 1991.
- 157 B. Milián-Medina and J. Gierschner, *Org. Electron.*, 2012, **13**, 985–991.
- 158 S. Sudheendran Swayamprabha, D. K. Dubey, Shah Nawaz, R. A. K. Yadav, M. R. Nagar, A. Sharma, F. C. Tung and J. H. Jou, *Adv. Sci.*, 2021, **8**, 2002254.
- 159 Z. D. Popovic and H. Aziz, *IEEE J. Sel. Top. Quantum Electron.*, 2002, **8**, 362–371.
- 160 M. Y. Wong and E. Zysman-Colman, *Adv. Mater.*, 2017, **29**, 1605444.
- 161 M. N. Berberan-Santos and J. M. M. Garcia, *J. Am. Chem. Soc.*, 1996, **118**, 9391–9394.
- 162 R. J. Vázquez, J. H. Yun, A. K. Muthike, M. Howell, H. Kim, I. K. Madu, T. Kim, P. Zimmerman, J. Y. Lee and T. G. Iii, *J. Am. Chem. Soc.*, 2020, **142**, 8074–8079.
- 163 Y. Wada, H. Nakagawa, S. Matsumoto, Y. Wakisaka and H. Kaji, *Nat. Photonics*, 2020, **14**, 643–649.
- 164 N. Haase, A. Danos, C. Pflumm, A. Morherr, P. Stachelek, A. Mekic, W. Brütting and A. P. Monkman, *J. Phys. Chem. C*, 2018, **122**, 29173–29179.
- 165 J. R. Kirchhoff, R. E. Gamache, Jr., M. W. Blaskie, A. A. Del Paggio, R. K. Lengel and D. R. McMillin, *Inorg. Chem.*, 1983, **22**, 2380–2384.
- 166 M. Iwamura, H. Watanabe, K. Ishii, S. Takeuchi and T. Tahara, *J. Am. Chem. Soc.*, 2011, **133**, 7728–7736.
- 167 N. Armaroli, G. Accorsi, F. Cardinali and A. Listorti, in *Photochemistry and Photophysics of Coordination Compounds I*, ed. V. Balzani and S. Campagna, Springer Berlin Heidelberg, Berlin, Heidelberg, 2007, pp. 69–115.
- 168 M. Iwamura, S. Takeuchi and T. Tahara, *Acc. Chem. Res.*, 2015, **48**, 782–791.
- 169 R. Hamze, S. Shi, S. C. Kapper, D. S. Muthiah Ravinson, L. Estergreen, M.-C. Jung, A. C. Tadde, R. Haiges, P. I. Djurovich, J. L. Peltier, R. Jazsar, G. Bertrand, S. E. Bradforth and M. E. Thompson, *J. Am. Chem. Soc.*, 2019, **141**, 8616–8626.
- 170 D. S. M. Ravinson and M. E. Thompson, *Mater. Horiz.*, 2020, **7**, 1210–1217.
- 171 E. Fresta, G. U. Mahoro, L. M. Cavinato, J.-F. Lohier, J.-L. Renaud, S. Gaillard and R. D. Costa, *Adv. Opt. Mater.*, 2022, **10**, 2101999.
- 172 G. U. Mahoro, J. Fernandez-Cestau, J.-L. Renaud, P. B. Coto, R. D. Costa and S. Gaillard, *Adv. Opt. Mater.*, 2020, **8**, 2000260.
- 173 C. M. Brown, C. Li, V. Carta, W. Li, Z. Xu, P. H. F. Stroppa, I. D. Samuel, E. Zysman-Colman and M. O. Wolf, *Inorg. Chem.*, 2019, **58**, 7156–7168.
- 174 Y. Tsuchiya, S. Diesing, F. Bencheikh, Y. Wada, P. L. dos Santos, H. Kaji, E. Zysman-Colman, I. D. W. Samuel and C. Adachi, *J. Phys. Chem. A*, 2021, **125**, 8074–8089.
- 175 D. Y. Kondakov, *Philos. Trans. R. Soc. A*, 2015, **373**, 20140321.
- 176 Y. Sun, N. C. Giebink, H. Kanno, B. Ma, M. E. Thompson and S. R. Forrest, *Nature*, 2006, **440**, 908–912.
- 177 G. Schwartz, M. Pfeiffer, S. Reineke, K. Walzer and K. Leo, *Adv. Mater.*, 2007, **19**, 3672–3676.
- 178 C.-J. Zheng, J. Wang, J. Ye, M.-F. Lo, X.-K. Liu, M.-K. Fung, X.-H. Zhang and C.-S. Lee, *Adv. Mater.*, 2013, **25**, 2205–2211.
- 179 L. M. Cavinato, K. Yamaoka, S. Lipinski, V. Calvi, D. Wehenkel, R. van Rijn, K. Albrecht and R. D. Costa, *Adv. Funct. Mater.*, 2023, **33**, 2302483.
- 180 K. Nakao, H. Sasabe, Y. Shibuya, A. Matsunaga, H. Katagiri and J. J. A. C. Kido, *Angew. Chem.*, 2021, **133**, 6101–6106.
- 181 H. Yersin, R. Czerwieniec, M. Z. Shafikov and A. F. Suleymanova, *ChemPhysChem*, 2017, **18**, 3508–3535.
- 182 Y. Zhang, T. S. Lee, J. M. Favale, D. C. Leary, J. L. Petersen, G. D. Scholes, F. N. Castellano and C. Milsmann, *Nat. Chem.*, 2020, **12**, 345–352.
- 183 M. Matsuya, H. Sasabe, S. Sumikoshi, K. Hoshi, K. Nakao, K. Kumada, R. Sugiyama, R. Sato and J. Kido, *Bull. Chem. Soc. Jpn.*, 2023, **96**, 183–189.
- 184 R. D. Costa, F. J. Céspedes-Guirao, E. Ortí, H. J. Bolink, J. Gierschner, F. Fernández-Lázaro and A. Sastre-Santos, *Chem. Commun.*, 2009, 3886–3888.
- 185 A. Tsuboyama, H. Iwawaki, M. Furugori, T. Mukaide, J. Kamatani, S. Igawa, T. Moriyama, S. Miura, T. Takiguchi, S. Okada, M. Hoshino and K. Ueno, *J. Am. Chem. Soc.*, 2003, **125**, 12971–12979.
- 186 L. He, L. Duan, J. Qiao, D. Zhang, L. Wang and Y. Qiu, *Chem. Commun.*, 2011, **47**, 6467–6469.
- 187 R. Bai, X. Meng, X. Wang and L. J. A. F. M. He, *Adv. Funct. Mater.*, 2020, **30**, 1907169.
- 188 G. Albrecht, C. Geis, J. Herr, J. Ruhl, R. Göttlich and D. Schlettwein, *Org. Electron.*, 2019, **65**, 321–326.
- 189 J. M. Herr, C. Rössiger, H. Locke, M. Wilhelm, J. Becker, W. Heimbrod, D. Schlettwein and R. Göttlich, *Dyes Pigm.*, 2020, **180**, 108512.
- 190 H. Na and T. S. Teets, *J. Am. Chem. Soc.*, 2018, **140**, 6353–6360.
- 191 Y.-J. Gao, T.-T. Zhang and W.-K. Chen, *J. Phys. Chem. C*, 2021, **125**, 5670–5677.
- 192 M. Z. Shafikov, R. Martinscroft, C. Hodgson, A. Hayer, A. Auch and V. N. Kozhevnikov, *Inorg. Chem.*, 2021, **60**, 1780–1789.
- 193 L.-Y. Peng, Z.-W. Li, G.-N. Pan, W.-K. Chen, Y.-J. Gao and G. Cui, *Phys. Chem. Chem. Phys.*, 2023, **25**, 6454–6460.
- 194 P. Pander, A. V. Zaytsev, A. Sil, G. V. Baryshnikov, F. Siddique, J. A. G. Williams, F. B. Dias and V. N. Kozhevnikov, *Chem. Sci.*, 2023, **14**, 13934–13943.
- 195 Z. Q. Zhu, T. Fleetham, E. Turner and J. Li, *Adv. Mater.*, 2015, **27**, 2533–2537.
- 196 Z.-Q. Zhu, C.-D. Park, K. Klimes and J. Li, *Adv. Opt. Mater.*, 2019, **7**, 1801518.



- 197 P. W. Zach, S. A. Freunberger, I. Klimant and S. M. Borisov, *ACS Appl. Mater. Interfaces*, 2017, **9**, 38008–38023.
- 198 G. Li, Q. Chen, J. Zheng, Q. Wang, F. Zhan, W. Lou, Y. F. Yang and Y. She, *Inorg. Chem.*, 2019, **58**, 14349–14360.
- 199 Y. She, K. Xu, X. Fang, Y. F. Yang, W. Lou, Y. Hu, Q. Zhang and G. Li, *Inorg. Chem.*, 2021, **60**, 12972–12983.
- 200 J.-G. Yang, X. Feng, N. Li, J. Li, X.-F. Song, M.-D. Li, G. Cui, J. Zhang, C. Jiang and C. J. S. A. Yang, *Sci. Adv.*, 2023, **9**, eadh0198.
- 201 P. Pander, R. Daniels, A. V. Zaytsev, A. Horn, A. Sil, T. J. Penfold, J. G. Williams, V. N. Kozhevnikov and F. B. Dias, *Chem. Sci.*, 2021, **12**, 6172–6180.
- 202 M. Z. Shafikov, R. Daniels, P. Pander, F. B. Dias, J. A. G. Williams and V. N. Kozhevnikov, *ACS Appl. Mater. Interfaces*, 2019, **11**, 8182–8193.
- 203 V. N. Kozhevnikov, M. C. Durrant and J. A. G. Williams, *Inorg. Chem.*, 2011, **50**, 6304–6313.
- 204 P. Pander, A. V. Zaytsev, A. Sil, J. A. G. Williams, P.-H. Lanoe, V. N. Kozhevnikov and F. B. Dias, *J. Mater. Chem. C*, 2021, **9**, 10276–10287.
- 205 W.-P. To, G. S.-M. Tong, W. Lu, C. Ma, J. Liu, A. L.-F. Chow and C.-M. Che, *Angew. Chem.*, 2012, **51**, 2654–2657.
- 206 W. P. To, K. T. Chan, G. S. M. Tong, C. Ma, W. M. Kwok, X. Guan, K. H. Low and C. M. Che, *Angew. Chem., Int. Ed.*, 2013, **52**, 6648.
- 207 F. F. Hung, W. P. To, J. J. Zhang, C. Ma, W. Y. Wong and C. M. Che, *Chem. – Eur. J.*, 2014, **20**, 8604–8614.
- 208 R. Kumar, A. Linden and C. J. A. C. Nevado, *Angew. Chem.*, 2015, **127**, 14495–14498.
- 209 W.-P. To, G. S. M. Tong, C.-W. Cheung, C. Yang, D. Zhou and C.-M. Che, *Inorg. Chem.*, 2017, **56**, 5046–5059.
- 210 M. Bachmann, O. Blacque and K. Venkatesan, *Chem. – Eur. J.*, 2017, **23**, 9451–9456.
- 211 L. Currie, J. Fernandez-Cestau, L. Rocchigiani, B. Bertrand, S. J. Lancaster, D. L. Hughes, H. Duckworth, S. T. Jones, D. Credgington and T. Penfold, *Chem. – Eur. J.*, 2017, **23**, 105–113.
- 212 B. Y.-W. Wong, H.-L. Wong, Y.-C. Wong, V. K.-M. Au, M.-Y. Chan and V. W. Yam, *Chem. Sci.*, 2017, **8**, 6936–6946.
- 213 J. Fernandez-Cestau, B. Bertrand, M. Blaya, G. A. Jones, T. J. Penfold and M. Bochmann, *Chem. Commun.*, 2015, **51**, 16629–16632.
- 214 W. P. To, D. Zhou, G. S. M. Tong, G. Cheng, C. Yang and C. Che, *Angew. Chem., Int. Ed.*, 2017, **56**, 14036–14041.
- 215 D. Zhou, G. Cheng, G. S. M. Tong and C. M. Che, *Chem. – Eur. J.*, 2020, **26**, 15718–15726.
- 216 D. Zhou, W. P. To, Y. Kwak, Y. Cho, G. Cheng, G. S. M. Tong and C. M. Che, *Adv. Sci.*, 2019, **6**, 1802297.
- 217 C. C. Au-Yeung, L.-K. Li, M.-C. Tang, S.-L. Lai, W.-L. Cheung, M. Ng, M.-Y. Chan and V. W.-W. Yam, *Chem. Sci.*, 2021, **12**, 9516–9527.
- 218 C. E. Johnson, J. Schwarz, M. Deegbey, O. Prakash, K. Sharma, P. Huang, T. Ericsson, L. Häggström, J. Bendix, A. K. Gupta, E. Jakubikova, K. Wärnmark and R. Lomoth, *Chem. Sci.*, 2023, **14**, 10129–10139.
- 219 L.-K. Li, C. C. Au-Yeung, M.-C. Tang, S.-L. Lai, W.-L. Cheung, M. Ng, M.-Y. Chan and V. W. Yam, *Mater. Horiz.*, 2022, **9**, 281–293.
- 220 D. Zhou, W. P. To, G. S. M. Tong, G. Cheng, L. Du, D. L. Phillips and C. M. Che, *Angew. Chem.*, 2020, **132**, 6437–6444.
- 221 W.-K. Kwok, L.-K. Li, S.-L. Lai, M.-Y. Leung, W. K. Tang, S.-C. Cheng, M.-C. Tang, W.-L. Cheung, C.-C. Ko, M.-Y. Chan and V. W.-W. Yam, *J. Am. Chem. Soc.*, 2023, **145**, 9584–9595.
- 222 M. Saigo, K. Miyata, S. I. Tanaka, H. Nakanotani, C. Adachi and K. Onda, *J. Phys. Chem. Lett.*, 2019, **10**, 2475–2480.
- 223 D. Zhou, W. To, G. Tong, G. Cheng, L. Du, D. Phillips and C. Che, *Angew. Chem., Int. Ed.*, 2020, **59**, 6375–6382.
- 224 K. Nozaki and M. Iwamura, *Highly efficient OLEDs: Materials based on thermally activated delayed fluorescence*, 2018, pp. 61–91.
- 225 J. Beaudelot, S. Oger, S. Peruško, T.-A. Phan, T. Teunens, C. Moucheron and G. Evano, *Chem. Rev.*, 2022, **122**, 16365–16609.
- 226 C. E. Housecroft and E. C. J. J. o M. C. C. Constable, *J. Mater. Chem. C*, 2022, **10**, 4456–4482.
- 227 G. U. Mahoro, E. Fresta, M. Elie, D. di Nasso, Q. Zhang, J.-F. Lohier, J.-L. Renaud, M. Linares, R. Wannemacher, J. Cabanillas-Gonzalez, R. D. Costa and S. Gaillard, *Dalton Trans.*, 2021, **50**, 11049–11060.
- 228 L. M. Cavinato, S. Wölfl, A. Pöthig, E. Fresta, C. Garino, J. Fernandez-Cestau, C. Barolo and R. D. Costa, *Adv. Mater.*, 2022, **34**, 2109228.
- 229 C. Sandoval-Pauker, M. Santander-Nelli and P. Dreyse, *RSC Adv.*, 2022, **12**, 10653–10674.
- 230 H. Takeda, A. Kobayashi and K. Tsuge, *Coord. Chem. Rev.*, 2022, **470**, 214700.
- 231 M. Klein, N. Rau, M. Wende, J. Sundermeyer, G. Cheng, C.-M. Che, A. Schinabeck and H. Yersin, *Chem. Mater.*, 2020, **32**, 10365–10382.
- 232 A. Kaeser, O. Moudam, G. Accorsi, I. Séguy, J. Navarro, A. Belbakra, C. Duhayon, N. Armaroli, B. Delavaux-Nicot and J.-F. Nierengarten, *Eur. J. Inorg. Chem.*, 2014, 1345–1355.
- 233 R. D. Costa, D. Tordera, E. Ortí, H. J. Bolink, J. Schönle, S. Graber, C. E. Housecroft, E. C. Constable and J. A. Zampese, *J. Mater. Chem.*, 2011, **21**, 16108–16118.
- 234 A. Kaeser, M. Mohankumar, J. Mohanraj, F. Monti, M. Holler, J. J. Cid, O. Moudam, I. Nierengarten, L. Karmazin-Brelot, C. Duhayon, B. Delavaux-Nicot, N. Armaroli and J. F. Nierengarten, *Inorg. Chem.*, 2013, **52**, 12140–12151.
- 235 C. Li, C. F. R. Mackenzie, S. A. Said, A. K. Pal, M. A. Haghighatbin, A. Babaei, M. Sessolo, D. B. Cordes, A. M. Z. Slawin, P. C. J. Kamer, H. J. Bolink, C. F. Hogan and E. Zysman-Colman, *Inorg. Chem.*, 2021, **60**, 10323–10339.
- 236 T. A. Phan, N. Armaroli, A. Saavedra Moncada, E. Bandini, B. Delavaux-Nicot, J. F. Nierengarten and D. J. A. C. Armspach, *Angew. Chem.*, 2023, **135**, e202214638.



- 237 M. Matejdes, M. Stöter, R. Czerwieniec, M. Leidl, S. Rosenfeldt, T. Schumacher, J. Albert, M. Lippitz, H. Yersin and J. Breu, *Adv. Opt. Mater.*, 2021, **9**, 2100516.
- 238 M. Mohankumar, M. Holler, E. Meichsner, J.-F. Nierengarten, F. Niess, J.-P. Sauvage, B. Delavaux-Nicot, E. Leoni, F. Monti, J. M. Malicka, M. Cocchi, E. Bandini and N. Armaroli, *J. Am. Chem. Soc.*, 2018, **140**, 2336–2347.
- 239 C. L. Linfoot, M. J. Leidl, P. Richardson, A. F. Rausch, O. Chepelin, F. J. White, H. Yersin and N. Robertson, *Inorg. Chem.*, 2014, **53**, 10854–10861.
- 240 M. Meyer, A. Prescimone, E. C. Constable and C. E. Housecroft, *Dalton Trans.*, 2024, **53**, 5453–5465.
- 241 D. Gejsnæs-Schaad, M. Meyer, A. Prescimone, C. E. Housecroft and E. C. Constable, *CrystEngComm*, 2023, **25**, 3000–3012.
- 242 I. Nohara, C. Wegeberg, M. Devereux, A. Prescimone, C. E. Housecroft and E. C. Constable, *J. Mater. Chem. C*, 2022, **10**, 3089–3102.
- 243 K. Zhang and D. Zhang, *Spectrochim. Acta, Part A*, 2014, **124**, 341–348.
- 244 M. Osawa and M. Hoshino, in *Highly Efficient OLEDs*, ed. H. Yersin, 2018, pp. 119–176.
- 245 S. Keller, E. C. Constable, C. E. Housecroft, M. Neuburger, A. Prescimone, G. Longo, A. Pertegás, M. Sessolo and H. J. Bolink, *Dalton Trans.*, 2014, **43**, 16593–16596.
- 246 R. Czerwieniec, K. Kowalski and H. Yersin, *Dalton Trans.*, 2013, **42**, 9826–9830.
- 247 R. Czerwieniec and H. Yersin, *Inorg. Chem.*, 2015, **54**, 4322–4327.
- 248 M. J. Leidl, V. A. Krylova, P. I. Djurovich, M. E. Thompson and H. Yersin, *J. Am. Chem. Soc.*, 2014, **136**, 16032–16038.
- 249 M. Elie, F. Sguerra, F. Di Meo, M. D. Weber, R. Marion, A. Grimault, J.-F. Lohier, A. Stallivieri, A. Brosseau, R. B. Pansu, J.-L. Renaud, M. Linares, M. Hamel, R. D. Costa and S. Gaillard, *ACS Appl. Mater. Interfaces*, 2016, **8**, 14678–14691.
- 250 M. Elie, M. D. Weber, F. Di Meo, F. Sguerra, J. F. Lohier, R. B. Pansu, J. L. Renaud, M. Hamel, M. Linares and R. D. Costa, *Chem. – Eur. J.*, 2017, **23**, 16328–16337.
- 251 A. M. T. Muthig, O. Mrózek, T. Ferschke, M. Rödel, B. Ewald, J. Kuhnt, C. Lenczyk, J. Pflaum and A. Steffen, *J. Am. Chem. Soc.*, 2023, **145**, 4438–4449.
- 252 A. Tsuboyama, K. Kuge, M. Furugori, S. Okada, M. Hoshino and K. Ueno, *Inorg. Chem.*, 2007, **46**, 1992–2001.
- 253 M. J. Leidl, F.-R. Kuchle, H. A. Mayer, L. Wesemann and H. Yersin, *J. Phys. Chem. A*, 2013, **117**, 11823–11836.
- 254 A. Schinabeck, J. Chen, L. Kang, T. Teng, H. H. H. Homeier, A. F. Suleymanova, M. Z. Shafikov, R. Yu, C.-Z. Lu and H. Yersin, *Chem. Mater.*, 2019, **31**, 4392–4404.
- 255 S. Igawa, M. Hashimoto, I. Kawata, M. Yashima, M. Hoshino and M. Osawa, *J. Mater. Chem. C*, 2013, **1**, 542–551.
- 256 V. A. Krylova, P. I. Djurovich, M. T. Whited and M. E. Thompson, *Chem. Commun.*, 2010, **46**, 6696–6698.
- 257 V. A. Krylova, P. I. Djurovich, B. L. Conley, R. Haiges, M. T. Whited, T. J. Williams and M. E. Thompson, *Chem. Commun.*, 2014, **50**, 7176–7179.
- 258 P. A. Breddels, P. A. Berdowski, G. Blasse and D. McMillin, *J. Chem. Soc., Faraday Trans. 2*, 1982, **78**, 595–601.
- 259 D. Felder, J.-F. Nierengarten, F. Barigelletti, B. Ventura and N. Armaroli, *J. Am. Chem. Soc.*, 2001, **123**, 6291–6299.
- 260 Z. A. Siddique, Y. Yamamoto, T. Ohno and K. Nozaki, *Inorg. Chem.*, 2003, **42**, 6366–6378.
- 261 N. C. Giebink and S. R. Forrest, *Phys. Rev. B: Condens. Matter Mater. Phys.*, 2008, **77**, 235215.
- 262 R. Czerwieniec, M. J. Leidl, H. H. H. Homeier and H. Yersin, *Coord. Chem. Rev.*, 2016, **325**, 2–28.
- 263 Y. Okano, H. Ohara, A. Kobayashi, M. Yoshida and M. Kato, *Inorg. Chem.*, 2016, **55**, 5227–5236.
- 264 A. V. Artem'ev, M. P. Davydova, A. S. Berezin, M. R. Ryzhikov and D. G. Samsonenko, *Inorg. Chem.*, 2020, **59**, 10699–10706.
- 265 X.-W. Zhang, C.-H. Huang, M. Yang, X.-L. Chen and C.-Z. Lu, *Dalton Trans.*, 2023, **52**, 9893–9898.
- 266 D. Volz, D. M. Zink, T. Bocksrocker, J. Friedrichs, M. Nieger, T. Baumann, U. Lemmer and S. Bräse, *Chem. Mater.*, 2013, **25**, 3414–3426.
- 267 C.-W. Hsu, C.-C. Lin, M.-W. Chung, Y. Chi, G.-H. Lee, P.-T. Chou, C.-H. Chang and P.-Y. Chen, *J. Am. Chem. Soc.*, 2011, **133**, 12085–12099.
- 268 M. Z. Shafikov, A. F. Suleymanova, R. Czerwieniec and H. Yersin, *Chem. Mater.*, 2017, **29**, 1708–1715.
- 269 M. Z. Shafikov, A. F. Suleymanova, R. Czerwieniec and H. Yersin, *Inorg. Chem.*, 2017, **56**, 13274–13285.
- 270 M. Z. Shafikov, A. F. Suleymanova, A. Schinabeck and H. Yersin, *J. Phys. Chem. Lett.*, 2018, **9**, 702–709.
- 271 X.-M. Gan, R. Yu, X.-L. Chen, M. Yang, L. Lin, X.-Y. Wu and C.-Z. Lu, *Dalton Trans.*, 2018, **47**, 5956–5960.
- 272 J.-H. Jia, D. Liang, R. Yu, X.-L. Chen, L. Meng, J.-F. Chang, J.-Z. Liao, M. Yang, X.-N. Li and C.-Z. Lu, *Chem. Mater.*, 2020, **32**, 620–629.
- 273 T. Teng, K. Li, G. Cheng, Y. Wang, J. Wang, J. Li, C. Zhou, H. Liu, T. Zou, J. Xiong, C. Wu, H.-X. Zhang, C.-M. Che and C. Yang, *Inorg. Chem.*, 2020, **59**, 12122–12131.
- 274 M. Osawa, M. Hashimoto, I. Kawata and M. Hoshino, *Dalton Trans.*, 2017, **46**, 12446–12455.
- 275 A. S. Romanov, S. T. Jones, L. Yang, P. J. Conaghan, D. Di, M. Linnolahti, D. Credgington and M. Bochmann, *Adv. Opt. Mater.*, 2018, **6**, 1801347.
- 276 D. Liang, J.-H. Jia, X.-B. Cai, Y.-Q. Zhao, Z.-Q. Wang and C.-Z. Lu, *Inorg. Chem. Front.*, 2022, **9**, 6561–6566.
- 277 A. Ying and S. Gong, *Chem. – Eur. J.*, 2023, **29**, e202301885.
- 278 T.-y Li, J. Schaab, P. I. Djurovich and M. E. Thompson, *J. Mater. Chem. C*, 2022, **10**, 4674–4683.
- 279 Y. Sakai, Y. Sagara, H. Nomura, N. Nakamura, Y. Suzuki, H. Miyazaki and C. Adachi, *Chem. Commun.*, 2015, **51**, 3181–3184.
- 280 B. Goswami, T. J. Feuerstein, R. Yadav, S. Lebedkin, P. J. Boden, S. T. Steiger, G. Niedner-Schatteburg, M. Gerhards, M. M. Kappes and P. W. Roesky, *Chem. – Eur. J.*, 2021, **27**, 15110–15119.
- 281 N. Lüdtke, J. Kuhnt, T. Heil, A. Steffen and C. M. Marian, *ChemPhotoChem*, 2023, **7**, e202200142.



- 282 O. Mrózek, M. Mitra, B. Hupp, A. Belyaev, N. Lüdtke, D. Wagner, C. Wang, O. S. Wenger, C. M. Marian and A. Steffen, *Chem. – Eur. J.*, 2023, **29**, e202203980.
- 283 M. Mitra, O. Mrózek, M. Putscher, J. Guhl, B. Hupp, A. Belyaev, C. M. Marian and A. Steffen, *Angew. Chem., Int. Ed.*, 2024, **63**, e202316300.
- 284 K. Zhang, X. Meng and L. He, *Inorg. Chem.*, 2023, **62**, 2135–2145.
- 285 G. Crosby, R. Highland and K. Truesdell, *Coord. Chem. Rev.*, 1985, **64**, 41–52.
- 286 R. G. Highland and G. A. Crosby, *Chem. Phys. Lett.*, 1985, **119**, 454–458.
- 287 R. G. Highland, J. G. Brummer and G. A. Crosby, *J. Phys. Chem.*, 1986, **90**, 1593–1598.
- 288 N. Lüdtke, A. Steffen and C. M. Marian, *Inorg. Chem.*, 2022, **61**, 20896–20905.
- 289 Innovation Center for Organic Electronics (INOEL), <https://inoel.yz.yamagata-u.ac.jp/research-group/>, <https://inoel.yz.yamagata-u.ac.jp/yu-flec/tech-result/>.
- 290 L. Bergmann, D. M. Zink, S. Bräse, T. Baumann and D. Volz, *Top. Curr. Chem.*, 2016, **374**, 22.
- 291 M. Godumala, S. Choi, M. J. Cho and D. H. Choi, *J. Mater. Chem. C*, 2016, **4**, 11355–11381.
- 292 B. Wex and B. R. Kaafarani, *J. Mater. Chem. C*, 2017, **5**, 8622–8653.
- 293 X. Cao, D. Zhang, S. Zhang, Y. Tao and W. Huang, *J. Mater. Chem. C*, 2017, **5**, 7699–7714.
- 294 Z. Yang, Z. Mao, Z. Xie, Y. Zhang, S. Liu, J. Zhao, J. Xu, Z. Chi and M. P. Aldred, *Chem. Soc. Rev.*, 2017, **46**, 915–1016.
- 295 X. Yang, X. Zhou, Y. X. Zhang, D. Li, C. Li, C. You, T. C. Chou, S. J. Su, P. T. Chou and Y. Chi, *Adv. Sci.*, 2022, **9**, e2201150.
- 296 A. Thamarappalli, C. S. K. Ranasinghe, J. Jang, M. Gao, P. L. Burn, E. V. Puttock and P. E. Shaw, *Adv. Funct. Mater.*, 2022, **32**, 2205077.
- 297 Y. Liu, Y. Xie, Y. Cheng, X. Tian, L. Hua, S. Ying, S. Yan and Z. Ren, *Chem. Eng. J.*, 2023, **455**, 140747.
- 298 J. Yan, S. F. Wang, C. H. Hsu, E. H. Shi, C. C. Wu, P. T. Chou, S. M. Yiu, Y. Chi, C. You, I. C. Peng and W. Y. Hung, *ACS Appl. Mater. Interfaces*, 2023, **15**, 21333–21343.
- 299 J. Yan, D. Y. Zhou, L. S. Liao, M. Kuhn, X. Zhou, S. M. Yiu and Y. Chi, *Nat. Commun.*, 2023, **14**, 6419.
- 300 Y. Miao, G. Wang, M. Yin, Y. Guo, B. Zhao and H. Wang, *Chem. Eng. J.*, 2023, **461**, 141921.
- 301 H. T. Kidanu and C.-T. Chen, *J. Mater. Chem. C*, 2021, **9**, 15470–15476.
- 302 Q. Wang, J.-Y. Wang, H. Zeng, L.-Y. Zhang and Z.-N. Chen, *Sci. China: Chem.*, 2022, **65**, 1559–1568.
- 303 Y. Feng, X. Zhuang, Y. Xu, J. Xue, C. Qu, Q. Wang, Y. Liu and Y. Wang, *Chem. Eng. J.*, 2023, **478**, 147123.
- 304 P. J. Conaghan, S. M. Menke, A. S. Romanov, S. T. Jones, A. J. Pearson, E. W. Evans, M. Bochmann, N. C. Greenham and D. Credgington, *Adv. Mater.*, 2018, **30**, 1870265.
- 305 R. Tang, S. Xu, L. Du, F. F. Hung, T. L. Lam, G. Cheng, K. H. Low, Q. Wan, S. Wu, Y. Chen and C. M. Che, *Adv. Opt. Mater.*, 2023, **11**, 2300950.
- 306 S. Avula, B. H. Jhun, U. Jo, S. Heo, J. Y. Lee and Y. You, *Adv. Sci.*, 2024, **11**, 2305745.
- 307 S. Heo, Y. Jung, J. Kim, I. Kim, H. J. Bae, W. J. Son, H. Choi and Y. You, *Adv. Opt. Mater.*, 2022, **10**, 2201610.
- 308 S. Cai, G. S. M. Tong, L. Du, G. K. So, F. F. Hung, T. L. Lam, G. Cheng, H. Xiao, X. Chang, Z. X. Xu and C. M. Che, *Angew. Chem.*, 2022, **61**, e202213392.
- 309 X. Feng, J. G. Yang, J. Miao, C. Zhong, X. Yin, N. Li, C. Wu, Q. Zhang, Y. Chen, K. Li and C. Yang, *Angew. Chem., Int. Ed.*, 2022, **61**, e202209451.
- 310 W. P. To, D. Zhou, G. S. M. Tong, G. Cheng, C. Yang and C. M. Che, *Angew. Chem.*, 2017, **129**, 14224–14229.
- 311 D. Zhou, G. S. M. Tong, G. Cheng, Y. K. Tang, W. Liu, D. Ma, L. Du, J. R. Chen and C. M. Che, *Adv. Mater.*, 2022, **34**, e2206598.
- 312 C. C. Au-Yeung, M. Y. Leung, S. L. Lai, S. C. Cheng, L. K. Li, M. C. Tang, W. K. Kwok, C. C. Ko, M. Y. Chan and V. W. Yam, *Mater. Horiz.*, 2024, **11**, 151–162.
- 313 L. K. Li, W. K. Kwok, M. C. Tang, W. L. Cheung, S. L. Lai, M. Ng, M. Y. Chan and V. W. Yam, *Chem. Sci.*, 2021, **12**, 14833–14844.
- 314 C. Y. Wong, M. C. Tang, L. K. Li, M. Y. Leung, W. K. Tang, S. L. Lai, W. L. Cheung, M. Ng, M. Y. Chan and V. W. Yam, *Chem. Sci.*, 2022, **13**, 10129–10140.
- 315 M. Osawa, I. Kawata, R. Ishii, S. Igawa, M. Hashimoto and M. Hoshino, *J. Mater. Chem. C*, 2013, **1**, 4375–4383.
- 316 D. Di, A. S. Romanov, L. Yang, J. M. Richter, J. P. H. Rivett, S. Jones, T. H. Thomas, M. Abdi Jalebi, R. H. Friend, M. Linnolahti, M. Bochmann and D. Credgington, *Science*, 2017, **356**, 159–163.
- 317 X.-L. Chen, R. Yu, Q.-K. Zhang, L.-J. Zhou, X.-Y. Wu, Q. Zhang and C.-Z. Lu, *Chem. Mater.*, 2013, **25**, 3910–3920.
- 318 D. Volz, Y. Chen, M. Wallesch, R. Liu, C. Fléchon, D. M. Zink, J. Friedrichs, H. Flügge, R. Steininger and J. Göttlicher, *Adv. Mater.*, 2015, **27**, 2538–2543.
- 319 M. Osawa, M. Hoshino, M. Hashimoto, I. Kawata, S. Igawa and M. Yashima, *Dalton Trans.*, 2015, **44**, 8369–8378.
- 320 X.-L. Chen, C.-S. Lin, X.-Y. Wu, R. Yu, T. Teng, Q.-K. Zhang, Q. Zhang, W.-B. Yang and C.-Z. Lu, *J. Mater. Chem. C*, 2015, **3**, 1187–1195.
- 321 D. Liang, X.-L. Chen, J.-Z. Liao, J.-Y. Hu, J.-H. Jia and C.-Z. Lu, *Inorg. Chem.*, 2016, **55**, 7467–7475.
- 322 F. Zhang, Y. Guan, X. Chen, S. Wang, D. Liang, Y. Feng, S. Chen, S. Li, Z. Li and F. Zhang, *Inorg. Chem.*, 2017, **56**, 3742–3753.
- 323 X. Hong, B. Wang, L. Liu, X.-X. Zhong, F.-B. Li, L. Wang, W.-Y. Wong, H.-M. Qin and Y. H. Lo, *J. Lumin.*, 2016, **180**, 64–72.
- 324 Y.-H. Zhou, A.-W. Zhang, R.-J. Huang, Y.-H. Sun, Z.-J. Chen, B.-S. Zhu and Y.-X. Zheng, *J. Mater. Chem. C*, 2023, **11**, 1329–1335.
- 325 M. Wallesch, A. Verma, C. Fléchon, H. Flügge, D. M. Zink, S. M. Seifermann, J. M. Navarro, T. Vitova, J. Göttlicher and R. Steininger, *Chem. – Eur. J.*, 2016, **22**, 16400–16405.
- 326 J. Zhang, C. Duan, C. Han, H. Yang, Y. Wei and H. Xu, *Adv. Mater.*, 2016, **28**, 5975–5979.



- 327 L. Lin, D.-H. Chen, R. Yu, X.-L. Chen, W.-J. Zhu, D. Liang, J.-F. Chang, Q. Zhang and C.-Z. Lu, *J. Mater. Chem. C*, 2017, **5**, 4495–4504.
- 328 G. K. M. So, G. Cheng, J. Wang, X. Chang, C. C. Kwok, H. Zhang and C. M. Che, *Chem. – Asian J.*, 2017, **12**, 1490–1498.
- 329 S. Shi, M. C. Jung, C. Coburn, A. Tadde, D. Sylvinson MR, P. I. Djurovich, S. R. Forrest and M. E. Thompson, *J. Am. Chem. Soc.*, 2019, **141**, 3576–3588.
- 330 H. J. Wang, Y. Liu, B. Yu, S. Q. Song, Y. X. Zheng, K. Liu, P. Chen, H. Wang, J. Jiang and T. Y. Li, *Angew. Chem., Int. Ed.*, 2023, **62**, e202217195.
- 331 A. Ying, Y. H. Huang, C. H. Lu, Z. Chen, W. K. Lee, X. Zeng, T. Chen, X. Cao, C. C. Wu, S. Gong and C. Yang, *ACS Appl. Mater. Interfaces*, 2021, **13**, 13478–13486.
- 332 R. Tang, S. Xu, T. L. Lam, G. Cheng, L. Du, Q. Wan, J. Yang, F. F. Hung, K. H. Low, D. L. Phillips and C. M. Che, *Angew. Chem., Int. Ed.*, 2022, **61**, e202203982.
- 333 M. Olaru, E. Rychagova, S. Ketkov, Y. Shynkarenko, S. Yakunin, M. V. Kovalenko, A. Yablonskiy, B. Andreev, F. Kleemiss and J. Beckmann, *J. Am. Chem. Soc.*, 2019, **142**, 373–381.
- 334 B.-K. Guo, F. Yang, Y.-Q. Wang, Q. Wei, L. Liu, X.-X. Zhong, L. Wang, J.-K. Gong, F.-B. Li and W.-Y. Wong, *J. Lumin.*, 2020, **220**, 116963.
- 335 T. Teng, J. Xiong, G. Cheng, C. Zhou, X. Lv and K. Li, *Molecules*, 2021, **26**, 1125.
- 336 A. Ruduss, B. Turovska, S. Belyakov, K. A. Stucere, A. Vembris, G. Baryshnikov, H. Agren, J. C. Lu, W. H. Lin, C. H. Chang and K. Traskovskis, *ACS Appl. Mater. Interfaces*, 2022, **14**, 15478–15493.
- 337 J. Guo, Z. Zhang, P. Wu, J. Zhu, D. Dou, Z. Liao, R. Xia, K. Wang and Z. Wang, *J. Lumin.*, 2021, **239**, 118354.
- 338 G. Cheng, D. Zhou, U. Monkowius and H. Yersin, *Micro-machines*, 2021, **12**, 1500.
- 339 S. Keller, F. Brunner, J. M. Junquera-Hernandez, A. Pertegas, M. G. La-Placa, A. Prescimone, E. C. Constable, H. J. Bolink, E. Orti and C. E. Housecroft, *ChemPlusChem*, 2018, **83**, 217–229.
- 340 M. Alkan-Zambada, S. Keller, L. Martínez-Sarti, A. Prescimone, J. M. Junquera-Hernández, E. C. Constable, H. J. Bolink, M. Sessolo, E. Ortí and C. E. Housecroft, *J. Mater. Chem. C*, 2018, **6**, 8460–8471.
- 341 S. Keller, A. Pertegás, G. Longo, L. Martínez, J. Cerdá, J. M. Junquera-Hernández, A. Prescimone, E. C. Constable, C. E. Housecroft and E. Ortí, *J. Mater. Chem. C*, 2016, **4**, 3857–3871.
- 342 M. D. Weber, M. Viciano-Chumillas, D. Armentano, J. Cano and R. D. Costa, *Dalton Trans.*, 2017, **46**, 6312–6323.
- 343 S. Keller, A. Prescimone, M. G. La Placa, J. M. Junquera-Hernandez, H. J. Bolink, E. C. Constable, M. Sessolo, E. Orti and C. E. Housecroft, *RSC Adv.*, 2020, **10**, 22631–22644.
- 344 G. Giobbio, L. M. Cavinato, E. Fresta, A. Montrieul, G. L. Umuhire Mahoro, J. François, J.-L. Renaud, M. Linares, S. Gaillard and R. D. Costa, *Adv. Funct. Mater.*, 2023, **33**, 2304668–2304678.
- 345 M. D. Weber, E. Fresta, M. Elie, M. E. Miehlich, J. L. Renaud, K. Meyer, S. Gaillard and R. D. Costa, *Adv. Funct. Mater.*, 2018, **28**, 1707423.
- 346 L. Zhang, B. Li and Z. Su, *J. Phys. Chem. C*, 2009, **113**, 13968–13973.
- 347 M. Wallesch, D. Volz, D. M. Zink, U. Schepers, M. Nieger, T. Baumann and S. Bräse, *Chem. – Eur. J.*, 2014, **20**, 6578–6590.
- 348 M. Hashimoto, S. Igawa, M. Yashima, I. Kawata, M. Hoshino and M. Osawa, *J. Am. Chem. Soc.*, 2011, **133**, 10348–10351.
- 349 Q. Zhang, T. Komino, S. Huang, S. Matsunami, K. Goushi and C. Adachi, *Adv. Funct. Mater.*, 2012, **22**, 2327–2336.
- 350 D. R. Evans and C. A. Reed, *J. Am. Chem. Soc.*, 2000, **122**, 4660–4667.
- 351 J. C. Deaton, S. C. Switalski, D. Y. Kondakov, R. H. Young, T. D. Pawlik, D. J. Giesen, S. B. Harkins, A. J. Miller, S. F. Mickenberg and J. C. Peters, *J. Am. Chem. Soc.*, 2010, **132**, 9499–9508.
- 352 Z. Liu, M. F. Qayyum, C. Wu, M. T. Whited, P. I. Djurovich, K. O. Hodgson, B. Hedman, E. I. Solomon and M. E. Thompson, *J. Am. Chem. Soc.*, 2011, **133**, 3700–3703.
- 353 X. Liu, T. Zhang, T. Ni, N. Jiang, Z. Liu, Z. Bian, Z. Lu and C. Huang, *Adv. Funct. Mater.*, 2014, **24**, 5385–5392.
- 354 G. Cheng, G. K.-M. So, W.-P. To, Y. Chen, C.-C. Kwok, C. Ma, X. Guan, X. Chang, W.-M. Kwok and C.-M. Che, *Chem. Sci.*, 2015, **6**, 4623–4635.
- 355 Q. Zhang, X.-L. Chen, J. Chen, X.-Y. Wu, R. Yu and C.-Z. Lu, *Dalton Trans.*, 2015, **44**, 10022–10029.
- 356 X. Li, H. Yan and Q. Zhao, *Chem. – Eur. J.*, 2016, **22**, 1888–1898.
- 357 B. P. Dash, R. Satapathy, E. R. Gaillard, J. A. Maguire and N. S. Hosmane, *J. Am. Chem. Soc.*, 2010, **132**, 6578–6587.
- 358 A. Ferrer-Ugalde, A. González-Campo, C. Viñas, J. Rodríguez-Romero, R. Santillan, N. Farfán, R. Sillanpää, A. Sousa-Pedrares, R. Núñez and F. Teixidor, *Chem. – Eur. J.*, 2014, **20**, 9940–9951.
- 359 R. Núñez, P. Farràs, F. Teixidor, C. Viñas, R. Sillanpää and R. Kivekäs, *Angew. Chem.*, 2006, **118**, 1292–1294.
- 360 L. Zhu, W. Lv, S. Liu, H. Yan, Q. Zhao and W. Huang, *Chem. Commun.*, 2013, **49**, 10638–10640.
- 361 C. Shi, H. Sun, Q. Jiang, Q. Zhao, J. Wang, W. Huang and H. Yan, *Chem. Commun.*, 2013, **49**, 4746–4748.
- 362 N. S. Hosmane, *Boron science: new technologies and applications*, CRC Press, 2016.
- 363 H. Naito, Y. Morisaki and Y. Chujo, *Angew. Chem., Int. Ed.*, 2015, **54**, 5084–5087.
- 364 A. Ferrer-Ugalde, E. J. Juárez-Pérez, F. Teixidor, C. Viñas, R. Sillanpää, E. Pérez-Inestrosa and R. Núñez, *Chem. – Eur. J.*, 2012, **18**, 544–553.
- 365 Y. Ma, S. Liu, H. Yang, Y. Wu, C. Yang, X. Liu, Q. Zhao, H. Wu, J. Liang and F. Li, *J. Mater. Chem.*, 2011, **21**, 18974–18982.
- 366 A. M. Prokhorov, T. Hofbeck, R. Czerwieniec, A. F. Suleymanova, D. N. Kozhevnikov and H. Yersin, *J. Am. Chem. Soc.*, 2014, **136**, 9637–9642.



- 367 J. Guo, D. Liu, J. Zhang, J. Zhang, Q. Miao and Z. Xie, *Chem. Commun.*, 2015, **51**, 12004–12007.
- 368 C. Shi, H. Sun, X. Tang, W. Lv, H. Yan, Q. Zhao, J. Wang and W. Huang, *Angew. Chem.*, 2013, **125**, 13676–13680.
- 369 M. Mohankumar, F. Monti, M. Holler, F. Niess, B. Delavaux-Nicot, N. Armaroli, J. P. Sauvage and J. F. Nierengarten, *Chem. – Eur. J.*, 2014, **20**, 12083–12090.
- 370 M. Mohankumar, M. Holler, J. F. Nierengarten and J. P. Sauvage, *Chem. – Eur. J.*, 2012, **18**, 12192–12195.
- 371 N. Armaroli, G. Accorsi, M. Holler, O. Moudam, J. F. Nierengarten, Z. Zhou, R. T. Wegh and R. Welter, *Adv. Mater.*, 2006, **18**, 1313–1316.
- 372 D. G. Cuttall, S.-M. Kuang, P. E. Fanwick, D. R. McMillin and R. A. Walton, *J. Am. Chem. Soc.*, 2002, **124**, 6–7.
- 373 S.-M. Kuang, D. G. Cuttall, D. R. McMillin, P. E. Fanwick and R. A. Walton, *Inorg. Chem.*, 2002, **41**, 3313–3322.
- 374 G. A. Blake, J. P. Moerdyk and C. W. Bielawski, *Organometallics*, 2012, **31**, 3373–3378.
- 375 M. Braun, W. Frank, G. J. Reiss and C. Ganter, *Organometallics*, 2010, **29**, 4418–4420.
- 376 T. W. Hudnall and C. W. Bielawski, *J. Am. Chem. Soc.*, 2009, **131**, 16039–16041.
- 377 V. César, N. Lugan and G. Lavigne, *Eur. J. Inorg. Chem.*, 2010, 361–365.
- 378 L. Kang, J. Chen, T. Teng, X.-L. Chen, R. Yu and C.-Z. Lu, *Dalton Trans.*, 2015, **44**, 11649–11659.
- 379 P. Jin, Z. Zhou, H. Wang, J. Hao, R. Chen, J. Wang and C. Zhang, *J. Phys. Chem. Lett.*, 2022, **13**, 2516–2522.
- 380 E. Fresta, M. D. Weber, J. Fernandez-Cestau and R. D. J. A. O. M. Costa, *Adv. Opt. Mater.*, 2019, **7**, 1900830.
- 381 S. Lipinski, L. M. Cavinato, T. Pickl, G. Biffi, A. Pöthig, P. B. Coto, J. Fernández-Cestau and R. Costa, *Adv. Opt. Mater.*, 2023, **11**, 2203145.
- 382 E. Fresta, J. M. Carbonell-Vilar, J. Yu, D. Armentano, J. Cano, M. Viciano-Chumillas and R. D. J. A. F. M. Costa, *Adv. Funct. Mater.*, 2019, **29**, 1901797.
- 383 E. Fresta and R. D. Costa, *Adv. Funct. Mater.*, 2020, **30**, 1908176.
- 384 R. Bai, X. Meng, X. Wang and L. He, *Adv. Funct. Mater.*, 2021, **31**, 2007167.
- 385 Y.-M. Wang, F. Teng, Y.-B. Hou, Z. Xu, Y.-S. Wang and W.-F. Fu, *Appl. Phys. Lett.*, 2005, **87**, 233512.
- 386 M. D. Weber, C. Garino, G. Volpi, E. Casamassa, M. Milanesio, C. Barolo and R. D. Costa, *Dalton Trans.*, 2016, **45**, 8984–8993.
- 387 G. Kalyuzhny, M. Buda, J. McNeill, P. Barbara and A. J. Bard, *J. Am. Chem. Soc.*, 2003, **125**, 6272–6283.
- 388 E. Fresta, G. Volpi, M. Milanesio, C. Garino, C. Barolo and R. D. Costa, *Inorg. Chem.*, 2018, **57**, 10469–10479.
- 389 O. Moudam, A. C. Tsipis, S. Kommanaboyina, P. N. Horton and S. J. Coles, *RSC Adv.*, 2015, **5**, 95047–95053.
- 390 J. Ràfols-Ribé, E. Gracia-Espino, S. Jenatsch, P. Lundberg, A. Sandström, S. Tang, C. Larsen and L. J. A. O. M. Edman, *Adv. Opt. Mater.*, 2021, **9**, 2001405.
- 391 M. D. Weber, J. E. Wittmann, A. Burger, O. B. Malcıoğlu, J. Segarra-Martí, A. Hirsch, P. B. Coto, M. Bockstedte and R. D. J. A. F. M. Costa, *Adv. Funct. Mater.*, 2016, **26**, 6737–6750.
- 392 E. Fresta, K. Baumgärtner, J. Cabanillas-Gonzalez, M. Mastalerz and R. D. Costa, *Nanoscale Horiz.*, 2020, **5**, 473–480.
- 393 E. Fresta, J. Dosso, J. Cabanillas-Gonzalez, D. Bonifazi and R. D. Costa, *ACS Appl. Mater. Interfaces*, 2020, **12**, 28426–28434.
- 394 E. Fresta, J. Dosso, J. Cabanillas-González, D. Bonifazi and R. Costa, *Adv. Funct. Mater.*, 2020, **30**, 1906830.
- 395 S. Keller, A. Prescimone, H. Bolink, M. Sessolo, G. Longo, L. Martínez-Sarti, J. M. Junquera-Hernández, E. C. Constable, E. Ortí and C. E. Housecroft, *Dalton Trans.*, 2018, **47**, 14263–14276.
- 396 Y. Liu, C. Li, Z. Ren, S. Yan and M. R. Bryce, *Nat. Rev. Mater.*, 2018, **3**, 18020.
- 397 M. Karaman, A. Kumar Gupta, S. Madayanad Suresh, T. Matulaitis, L. Mardegan, D. Tordera, H. J. Bolink, S. Wu, S. Warriner, I. D. Samuel and E. Zysman-Colman, *Beilstein J. Org. Chem.*, 2022, **18**, 1311–1321.
- 398 K. Zhang, X. Pang, Y. Song, Y. Xiu, R. Yu and L. He, *Adv. Opt. Mater.*, 2024, **12**, 2400467.

